

Diss. ETH No. 19842

Functional bone imaging in an *in vivo* mouse model of bone adaptation, aging and disease

A dissertation submitted to

ETH ZURICH

for the degree of

Doctor of Sciences

presented by

Floor Lambers

Master of Science

born 25th of September, 1981

Amsterdam, The Netherlands

accepted on the recommendation of

Prof. Dr. Ralph Müller, examiner

Prof. Dr. Markus Rudin, co-examiner

Dr. med. vet. Gisela Kuhn, co-examiner

2011

Table of Contents

Acknowledgements	iii
Summary	vii
Zusammenfassung	xi
1 Introduction	1
1.1 Motivation for thesis	1
1.2 Specific aims	4
1.3 Outline of the thesis	4
2 Background	7
2.1 Bone remodeling and adaptation	9
2.2 <i>In vivo</i> models of bone formation	12
2.3 Age-related changes in bone microstructure	17
2.4 Effect of disease on bone microstructure	18
2.5 Multimodality imaging in bone research	31
3 Functional bone imaging in an <i>in vivo</i> mouse model of bone adaptation	73
3.1 Load-induced bone adaptation	75
3.2 Optimization of <i>in vivo</i> response to mechanical loading	105
3.3 Longitudinal effects of load adaptation	111
3.4 Multimodality imaging of load-induced bone adaptation	127
4 Functional bone imaging in an <i>in vivo</i> mouse model of aging and disease	147
4.1 Validation of osteoporosis model	149
4.2 Effect of age on bone microstructure	171
4.3 Effect of age on mechanosensitivity	191
5 Synthesis	211
5.1 Main findings and implications	211
5.2 Limitations / evaluation of methods	218

Table of Contents

5.3	Future research	221
5.4	Conclusions	225
	Curriculum Vitae	227

Acknowledgements

During the end of my studies Biomedical Engineering I realized the joy that research brought me, and decided to look for a Ph.D. position. I wanted to see another institute and broaden my horizon by moving abroad. Luckily Prof. Dr. Keita Ito knew that Prof. Dr. Ralph Müller was looking for a doctoral candidate and suggested I apply. After the following interview and visit to the ETH I knew "I want to work with these people!" and was extremely happy to hear that I was accepted for the position. My expectations have been fulfilled; the Institute for Biomechanics truly is a great group of people to work with, where everybody makes time to help each other, creating a stimulating environment. Also, the genuine interest in personal circumstances made it fun to share lunch breaks, aperitifs, and outside-of-work activities with the Institute. I am very thankful to all of the former and present members of the Institute for making these past four years a great time. I am grateful for all of those that have encouraged me in this work, and helped me to achieve this goal of writing my Ph.D. thesis. I would like to specifically express my gratitude to a number of people without whom the present thesis would never have been as successful.

Prof. Dr. Ralph Müller, thank you for giving me the opportunity to accomplish my Ph.D. thesis at your Institute. I have enjoyed your enthusiastic manner of discussing about research, and admire your always one step-ahead thinking. Your advise has been invaluable, and taught me a great deal on what is important for writing high quality papers. Your motivation and interest made me confident and helped me a lot when I was overwhelmed with all the work. Furthermore, I appreciated your social interaction at conferences and Institute events.

I am equally grateful to my other supervisor Dr. med. vet. Gisela Kuhn. I appreciated you always being there for me for all kinds of questions, work related or not, and for your trust in me. You taught me a lot about bone biology and helped me gain expertise in how to plan and perform laboratory animal experiments correctly. But next to work, you also organized several group activities and put value on getting to know each other, which made the work environment pleasant.

Thank you also for pushing the work forward and for your practical help during the experiments (so that I could have a lunch break). I am not sure whether the word exists, but you have been a great Doctor-mother!

I would also like to acknowledge Prof. Dr. Markus Rudin, for enabling collaboration with the Animal Imaging Center and for the input as a co-examiner from which this work has benefited.

Dear Dr. Friederike Schulte, I particularly appreciated to be a super team with you and to share so much with you, both at and outside of work. If it was not for you, this work would not have been as complete. Thank you for all the useful programs you developed and I could use, and even more for all the inspiring discussions (often with a cup of tea) about the interpretation of results and approaches for tackling problems with the data analysis. It was great to undertake many fun activities with you, Jens, and Lara in Zurich, Scotland, and Lindenberg. I cherish our friendship and your listening ear and am sure that we will long continue to stay friends.

Special thanks also go to Claudia Weigt and Kathleen Koch for making the vivaCT room have some "sunlight"! Your support was enormously appreciated. Claudia, I have been amazed about your profound animal-knowledge, which was of great use for me. I enjoyed the activities you organized, e.g. the BBQs in your WG, and hope that in a few years from now we can look back on many more good times together. Kathleen, your drive, initiative, and quick grasping of all procedures contributed to this work. Your amusing stories were a welcome distraction during all the measurements.

I am grateful for all those that gave me technical support. Dr. Duncan Webster and Dr. Elad Wasserman thanks for your help and for explaining me the surgical and loading methods. Thanks go to Dr. Martin Stauber and Dr. Thomas Kohler for their support with the *in vivo* micro-CT scanner and help with image analysis scripts. Peter Schwilch and Marco Hitz thanks for the help with the design and development of the CT mouse holders, loading device, and for the attempt to optimize the pinning procedure. David Christen, thanks for your support with sapho (my linux system). I would like to thank all other members of the Institute for Biomechanics for their contributions.

I would also like to express my gratitude to Dr. Florian Stuker and Katerina Dikaiou for helpful support on fluorescence molecular tomography and for their friendly collaboration.

Regine Ochsner and all other tapdancers, I have learned a new hobby through you! Thank you for all the fun lectures, workshops, and shows: they were very stimulating.

Furthermore, I am very thankful to all my friends who showed me the other important things in life. I extremely enjoyed your open doors, your taking me out, and your visits, usually inherent to a dinner with a glass of wine, cups of tea, hiking, and dancing. This gave me a good time outside of work.

Special thanks also go to my family in law: Herman, Marijke, Bart, Beryl, Rob, Geertje, Merlijn and Julia for the frequent visits, encouraging cards, drawings and words, dazzling cocktails, and for letting us use your homes as Bed&Breakfast. I owe very special thanks to my twinbrother Jeroen and sister Irene. By choosing a completely different career you taught me how to put my work in a different perspective and made me realize that research was the right choice for me. I loved to hear from your diverse experiences of traveling, costumer-contacts, and photoshoots which helped me to relativate my work. I am proud of you!

I am forever thankful to my parents who always encouraged and believed in me during all these years of studying. I am very happy that I could always follow my own interest and that you shared similar interests with me. Hans and Wietske, I feel very blessed that we could discuss about my work and the problems I encountered. Thank you for your share in amusement, taking us on holidays, and for your everlasting love.

Jochem, without you I would never have made it. Thank you for all your support, love, and sweet encouragement. Thank you for moving to Switzerland for me, spending great weekends in the mountains with me, cooking delicious dinners for me, and last but not least for showing interest in my work, and actually understanding it!

Finally, financial support of the European Union for the osteoporotic virtual physiological human project (VPHOP FP7-ICT2008-223865) is gratefully acknowledged.

June 2011
Floor Lambers

Summary

Healthy bone adapts its microstructure to optimally withstand loads with a minimal bone mass through balanced bone resorption (governed by osteoclasts) and formation (governed by osteoblasts). In several bone diseases, with osteoporosis being the most common, this balance is disturbed, with bone resorption exceeding bone formation. This results in a deterioration of the bone microstructure, and consequently leads to an increased fragility and susceptibility to fracture. The cause for this shift in the bone remodeling balance is not well understood, and a major topic of research. By using *in vivo* mouse models that resemble human physiology, and imaging modalities that allow visualization of the bone microstructure, as well as bone dynamics in a longitudinal manner (functional imaging), better insight in bone remodeling can be gained. With these imaging modalities, the present thesis is divided into three aims: (i) to develop a functional bone imaging approach for an *in vivo* mouse model, (ii) to apply the functional bone imaging approach to monitor *in vivo* load adaptation, and (iii) to apply the functional bone imaging approach to monitor osteoporosis and aging.

Initially, in order to develop a functional bone imaging approach, *in vivo* micro-computed tomography (micro-CT) and fluorescence molecular tomography (FMT), two relatively new imaging techniques that allow longitudinal 3D assessment of bone, were examined. From *in vivo* micro-CT data, dynamic bone parameters can be extracted which correspond to a measure of cell activity; that is, bone formation parameters represent osteoblast activity and resorption parameters describe osteoclast activity. Similarly, from FMT measurements, osteoblast activity can be determined from the intensity of the fluorescence signal. This signal depends on how much of a fluorophore, which is linked to a reporter that binds with great affinity to newly mineralizing surfaces, is present. The decrease in fluorescence, caused by resorption of the fluorescent label, represents osteoclast activity. Even though both imaging methods are reproducible and have specific advantages, the spatial resolution of FMT is too low to allow selection of the region of interest only, and thus the sensitivity is limited for our purpose. Consequently, the functional imaging approach with *in vivo* micro-CT was chosen for further use.

Previously, an *in vivo* loading mouse model had been developed at the Institute for Biomechanics, which enables application of controlled loads to a caudal vertebra. This model is used, together with the functional bone imaging approach to investigate load adaptation to 8 N in the sixth caudal vertebra (CV6) in comparison to a non loaded control group. Results show that loading significantly increases bone formation rate by 23% and significantly decreases bone resorption rate by 25%. Regarding the shape of the remodeling sites, the surface of the remodeling sites is modulated 3 to 4 times more than the thickness of formation packages or depth of resorption pits. As the amount of remodeling sites is constant over time, this indicates that load-induced bone adaptation is governed by an increase in net osteoblastic activity and a decrease in net osteoclastic activity. Furthermore, the change in bone strength is significantly correlated with the change in bone volume density, suggesting that remodeling is targeted, and consequently leads to an overall increase in bone strength for the loaded group.

To investigate how bone remodeling is influenced by disease, ovariectomy, the most commonly used model for postmenopausal osteoporosis, was examined for its effect on bone microstructure, bone remodeling, and bone strength. Similarly to osteoporosis in humans, high turnover bone loss is observed, with the bone formation rate 1.6 times greater and bone resorption rate 3.7 times greater for ovariectomized than for sham operated mice. Also, as with human osteoporosis, ovariectomy causes a direct increase in bone resorption rate, while the increase in bone formation rate lags behind (remodeling transient). This leads to a deterioration of the bone microstructure, with a tremendous decline in bone volume density of 35% and cortical area fraction of 9%. Furthermore, in agreement with an increase in bone fragility in osteoporotic humans, strain energy density, which is inversely related to bone strength, increases by 37% in the proximal and 50% in the distal region of the trabecular bone. In conclusion, CV6 is a suitable skeletal site to use as a model for postmenopausal osteoporosis.

To investigate the effect of aging on bone remodeling, mice were monitored with the functional bone imaging approach between an age of 16 and 88 weeks. In CV6, bone formation rate and bone resorption rate reduce drastically with age, while the bone volume density and bone strength continue to increase with age, with a stabilization around an age of 52 weeks. In the tibia, the bone volume fraction reduces from an early age. Nevertheless, the resistance to bending and torsion as observed from micro-CT data is sustained, indicating that bones remain mechanosensitive. To further substantiate this observation, load-induced bone adaptation was monitored in mice aged 15, 52 and 82 weeks. For all three age groups there is a beneficial effect of

loading on the bone microstructure and on bone remodeling. Bone formation rates are increased, while bone resorption rates are decreased compared to non loaded controls. Furthermore, for all three age groups bone is formed at sites subjected to high loads, and resorbed at sites subjected to low loads, leading to an overall increase in bone strength. This further supports the premise that CV6 remains mechanosensitive throughout aging.

In conclusion, the application of a functional imaging approach, as developed in this Ph.D. thesis, is shown to be very useful for gaining new insights in how bone remodeling is influenced by mechanical loading, disease or aging. In future, this functional imaging approach will facilitate further exploration of bone remodeling in a number of treatments, strengthen the understanding of the relation between bone remodeling and micro-mechanical environment, and permit investigation of genetic and molecular pathways involved in bone remodeling and bone adaptation.

Zusammenfassung

Gesunder Knochen passt seine Mikrostruktur mittels ausgewogenem Knochenabbau (durch Osteoklasten) und Knochenaufbau (durch Osteoblasten) laufend an, um Belastungen mit einem Minimum an Material widerstehen zu können. Bei verschiedenen Knochenkrankheiten, von denen Osteoporose die häufigste ist, ist diese Balance gestört, wobei die Abbaurate höher als die Neubildung von Knochen ist. Dies führt zu einer Auflösung/Zerfall der Mikrostruktur woraus eine erhöhte Knochenbrüchigkeit resultiert, die mit einem erhöhten Frakturrisiko einhergeht. Der Grund für diese Verschiebung des Gleichgewichts ist noch weitgehend unverstanden und deshalb von grossem Interesse für die Forschung. Mit Hilfe von *in vivo* Maus Modellen, die die menschliche Physiologie widerspiegeln, sowie Bildgebungstechniken, die die Möglichkeit bieten, sowohl die Knochenstruktur zu visualisieren, als auch dynamische Prozesse im Knochen über einen längeren Zeitraum zu beobachten, kann ein besserer Einblick in den Knochenstoffwechsel gewonnen werden. Anhand dieser Kriterien wurden die folgenden drei Hauptziele dieser Dissertation definiert: (i) Entwicklung einer funktionellen Knochenbildungsmethode für ein *in vivo* Maus Modell, (ii) Anwendung der funktionellen Knochenbildungsmethode auf ein Modell für mechanische Adaptation, (iii) Anwendung der funktionellen Knochenbildungsmethode um Osteoporose und das Altern zu beobachten.

Bei der Entwicklung der funktionellen Knochenbildungsmethode lag der Schwerpunkt auf *in vivo* Mikro-Computertomographie (Mikro-CT) und Fluoreszenz-Molekular-Tomographie (FMT). *In vivo* Mikro-CT Aufnahmen erlaubten die Analyse statischer und dynamischer Knochenparameter über einen längeren Zeitraum, während mit Hilfe von FMT Erkenntnisse über die Osteoblasten- und Osteoklastenaktivität erlangt werden konnten. Beide Bildgebungsmethoden waren reproduzierbar. Während der Vorteil des Mikro-CT die hohe räumliche Auflösung von 10,5 μm war, zeichnete sich FMT durch kurze Aufnahmezeiten aus. Allerdings war die räumliche Auflösung des FMT zu gering, um Messungen nur in der relevanten Region durchzuführen, wodurch die Sensitivität des FMT für unsere Zwecke nicht ausreichte. Daher wurde für weitere Experimente die funktionale Bildgebungsmethode mit *in vivo* Mikro-CT gewählt.

Am Institut für Biomechanik ist bereits ein *in vivo* Maus Modell entwickelt worden, welches es ermöglicht den 6. Schwanzwirbel kontrolliert einer Belastung durch mechanische Kräfte auszusetzen. Dieses Modell wurde mit funktioneller Knochenbildung kombiniert, um zu untersuchen, wie der Knochen sich an die Belastung anpasst. Durch die mechanische Belastung stieg die Knochenaufbaurrate in einem höheren Mass, als die Knochenabbaurate sank. Während sich die Umbaufläche vergrösserte, waren kaum Veränderungen in der Dicke des neugebildeten Knochen oder der Tiefe der Resorptionslakunen zu sehen. Da die Anzahl der Umbaustellen während der Messungen konstant blieb, kann davon ausgegangen werden, dass die Anpassung des Knochens auf die Einwirkung der mechanischen Kraft durch eine Erhöhung der Osteoblastenaktivität sowie Verringerung der Osteoklastenaktivität geschieht. Ausserdem korrelierte die Veränderung der Knochenfestigkeit signifikant mit Veränderungen der Knochendichte. Dies lässt den Schluss zu, dass der Umbau gezielt abläuft und mechanische Belastung die Knochenfestigkeit insgesamt verbessert.

Um zu erforschen wie Krankheiten den Knochenumbau beeinflussen, wurde die Auswirkung einer Ovariectomie, welche ein weit verbreitetes Modell für postmenopausale Osteoporose ist, auf die Knochenmikrostruktur, den Knochenumbau und die Knochenfestigkeit untersucht. Ähnlich wie beim Menschen stieg durch die Ovariectomie die Knochenresorptionsrate sofort an, während der Anstieg der Knochenaufbaurrate erst später erfolgte. Dies führte zu einer Zerstörung der Knochenmikrostruktur, die von einer starken Verringerung der trabekulären Knochendichte und dem Anteil der kortikalen Knochenfläche begleitet war, wodurch auch die Knochenfestigkeit sank. Somit kann gefolgert werden, dass der 6. Schwanzwirbel geeignet ist, postmenopausale Osteoporose zu imitieren.

Des Weiteren wurde der Einfluss des Alterns auf den Knochenumbau untersucht. Dafür wurden mit der funktionellen Knochenbildungsmethode Messungen an Mäusen in einem Alter von 16 bis 88 Wochen durchgeführt. Im Laufe des Alterns sanken sowohl die Knochenaufbau-, als auch die Knochenabbaurate im 6. Schwanzwirbel drastisch, während die trabekuläre Knochendichte und die Knochenfestigkeit zunächst anstiegen und ab einem Alter von etwa 52 Wochen stabil blieben. In der Tibia sank die trabekuläre Knochendichte bereits frühzeitig, jedoch blieb die Widerstandsfähigkeit gegen Verbiegen und Verdrehen bewahrt, was schlussfolgern lässt, dass die Knochen weiterhin mechanosensitiv sind. Um dies tiefergehend zu erforschen, wurde die Belastungs-induzierte Knochenanpassung an Mäusen untersucht, die bei Versuchsbeginn 15; 52 oder 82 Wochen alt waren. Bei allen drei Altersgruppen konnte durch diese Belastung ein positiver Effekt auf die

Knochenmikrostruktur und den Knochenumbau festgestellt werden. Im Vergleich zur nichtbelasteten Kontrollgruppe war die Knochenaufbaurrate erhöht und die Knochenabbaurate erniedrigt. Alle drei Altersgruppen zeigten darüber hinaus einen Knochenaufbau an Stellen mit starker mechanischer Belastung, während an kaum belasteten Stellen Knochen resorbiert wurde, was insgesamt zu einem Anstieg der Knochenfestigkeit führte. Dies unterstützt die Annahme, dass der 6. Schwanzwirbel auch mit dem Alter mechanosensitiv bleibt.

Zusammenfassend lässt sich sagen, dass die Anwendung der in dieser Doktorarbeit entwickelten funktionellen Bildgebungsmethode neue Einblicke in die Beeinflussung des Knochenumbaus durch mechanische Belastung, Krankheit und Altern verschafft. Zukünftig wird diese Bildgebungsmethode hilfreich sein, den Knochenumbau bei verschiedenen Behandlungen zu erforschen, das Verständnis für die Verbindung zwischen Knochenumbau und dem mikromechanischen Umfeld zu verbessern und es erlauben verschiedene genetische und molekulare Prozesse des Knochenumbaus zu untersuchen.

Chapter 1

Introduction

1.1 Motivation for thesis

In healthy bone there is a balance between osteoclasts that resorb bone by secreting acids and proteases, and osteoblasts that form new bone by laying down bone matrix, later mineralizing to yield mature bone. This is a continuous and dynamic process called bone remodeling, through which the bone microstructure is modulated and renewed with the purpose of preserving bone strength. The fact that bone remodeling is important for maintaining bone strength at a global level has already been observed a long time ago [1]. This relationship is commonly known as Wolff's law and implicates that the bone microstructure adapts to its micro-mechanical environment and mechanical need, by forming bone at sites subjected to high strains and removing bone at sites subjected to low strains [2]. Nevertheless, in several bone diseases, with osteoporosis being the most common one, bone remodeling is disturbed, resulting in a deterioration of the bone microstructure, and consequently leads to an increased fragility and susceptibility for fractures. It is known that in osteoporosis bone resorption exceeds bone formation, but the mechanisms underlying this shift in the bone remodeling balance remain unclear. It is important, however, to get a more fundamental understanding of bone remodeling in health and disease, and how this is influenced by mechanical forces, as this would likely aid in the development of safer and more efficient treatment for bone diseases and disorders. Thus, there is need for a more thorough exploration of the mechanisms that control bone remodeling.

To investigate the effect of mechanical forces on bone remodeling, several *in vivo* mouse models have been developed. Although animal physiology cannot directly be compared to human physiology, animal models that approximate human characteristics are essential for research purposes [3]. Most animal loading

models rely on mice, because they show similarities to human bone remodeling, are cheap, are easy to handle and house, and with the genome being mapped, enable genetic manipulations [4]. A model in which caudal vertebrae are loaded has been developed at the Institute for Biomechanics [5]. The advantage of this model over other loading models [6–11] is firstly, that the whole bone can be imaged at high resolution, and owing to the relatively simple geometry, enables to create finite element models with more realistic boundary conditions. Secondly, the caudal vertebra includes both trabecular and cortical bone, making it possible to study load-induced effects in both types of bone. Thirdly, as a relatively large volume of trabecular bone is present, gene detection technologies which require a large trabecular volume can be used in the future. Fourthly, it contains yellow bone marrow, and is thus less sensitive to radiation, and suitable for investigating aging or ovariectomy. Fifthly, the caudal vertebrae are less dependent of the activity level of the mouse. The combination of this loading model with recently developed imaging techniques enables to investigate the effect of mechanical forces on bone remodeling.

To investigate the effect of aging and disease on bone remodeling, several animal models exist. The effect of aging is most often evaluated by analyzing bone structural parameters at the tibia or lumbar vertebrae at multiple ages in mice [12–14]. To mimic the most common bone disease, osteoporosis, inbred mice that spontaneously develop senile osteoporosis (SAMP6) exist [15, 16]. A more commonly used animal model to study osteoporosis is the removal of the ovaries (ovariectomy) [17–19], leading to an estrogen-deficiency induced bone loss. Also unloading models, which cause bone loss due to a lack of mechanical forces acting on the bone, are widely used to investigate osteoporosis-like bone loss [20]. With these existing models important regulators of bone remodeling can be studied.

The previously described models most often were of cross-sectional nature. This can sometimes complicate evaluation or obscure the results. For example, when differences between treatment and control groups are found, this can either be an effect of different starting values, or truly an effect of the treatment. In a cross-sectional study, it is impossible to control for this possibility and thus to be sure about the outcome of the study. On the contrary, when longitudinal *in vivo* study designs are used, this possibility can be ruled out. The exact effect of treatment can be analyzed by using normalization techniques, or comparing end and start points with one another, removing the possibility that initial values determine

the outcomes. Another advantage of *in vivo* study designs over cross-sectional study designs is that effects can be visualized and localized *in vivo*. Therefore, there is a need for *in vivo* monitoring of the effect of bone adaptation, aging and disease on bone remodeling.

A few years ago *in vivo* micro-computed tomography (micro-CT) for rodents was developed. This imaging technique makes it possible to scan the bone microstructure of rodents at multiple time points at high resolution, through which changes in the bone microstructure as an effect of load adaptation, aging or disease can accurately be analyzed. Furthermore, by registering follow-up scans, the exact location of bone formation and bone resorption can be visualized and quantified, enabling the calculation of dynamic bone parameters in single animals over time [21]. Up till now it was only possible to determine bone dynamic parameters from histology in a cross-sectional manner, or from non-specific systemic biochemical markers. Additionally, *in vivo* micro-CT data can be converted in micro-finite element models, which grants access to the estimation of bone strength of the whole bone and local strain signals. The combination of monitoring the bone microstructure, dynamic bone parameters, and mechanical parameters over time allows functional bone imaging and is a great advantage over more traditional imaging techniques.

Functional imaging refers to imaging techniques that can further enhance the understanding of bone remodeling, and are methods through which biological pathways underlying anatomical changes can be elucidated. Recently, *in vivo* fluorescence molecular tomography (FMT) was developed. This imaging technique allows to visualize 3D fluorophore distributions, which are linked to cell activity or gene expression. OsteoSense[®]680 is such a fluorophore, which binds to newly forming bone surfaces, and thus enables to measure osteoblast activity *in vivo*.

The combination of complimentary imaging techniques such as FMT and micro-CT, so called multimodality imaging, is promising for gaining a more fundamental understanding of bone remodeling, as it permits the simultaneous visualization of biological processes, such as the osteoblast activity, and changes in the bone microstructure. The longitudinal application of functional imaging approaches are indispensable for understanding the influence of bone adaptation, aging and disease on bone remodeling.

1.2 Specific aims

The global aim of this thesis was to elucidate how bone remodeling is affected by load adaptation, aging and disease, by using a functional imaging approach in an *in vivo* mouse model. Specifically, the following three aims were defined:

Specific aim 1 Development of a functional bone imaging approach in an *in vivo* mouse model.

Specific aim 2 Application of a functional bone imaging approach to monitor *in vivo* load adaptation.

Specific aim 3 Application of a functional bone imaging approach to monitor osteoporosis and aging.

1.3 Outline of the thesis

Chapter 2 provides the background for this thesis. The first part describes the stimuli for bone remodeling, gives an overview of the current *in vivo* loading models, and describes the influence of aging and bone diseases on the bone microstructure. In the second part of this chapter available multimodality imaging approaches in bone research are reviewed.

Chapter 3 deals with the application of functional and multimodality imaging of load adaptation. Firstly, functional bone imaging of load-induced adaptation is provided. Secondly, it was investigated whether the loading response could be further optimized by reducing the amount of cycles or the load, but keeping the anabolic effect, and additionally, the long-term effect of loading was investigated. Thirdly, it was investigated whether multimodality imaging would enhance the understanding of load-induced bone adaptation.

Chapter 4 describes the application of the developed functional imaging approach in osteoporosis and aging. In the first part, a novel murine osteoporosis model is validated. The second part concerns aging, i.e. firstly describes normal aging patterns, and secondly the influence of aging on load-induced bone adaptation.

Chapter 5 is the synthesis of this thesis. This chapter first gives an overview of the most important findings, then evaluates the techniques that were used in the thesis, and lastly provides an outlook for future research.

The development of the functional imaging approach is described elsewhere (<http://e-collection.library.ethz.ch/collection/>).

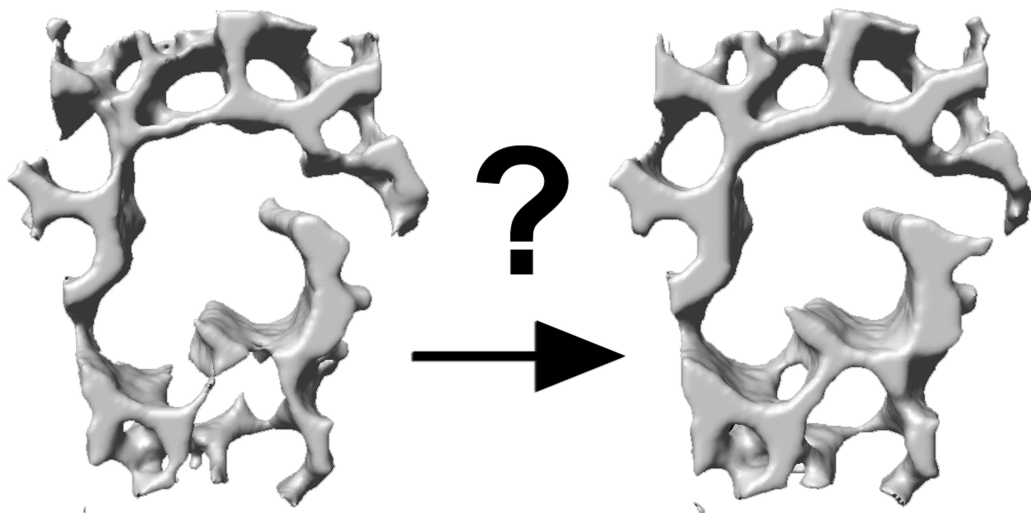
References

- [1] J. Wolff. *Das Gesetz der Transformation der Knochen (The law of bone remodeling)*. Springer-Verlag, Berlin, Germany, 1892.
- [2] H.M. Frost. Bone's mechanostat: a 2003 update. *Anat Rec A Discov Mol Cell Evol Biol*, 275(2):1081–1101, 2003.
- [3] S. Reinwald and D. Burr. Review of nonprimate, large animal models for osteoporosis research. *J Bone Miner Res*, 23(9):1353–1368, 2008.
- [4] R.F. Klein. Genetics of osteoporosis—utility of mouse models. *J Musculoskeletal Neuronal Interact*, 8(4):287–290, 2008.
- [5] Webster D.J., Morley P.L., van Lenthe G.H., and Müller R. A novel in vivo mouse model for mechanically stimulated bone adaptation—a combined experimental and computational validation study. *Comput Methods Biomech Biomed Engin*, 11(5):435–441, 2008.
- [6] P. Zhang, S.M. Tanaka, H. Jiang, M. Su, and H. Yokota. Diaphyseal bone formation in murine tibiae in response to knee loading. *J Appl Physiol*, 100(5):1452–1459, 2006.
- [7] A.G. Robling and C.H. Turner. Mechanotransduction in bone: genetic effects on mechanosensitivity in mice. *Bone*, 31(5):562–569, 2002.
- [8] A.G. Robling, D.B. Burr, and C.H. Turner. Partitioning a daily mechanical stimulus into discrete loading bouts improves the osteogenic response to loading. *J Bone Miner Res*, 15(8):1596–1602, 2000.
- [9] C. Rubin, R. Recker, D. Cullen, J. Ryaby, J. McCabe, and K. McLeod. Prevention of postmenopausal bone loss by a low-magnitude, high-frequency mechanical stimuli: a clinical trial assessing compliance, efficacy, and safety. *J Bone Miner Res*, 19(3):343–351, 2004.
- [10] C. Rubin, A.S. Turner, R. Müller, E. Mittra, K. McLeod, W. Lin, and Y.X. Qin. Quantity and quality of trabecular bone in the femur are enhanced by a strongly anabolic, noninvasive mechanical intervention. *J Bone Miner Res*, 17(2):349–357, 2002.
- [11] M.C.H. van der Meulen, X. Yang, T.G. Morgan, and M.P.G. Bostrom. Bone remodelling algorithms incorporating both strain and microdamage stimuli. *Clin Orthop Relat Res*, 467(8):1381–1391, 2009.

- [12] V. Glatt, E. Canalis, L. Stadmeier, and M.L. Bouxsein. Age-related changes in trabecular architecture differ in female and male C57BL/6J mice. *J Bone Miner Res*, 22(8):1197–1207, 2007.
- [13] B.P. Halloran, V.L. Ferguson, S.J. Simske, A. Burghardt, L.L. Venton, and S. Majumdar. Changes in bone structure and mass with advancing age in the male C57BL/6J mouse. *J Bone Miner Res*, 17(6):1044–1050, 2002.
- [14] M.D. Willinghamm, M.D. Brodt, K.L. Lee, A.L. Stephens, J. Ye, and M.J. Silva. Age-related changes in bone structure and strength in female and male BALB/c mice. *Calcif Tissue Int*, 86(6):470–483, 2010.
- [15] M.J. Silva, M.D. Brodt, and B.A. Uthgenannt. Morphological and mechanical properties of caudal vertebrae in the SAMP6 mouse model of senile osteoporosis. *Bone*, 35(2):425–431, 2004.
- [16] H. Chen, X. Zhou, S. Emura, and S. Shoumura. Site-specific bone loss in senescence-accelerated mouse (SAMP6): a murine model for senile osteoporosis. *Exp Gerontol*, 44(12):792–798, 2009.
- [17] M.L. Bouxsein, K.S. Myers, K.L. Shultz, L.R. Donahue, C.J. Rosen, and W.G. Beamer. Ovariectomy-induced bone loss varies among inbred strains of mice. *J Bone Miner Res*, 20(7):1085–1092, 2005.
- [18] U.T. Iwaniec, D. Yuan, R.A. Power, and T.J. Wronski. Strain-dependent variations in the response of cancellous bone to ovariectomy in mice. *J Bone Miner Res*, 21(7):1068–1074, 2006.
- [19] C.Y. Li, M.B. Schaffler, H.T. Wolde-Semait, C.J. Hernandez, and K.J. Jepsen. Genetic background influences cortical bone response to ovariectomy. *J Bone Miner Res*, 20(12):2150–2158, 2005.
- [20] J.E.M. Brouwers, F.M. Lambers, B. van Rietbergen, K. Ito, and R. Huiskes. Comparison of bone loss induced by ovariectomy and neurectomy in rats analyzed by in vivo micro-CT. *J Orthop Res*, 27(11):1521–1527, 2009.
- [21] F.A. Schulte, F.M. Lambers, G. Kuhn, and R. Müller. In vivo micro-computed tomography allows direct three-dimensional quantification of both bone formation and bone resorption parameters using time-lapsed imaging. *Bone*, 48:433–442, 2011.

Chapter 2

Background



2.1 Bone remodeling and adaptation

Bone is a dynamic tissue that adapts continuously to its mechanical needs. Bone is added where it is needed to maintain its mechanical integrity and removed from sites where the load is no longer being transferred through the bone. In healthy bone there is a balance between the osteoblasts that form new bone by laying down bone matrix, which later mineralizes to yield mature bone, and the osteoclasts that resorb the bone by secreting acids and proteases. However, with high impact loading as in sports or absence of loading as in long bed rest, there is a net gain or loss of bone mass respectively. It has been demonstrated that mechanical loading leads to an increase in bone formation [1] and bone strength [2]. Accordingly, with unloading the bone mass decreases [3] and subsequently the strength of the bone is diminished [4].

Osteocytes are further differentiated osteoblasts that have become completely embedded in the bone matrix. It is believed that osteocytes act as mechanosensors in bone. Osteocytes can detect mechanical stimuli and send signals to other effector cells that regulate bone formation and resorption [5]. Pathways suggested for how osteocytes detect mechanical stimuli include fluid flow that can be sensed by the osteocyte processes [6], strain energy density [7], and micro-damage [8], however the exact mechanisms remain unclear.

Osteocytes exposed to mechanical stimuli release signals that inhibit osteoclast formation [5]. The amount of osteoclast formation is controlled by the binding of RANK-L (receptor activator of nuclear factor κ B ligand) to the RANK (receptor activator of nuclear factor κ B) receptors on osteoclasts and preosteoclasts. Osteoprotegerin (OPG) blocks the RANK receptors by competitive binding to RANK-L binding sites, and consequently reduces the osteoclast formation and induces osteoclast apoptosis [9]. Ichinose et al. showed that tail-suspended rats treated with OPG improved bone mineral content, bone mineral density and bone strength to the levels of normally loaded rats treated with vehicle. Thus when osteocytes do not inhibit osteoclast formation due to the absence of mechanical stimuli, OPG may inhibit this unloading-induced bone loss [10].

Anabolic signals that are released in the bone within seconds after loading involve a cascade of events including ATP and Ca^{2+} signaling, prostaglandin (PG) and nitric oxide (NO) release, and Wnt/ β -catenin signaling [12]. As shown in figure 2.1, fluid shear forces on marrow stromal cells may stimulate nitric oxide synthase (NOS)

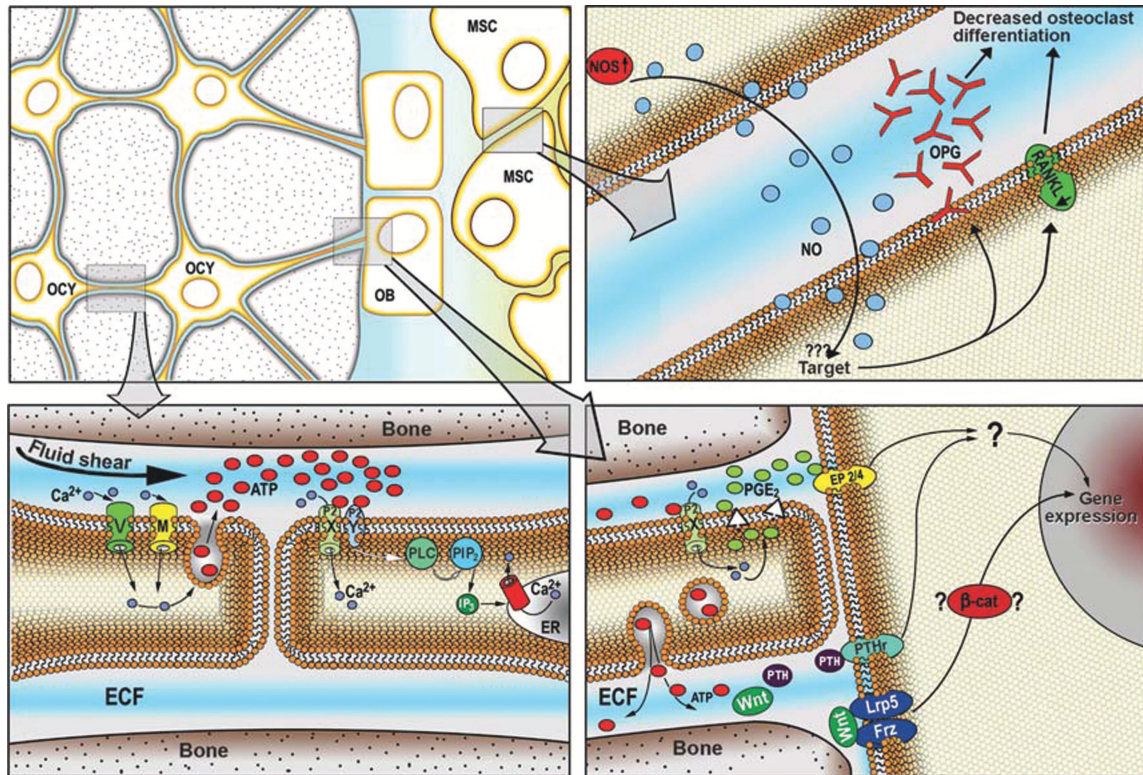


Figure 2.1: Model for mechanotransduction in bone. OCY = osteocyte, MSC = marrow stromal cell, OB = osteoblast. (Reproduced from [11]).

activity and NO release, which is a strong inhibitor of bone resorption by increasing OPG. Fluid shear stress on osteocytes induces an influx of extracellular Ca^{2+} , enhancing ATP release, which in turn causes release of PG. Of the PGs produced in bone PGE_2 is the most common. PGE_2 undergoes interaction with G-protein coupled receptors such as EP_2 and EP_4 and can stimulate bone formation. It has been suggested that PGE_2 is crucial to the initial transduction of the mechanical stimulus into an osteogenic response [13].

Cyclooxygenase-2 (COX-2) is an enzyme that catalyzes the rate limiting step in the synthesis of PGs. PGs secondary to COX-2 expression decreased osteoblastic proliferation in cultured calvarial cells but increased growth of osteoblastic precursors in marrow stromal cell (MSC) cultures [14]. When rats underwent mechanical loading of the tibia, and an agonist for EP_4 was administered, bone mineral content increased significantly compared to the rats that had been treated with vehicle [15]. Rats treated with a COX-2 inhibitor during the early stages of fracture repair showed significantly reduced mechanical properties of the fracture callus at later stages of healing and the proportion of nonunions in the animals

increased [16]. Similarly when rats underwent mechanical loading in the tibia with four-point bending, the bone formation rate increased, however when the rats were treated with a COX-2 inhibitor the bone formation was blocked completely [17].

NOS is an enzyme that synthesizes NO. Early release of NO is a key signal in the transduction of mechanical stimuli into subsequent bone formation [13, 18]. The endothelial NOS pathway plays an essential role in regulating bone mass and bone turnover by modulating osteoblast function [19]. When rats were subjected to mechanical bending of the tibia and treated with a competitive inhibitor of NOS, the bone formation was reduced by 66% compared to the control group. However, nonloaded or sham loaded limbs were not affected by the treatment. This also suggests that NO plays a role in mechanotransduction [20]. When female mice were administered 17β -estradiol (E_2) in combination with an inhibitor of NOS for 24 days the bone formation was significantly reduced compared to bone formation when only E_2 was administered [21].

Another anabolic pathway that appears to be activated after mechanical loading is the canonical Wnt/ β -catenin pathway. It has been proposed that Wnt/ β -catenin is an initiator of load-induced bone formation [22]. Transgenic mice, with denser and stronger bones, and non-transgenic mice were monitored for expression of Wnt/ β -catenin target genes after loading of the tibia. The expression of the Wnt/ β -catenin target genes increased for the transgenic mice and a similar increase was observed when non-transgenic mice were treated with a canonical Wnt pathway activator. These results support the theory that the Wnt/ β -catenin signaling plays a role in the response to mechanical loading and enhances the sensitivity of osteocytes [23].

Insulin-like growth factors (IGFs) are involved in bone formation after mechanical stimulation. Six hours after four-point bending of the tibial shaft in rats, IGF binding protein 2 (IGFBP-2) mRNA expression was not affected in osteoblasts, bone marrow cells and chondrocytes, but had increased in endocortical osteocytes; thus mechanical stimulation modulates IGFBP-2 mRNA expression in osteocytes [24]. Caudal vertebral compression of rats increased IGF-I expression slightly earlier than the increase seen in trabecular bone formation, suggesting a role for IGF-I in the osteogenic response [25]. When transgenic mice over-expressing IGF-I underwent loading, the periosteal bone formation was elevated 5-fold compared to wildtypes [26]. In rats that were neurectomized 9% of bone mineral density was lost, however when treated with IGF-II/IGFBP-2 this loss was completely

prevented. On the control limb there was no loss of bone mineral density and treatment resulted in a 9% increase of BMD [27]. IGF-I also increased trabecular bone formation and osteoblastic cell proliferation in hindlimb unloaded rats [28].

Sclerostin, the protein of the SOST gene, is expressed by mature osteocytes and inhibits the differentiation and mineralization of murine preosteoblastic cells [29]. Sclerostin has antagonistic effects on the Wnt/ β -catenin pathway and therefore might be important in mechanotransduction [12]. When the mechanoregulation of SOST and sclerostin were investigated under ulnar loading and under hindlimb unloading, it was found that sclerostin levels were dramatically reduced by ulnar loading, but significantly increased by hindlimb unloading, suggesting that sclerostin levels appear to be tuned by mechanical stimulation [30].

Parathyroid hormone (PTH) can stimulate bone formation, or enhance bone healing in rats that underwent osteotomy [31]. PTH administration also can prevent immobilization-induced bone loss by suppressing the osteoclast formation and by increasing osteoblast number and bone formation [32–36]. When rats were immobilized for 18 weeks and subsequently remobilized for 20 weeks the reloading could not recover the cortical bone mass, but PTH treatment could restore immobilization induced bone loss independently of mechanical stimulation. However, when PTH treatment was combined with remobilization, a synergistic anabolic effect on bone formation occurred which increased the cross-sectional area [37]. Also when rats were treated with PTH, bone formation was not significantly changed; but when it was combined with loading, the bone formation increased by 53% and 76% on the endocortical and periosteal surfaces, respectively [38]. A mechanism by which PTH potentiates mechanical responsiveness could be by enabling Ca^{2+} influx pathways in osteocytes [39]. PTH has no influence on the Wnt/ β -catenin pathway [40], but suppresses SOST expression [41].

An understanding of the biological pathways by which mechanical forces regulate the structure of bone would provide opportunities to develop new and adequate treatment for bone diseases and disorders.

2.2 *In vivo* models of bone formation

To better understand the processes of bone remodeling, different models for *in vivo* loading of bones have been developed to study bone adaptation. Models described

are knee loading, ulna loading, three-and four-point bending of the tibia, whole body vibration, femur loading, and caudal vertebra loading. These models are shown and described below. Thereafter the findings of these studies are shortly summarized.

In the knee loading model (Fig.2.2a), mechanical loads are applied with a piezoelectric loader to one knee. The lateral and the medial sides of the tibia are in contact to the loader and the stator, respectively. To position the knee properly for the loading experiment, lateral and medial condyles of the tibia are confined in a semispherical cup at the upper end of the supporter. The medial and lateral epicondyles of the femur are confined in a cup at the lower end of the loading rod. The tip of the loader has a contact area of 4 mm in diameter. To avoid a local stress concentration between the knee and the loader, both the loading surface and supporter are covered with silicon rubber [42].

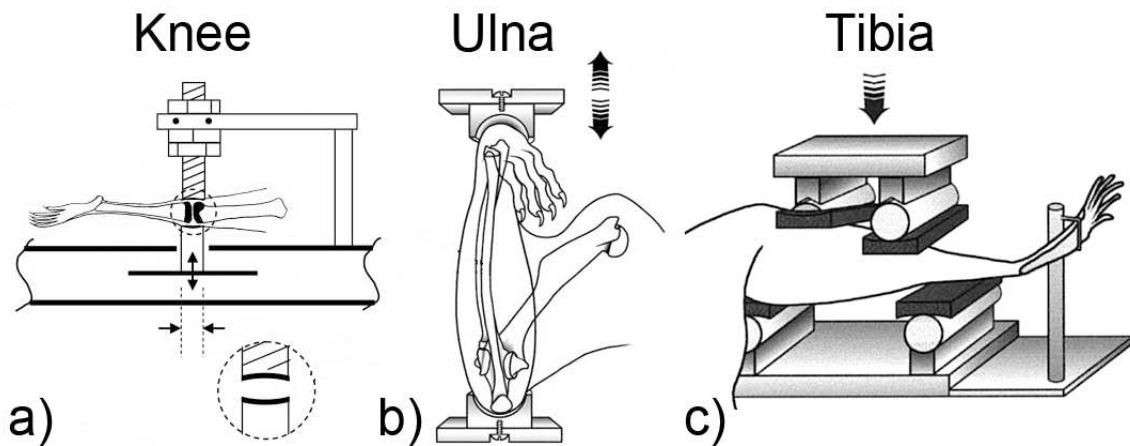


Figure 2.2: Image of a) the knee loading model, b) the ulna loading model, and c) the four-point bending model (Reproduced from [42–44]).

In the ulna loading model (Fig.2.2b) the distal forelimb is subjected to axially applied compressive loads using a nonsurgical loading preparation that transmits mechanical forces to the ulna through the olecranon and flexed carpus. The natural curvature of the ulnar diaphysis results in a bending moment in the middiaphysis that produces tension in the lateral cortex and compression in the medial cortex. The system consists of four computer-driven bimorph-type piezoelectric actuators with feedback control at $250 \mu\text{s}$ intervals enabled by a load cell. Load is applied using an open loop stepper motor-driven spring linkage [43, 45]. A similar model has been developed more recently to compress the tibia [26, 46, 47].

In the four-point bending device (Fig.2.2c) the lateral side of the tibia is placed in compression and the medial surface in tension. The loading pads are arranged such that they squeeze the leg without creating significant bending moments. Loading is applied by an open-loop stepper motor driven spring linkage. The loading apparatus incorporates a load cell so the applied load on each rat tibia can be monitored [48]. For controls either an untreated group or a load-control group (0 strain) is used.

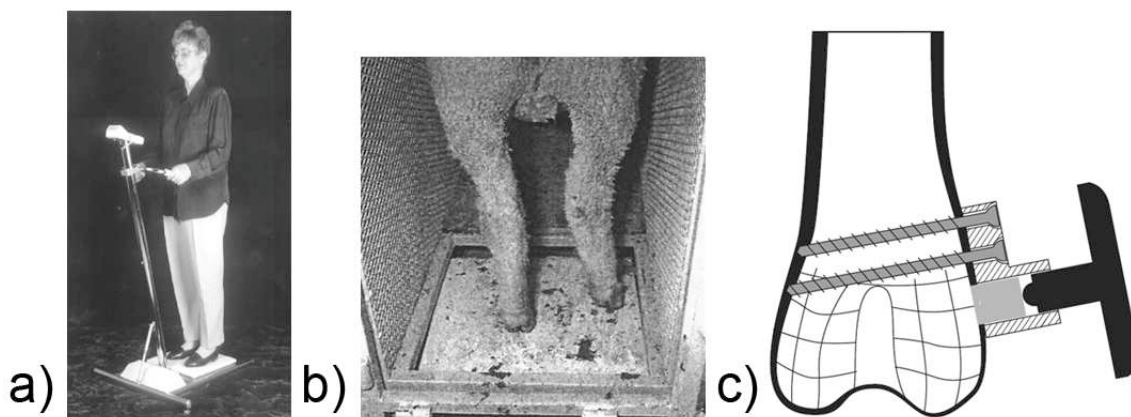


Figure 2.3: Image of a) the human vibration plate, b) the sheep vibration model, and c) the rabbit femur loading model (Reproduced from [49–51]).

The only loading modality that is currently implemented for humans is whole body vibration, where one stands on a vibration plate (Fig.2.3a). In the animal model, sheep are only standing on the plate with their hindlimbs (Fig.2.3b), and in the case of mice or rats, the animals are anesthetized while laying on the vibration plate or have only one hindlimb connected to the vibration [1, 52, 53]. High frequency vibration produces small displacements and generates strains in cortical bone below those associated with physical activity [54].

In the rabbit femur loading model a device is implanted bilaterally into the distal femur. The device consists of a stationary base mounted on the lateral femoral condyle, a movable loading core, and a top through which by rotation, loads can be applied manually (Fig. 2.3c). The loading core extends through the cortex, allowing directly loading of the trabecular bone. Loading is applied to the right leg, while the left leg serves as sham control [55].

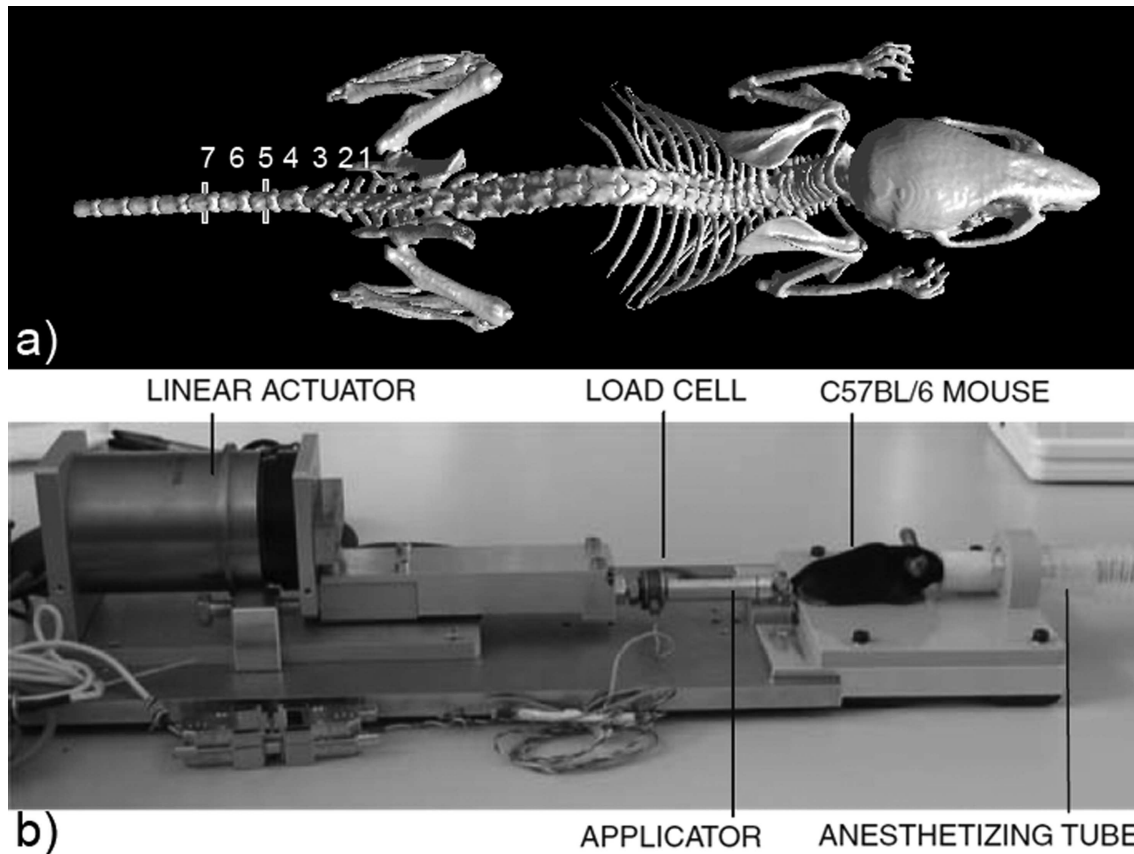


Figure 2.4: Image of a) A whole mouse skeleton, showing the position of the pins to allow for loading and numbers indicating the number of caudal vertebra, b) the caudal vertebra axial compression device (Reproduced from [56]).

A Caudal Vertebra Axial compression Device (CVAD) was developed at the Institute for Biomechanics, ETH Zurich, for caudal vertebral loading [57]. The CVAD is a closed, dual loop force controlled system consisting of two identical loading axes, where each axis is comprised of a linear voice coil connected in series to a load cell (Fig.2.4b). Axial, cyclic compression of the sixth caudal vertebra is achieved by transmitting the applied force via two metallic pins inserted into adjacent vertebrae (C5 and C7, Fig.2.4a). By clamping the proximal pin and securely connecting the distal pin to the sliding structure driven by the linear actuator, the target vertebra can be cyclically compressed [56]. The rationale for choosing this loading setup is that with caudal vertebral compression the loading is controllable (unlike whole body vibration), purely compression (unlike the bending or ulna loading models), and that the mouse tail is naturally not weight bearing, thus mechanically-induced changes seen in the bone are mostly an effect of the mechanical loading through CVAD.

Rats that had undergone ulna loading for 5 weeks had a 100-fold increase in fatigue resistance compared to unloaded rats as assessed by mechanical testing [2]. Sheep subjected to extremely low hindlimb vibration for 20 min/day for one year had significant increases in bone mineral content and in strength in the loading direction [50]. Also women that stood on a vibration plate for 10 min/day for one year had increases in bone mineral density [49, 58]. Mice that were hindlimb suspended and underwent vibrational loading for 20 min/day for 5 days/week in one of the hindlimbs had 70% greater bone formation rates in the loaded hindlimb than the non loaded hindlimb [59]. From these results it could be suggested that loading always increased the bone formation. However, when the ulna of growing rats was loaded at 17 N for 10 minutes per day for 8 days, the bone growth was suppressed even after one week of no loading, and the morphology of the growth plate had changed. Also for lower forces the growth was significantly suppressed, but recovered within 1 week of no loading [60]. Similarly, when knee loading was applied after fracture, tibia healing in mice was inhibited, whereas when loading was applied 4 days after fracture at a lower load, healing was enhanced [61]. This all indicates that mechanical stimulation causes an osteogenic response in bone when the load is not excessive.

Warden et al. found that the bone formation response of mice loaded with the ulna loading model was higher for loading applied at lower frequencies, between 5-10 Hz, and plateaued for higher frequencies [45]. Also mice loaded with a knee loading model at 0.5 N for 3 min/day for three days had more bone formation at 5 Hz than at 10 or 15 Hz [42]. However Hsieh et al. found that bone formation increased with increasing frequency with the ulna loading model [62]. Also when rats were subjected to whole body vibration more bone formation occurred at 90 Hz than at 45 Hz [1]. This difference could lie in the fact that strains in the ulna reduce as the frequency increases due to viscoelastic behavior. Consequently when the strain is to be kept constant a higher force should be applied as the frequency increases [63]. When random noise was added to the loading waveform bone formation was higher [53]. This suggests that mechanical loading induces the highest bone formation when applied at a frequency of 10 Hz, and for vibration at a frequency of 90 Hz.

From *in vivo* ulna loading in rats it was found that short bouts induce more bone formation than longer loading, whether the loading is applied daily or weekly [64]. Also, when rats were loaded for 5 weeks, followed by 5 weeks off and then loaded again for 5 weeks, bone formation rate improved compared to rats loaded for 15 weeks in a row [65]. When a rat tibia was loaded with three

point bending *in vivo*, daily loading cycles applied at intervals represented a more osteogenic stimulus than when cycles were applied all at once [44]. Furthermore Chambers et al., using a caudal vertebral loading model, found that in rats short bouts of 36 cycles loading daily for 10 days at 0.5 Hz provided a better bone formation response than rats loaded once for 360 cycles [66]. These findings all suggest that mechanical loading improves the mechanosensitivity when divided into discrete loading bouts [65]. However, adding resting periods between loading schemes of whole body vibration does not increase the bone mass any more than without resting periods [54].

2.3 Age-related changes in bone microstructure

To study the effect of aging on the bone microstructure, often bones of mice have been analyzed at multiple ages in a cross-sectional manner. It has been found that age-related declines in trabecular bone volume fraction in mice occur from an age of 3 months onwards in the distal femur and proximal tibia, while conflicting results exist for the fifth lumbar vertebra. Cortical area fraction remained stable or declined from an age of 6-7 months onwards in the femur, tibia, and ulna [67–69]. For both trabecular and cortical bone, the bone mineral density increased up to 12 months and stabilized thereafter.

Aging significantly increases osteoclast formation, promotes expansion of the osteoclast precursor pool and alters the relationship between osteoblasts and osteoclasts in cancellous bone [70]. This unbalance between osteoblasts and osteoclasts, which leads to bone loss, could be the result of a change in RANKL and OPG expression with aging [71]. It could also be an effect of changes in the periosteum, which is important in osteogenesis and osteoclastogenesis, and reduces cell number and thickness with aging [72].

Studies about mechanosensitivity with age are conflicting. Several studies have shown that mechanosensitivity declines with age. For example, in 20-month-old mice tibial loading was not sufficient to initiate bone formation. When 10 s of rest were inserted between each load cycle, the loading response was enhanced, but still 2.5 fold less than the response of young adult mice subjected to the same loading regimen [73]. Others have reported no difference in mechanosensitivity with age. Turner et al. found that the load to initiate bone formation in 19-month-old aged rats was greater than the load needed in younger rats, but when a response

was elicited, the cells had the same osteogenic capacity [74]. Furthermore, some studies have shown that mechanosensitivity remains with age. When loading was applied in 22-month-old mice, age related bone loss was prevented [75]. Probably these discrepancies in whether bones remain mechanosensitive with age are related to differences in species, strain, skeletal site, loading modality, design, and length of the study.

2.4 Effect of disease on bone microstructure

2.4.1 Osteoporosis

Osteoporosis is the most common bone disease. It has been defined as a systemic disease characterized by low bone mass and micro-architectural deterioration, leading to greater susceptibility to fractures [76]. Primary osteoporosis most often occurs in postmenopausal women, while secondary osteoporosis affects both sexes and can occur as a side effect of other diseases and disorders, or aging. Osteoporosis develops when the balance between bone formation and resorption is disturbed with resorption exceeding formation, which has been prescribed to an increase in activation frequency. In healthy bone, in a bone remodeling unit, osteoclasts that degrade old bone and osteoblasts that replace the removed bone with new bone, work in concert [77]. When the amount of bone remodeling units (activation frequency) increases, there is an instant increase in osteoclasts, while the increase in osteoblasts lags behind, leading to net bone loss [78]. It is not exactly clear what causes the activation frequency to rise, although it is likely related to a loss in estrogen level [79].

The World Health Organization defines osteoporosis as a bone mineral density (BMD) of 2.5 standard deviations below the young normal mean [80]. This definition, however, has some drawbacks. When women are measured at different sites, also the diagnosis differs [81]. Furthermore, BMD does not take the bone microstructure into account, and might thus not reflect the bone fragility. Bone fragility, which is a combination of bone strength, brittleness, and work to failure [82], can more adequately be predicted from high-resolution peripheral quantitative computed tomography (HR-pQCT) measurements, where the bone microstructure can be taken into account, for this however, the radiation dose is a concern [83, 84].

The prevalence of osteoporosis is 35% in women and 19% in men aged 50 years and older [85]. About 40% of white women and 13% of white men of this age are predicted to sustain at least one fracture of the hip, spine, or distal forearm [86]. Fractures lead to increased morbidity (pain and reduced mobility) and mortality in patients, e.g. hip fracture patients have a substantially increased risk of death up to 6 years after fracture [87]. Osteoporosis is also a major burden on the society. Annual costs for treatment of osteoporotic patients is about \$20 billion in America and €25 billion in Europe. With the demographic shift these numbers are expected to increase tremendously in the coming years, with doubling of the costs in 2055 [88].

2.4.2 Other bone diseases

There are several other bone diseases that are rare and of which the cause is often known. Parathyroid hormone (PTH) regulates extracellular calcium, through mobilization of calcium from the bone into the blood circulation, by stimulating re-adsorption of calcium in the kidney, and by enhancing absorption of calcium in the intestine through increasing renal synthesis of vitamin D. In the disease hyperparathyroidism, an excess PTH is secreted, and causes osteoclast recruitment and increased osteoclastic activity, resulting in secondary osteoporosis (and sometimes kidney stones due to calcium inhomeostasis). Primary hyperparathyroidism is often treated by (partial) removal of the PTH adenomas.

In another disease that influences bone metabolism, osteomalacia, mineralization of newly formed bone is inadequate. Similarly, in rickets, the juvenile form of osteomalacia, defective mineralization manifests in bone and growth plates. Osteomalacia and rickets are associated with low calcium and phosphate concentrations, high parathyroid hormone (PTH) concentration, high alkaline phosphatase activity, lack of vitamin D (1,25(OH)₂D), abnormalities in vitamin D metabolism, and defects in the mineralization process itself, and can lead to fractures in osteomalacia, and weak muscles and bone deformities in rickets. The prevalence of rickets and osteomalacia increases due to cultural practices, breast-feeding, decreased sun exposure, and increased sunscreen usage [89]. Depending on the cause, treatment includes controlled administration of vitamin D or intravenous administration of calcium, while for inadequate bone mineralization no effective treatment is available [90].

Furthermore, also in Paget's disease bone metabolism is influenced, but only locally, and usually only involves a few bones. The exact aetiology is unclear and

might be of viral origin. Paget's disease can be characterized by an increase in osteoclast-mediated bone resorption, with extremely enlarged osteoclasts harboring over 100 nuclei, and compensatory excessive osteoblast activation [91]. For patients, this often results in pain in bones and skeletal deformities [92].

In a rare genetic disorder, osteopetrosis (marble bone disease), genes that govern osteoclast formation and function are mutated, causing bones to become too dense (lack of remodeling) and fracture easily. By transplanting bone marrow, which induces formation of functional osteoclasts, osteopetrosis is often healed [93].

In another genetic disorder, Osteogenesis Imperfecta (OI, or brittle bone disease), there are mutations in the genes for type I collagen, leading to extremely fragile bones and multiple fractures [94]. The severity of the disease depends on the type of OI, ranging from death of newborns within a few days, to skeletal abnormalities, with reduced life expectancy. No treatment for OI exists.

References

- [1] S. Judex, X. Lei, D. Han, and C. Rubin. Low-magnitude mechanical signals that stimulate bone formation in the ovariectomized rat are dependent on the applied frequency but not on the strain magnitude. *J Biomech*, 40(6):1333–1339, 2007.
- [2] S.J. Warden, J.A. Hurst, M.S. Sanders, C.H. Turner, D.B. Burr, and J. Li. Bone adaptation to a mechanical loading program significantly increases skeletal fatigue resistance. *J Bone Miner Res*, 20(5):809–816, 2005.
- [3] W. Dehority, B.P. Halloran, D.D. Bikle, T. Curren, P.J. Kostenuik, T.J. Wronski, Y. Shen, B. Rabkin, A. Bouraoui, and E. Morey-Holton. Bone and hormonal changes induced by skeletal unloading in the mature male rat. *Am J Physiol*, 276(1 Pt 1):E62–E69, 1999.
- [4] L. Mosekilde, J.S. Thomsen, M.S. Mackey, and R.J. Phipps. Treatment with risedronate or alendronate prevents hind-limb immobilization-induced loss of bone density and strength in adult female rats. *Bone*, 27(5):639–645, 2000.
- [5] L. You, S. Temiyasathit, P. Lee, C.H. Kim, P. Tummala, W. Yao, W. Kingery, A.M. Malone, R.Y. Kwon, and C.R. Jacobs. Osteocytes as mechanosensors in

- the inhibition of bone resorption due to mechanical loading. *Bone*, 42(1):172–179, 2008.
- [6] D.P. Nicoletta, D.E. Moravits, A.M. Gale, L.F. Bonewald, and J. Lankford. Osteocyte lacunae tissue strain in cortical bone. *J Biomech*, 39(9):1735–1743, 2006.
- [7] R. Huiskes, R. Ruimerman, G.H. van Lenthe, and J.D. Janssen. Effects of mechanical forces on maintenance and adaptation of form in trabecular bone. *Nature*, 405(6787):704–706, 2000.
- [8] L.M. McNamara and P.J. Prendergast. Bone remodelling algorithms incorporating both strain and microdamage stimuli. *J Biomech*, 40(6):1381–1391, 2007.
- [9] M. Asagiri and H. Takayanagi. The molecular understanding of osteoclast differentiation. *Bone*, 40(2):251–264, 2007.
- [10] Y. Ichinose, H. Tanaka, M. Inoue, S. Mochizuki, E. Tsuda, and Y. Seino. Osteoclastogenesis inhibitory factor/osteoprotegerin reduced bone loss induced by mechanical unloading. *Calcif Tissue Int*, 75(4):338–343, 2004.
- [11] A.G. Robling, A.B. Castillo, and C.H. Turner. Biomechanical and molecular regulation of bone remodeling. *Annu Rev Biomed Eng*, 8:455–498, 2006.
- [12] Bonewald L. F. Mechanosensation and Transduction in Osteocytes. *Bonekey Osteovision*, 3(10):7–15, 2006.
- [13] T.J. Chambers, S. Fox, C.J. Jagger, J.M. Lean, and J.W. Chow. The role of prostaglandins and nitric oxide in the response of bone to mechanical forces. *Osteoarthritis Cartilage*, 7(4):422–423, 1999.
- [14] Z. Xu, S. Choudhary, Y. Okada, O. Voznesensky, C. Alander, L. Raisz, and C. Pilbeam. Cyclooxygenase-2 gene disruption promotes proliferation of murine calvarial osteoblasts in vitro. *Bone*, 41(1):68–76, 2007.
- [15] H. Hagino, M. Kuraoka, Y. Kameyama, T. Okano, and R. Teshima. Effect of a selective agonist for prostaglandin E receptor subtype EP4 (ONO-4819) on the cortical bone response to mechanical loading. *Bone*, 36(3):444–453, 2005.
- [16] A.M. Simon and J.P. O’Connor. Dose and time-dependent effects of cyclooxygenase-2 inhibition on fracture-healing. *J Bone Joint Surg Am*, 89(3):500–511, 2007.

- [17] M.R. Forwood. Inducible cyclo-oxygenase (COX-2) mediates the induction of bone formation by mechanical loading in vivo. *J Bone Miner Res*, 11(11):1688–1693, 1996.
- [18] S.W. Fox, T.J. Chambers, and J.W. Chow. Nitric oxide is an early mediator of the increase in bone formation by mechanical stimulation. *Am J Physiol*, 270(6 Pt 1):E955–E960, 1996.
- [19] K. E. Armour, K. J. Armour, M. E. Gallagher, A. Godecke, M. H. Helfrich, D. M. Reid, and Ralston S. H. Defective bone formation and anabolic response to exogenous estrogen in mice with targeted disruption of endothelial nitric oxide synthase. *Endocrinology*, 142(2):760–766, 2001.
- [20] C.H. Turner, Y. Takano, I. Owan, and G.A. Murrell. Nitric oxide inhibitor L-NAME suppresses mechanically induced bone formation in rats. *Am J Physiol*, 270(4 Pt 1):E634–E639, 1996.
- [21] A. Samuels, M.J. Perry, R.L. Gibson, S. Colley, and J.H. Tobias. Role of endothelial nitric oxide synthase in estrogen-induced osteogenesis. *Bone*, 29(1):24–29, 2001.
- [22] M.L. Johnson and M.A. Kamel. The Wnt signaling pathway and bone metabolism. *Curr Opin Rheumatol*, 19(4):376–382, 2007.
- [23] J.A. Robinson, M. Chatterjee-Kishore, P.J. Yaworsky, D.M. Cullen, W. Zhao, C. Li, Y. Kharode, L. Sauter, P. Babij, E.L. Brown, A.A. Hill, M.P. Akhter, M.L. Johnson, R.R. Recker, B.S. Komm, and F.J. Bex. Wnt/beta-catenin signaling is a normal physiological response to mechanical loading in bone. *J Biol Chem*, 281(42):31720–31728, 2006.
- [24] C.M. Reijnders, N. Bravenboer, P.J. Holzmann, F. Bhoelan, M.A. Blankenstein, and P. Lips. In vivo mechanical loading modulates insulin-like growth factor binding protein-2 gene expression in rat osteocytes. *Calcif Tissue Int*, 80(2):137–143, 2007.
- [25] J.M. Lean, C.J. Jagger, T.J. Chambers, and J.W. Chow. Increased insulin-like growth factor I mRNA expression in rat osteocytes in response to mechanical stimulation. *Am J Physiol*, 268(2 Pt 1):E318–E327, 1995.
- [26] T.S. Gross, S. Srinivasan, C.C. Liu, T.L. Clemens, and S.D. Bain. Noninvasive loading of the murine tibia: an in vivo model for the study of mechanotransduction. *J Bone Miner Res*, 17(3):493–501, 2002.

- [27] C.A. Conover, E.W. Johnstone, R.T. Turner, G.L. Evans, F.J. John Ballard, P.M. Doran, and S. Khosla. Subcutaneous administration of insulin-like growth factor (IGF)-II/IGF binding protein-2 complex stimulates bone formation and prevents loss of bone mineral density in a rat model of disuse osteoporosis. *Growth Horm IGF Res*, 12(3):178–183, 2002.
- [28] M. Machwate, E. Zerath, X. Holy, P. Pastoureau, and P.J. Marie. Insulin-like growth factor-I increases trabecular bone formation and osteoblastic cell proliferation in unloaded rats. *Endocrinology*, 134(3):1031–1038, 1994.
- [29] R.L. van Bezooijen, B.A. Roelen, A. Visser, L. van der Wee-Pals, E. de Wilt, M. Karperien, H. Hamersma, S.E. Papapoulos, P. ten Dijke, and C.W. Lowik. Sclerostin is an osteocyte-expressed negative regulator of bone formation, but not a classical BMP antagonist. *J Exp Med*, 199(6):805–814, 2004.
- [30] A.G. Robling, P.J. Niziolek, L.A. Baldrige, K.W. Condon, M.R. Allen, I. Alam, S.M. Mantila, J. Gluhak-Heinrich, T.M. Bellido, S.E. Harris, and C.H. Turner. Mechanical stimulation of bone in vivo reduces osteocyte expression of sost/sclerostin. *J Biol Chem*, 283(9):5866–5675, 2008.
- [31] K. Nozaka, N. Miyakoshi, Y. Kasukawa, S. Maekawa, H. Noguchi, and Y. Shimada. Intermittent administration of human parathyroid hormone enhances bone formation and union at the site of cancellous bone osteotomy in normal and ovariectomized rats. *Bone*, 42(1):90–97, 2008.
- [32] B.P. Halloran, D.D. Bikle, J. Harris, S. Tanner, T. Curren, and E. Morey-Holtan. Regional responsiveness of the tibia to intermittent administration of parathyroid hormone as affected by skeletal unloading. *J Bone Miner Res*, 12(7):1068–1074, 1997.
- [33] I. Moriyama, J. Iwamoto, T. Takeda, and Y. Toyama. Comparative effects of intermittent administration of human parathyroid hormone (1-34) on cancellous and cortical bone loss in tail-suspended and sciatic neurectomized young rats. *J Orthop Sci*, 7(3):379–385, 2002.
- [34] A. Sakai, T. Mori, M. Sakuma-Zenke, T. Takeda, K. Nakai, Y. Katae, H. Hirasawa, and T. Nakamura. Osteoclast development in immobilized bone is suppressed by parathyroidectomy in mice. *J Bone Miner Metab*, 23(1):8–14, 2005.

- [35] A. Sakai, T. Sakata, S. Ikeda, S. Uchida, R. Okazaki, T. Norimura, M. Hori, and T. Nakamura. Intermittent administration of human parathyroid Hormone(1-34) prevents immobilization-related bone loss by regulating bone marrow capacity for bone cells in ddY mice. *J Bone Miner Res*, 14(10):1691–1699, 1999.
- [36] R.T. Turner, G.L. Evans, J.M. Cavolina, B. Halloran, and E. Morey-Holton. Programmed administration of parathyroid hormone increases bone formation and reduces bone loss in hindlimb-unloaded ovariectomized rats. *Endocrinology*, 139(10):4086–4091, 1998.
- [37] Y. Ma, W.S. Jee, Z. Yuan, W. Wei, H. Chen, S. Pun, H. Liang, and C. Lin. Parathyroid hormone and mechanical usage have a synergistic effect in rat tibial diaphyseal cortical bone. *J Bone Miner Res*, 14(3):439–448, 1999.
- [38] J. Li, R.L. Duncan, D.B. Burr, V.H. Gattone, and C.H. Turner. Parathyroid hormone enhances mechanically induced bone formation, possibly involving L-type voltage-sensitive calcium channels. *Endocrinology*, 144(4):1226–1233, 2003.
- [39] A. Miyauchi, K. Notoya, Y. Mikuni-Takagaki, Y. Takagi, M. Goto, Y. Miki, T. Takano-Yamamoto, K. Jinnai, K. Takahashi, M. Kumegawa, K. Chihara, and T. Fujita. Parathyroid hormone-activated volume-sensitive calcium influx pathways in mechanically loaded osteocytes. *J Biol Chem*, 275(5):3335–3342, 2000.
- [40] K. Sawakami, A.G. Robling, M. Ai, N.D. Pitner, D. Liu, S.J. Warden, J. Li, P. Maye, D.W. Rowe, R.L. Duncan, M.L. Warman, and C.H. Turner. The Wnt co-receptor LRP5 is essential for skeletal mechanotransduction but not for the anabolic bone response to parathyroid hormone treatment. *J Biol Chem*, 281(33):23698–23711, 2006.
- [41] H. Keller and M. Kneissel. SOST is a target gene for PTH in bone. *Bone*, 37(2):148–158, 2005.
- [42] P. Zhang, S.M. Tanaka, H. Jiang, M. Su, and H. Yokota. Diaphyseal bone formation in murine tibiae in response to knee loading. *J Appl Physiol*, 100(5):1452–1459, 2006.
- [43] A.G. Robling and C.H. Turner. Mechanotransduction in bone: genetic effects on mechanosensitivity in mice. *Bone*, 31(5):562–569, 2002.

- [44] A.G. Robling, D.B. Burr, and C.H. Turner. Partitioning a daily mechanical stimulus into discrete loading bouts improves the osteogenic response to loading. *J Bone Miner Res*, 15(8):1596–1602, 2000.
- [45] S.J. Warden and C.H. Turner. Mechanotransduction in the cortical bone is most efficient at loading frequencies of 5-10 Hz. *Bone*, 34(2):261–270, 2004.
- [46] R.L. De Souza, M. Matsuura, F. Eckstein, S.C. Rawlinson, L.E. Lanyon, and A.A. Pitsillides. Non-invasive axial loading of mouse tibiae increases cortical bone formation and modifies trabecular organization: a new model to study cortical and cancellous compartments in a single loaded element. *Bone*, 37(6):810–818, 2005.
- [47] J.C. Fritton, E.R. Myers, T.M. Wright, and M.C. van der Meulen. Loading induces site-specific increases in mineral content assessed by microcomputed tomography of the mouse tibia. *Bone*, 36(6):1030–1038, 2005.
- [48] C.H. Turner, M.R. Forwood, and M.W. Otter. Mechanotransduction in bone: do bone cells act as sensors of fluid flow. *Faseb J*, 8(11):875–878, 1994.
- [49] C. Rubin, R. Recker, D. Cullen, J. Ryaby, J. McCabe, and K. McLeod. Prevention of postmenopausal bone loss by a low-magnitude, high-frequency mechanical stimuli: a clinical trial assessing compliance, efficacy, and safety. *J Bone Miner Res*, 19(3):343–351, 2004.
- [50] C. Rubin, A.S. Turner, R. Müller, E. Mittra, K. McLeod, W. Lin, and Y.X. Qin. Quantity and quality of trabecular bone in the femur are enhanced by a strongly anabolic, noninvasive mechanical intervention. *J Bone Miner Res*, 17(2):349–357, 2002.
- [51] M.C.H. van der Meulen, X. Yang, T.G. Morgan, and M.P.G. Bostrom. Bone remodelling algorithms incorporating both strain and microdamage stimuli. *Clin Orthop Relat Res*, 467(8):1381–1391, 2009.
- [52] B.A. Christiansen, A.A. Kotiya, and M.J. Silva. Constrained tibial vibration does not produce an anabolic bone response in adult mice. *Bone*, 45(4):750–759, 2009.
- [53] A.B. Castillo, I. Alam, S.M. Tanaka, J. Levenda, J. Li, S.J. Warden, and C.H. Turner. Low-amplitude, broad-frequency vibration effects on cortical bone formation in mice. *Bone*, 39(5):1087–1096, 2006.

- [54] L. Xie, J.M. Jacobson, E.S. Choi, B. Busa, L.R. Donahue, L.M. Miller, C.T. Rubin, and S. Judex. Low-level mechanical vibrations can influence bone resorption and bone formation in the growing skeleton. *Bone*, 39(5):1059–1066, 2006.
- [55] M.C.H. van der Meulen, T.G. Morgan, X. Yang, T.H. Baldini, E.R. Myers, T.M. Wright, and M.P.G. Bostrom. Cancellous bone adaptation to in vivo loading in a rabbit model. *Bone*, 38(6):871–877, 2006.
- [56] D. Webster, E. Wasserman, M. Ehrbar, F. Weber, I. Bab, and R. Müller. Mechanical loading of mouse caudal vertebrae increases trabecular and cortical bone mass-dependence on dose and genotype. *Biomech Model Mechanobiol*, 9(6):737–747, 2010.
- [57] Webster D.J., Morley P.L., van Lenthe G.H., and Müller R. A novel in vivo mouse model for mechanically stimulated bone adaptation—a combined experimental and computational validation study. *Comput Methods Biomech Biomed Engin*, 11(5):435–441, 2008.
- [58] V. Gilsanz, T.A. Wren, M. Sanchez, F. Dorey, S. Judex, and C. Rubin. Low-level, high-frequency mechanical signals enhance musculoskeletal development of young women with low BMD. *J Bone Miner Res*, 21(9):1464–1474, 2006.
- [59] R. Garman, C. Rubin, and S. Judex. Small oscillatory accelerations, independent of matrix deformations, increase osteoblast activity and enhance bone morphology. *PLoS ONE*, 2(7):e653, 2007.
- [60] N. Ohashi, A.G. Robling, D.B. Burr, and C.H. Turner. The effects of dynamic axial loading on the rat growth plate. *J Bone Miner Res*, 17(2):284–292, 2002.
- [61] M.J. Gardner, M.C. van der Meulen, D. Demetrakopoulos, T.M. Wright, E.R. Myers, and M.P. Bostrom. In vivo cyclic axial compression affects bone healing in the mouse tibia. *J Orthop Res*, 24(8):1679–1686, 2006.
- [62] Y.F. Hsieh and C.H. Turner. Effects of loading frequency on mechanically induced bone formation. *J Bone Miner Res*, 16(5):918–924, 2001.
- [63] Y.F. Hsieh, T. Wang, and C.H. Turner. Viscoelastic response of the rat loading model: implications for studies of strain-adaptive bone formation. *Bone*, 25(3):379–382, 1999.

- [64] A.G. Robling, F.M. Hinant, D.B. Burr, and C.H. Turner. Improved bone structure and strength after long-term mechanical loading is greatest if loading is separated into short bouts. *J Bone Miner Res*, 17(8):1545–1554, 2002.
- [65] L.K. Saxon, A.G. Robling, I. Alam, and C.H. Turner. Mechanosensitivity of the rat skeleton decreases after a long period of loading, but is improved with time off. *Bone*, 36(3):454–464, 2005.
- [66] T.J. Chambers, M. Evans, T.N. Gardner, A. Turner-Smith, and J.W. Chow. Induction of bone formation in rat tail vertebrae by mechanical loading. *Bone Miner*, 20(2):167–178, 1993.
- [67] V. Glatt, E. Canalis, L. Stadmeier, and M.L. Bouxsein. Age-related changes in trabecular architecture differ in female and male C57BL/6J mice. *J Bone Miner Res*, 22(8):1197–1207, 2007.
- [68] B.P. Halloran, V.L. Ferguson, S.J. Simske, A. Burghardt, L.L. Venton, and S. Majumdar. Changes in bone structure and mass with advancing age in the male C57BL/6J mouse. *J Bone Miner Res*, 17(6):1044–1050, 2002.
- [69] M.D. Willingham, M.D. Brodt, K.L. Lee, A.L. Stephens, J. Ye, and M.J. Silva. Age-related changes in bone structure and strength in female and male BALB/c mice. *Calcif Tissue Int*, 86(6):470–483, 2010.
- [70] J.J. Cao, T.J. Wronski, U. Iwaniec, L. Phleger, P. Kurimoto, B. Boudignon, and B.P. Halloran. Aging increases stromal/osteoblastic cell-induced osteoclastogenesis and alters the osteoclast precursor pool in the mouse. *J Bone Miner Res*, 20(9):1659–1668, 2005.
- [71] J. Cao, L. Venton, T. Sakata, and B.P. Halloran. Expression of RANKL and OPG correlates with age-related bone loss in male C57BL/6 mice. *J Bone Miner Res*, 18(2):270–277, 2003.
- [72] W. Fan, R. Crawford, and Y. Xiao. Structural and cellular differences between metaphyseal and diaphyseal periosteum in different aged rats. *Bone*, 1(42):81–89, 2008.
- [73] S. Srinivasan, S.C. Agans, K.A. King, N.Y. Moy, S.L. Poliachik, and T.S. Gross. Enabling bone formation in the aged skeleton via rest-inserted mechanical loading. *Bone*, 33(6):946–955, 2003.

- [74] C.H. Turner, Y. Takano, and I. Owan. Aging changes mechanical loading thresholds for bone formation in rats. *J Bone Miner Res*, 10(10):1544–1549, 1995.
- [75] M.D. Brodt and M.J. Silva. Aged mice have enhanced endocortical response and normal periosteal response compared with young-adult mice following 1 week of axial tibial compression. *J Bone Miner Res*, 25(9):2006–2015, 2010.
- [76] Anonymous. Consensus development conference: prophylaxis and treatment of osteoporosis. *Am J Med*, 1(90):107–110, 1991.
- [77] H.M. Frost. Tetracycline-based histological analysis of bone remodeling. *Calcif Tissue Res*, 3(3):211–237, 1969.
- [78] R.P. Heaney. The bone-remodeling transient: implications for the interpretation of clinical studies of bone mass change. *J Bone Miner Res*, 9(10):1515–1523, 1994.
- [79] H.K. Genant, C. Cooper, G. Poor, I. Reid, G. Ehrlich, J. Kanis, B.E. Nordin, E. Barrett-Connor, D. Black, J.P. Bonjour, B. Dawson-Hughes, P.D. Delmas, J. Dequeker, S. Ragi Eis, C. Gennari, O. Johnell, C.C.Jr. Johnston, E.M. Lau, U.A. Liberman, R. Lindsay, T.J. Martin, B. Masri, C.A. Mautalen, P.J. Meunier, N. Khaltsev, and et al. Interim report and recommendations of the World Health Organization Task-Force for Osteoporosis. *Osteoporos Int*, 10(4):259–264, 1999.
- [80] J.A. Kanis, L.J. 3rd Melton, C. Christiansen, C.C. Johnston, and N. Khaltsev. The diagnosis of osteoporosis. *J Bone Miner Res*, 9(8):1137–1141, 1994.
- [81] L. J. 3rd Melton, S. Khosla, S. J. Achenbach, M. K. O’Connor, W. M. O’Fallon, and B. L. Riggs. Effects of body size and skeletal site on the estimated prevalence of osteoporosis in women and men. *Osteoporos Int*, 11(11):977–983, 2000.
- [82] C.H. Turner. Biomechanics of bone: determinants of skeletal fragility and bone quality. *Osteoporos Int*, 13(2):97–104, 2002.
- [83] M. Jergas and H.K. Genant. Current methods and recent advances in the diagnosis of osteoporosis. *Arthritis Rheum*, 36(12):1649–1662, 1993.
- [84] K. C. Moio, G. Podolskaya, B. Barnhart, A. Berzins, and D. R. Sumner. pQCT provides better prediction of canine femur breaking load than does DXA. *J Musculoskelet Neuronal Interact*, 3(3):240–245, 2003.

- [85] L. J. 3rd Melton, E. J. Atkinson, M. K. O'Connor, W. M. O'Fallon, and B. L. Riggs. Bone density and fracture risk in men. *J Bone Miner Res*, 13(12):1915–1923, 1998.
- [86] L.J. 3rd. Melton, E.A. Chrischilles, C. Cooper, A.W. Lane, and B.L. Riggs. Perspective. How many women have osteoporosis? *J Bone Miner Res*, 7(9):1005–1010, 1992.
- [87] B. Y. Farahmand, K. Michaelsson, A. Ahlbom, S. Ljunghall, and J. A. Baron. Survival after hip fracture. *Osteoporos Int*, 16(12):1583–1590, 2005.
- [88] J.Y. Reginster, N. Sarlet, and M.P. Lecart. Fractures in osteoporosis: the challenge for the new millennium. *Osteoporos Int*, 16 Suppl 1:S1–S3, 2005.
- [89] K.E. Dittmer and K.G. Thompson. Vitamin D metabolism and rickets in domestic animals: a review. *Vet Pathol*, 48(2):389–407, 2011.
- [90] E. Rubin, F. Gorstein, R. Rubin, R. Schwarting, and D. Strayer. *Rubin's pathology: clinicopathologic foundations of medicine*. USA: Lippincott Williams&Williams, 4th ed. philadelphia edition, 2005.
- [91] K. Cortis, K. Micallef, and A. Mizzi. Imaging Paget's disease of bone-from head to toe. *Clin Radiol*, 2011.
- [92] L. Gkouva, M. Andrikoula, V. Kontogeorgakos, D.J. Papachristou, and A. Tsatsoulis. Active Paget's disease of bone with normal biomarkers of bone metabolism: a case report and review of the literature. *Clin Rheumatol*, 30(1):139–144, 2011.
- [93] A. Kulpiya, P. Mahachoklertwattana, S. Pakakasama, S. Hongeng, and P. Poomthavorn. Hypercalcemia and altered biochemical bone markers in post-bone marrow transplantation osteopetrosis: A case report and literature review. *Pediatr Transplant*, doi: 10.1111/j.1399-3046.2011.01475.x., 2011.
- [94] D. Basel and R.D. Steiner. Osteogenesis imperfecta: recent findings shed new light on this once well-understood condition. *Genet Med*, 11(6):375–385, 2009.

2.5 Advances in functional imaging and multimodality systems in bone research

Floor M. Lambers¹, Gisela Kuhn¹, Markus Rudin², and Ralph Müller¹

¹Institute for Biomechanics, ETH Zürich, Zürich, Switzerland

²University and ETH Zürich, Institute for Biomedical Engineering, Zürich, Switzerland

Abstract:

The skeleton is important to the body as a source of minerals and blood cells and provides a structural framework for strength, mobility and the protection of organs. Bone diseases and disorders have deteriorating effects on the skeleton. The biological processes underlying these diseases are often not well understood. *In vivo* imaging techniques and molecular markers have been developed that help to gain more knowledge of pathological pathways. This review aims to provide an overview of the latest developments in molecular imaging applied to bone. It emphasizes that multimodality imaging greatly enhances the interpretability of data and is imperative for the fundamental understanding of the biological processes underlying bone diseases.

Keywords:

In vivo micro-computed tomography; Fluorescence molecular tomography; Multimodality; Bone

2.5.1 Introduction

Bone is a dynamic tissue that is constantly renewed to maintain its quality and mechanical integrity [1]. Osteoclasts resorb the bone by secreting acids and proteases, while osteoblasts form new bone by laying down bone matrix, which later mineralizes to yield mature bone [2]. Robling et al. wrote an excellent review on the stimuli that affect bone remodeling [3].

Bone remodeling is affected by hormones, cytokines, and mechanical stimuli. Among these hormones, the most well known are estrogen and parathyroid hormone. Estrogen deficiency increases the rate of bone remodeling, as well as the amount of bone lost in each remodeling cycle, leading to bone loss as often occurs in postmenopausal women [4–6]. Hyperparathyroidism accelerates bone loss and increases skeletal fragility, but when given intermittently it increases bone mass [7–9]. Cytokines influence the differentiation of osteoclast progenitors [5]. For example receptor activator of $\text{NF}\kappa\beta$ ligand (RANKL) induces osteoclast differentiation, while osteoprotegerin inhibits it by blocking RANKL-binding [10]. Furthermore bone remodeling is affected by mechanical stimuli; impact loading induces bone formation [11–14], while absence of loading causes a reduction in the bone mass [11,15,16].

Because so many factors play an important role in bone remodeling it is difficult to understand the exact biological processes that regulate it. However, it is known that the careful balance and coupling between bone deposition and resorption is crucial for the proper development and maintenance of bone size, shape and integrity and for its mechanical properties [17,18]. Unbalance in bone remodeling, which causes bone diseases and disorders, has deteriorating effects on the skeleton and leads to a greater susceptibility to fractures [19,20]. Here, osteoporosis is taken as an example to show that the imaging techniques currently available are not adequate for detecting the disease at an early enough stage.

Osteoporosis is the most prevalent bone disease occurring in more than 50% of people aged above 80 [21]. It has been defined as a systemic disease characterized by low bone mass and microarchitectural deterioration of bone tissue, with a consequent increase in bone fragility and susceptibility to fracture [22]. The diagnosis of osteoporosis relies on bone mineral density measured with anatomical imaging techniques such as histomorphometry, dual-energy X-ray absorptiometry (DXA) or peripheral quantitative computed tomography (pQCT) [23–26]. When the bone mineral density is below a certain threshold, with the consequence of

a high fracture risk, a patient will be treated for osteoporosis [26]. However, the prediction of fracture risk estimated from the bone mineral density is rather inaccurate, as other factors like genetic background, age, fracture history cannot be taken into account, but have an important influence [27,28]. Furthermore, with the use of anatomical imaging techniques, the disease can be visualized only when changes in the bone mineral content have appeared, representing a later stage of the disease, because anatomical imaging gives insight into bone mineral density and bone structure but not into bone metabolic activity [29].

So in order to adequately evaluate a persons fracture risk, molecular imaging techniques, which can give an insight on bone metabolic activity, should be used in combination with the anatomical imaging techniques to correctly diagnose osteoporosis patients [30].

Molecular imaging was developed to allow imaging of biological processes that are important in the progression of diseases or for monitoring drug efficacy. Molecular imaging enables non invasive characterization, quantification and visualization of biological processes *in vivo* at the cellular and molecular level [31–33]. It allows monitoring of the progression of a disease within one subject and to image gene expression, leading to a more fundamental understanding of diseases and a greater predictive power [34]. Also a prognosis of diseases can be made at an earlier stage, leading to more appropriate treatment [35]. Furthermore, molecular imaging allows the effectiveness of treatment and of new classes of drugs directed at new therapeutic targets to be assessed [36]. Generally, molecular imaging has the advantage of providing a much faster read-out and is less time consuming than techniques like histology. Imaging is noninvasive and thus allows for longitudinal studies, which increase the statistical relevance [31]. However molecular imaging is limited by its low special resolution. Therefore, efforts have been made to combine molecular imaging with anatomical imaging, to simultaneously provide for the longitudinal cellular or molecular activity and for the localization or anatomical changes as a result of the cellular activity [37]. Thus to obtain a full understanding of bone growth, remodeling, and metabolism, anatomical imaging needs to be combined with a molecular imaging modality.

Molecular imaging plays an important role in many different fields [38–41], but because of the focus of this paper, only applications in the bone field will be overviewed here. In this paper the importance of multimodality imaging will

be emphasized. Firstly, imaging techniques and multimodality imaging will be introduced; secondly, molecular imaging in bone will be overviewed for different applications.

2.5.2 Imaging systems

The available imaging systems can be subdivided into molecular imaging systems or anatomical imaging systems. Molecular imaging systems can be further subdivided into nuclear imaging systems and optical imaging systems.

Nuclear imaging systems

Nuclear imaging methods rely on pharmaceuticals that have been labeled with radionuclides, and include scintigraphy, positron emission tomography (PET), and single photon emission computed tomography (SPECT) [42]. When bone scintigraphy is used with the tracer ^{99m}Tc -methylenediphosphonate (MDP) the bone metabolic activity can be evaluated [43]. The incorporation of ^{99m}Tc -MDP is not well understood, but it is most likely related to the exchange of phosphorous groups with the calcium of crystallizing bone hydroxyapatite [44]. Bone scintigraphy is cost-effective, but has limited anatomical precision and accuracy [45]. Therefore higher resolution imaging techniques are frequently performed after bone scintigraphy to further characterize lesions evident on bone scans [46]. Although bone scintigraphy is a highly sensitive method for functional bone imaging, it lacks specificity for imaging bone metastases and depicts them at a relatively advanced stage and only when there is an osteoblastic response [47].

Basically SPECT is 3D scintigraphy [48] and detects single γ -rays from multiple projections. For SPECT more isotopes are available and costs are lower than for PET, however the sensitivity is also reduced. SPECT is mostly used to collect physiological information and measure biodistribution.

For PET, radiolabeled substances are injected which emit positrons that annihilate with electrons under emission of two γ -photons in opposite directions [49]. PET is based on the coincidence detection of these two photons and records the location where the annihilation took place [50–53]. For bone imaging the radionuclide ^{18}F -fluoride is used. Fluoride ions exchange with hydroxyl groups in the hydroxyapatite crystal of bone ($\text{Ca}_{10}(\text{PO}_4)_6\text{OH}_2$), which is formed by osteoblasts in the process of mineralization, resulting in fluoroapatite ($\text{Ca}_{10}(\text{PO}_4)_6\text{F}_2$) [54].

^{18}F -fluoride has been shown to deposit preferentially at the surface of bone where the greatest activity of remodeling and turnover in healing is seen [51] and binds irreversibly [55]. ^{18}F -fluoride-PET is quantitatively more precise than γ -camera skeletal studies (SPECT) using bone-seeking radiopharmaceuticals such as $^{99\text{m}}\text{Tc}$ -MDP, because of the better resolution and quantitative precision of PET [56]. Micro-PET is a PET scanner that has a higher resolution, and was developed to allow measurements of rodents [57]. ^{18}F -fluoride-micro-PET imaging of bone is reproducible and can be used for serial monitoring [58]. Another tracer that is often used is ^{18}F -fluorodeoxyglucose (FDG), an indicator of cellular glucose metabolism. ^{18}F -FDG may describe tumor growth, proliferation of neoplasm and the extent of metastases [59].

In general, the advantages of nuclear imaging are high sensitivity, deep tissue penetration and the possibility of obtaining quantitative data [60, 61]. A disadvantage is the need for radioactive labels. Radiolabeling of cells allows dynamical imaging at high sensitivity, but a radiolabel is typically lost within a few hours, depending on the half life of the used isotope, and only allows low spatial resolution [62].

Optical imaging systems

Optical imaging techniques include fluorescence reflectance imaging (FRI), near infrared fluorescence imaging (NIRF), fluorescence molecular tomography (FMT), and bioluminescence imaging (BLI). All these techniques rely on the detection of photons.

For FRI exogenous fluorochromes are injected. These are excited by laser diodes, and emit light at a different frequency which can be detected with a charge coupled device (CCD) camera [63]. The main applications of fluorescence imaging include monitoring of tumor growth and metastasis formation as well as, occasionally, gene expression. For NIRF the same principle applies as for FRI, but the excitation wavelength is in the near-infrared range (700-900 nm) [64, 65]. Advantages of NIRF over FRI are deeper photon penetration, lower background autofluorescence, and higher photon yield [66].

FMT is a newer technology that takes FRI or NIRF images at multiple projections, building up a three dimensional image [67–69]. FMT allows for an even deeper photon penetration than NIRF, has a higher resolution and improves

quantification [70]. Recently Zaheer et al. developed OsteoSense[®], an exogenous fluorochrome that binds with great affinity to mineralizing bone and can be detected by optical imaging. Every time an osteoblast lays down bone, it also lays down the marker; hence bone formation responses can be quantified *in vivo* [71]. Since OsteoSense[®] is bound to bisphosphonates, which are used in the treatment of osteoporosis patients, OsteoSense[®] might have a therapeutic effect, however the dose injected into mice for imaging is less than 1% of the therapeutic dose [72]. In the most superficial layers, in the order of multiple centimeters [73], resolution and sensitivity of NIRF with OsteoSense[®] labelling is equivalent to, or surpasses, that of ^{99m}Tc-MDP-SPECT [74]. Kozloff et al. demonstrated that a cathepsin- κ activated near-infrared fluorescence probe can be used to non-invasively image osteoclast activity *in vivo* [29, 75].

Bioluminescence imaging is the detection of light produced within an organism by an energy dependent chemical reaction [76, 77]. For transgenic animals, a fluorescent protein, usually luciferase, is expressed simultaneously with the gene of interest. When luciferin is injected, luciferase catalyzes the oxidation of luciferin, from which light is emitted that is detectable with a CCD camera [78]. The advantages of BLI over FRI are the lower background noise, since light is only emitted upon interaction between luciferin and luciferase, and also the enhancement of signals, however, it relies on the use of genetically modified animals [79].

Osteocalcin (OC) is a bone tissue specific protein expressed by osteoblasts, odontoblasts, and hypertrophic chondrocytes at the onset of tissue mineralization and accumulating in the bone extracellular matrix [80]. Although the exact function of osteocalcin is unclear, it is assumed to play an important role in mineral deposition, bone remodeling and bone mineral maturation [81]. Mice expressing a luciferase reporter gene under regulation of the human osteocalcin (hOC) promoter can be used to monitor the calcein gene expression and principally detect changes in bone formation [82].

BLI is mainly applied for cell tracking and imaging of reporter gene expression. It was shown that the dynamics of hOC regulation can easily be achieved real time, quantitatively and non-invasively [83]. Cancer cell lines transfected with the firefly luciferase (Luc) or the green fluorescent protein (GFP) can be used to monitor local tumor growth and the development of metastases in mice *in vivo*. BLI allows continuous monitoring and precise quantification of bone metastatic growth

in vivo [84]. Human bone marrow mesenchymal stem cells (hBMSCs) are ideal candidates for autologous bone repair due to their proven capacity to differentiate into osteoblasts, their abundance, and ease of isolation [85]. By transfecting the hBMSCs with firefly luciferase, the survival and proliferation can be visualized [86].

Optical imaging is mainly used in research and hardly has any clinical applications, because the penetration depth is too little for humans. In general, the advantages of optical imaging are its high sensitivity and specificity, the fast imaging, and that it is simplistic [70]. Disadvantages are poor spatial resolution in the order of 1 mm, the difficulty of quantification, and the fact that only superficial structures can be imaged [87]. To make the technique more sensitive, auto quenched probes that only emit light upon interaction with the target can be used, i.e. the peptide link between the fluorochrome and the target-bound part is cleaved upon target interaction [87].

Anatomical imaging systems

Techniques that measure the anatomy include histomorphometry, DXA, computed tomography (CT), and magnetic resonance imaging (MRI). MRI is also a molecular imaging modality for applications other than bone. For histomorphometry, typically a biopsy is taken from the iliac crest [88] and embedded in hard resin or in paraffin after decalcification [89]. Slices from the embedded bone can be viewed under a microscope at a resolution of up to 200 nm and from these images morphometric indices can be calculated [90]. Calcein double labeling prior to biopsy extraction enables a quantitative analysis of dynamic parameters of bone formation such as mineral apposition rate, bone formation rate, and activation frequency [91]. Bone histomorphometry on bone biopsies is one of the methods for diagnosing metabolic bone diseases [92]. However, the disadvantages of this method are that it is invasive and thus unsuitable for longitudinal studies, the biopsies are destroyed during sample preparation, the procedure is two dimensional, and that it requires an injection of markers to evaluate dynamic processes [93]. Furthermore, the production of histological slides is time-consuming. Detection of bone formation rates by histomorphometric evaluation of labeled bone takes months from the actual *in vivo* experiment until the final readout [94].

DXA, CT, quantitative computed tomography (QCT), and pQCT are based on the transmission of an X-ray beam through an object, which is determined by the linear attenuation coefficients of all the structures through which the beam

passes [95–98]. For a DXA measurement one projection is made, thus the radiation dose is relatively low and measurements are cheap and fast [99]. The areal bone mineral density (aBMD) can be measured longitudinally, and correlates well with bone strength [100]. However, DXA is limited by several factors, namely: the aBMD measurement depends on the bone size and position (bone mineral content divided by the scanned area), it cannot discriminate between cortical and trabecular bone [101, 102], errors originate from the variation in surrounding soft tissues and bone marrow [103], and it is a 2-dimensional technique [104]. For CT, QCT, and pQCT projections are made at multiple angles from which a 3D image can be reconstructed [105]. For QCT, a bone mineral reference phantom is scanned at the same time as the subject and is used to calculate the bone mass of the subject [106]. pQCT is similar to QCT but is used to measure the appendicular bones such as the radius and the tibia [107]. Micro-CT systems can achieve a higher spatial resolution (1-10 μm), but are limited to *in vitro* specimen. Recently, *in vivo* micro-CT has been developed with which rodents are measured at an equal resolution to micro-CT [108] and where it is not the specimen but the X-ray/detector system that rotates [109]. HR-pQCT does allow nondestructive 3-dimensional analysis and can differentiate between the trabecular and cortical bone of the peripheral skeleton with high reproducibility and accuracy [93, 107, 110–112]. When bone changes occur predominantly in the trabecular bone, the magnitude of measured bone loss is greater with HR-pQCT than with DXA and can thus be detected earlier. It also provides a more accurate measurement at a resolution of about 80 μm compared to the order of 1 mm for DXA [101, 113].

Magnetic resonance imaging (MRI) is based on the resonance of protons in atomic nuclei [33]. When placed in a strong magnetic field the protons of the nuclei align [39]. When this equilibrium is disturbed by a radiofrequency pulse, magnetization is recovered with a tissue-specific relaxation time, providing the basis for contrast [39, 114, 115]. By repeated radiofrequency pulses a 3D image can be built up from cross-sectional images [116]. The application of MRI for the anatomical imaging of bone has emerged rapidly in the past decade [117]. The trabecular bone marrow can be resolved with MRI, when the relaxation rate is measured, and the trabecular bone volume fraction can be measured, when the attenuation of the spin-echo amplitude is measured. Also, MRI can be performed at high resolution allowing single trabeculae to be visualized [118]. Furthermore, MRI can be used for the quantification of bone water as a measurement of mineralization [119]. The methods to determine trabecular architecture with MRI rely

on the signal from the bone marrow rather than from the bone itself [120], but still MRI measurements of geometric parameters of the peripheral skeleton are accurate and repeatable [121–124]. MRI is capable of detecting subtle changes in renal disease [125], but shows significantly different results from pQCT measurements in osteoporotic women [126]. The advantages of MRI over CT are the absence of ionizing radiation, and the high innate contrast between bone and bone marrow, but a long acquisition time, a lower resolution in the order of 100 μm , and high costs [127] are the current limitations.

Multimodality imaging

All the presented imaging techniques have distinct benefits and appropriate applications, but none provides high sensitivity as well as high spatial resolution. Combinations of imaging modalities that integrate molecular with structural information, and at the same time eliminate one or more inadequacies of an individual modality, offer the prospect of improved diagnostics, therapeutic monitoring, and preclinical research using imaging approaches [128]. Basically, there are two different ways of multimodality imaging, one in which multiple imaging modalities are combined into one system (multimodality scanners), and one in which, after imaging on multiple imaging systems, the images are registered and fused [129].

Multimodality scanners can acquire functional and structural images either simultaneously or sequentially without moving the subject from the bed, since the hardware of both imaging systems is combined [130]. These scanners thus provide the most precise fusion of images and enable a more specific diagnosis, but have a complicated design that involves compromising the image quality, and they are also very expensive [131]. Multimodality scanners developed so far include PET/CT [132], SPECT/CT [46, 133], PET/MRI [134, 135], and PET/optical imaging [136]. Applications of multimodality scanners are especially numerous in the field of oncology [46, 137–141].

The second form of multimodality imaging often uses one bed to transport the subject between modalities and needs registration algorithms to superimpose images from different modalities [142]. This enables the matching of any kind of imaging modality [37]. An imaging chamber or bed that fixes the subject, and fiducial markers which are visible in both modalities, facilitate the registration between them [143, 144], however involuntary movement and shape changing of organs remains a complication [46].

Registration can be rigid, and can only be used correctly when there is no movement between modalities [30], or non-rigid, which is more complicated computationally [37]. A requirement for the fusion of images is that data formats must be compatible between imaging modalities.

Multimodality imaging systems allow the combination of high sensitivity, high specificity and high spatial resolution.

2.5.3 Applications

Bone metabolism

Bone remodeling serves for the repair of microcracks, the prevention of accumulation of micro-damage [145], the adaptation to local stresses [146], and the maintenance of calcium homeostasis in the blood [147]. To image bone metabolism with molecular imaging modalities, ^{18}F -fluoride-PET [94], OsteoSense[®]-FRI [72], or BLI [83] have been used. To assess bone remodeling *in vivo*, Kozloff et al. analyzed one 8-day neonatal mouse and two 9-week old mice with OsteoSense[®]-FRI. A high fluorescence signal was obtained in regions typical of active mineralization. When adult mice were imaged (figure 2.5) the highest signal was obtained at the growth plates [72]. When osteocalcin levels in skeletal organs during the development of mice were investigated, by use of luciferase gene expression, regulated by the osteocalcin promoter, luciferase was expressed mostly in hypertrophic cartilage and trabecular bone and peaked between one week and one month of age. After this, the luciferase expression and thus the osteocalcin levels decreased in all skeletal sites, except for the tail [83].

An unbalance in bone metabolism leads to bone diseases and disorders. To allow the appropriate treatment of these diseases, their pathogenic mechanisms need to be visualized. To simulate osteoporosis in mice, the ovaries can be removed. In a study of Kozloff et al. mice were divided in groups that were ovariectomized (OVX), OVX with pamidronate treatment, or sham operated. The mice were imaged 8 days after the operation with cathepsin- κ -FMT. The fluorescence signal was 38% higher in the OVX group than in the pamidronate treated ovariectomized group or the sham-operated group, indicating a higher osteoclastic activity in the OVX group. The binding of the probe to osteoclasts was proven with confocal laser

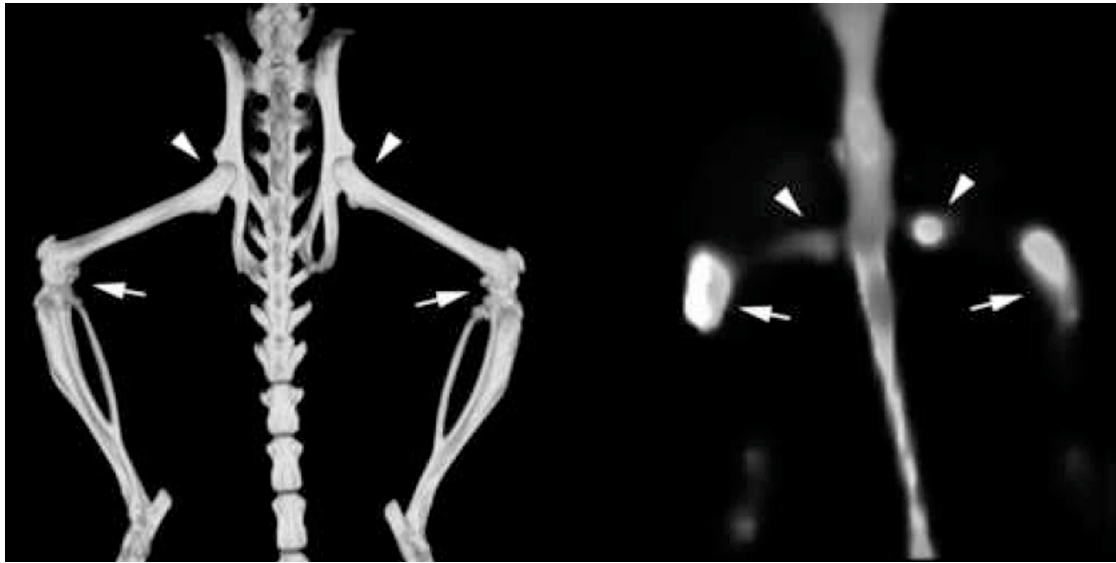


Figure 2.5: CT image (left) and FMT image (right) of a 9 week female nu/nu mouse that was labeled with OsteoSense[®]. High signals are obtained from the spine, tail, knee (arrows) and femoral heads (arrowheads). (Figure reproduced from Kozloff et al. [72]).

scanning microscopy. Probe activation was sensitive to changes in resorption and correlated to bone formation measured with ^{99m}Tc -MDP [75]. In a follow-up study, mice were divided into similar groups, but split into a short-term bone loss (day 7) and a long-term bone loss (day 13) group. Two mice per group were additionally injected with OsteoSense[®]. After FMT imaging, the mice were sacrificed and the right tibias were scanned with micro-CT. Osteoclast activity as measured with cathepsin- κ -FMT was evident at an earlier time point than bone loss as detected with micro-CT. In the mice injected with OsteoSense[®] and cathepsin- κ it was found that the OVX mice had a faster bone turnover than sham or pamidronate-treated OVX mice [29].

Other diseases resulting in disturbed bone remodeling that have a high prevalence include renal osteodystrophy, osteomalacia, hyperparathyroidism, and Paget's disease [148]. Messa et al. evaluated the metabolic activity of bone in patients suffering from renal osteodystrophy using ^{18}F -fluoride-PET. Renal osteodystrophy can cause reduced bone formation and impaired mineralization, but also may lead to a markedly increased bone turnover [149]. It was found that ^{18}F -fluoride can differentiate low turnover lesions from high turnover lesions and provide quantitative estimates of bone cell activity [150].

Stable ingrowth of implants is imperative for regaining mobility after hip surgery [151]. To compare bone remodeling due to the effects of surgery and to bone grafting Temmerman et al. evaluated bone formation in patients after total hip revision surgery with allografts and in patients after primary cemented total hip arthroplasty. Patients undergoing hip replacement had higher ^{18}F -fluoride uptake around the implant when they had received allogeneic bone grafts, indicating faster bone remodeling and ingrowth [45]. Ullmark et al. used ^{18}F -fluoride PET to produce quantitative images of new bone formation in allografts surrounding the femur stem 6 years after hip replacement. Compared to the values measured in the first year after surgery, bone metabolism was significantly reduced in most areas of the proximal femur after 6 years. Also, bone metabolism was normalized compared to the contralateral healthy femur. It was concluded that PET scans during the first year can reliably predict ingrowth success [152]. In this study, only patients with radiologically confirmed healing were investigated. Therefore, no statements are made on ^{18}F -fluoride uptake in cases where no ingrowth takes place.

Fracture healing

Fracture repair is typically divided into three phases: the inflammatory phase, the reparative phase, and the remodeling phase [148]. The inflammatory response is initiated by disruption of the local soft tissue, vasculature, and a distortion of the bone marrow due to the fracture. This damage leads to activation of wound healing pathways [153]. To stabilize the wound mechanically, a cartilaginous callus is formed initially, to bridge the gap. This cartilaginous callus is replaced with woven bone during remodeling [154]. In the final stage of fracture repair the woven bone is remodeled into cortical and trabecular bone [155]. Usually it takes several weeks for the bone to heal depending on age, site of fracture and overall health [156]. Five to ten percent of the fractures that occur annually in the United States demonstrate delayed healing or nonunion [157], leading to high morbidity especially when this involves mobility. Fracture non-unions and delayed unions require multiple surgical procedures and are associated with disability, pain, and prolonged rehabilitation periods [158]. Sometimes it takes 9 months to a year before a patient is diagnosed with a nonunion, because of limitations with imaging tools [159]. Micro-CT and radiography have not been useful in the prediction of delayed healing of bones in humans, as bone mineral is a late manifestation of the fracture healing process [51]. Animal models have been employed to study processes of delayed fracture healing or non-union [160]. In these models relatively large defects are created in the bones and sometimes spacers are used to simulate non-union. For studying normal bone

healing small defects are created or the bones are broken. Hsu et al. assessed bone healing with ^{18}F -fluoride-PET and with ^{18}F -FDG-PET in rats. Fractures created via three-point bending showed abundant callus formation and bone healing as revealed with ^{18}F -fluoride-PET and confirmed with radiography and histology (figure 2.6). In another group that underwent femoral osteotomy with placement of a 2 mm spacer, none of the femurs healed and all showed minimal ^{18}F -fluoride uptake. This suggests that ^{18}F -fluoride-PET can identify fracture non-unions at an early time point and may have a role in the assessment of longitudinal fracture healing. No significant differences between these two groups were seen using ^{18}F -FDG-PET. ^{18}F -FDG-PET is a tracer for cellular glucose metabolism, and could principally reveal inflammation, but was not helpful in differentiating metabolic activity between successful and delayed bone, probably because ^{18}F -FDG is not specific for bone [51]. On plain radiographs it was also evident whether the bone was, or was not, healing from week 2 onwards; callus formation was visible in the fracture group, while no bone formation was visible in the non-union group. From this point of view the ^{18}F -fluoride did not provide a better prediction than radiography. However, if PET measurements had been made at earlier time points, they would probably have allowed an earlier prediction of healing response.

Besides delayed- or non-unions, infections are a common complication of fracture healing. Lankinen et al. used a new tracer: ^{68}Ga -labeled 1,4,7,10-tetraazacyclododecane- $\text{N}',\text{N}'',\text{N}''',\text{N}''''$ -tetraacetic acid conjugated synthetic peptide (^{68}Ga -DOTAVAP-P1). This tracer is targeted to vascular adhesion protein 1/semicarbazide sensitive amine oxidase (VAP-1/SSAO), which is only expressed at sites of inflammatory reaction. ^{68}Ga -DOTAVAP-P1 was evaluated at sites of inflammatory reaction to assess the feasibility of this tracer to detect early inflammatory and infection processes in healing bones in rats with a defect in the left tibia. In one group, normal bone healing was monitored, in another group osteomyelitis was induced with a bacteria. PET and pQCT were performed at 24 h or at 7 days after surgery. It was shown that the tracer was capable of accurately demonstrating the phase of inflammation in healing bones and the progress of bacterial infection in osteomyelitic bones. This novel imaging agent allowed for the differentiation of bacterial bone infection and normal bone healing as soon as 7 days after onset [161]. With pQCT, the difference between the normal healing and the osteomyelitic group was also evident at 7 days post operative. In the osteomyelitic animals, cortical bone destruction with circumferential periosteal reaction was visible, whereas a normal healing response was seen in animals with a normal defect.

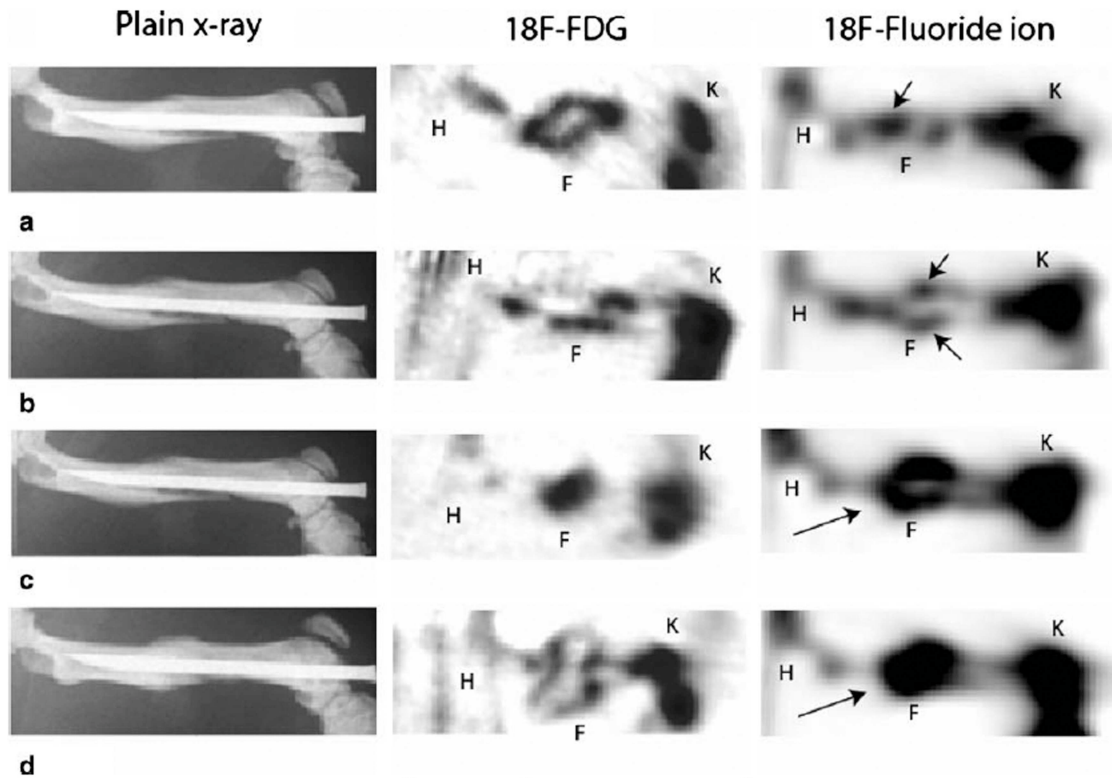


Figure 2.6: Radiograph and corresponding ^{18}F -FDG and ^{18}F -fluoride PET images from a femur of a rat with fracture at 1 week (a), 2 weeks (b), 3 weeks (c), and 4 weeks (d) post fracture. While callus formation can be identified on plain radiographs as early as 2 weeks (b), PET scan images using ^{18}F -fluoride ion show increasing biologic activity (arrows) in the union site during fracture repair at successive time points. In contrast, no significant differences were seen in ^{18}F -FDG tracer uptake at any time point. K knee, F fracture site, H hip (Reproduced from [51]).

To facilitate healing of complicated fractures, mesenchymal stem cells (MSCs) can be delivered to the site of injury [162]. Lee et al. used this strategy to investigate healing in a 0.5 mm defect in the femur of mice with ^{18}F -fluoride-PET and micro-CT and monitored homing of the MSCs with BLI [163]. Micro-CT measurements showed increased bone healing in the MSC-cell-injected group compared to the non-injected group. With ^{18}F -fluoride PET in both groups the signal was higher than in the contralateral femur, but there was no difference between groups. BLI revealed that on day 3 after the operation the MSC-cell-injected injured mice had a higher BLI signal than the non-injected injured mice at the site of operation. For all injured mice the BLI signal was higher than for the uninjured mice, until day 15, when the signal from all groups disappeared. This indicated that MSCs were attracted to the injured tissue and retained there and promoted healing. Degano et al. created a calvarial bone defect filled with hydrogel in nude mice. These hydrogels were filled with human bone marrow stem cells (hBMSCs) or human adipose-derived mesenchymal stem cells (hAMSCs), genetically manipulated to

express luciferase. Thus BLI could be used to quantify changes in the number of hBMSCs and hAMSCs implanted in the calvaria. Four out of ten scaffolds seeded with hAMSCs and seven out of ten scaffolds seeded with hBMSCs retained light-producing cells until the end of the experiment. Bone density in the defect increased in all tested groups, but none of them reached the original bone density by the end of the experiment. Although hBMSCs appeared to survive better than hAMSCs, suggesting the former a more effective tool for bone repair, increments in tissue density induced by both cell types were similar and higher than those generated by scaffolds without stem cells [86]. A discrepancy of this study was that a difference in fluorescence was found in defects with and without scaffold, which was not reflected by the amount of bone formed. Also each mouse received two different implants in the calvaria, but as BLI gives a very diffuse signal it was difficult to distinguish between these two implant sites.

Zilberman et al. analyzed longitudinal bone formation using OsteoSense[®]-FMT and micro-CT in mice with a nonunion bone defect in the radius. Bone formation was enhanced by implantation of genetically modified murine mesenchymal stem cells (mMSCs) overexpressing bone morphogenic protein-2 (BMP2), which induces bone formation. Mice injected with mMSCs-BMP2 showed a significant fluorescent signal, whereas little or no signal could be detected in mice injected with mMSCs, which did not overexpress BMP2 (figure 2.7). In mice implanted with mMSCs-BMP2 in the radial defect, the bulk of new mineral deposition occurred in the regenerating fracture site between week 2 and 3. In mice that did not have mMSCs overexpressing BMP2, no bone formation was found. [164]. In this study both imaging techniques provided a three-dimensional image, and complimentary information. With FMT the osteoblast activity was measured, and with micro-CT the bone that had formed after 3 weeks could be visualized. The fact that the fluorescence signal was higher in the BMP2 overexpressing group indeed was an indicator that more bone had been formed as revealed with micro-CT analysis.

Iris et al. investigated osteocalcin regulation during fracture healing in transgenic mice harboring a luciferase marker gene under the regulation of the human osteocalcin promoter. Osteogenic differentiation was studied in a long bone fracture model and in a bone marrow ablation model. Both bone regeneration models revealed a luciferase expression level peak six days post surgery which was significantly higher than the signal of the contralateral side and significantly higher compared to days 0 and 14. After day 14 the values were similar to that of the contralateral bone. Although similar values of osteocalcin expression were detected for both

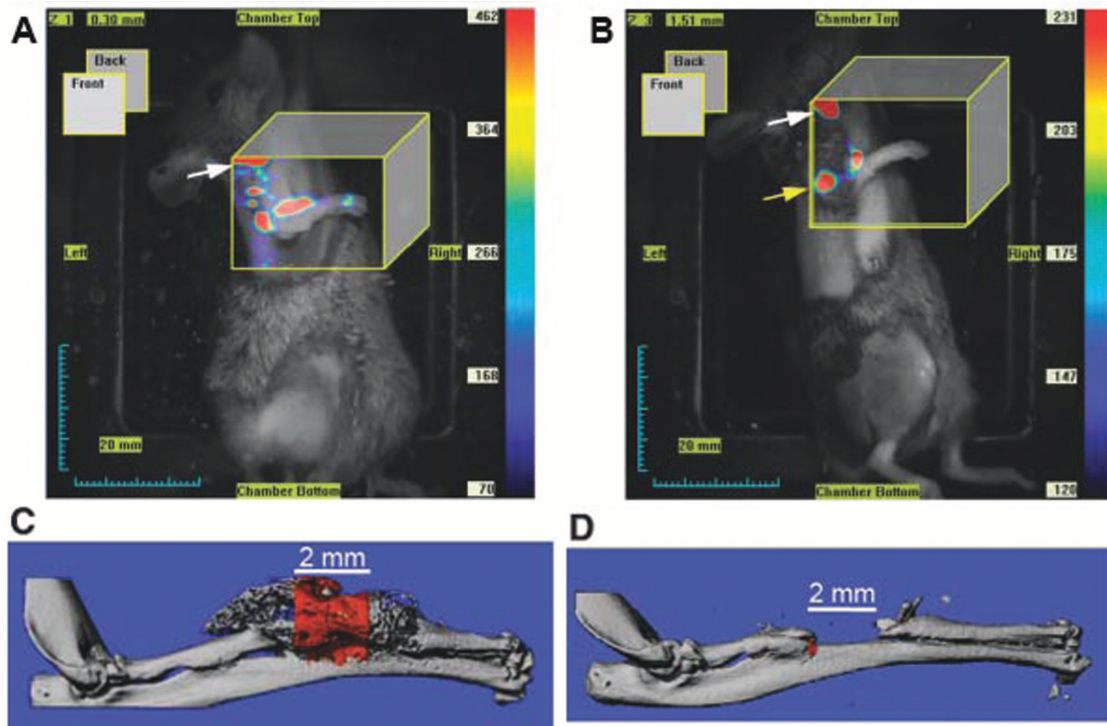


Figure 2.7: FMT images after 3 weeks (A, B) and micro-CT images (C, D) of group implanted with mMSCs cells overexpressing BMP2 (A, C) and in C3H/LacZ control group (B, D). Signals from the elbow (yellow arrow) and shoulder (white arrow) indicate continual bone erosion and growth. The total amount of fluorescence is significantly different between the two groups. Also significant new bone formation is shown in the radial nonunion defect where the mMSCs-BMP2 cells were transplanted (C) and almost no bone formation in the C3H/LacZ control group (D) (Reproduced from [164]).

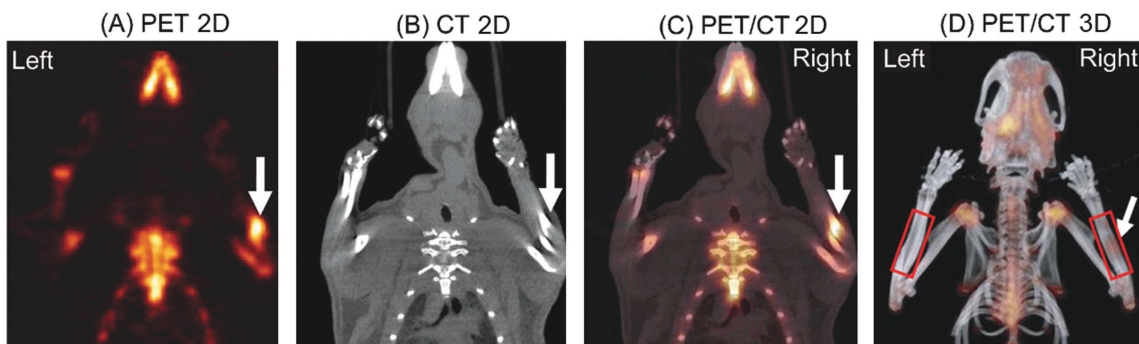


Figure 2.8: Single slice of PET (A), CT (B), registered slice (C), and co-registered PET/CT projection image of the cranial half of a rat on day 4 after fatigue loading in the high displacement group. Symmetric ^{18}F uptake was observed in regions of higher bone turnover. More ^{18}F uptake was observed in the central region of the loaded forelimb (arrow) than in the unloaded forelimb (Figure reproduced from [165]).

models, this does not mean that a similar amount of bone was formed, because the mechanism of bone formation differs between both models. This was however not confirmed with another imaging technique [83].

It has been shown that for fracture healing monitoring, it is helpful to combine a molecular imaging modality with an anatomical imaging modality. With molecular imaging the early healing response can be imaged which can later be confirmed by anatomical imaging.

Mechanical loading response

In healthy bone the osteocytes act as mechanosensors and send signals to other effector cells that regulate bone resorption and formation to maintain bone integrity [166]. In absence of osteocytes the bone deteriorates and there is no response to loading or unloading [167]. With unloading (such as prolonged bed rest) the bone mass decreases and subsequently the strength of the bone is diminished [16,168,169]. Accordingly, mechanical loading leads to an increase in bone formation and bone strength [170]. These mechanical signals can be in orders of magnitude below those of exercise and may present a non-pharmacologic means of preventing or reversing osteoporosis without putting the skeleton at risk of damage [171]. Another strategy in animal research is to induce micro-damage by impact loading, which causes higher bone remodeling activity, through which the bone becomes stronger [172]. Silva et al. analyzed the skeletal response following a single bout of fatigue loading in the forelimb of rats. Four groups of rats were subjected to displacements between 30 to 85% of the average displacement to complete fracture (2.0 mm) to induce damage in the forelimb. On day 2, 4, 7, 9, 11, 18, 24, and 30 post fatigue loading, the rats were imaged with ^{18}F -fluoride-PET. Subsets of the animals were additionally imaged with micro-CT on day 4, 9, and 18 after loading. PET imaging revealed an increased uptake of ^{18}F -fluoride in the central portion of the loaded forelimb in the groups exposed to the higher displacements (figure 2.8). The fluoride uptake increased in proportion to the amount of bone damage, but was also related to an increased presence of vessels [165]. The resolution of the CT was not sufficient to see whether the cortex thickened or how the bone morphology changed, however this was analyzed with histology. In this case CT only served as an anatomical reference for PET. Accurate overlaying of the two modalities was achieved by use of landmarks.

Bone metastases

Bone metastases are a frequent complication of many common cancer types, occurring in about 80% of patients with breast, lung or prostate cancer [173]. Ninety percent of patients who die of prostate cancer harbor bone metastases [140]. Skeletal metastatic disease is the cause of considerable morbidity, including pain,

hypercalcaemia, pathologic fractures, spinal instability, and compression of the spinal cord [174]. Bone metastases are typically referred to as osteolytic when the main effect is bone destruction, and sclerotic when there is mainly increased osteoblastic activity [175]. Although osteolytic disease is usually most evident at sites of bone metastases, osteosclerosis may sometimes predominate, at least for 15-20% of breast cancer patients, but particularly in prostatic cancer [175]. Osteolytic metastases lead to increased bone fragility and susceptibility to fracture [176].

^{99m}Tc -MDP bone scintigraphy has been the most widely used method for evaluating skeletal metastases [141], however ^{18}F -fluoride PET/CT was shown to be more sensitive than bone scintigraphy [140], and MRI and FDG-PET/CT studies are far more accurate than bone scintigraphy [47]. Taira et al. showed that ^{18}F -FDG-PET in combination with CT has a very high positive predictive value for bone metastases (98%) when the findings at PET and CT are concordant. However, in metastases with discordant PET and CT findings, the positive predictive value is markedly diminished. Independently, the positive predictive value of all lesions was significantly higher with PET than with CT [177]. Although malignant bone lesions have a generally higher ^{18}F -FDG uptake than benign bone tumors, there is a considerable overlap regarding the amount of ^{18}F -FDG uptake. The differentiation of benign and malignant lesions can usually be achieved by registration of ^{18}F -FDG-PET with CT [139]. ^{99m}Tc -MDP-SPECT is insensitive to metastases that involve no bone formation and poorly detects early metastases [138, 178], but can differentiate between malignant and benign metastases when ^{99m}Tc -MDP-SPECT and CT are registered [46].

Winkelmann et al. characterized the development, metabolism, and progression of metastatic tumor formation in mice with induced lung tumors by using small-animal PET imaging and *in vivo* micro-CT. Mice were imaged with micro-CT every other day until tumors were anatomically identified, at which point ^{18}F -FDG-PET was performed in the same mouse holder. ^{18}F -FDG-PET is not specific for bone, but rather for new tissue growth. Bone metastases were noted in 65% of the mice, observed in the mandible, femur, tibia, and vertebrae. Small-animal PET imaging did not identify any metastases that were not previously detected by *in vivo* micro-CT. Micro-CT was capable of detecting metastases that were not detected by small-animal PET based on the resolution limits of the used instrumentation. CT/PET fusion imaging correctly correlated radiotracer uptake with anatomical location, demonstrating the utility of multimodality imaging in oncology. However,

only 36% of the tumors confirmed on histopathology were found with micro-CT, because for some tissues the contrast of CT was not adequate for the identification of tumors and for other tissues the size of the tumors was too small [143]. This study is striking in that only CT measurements are made until the presence of a bone metastasis is evident, after which PET is used to confirm this, whereas Kim et al. [179] use PET until a bone metastasis is detected and then use anatomical imaging to locate the malignancy. However Berger et al. also found that lesions smaller than 2.5 mm³ were more reliably detected by micro-CT than by micro-PET, because although PET has a higher sensitivity, the resolution of PET is limiting [58].

Berger et al. created bone tumors in the tibia in mice by inserting a needle through the tibia plateau into the intramedullary canal and injecting three different prostate cancer cell lines. Bone tumor growth was repeatedly imaged by ¹⁸F-fluoride-micro-PET, micro-CT and radiography over a period of three months. Two of the prostate cancer cell lines caused osteolysis, while the third induced sclerotic bone metastasis. The osteolytic metastasis sometimes showed high bone turnover at metastatic edges, but in most cases were presented as lesions with low bone turnover (cold lesions) in the functional scans, and were accordingly more difficult to detect with ¹⁸F-fluoride-micro-PET when the diameter was smaller than 2.5 mm. This underlines the importance of correlating molecular imaging with anatomical imaging. The sclerotic metastases led to distinctly elevated bone turnover that was easy to detect and monitor on ¹⁸F-fluoride scans [58].

Kozloff et al. injected mice in the tibia with prostate cancer cells to analyze the osteolytic response. The mice were imaged by X-ray on day 24, injected with OsteoSense[®] on day 28, imaged with FMT on day 29, and sacrificed for histology thereafter. X-ray revealed a fracture in one mouse and osteolytic areas in the four other mice. For both fracture and severe osteolysis a high fluorescence signal was detected by FMT, but for the three mice with moderate osteolysis no signal was detected [72].

For the above described studies, anatomical imaging allowed an earlier detection of metastases than molecular imaging, due to the lack of marked increases in bone formation and resolution limits. BLI allows faster detection of bone metastases than anatomical imaging modalities. Wetterwald et al. used the strategy of transfecting human mammary carcinoma cell lines with luciferase to visualize the development of bone metastases after injection of the cells into the

left cardiac ventricle of mice or after intraosseous implantation. After intracardiac injection of cancer cells all mice developed bone metastases as detected by BLI. After four weeks, distinct areas of photon accumulation, suggestive of metastatic tumor growth, could be detected over the distal metaphyses of the femurs and over the dorsal side of the thoracic vertebrae. Whole body radiographs taken after 4 weeks did not show any sight of osteolysis in any of the bones, however immunohistochemical analysis did confirm the presence of cancer cells in all of the bones that were shown by BLI to be the site of bioluminescent emission. In mice with intraosseous implantation of cancer cells, bone metastases were detected by BLI after four days after which the signal became stronger. With radiography the metastases were evident from day 14 onwards (figure 2.9).

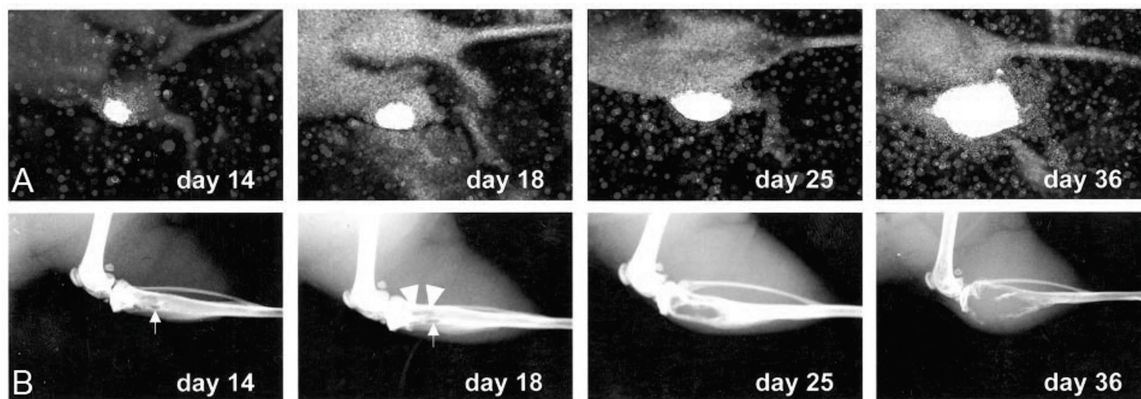


Figure 2.9: BLI and radiographic monitoring *in vivo* of the growth kinetics of the cancer cells implanted in the marrow cavity of the right tibia. Signals are displayed as pseudo-color image at the most sensitive 0- to 3-bit range. Small arrows at days 14 and 18 point at the cortical hole that resulted from surgical drilling. Arrowheads at day 18 highlight the initial area of osteolysis (Figure reproduced from [84]).

BLI offers the important advantage of detecting tumor growth in the marrow cavity long before development of radiologically evident osteolytic and/or osteosclerotic lesions [84]. Fritz et al. investigated the advantage of combining micro-CT and BLI to detect bone metastases in mice injected with human prostate cancer cells. Irrespective of the amount of injected tumor cells into the bone marrow space, photon emission, evidence of the presence of a bone lesion, was detectable after 2 days with BLI. With micro-CT the osteolytic metastases were evident after 7 days. A significant correlation was found when comparing temporal BLI with the micro-CT bone density. Taken together, the multimodality approach allowed an earlier characterization of bone metastases in prostate cancer [176].

Cell imaging on biomaterials

There is a great need for bone cell seeded implants and grafts in orthopedic surgery and biomedical engineering [180, 181]. Although for the repair of large bone defects, autografts are usually preferred, drawbacks are donor site morbidity, limited donor bone supply, anatomical and structural problems, and elevated levels of resorption during healing [182]. Bone implants would eliminate problems of donor site scarcity, and when autogenous cells are used reduce immune rejection and pathogen transfer [183]. For cell seeded implants it is important to quantify the amount of remaining living cells on a scaffold and to image their behavior, growth, and movement [184]. This needs to be imaged with a non-invasive non-destructive approach [185]. The difficulties in quantifying the amount of cells originate from the dependency on the amount of injected cells, varying tissue depths, time between injection and measurement, and for some modalities attenuation of light. An approach to allow for *in vivo* monitoring of cell trafficking involves radiolabeled cells imaged with PET. Gao et al. aimed to analyze homing of bone marrow derived MSCs by labeling them with ^{111}In -oxine. MSCs have the potential to differentiate along multiple lineages [186, 187] and therefore are ideal candidates for therapeutic strategies of bone diseases [188, 189]. There is however not much known about the dynamics and homing of these cells. The aim of this study was to monitor the fate of MSCs in rats with a gamma camera. First, dynamic distribution of MSCs was monitored by real-time imaging right after infusion and 48 hours thereafter. Subsequently, organs were excised and radioactivity was measured in a well counter. As measured with the gamma camera the highest radioactivity was detected in the lungs and gradually increased in the liver. After 48 hours the main radioactivity came from the liver and little signal from lungs and kidneys. After excision the highest accumulation of MSCs was found in the lungs and other organs, but little in the marrow of long bones [190].

Olivo et al. used BLI to monitor bone marrow derived stromal cells (BMSCs) seeded on porous calcium phosphate scaffolds *in vivo*. Scaffolds were implanted subcutaneously in mice. A decrease of the light signal, indicating BMSCs death, was observed in implants seeded with a low number of cells, suggesting that a minimum amount of BMSCs must be seeded to obtain a vital implant after surgery. Implanted BMSCs could be traced by BLI *in vivo* in a quantitative manner [191]. Oskouian et al. tested whether luciferase-labeled MSCs that overexpress BMP2 could induce regulated bone formation and lead to interbody anterior spinal fusion when they are injected in the intervertebral discs in mice. With BLI a high signal

remained over the 4 weeks post injection, indicating that MSCs survived. Micro-CT after sacrifice revealed fusion of vertebral bodies in mice injected with MSCs overexpressing BMP2, but not in mice in which MSCs were not overexpressing BMP2. From these results it was suggested that interbody fusion *in vivo* could be regulated by using genetically engineered MSCs that overexpress BMP2 [192].

Mayer-Kuckuck et al. labeled bone precursor cells (BPC) with iron oxide containing particles to monitor them with MRI and with luciferase to allow imaging with BLI within the bone marrow of the femur in living mice. With MRI the signal clearly increased after BPC infusion, furthermore the BLI signal was 11 times higher in the femurs with BPC transplanted than in the control femur. This strategy was suitable for cell tracking and combines anatomical with functional imaging [193].

Mayer-Kuckuk et al. developed a reporter gene-based multimodality imaging tool to monitor the expansion of transplanted murine bone marrow cells in mice. Initially, BLI was used as a scout to monitor the biodistribution of the bone marrow cells and to assess the dynamics of cell engraftment in the whole body. For subsequent mapping of the skeletal engraftment sites PET and CT were combined. This allowed three-dimensional reconstruction and fusion of the images, which identified that bone marrow cells localized to bones. For registration, the animal had been transported in a fixed position from PET to CT. This method allowed close monitoring of local sites of engraftment *in vivo* [194]. This study shows the advantage of the multimodality procedure. If in this case only BLI had been used, the location of the cells would have been unclear, and PET or CT only would not have been specific enough to detect the cells. Only the combination of the anatomical modality with the functional modality allowed the correct monitoring of bone marrow cells.

2.5.4 Discussion and Conclusion

This paper overviews the methods currently available for molecular imaging in bone. Molecular imaging allows noninvasive monitoring of specific biological processes within living subjects and is complimentary to anatomical imaging. In the molecular imaging field, considerable progress has been made in the further development of imaging techniques and probes over the past decade. These advances have led to a greater understanding of diseases and treatment effects and enhance our understanding of interactions at the molecular level.

^{18}F -fluoride-PET, $^{99\text{m}}\text{Tc}$ -SPECT, NIRF with OsteoSense[®], or reporter gene expression with bioluminescence provide sensitive measurements of bone metabolic activity. NIRF with cathepsin- κ allows the measurement of osteoclast activity. Research is ongoing to develop more sensitive and more specific imaging probes possibly also targeted at other cells.

^{18}F -fluoride PET imaging provides a diagnostic tool for detecting the presence of bone metastases, however the exact location cannot be found without using other techniques when the metastasis is very small. It is also a sensitive marker for assessing the fracture healing success. OsteoSense[®] has been used for research in bone metabolism, bone fracture healing and bone metastases. BLI with a reporter gene is exclusively employed in research, because transgenic animals are needed. Applications for reporter genes are mainly in monitoring cell trafficking, but also in investigations of bone metabolism, fracture healing, and bone metastasis.

The sensitivity of ^{18}F -fluoride PET and $^{99\text{m}}\text{Tc}$ -MDP-SPECT has been demonstrated, however these techniques have limited spatial resolution. Also for the optical imaging systems the spatial resolution is limiting. For CT the spatial resolution is high, but the sensitivity is very low. There is not a single imaging modality that can provide high sensitivity, specificity and high spatial resolution all in one: none of the imaging modalities can perform anatomical imaging and molecular imaging simultaneously. The combination of anatomical and molecular imaging does however greatly enhance the interpretability. Therefore, multiple modalities should be combined either as in a multimodality scanner, or by transferring the subject between modalities and using registration software. By overlaying the anatomical image with the molecular image, there is an anatomical reference for where the molecular processes are taking place, but also longitudinal anatomical data can be related to the previous molecular data to find structure-function relations.

Generally, in the field of bone research, there has been little focus on multimodality imaging techniques, but it is becoming more popular (bone disease, fracture, mechanical loading), in others (cancer) it is established. In conclusion, molecular imaging allows non-invasive, longitudinal studies of biological processes. Multimodality imaging and registration techniques in longitudinal studies will further advance our knowledge of the biological processes underlying bone remodeling, bone diseases, and bone healing.

References

- [1] C.T. Rubin and L.E. Lanyon. Kappa Delta Award paper. Osteoregulatory nature of mechanical stimuli: function as a determinant for adaptive remodeling in bone. *J Orthop Res*, 5(2):300–310, 1987.
- [2] S.C. Cowin. *Bone mechanics handbook*. In. 2nd ed. Boca Raton: CRC Press, 2001.
- [3] A.G. Robling, A.B. Castillo, and C.H. Turner. Biomechanical and molecular regulation of bone remodeling. *Annu Rev Biomed Eng*, 8:455–498, 2006.
- [4] F. Syed and S. Khosla. Mechanisms of sex steroid effects on bone. *Biochem Biophys Res Commun*, 328(3):688–696, 2005.
- [5] R.L. Jilka. Cytokines, bone remodeling, and estrogen deficiency: a 1998 update. *Bone*, 23(2):75–81, 1998.
- [6] Y. Imai, S. Kondoh, A. Kouzmenko, and S. Kato. Regulation of bone metabolism by nuclear receptors. *Mol Cell Endocrinol*, 310(1-2):3–10, 2009.
- [7] G.J. Pettway, J.A. Meganck, A.J. Koh, E.T. Keller, S.A. Goldstein, and L.K. McCauley. Parathyroid hormone mediates bone growth through the regulation of osteoblast proliferation and differentiation. *Bone*, 42(4):806–818, 2008.
- [8] J. Pleiner-Duxneuner, E. Zwettler, E. Paschalis, P. Roschger, V. Nell-Duxneuner, and K. Klaushofer. Treatment of Osteoporosis with Parathyroid Hormone and Teriparatide. *Calcif Tissue Int*, 84(3):159–170, 2009.
- [9] T. Thomas. Intermittent parathyroid hormone therapy to increase bone formation. *Joint Bone Spine*, 73(3):262–269, 2006.
- [10] S. Khosla. Minireview: the OPG/RANKL/RANK system. *Endocrinology*, 142(12):5050–5055, 2001.
- [11] A.G. Robling, F.M. Hinant, D.B. Burr, and C.H. Turner. Improved bone structure and strength after long-term mechanical loading is greatest if loading is separated into short bouts. *J Bone Miner Res*, 17(8):1545–1554, 2002.
- [12] S.J. Warden, J.A. Hurst, M.S. Sanders, C.H. Turner, D.B. Burr, and J. Li. Bone adaptation to a mechanical loading program significantly increases skeletal fatigue resistance. *J Bone Miner Res*, 20(5):809–816, 2005.

- [13] Webster D.J., Morley P.L., van Lenthe G.H., and Müller R. A novel in vivo mouse model for mechanically stimulated bone adaptation—a combined experimental and computational validation study. *Comput Methods Biomech Biomed Engin*, 11(5):435–441, 2008.
- [14] M.J. Gardner, M.C. van der Meulen, D. Demetrakopoulos, T.M. Wright, E.R. Myers, and M.P. Bostrom. In vivo cyclic axial compression affects bone healing in the mouse tibia. *J Orthop Res*, 24(8):1679–1686, 2006.
- [15] B. Lecoq, C. Potrel-Burgot, P. Granier, J.P. Sabatier, and C. Marcelli. Comparison of bone loss induced in female rats by hindlimb unloading, ovariectomy, or both. *Joint Bone Spine*, 73(2):189–195, 2006.
- [16] J.E.M. Brouwers, B. van Rietbergen, R. Huiskes, and K. Ito. Effects of PTH treatment on tibial bone of ovariectomized rats assessed by in vivo micro-CT. *Osteoporos Int*, 20(11):1823–1835, 2009.
- [17] M. Zaidi. Skeletal remodeling in health and disease. *Nat Med*, 13(7):791–801, 2007.
- [18] S.C. Manolagas and R.L. Jilka. Bone marrow, cytokines, and bone remodeling. Emerging insights into the pathophysiology of osteoporosis. *N Engl J Med*, 332(5):305–311, 1995.
- [19] L.G. Raisz. Pathogenesis of osteoporosis: concepts, conflicts, and prospects. *J Clin Invest*, 115(12):3318–3325, 2005.
- [20] U.H. Lerner. Bone remodeling in post-menopausal osteoporosis. *J Dent Res*, 85(7):584–595, 2006.
- [21] A.N. Tosteson, R.T. Burge, D.A. Marshall, and R. Lindsay. Therapies for treatment of osteoporosis in US women: cost-effectiveness and budget impact considerations. *Am J Manag Care*, 14(9):605–615, 2008.
- [22] Anonymous. Consensus development conference: prophylaxis and treatment of osteoporosis. *Am J Med*, 1(90):107–110, 1991.
- [23] R. Brunader and D.K. Shelton. Radiologic bone assessment in the evaluation of osteoporosis. *Am Fam Physician*, 65(7):1357–1364, 2002.
- [24] M. Jergas and H.K. Genant. Current methods and recent advances in the diagnosis of osteoporosis. *Arthritis Rheum*, 36(12):1649–1662, 1993.

- [25] H.K. Genant. Current state of bone densitometry for osteoporosis. *Radiographics*, 18(4):913–918, 1998.
- [26] L.G. Raisz. Osteoporosis: current approaches and future prospects in diagnosis, pathogenesis, and management. *J Bone Miner Metab*, 17(2):79–89, 1999.
- [27] J.A. Kanis, F. Borgstrom, C. De Laet, H. Johansson, O. Johnell, B. Jonsson, A. Oden, N. Zethraeus, B. Pfeleger, and N. Khaltsev. Assessment of fracture risk. *Osteoporos Int*, 16(6):581–589, 2005.
- [28] J.Y. Reginster, N. Sarlet, and M.P. Lecart. Fractures in osteoporosis: the challenge for the new millennium. *Osteoporos Int*, 16 Suppl 1:S1–S3, 2005.
- [29] K.M. Kozloff, L. Quinti, S. Patntirapong, P.V. Hauschka, C.H. Tung, R. Weissleder, and U. Mahmood. Non-invasive optical detection of cathepsin K-mediated fluorescence reveals osteoclast activity in vitro and in vivo. *Bone*, 44(2):190–198, 2009.
- [30] P. Mayer-Kuckuk and A.L. Boskey. Molecular imaging promotes progress in orthopedic research. *Bone*, 39(5):965–977, 2006.
- [31] M. Rudin and R. Weissleder. Molecular imaging in drug discovery and development. *Nat Rev Drug Discov*, 2(2):123–131, 2003.
- [32] R. Weissleder and U. Mahmood. Molecular imaging. *Radiology*, 219(2):316–333, 2001.
- [33] M. Rudin. *Molecular imaging. Basic principles and applications in biomedical research*. London: Imperial College Press, 2005.
- [34] M.J. Paulus, S.S. Gleason, M.E. Easterly, and C.J. Foltz. A review of high-resolution X-ray computed tomography and other imaging modalities for small animal research. *Lab Anim (NY)*, 30(3):36–45, 2001.
- [35] N. Beckmann, R. Kneuer, H. U. Gremlich, H. Karmouty-Quintana, F. X. Ble, and M. Muller. In vivo mouse imaging and spectroscopy in drug discovery. *NMR Biomed*, 20(3):154–185, 2007.
- [36] R. Weissleder and V. Ntziachristos. Shedding light onto live molecular targets. *Nat Med*, 9(1):123–128, 2003.
- [37] B. J. Beattie, G. J. Forster, R. Govantes, C. H. Le, V. A. Longo, P. B. Zanzonico, L. Bidaut, R. G. Blasberg, and J. A. Koutcher. Multimodality registration without a dedicated multimodality scanner. *Mol Imaging*, 6(2):108–120, 2007.

- [38] F.M. McQueen and M. Ostergaard. Established rheumatoid arthritis - new imaging modalities. *Best Pract Res Clin Rheumatol*, 21(5):841–856, 2007.
- [39] J. P. Basilion, S. Yeon, and R. Botnar. Magnetic resonance imaging: utility as a molecular imaging modality. *Curr Top Dev Biol*, 70:1–33, 2005.
- [40] G. Choy, P. Choyke, and S.K. Libutti. Current advances in molecular imaging: noninvasive in vivo bioluminescent and fluorescent optical imaging in cancer research. *Mol Imaging*, 2(4):303–312, 2003.
- [41] J. Zhang, R.E. Campbell, A.Y. Ting, and R.Y. Tsien. Creating new fluorescent probes for cell biology. *Nat Rev Mol Cell Biol*, 3(12):906–918, 2002.
- [42] A. Rahmim and H. Zaidi. PET versus SPECT.strengths, limitations and challenges. *Nucl Med Commun*, 29(3):193–207, 2008.
- [43] C.L. de Ligny, W.J. Gelsema, T.G. Tji, Y.M. Huigen, and H.A. Vink. Bone seeking pharmaceuticals. *Int J Rad Appl Instrum B*, 17(2):161–179, 1990.
- [44] D. Kanishi. ^{99m}Tc-MDP accumulation mechanisms in bone. *Oral Surg Oral Med Oral Pathol*, 75(2):239–246, 1993.
- [45] O.P. Temmerman, P.G. Raijmakers, I.C. Heyligers, E.F. Comans, M. Lubberink, G.J. Teule, and A.A. Lammertsma. Bone metabolism after total hip revision surgery with impacted grafting: evaluation using H₂ ¹⁵O and [¹⁸F]fluoride PET; a pilot study. *Mol Imaging Biol*, 10(5):288–293, 2008.
- [46] A.K. Buck, S. Nekolla, S. Ziegler, A. Beer, B.J. Krause, K. Herrmann, K. Scheidhauer, H.J. Wester, E.J. Rummeny, M. Schwaiger, and A. Drzezga. Spect/Ct. *J Nucl Med*, 49(8):1305–1319, 2008.
- [47] J. Kumar, A. Seith, A. Kumar, R. Sharma, S. Bakhshi, R. Kumar, and S. Agarwala. Whole-body MR imaging with the use of parallel imaging for detection of skeletal metastases in pediatric patients with small-cell neoplasms: comparison with skeletal scintigraphy and FDG PET/CT. *Pediatr Radiol*, 38(9):953–962, 2008.
- [48] T. Ota, I. Yamamoto, H. Ohnishi, I. Yuh, Y. Kigami, T. Suzuki, Y. Yamamura, K. Murata, and R. Morita. Three-dimensional bone scintigraphy using volume-rendering technique and SPECT. *J Nucl Med*, 37(9):1567–1570, 1996.

- [49] Jr. A. A. Bogdanov and K. Licha. *Molecular Imaging: An essential tool in pre-clinical research, diagnostic imaging, and therapy*. Springer Berlin Heidelberg New York, 2005.
- [50] P.A. Schubiger, L. Lehmann, and M. Friebe. *PET Chemistry: The driving force in molecular imaging*. Berlin Heidelberg New York: Springer-Verlag, 2007.
- [51] W.K. Hsu, B.T. Feeley, L. Krenek, D.B. Stout, A.F. Chatziioannou, and J.R. Lieberman. The use of ^{18}F -fluoride and ^{18}F -FDG PET scans to assess fracture healing in a rat femur model. *Eur J Nucl Med Mol Imaging*, 34(8):1291–1301, 2007.
- [52] D.E. Kuhl and R.Q. Edwards. Cylindrical and Section Radioisotope Scanning of the Liver and Brain. *Radiology*, 83:926–936, 1964.
- [53] D.E. Kuhl, R.Q. Edwards, A.R. Ricci, and M. Reivich. Quantitative section scanning using orthogonal tangent correction. *J Nucl Med*, 14(4):196–200, 1973.
- [54] R.A. Hawkins, Y. Choi, S.C. Huang, C.K. Hoh, M. Dahlbom, C. Schiepers, N. Satyamurthy, J.R. Barrio, and M.E. Phelps. Evaluation of the skeletal kinetics of fluorine-18-fluoride ion with PET. *J Nucl Med*, 33(5):633–642, 1992.
- [55] S. Toegel, O. Hoffmann, W. Wadsak, D. Ettliger, L.K. Mien, K. Wiesner, J. Nguemo, H. Viernstein, K. Kletter, R. Dudczak, and M. Mitterhauser. Uptake of bone-seekers is solely associated with mineralisation! A study with $^{99\text{m}}\text{Tc}$ -MDP, ^{153}Sm -EDTMP and ^{18}F -fluoride on osteoblasts. *Eur J Nucl Med Mol Imaging*, 33(4):491–494, 2006.
- [56] G. Karsenty, N. Vigneron, and V. Jorgetti. Value of the $^{99\text{m}}\text{Tc}$ -methylene diphosphonate bone scan in renal osteodystrophy. *Kidney Int*, 29:1058–1065, 1986.
- [57] H.R. Herschman. Micro-PET imaging and small animal models of disease. *Curr Opin Immunol*, 15(4):378–384, 2003.
- [58] F. Berger, Y. P. Lee, A. M. Loening, A. Chatziioannou, S. J. Freedland, R. Leahy, J. R. Lieberman, A. S. Belledegrun, C. L. Sawyers, and S. S. Gambhir. Whole-body skeletal imaging in mice utilizing microPET: optimization of

- reproducibility and applications in animal models of bone disease. *Eur J Nucl Med Mol Imaging*, 29(9):1225–1236, 2002.
- [59] F.G. Duhaylongsod, V.J. Lowe, E.F. Patz, A.L. Vaughn, R.E. Coleman, and W.G. Wolfe. Detection of primary and recurrent lung cancer by means of F-18 fluorodeoxyglucose positron emission tomography (FDG PET). *J Thorac Cardiovasc Surg*, 110(1):130–140, 1995.
- [60] M.E. Phelps. PET: the merging of biology and imaging into molecular imaging. *J Nucl Med*, 41(4):661–681, 2000.
- [61] M.M. Thornton. Multi-modality imaging of musculoskeletal disease in small animals. *J Musculoskelet Neuronal Interact*, 4(364):364, 2004.
- [62] B. Ma, K.D. Hankenson, J.E. Dennis, A.I. Caplan, S.A. Goldstein, and M.R. Kilbourn. A simple method for stem cell labeling with fluorine 18. *Nucl Med Biol*, 32(7):701–705, 2005.
- [63] B.W. Rice, M.D. Cable, and M.B. Nelson. In vivo imaging of light-emitting probes. *J Biomed Opt*, 6(4):432–440, 2001.
- [64] V. Ntziachristos, C. Bremer, and R. Weissleder. Fluorescence imaging with near-infrared light: new technological advances that enable in vivo molecular imaging. *Eur Radiol*, 13(1):195–208, 2003.
- [65] V. Humblet, R. Lapidus, L.R. Williams, T. Tsukamoto, C. Rojas, P. Majer, B. Hin, S. Ohnishi, A.M. De Grand, A. Zaheer, J.T. Renze, A. Nakayama, B.S. Slusher, and J.V. Frangioni. High-affinity near-infrared fluorescent small-molecule contrast agents for in vivo imaging of prostate-specific membrane antigen. *Mol Imaging*, 4(4):448–462, 2005.
- [66] A. Zaheer, M. Murshed, A.M. De Grand, T.G. Morgan, G. Karsenty, and J.V. Frangioni. Optical imaging of hydroxyapatite in the calcified vasculature of transgenic animals. *Arterioscler Thromb Vasc Biol*, 26(5):1132–1136, 2006.
- [67] V. Ntziachristos, C. Bremer, E.E. Graves, J. Ripoll, and R. Weissleder. In vivo tomographic imaging of near-infrared fluorescent probes. *Mol Imaging*, 1(2):82–88, 2002.
- [68] E.E. Graves, J. Ripoll, R. Weissleder, and V. Ntziachristos. A submillimeter resolution fluorescence molecular imaging system for small animal imaging. *Med Phys*, 30(5):901–911, 2003.

- [69] E.E. Graves, D. Yessayan, G. Turner, R. Weissleder, and V. Ntziachristos. Validation of in vivo fluorochrome concentrations measured using fluorescence molecular tomography. *J Biomed Opt*, 10(4):44019, 2005.
- [70] V. Ntziachristos, C.H. Tung, C. Bremer, and R. Weissleder. Fluorescence molecular tomography resolves protease activity in vivo. *Nat Med*, 8(7):757–760, 2002.
- [71] A. Zaheer, R.E. Lenkinski, A. Mahmood, A.G. Jones, L.C. Cantley, and J.V. Frangioni. In vivo near-infrared fluorescence imaging of osteoblastic activity. *Nat Biotechnol*, 19(12):1148–1154, 2001.
- [72] K.M. Kozloff, R. Weissleder, and U. Mahmood. Noninvasive optical detection of bone mineral. *J Bone Miner Res*, 22(8):1208–1216, 2007.
- [73] B. Chance. Optical method. *Annu Rev Biophys Biophys Chem*, 20:1–30, 1991.
- [74] J.S. Souris. Seeing the light in bone metabolism imaging. *Trends Biotechnol*, 20(9):364–366, 2002.
- [75] K.M. Kozloff, L. Quinti, C. Tung, R. Weissleder, and U. Mahmood. Non-invasive imaging of osteoclast activity via near-infrared cathepsin-K activatable optical probe. *J Musculoskelet Neuronal Interact*, 6(4):353, 2006.
- [76] J.A. Koo, S.P. Schmidt, and G.B. Schuster. Bioluminescence of the firefly: key steps in the formation of the electronically excited state for model systems. *Proc Natl Acad Sci U S A*, 75(1):30–33, 1978.
- [77] R.Y. Tsien. The green fluorescent protein. *Annu Rev Biochem*, 67:509–544, 1998.
- [78] C.W.G.M. Lowik, M.G. Cecchini, A. Maggi, and G. van der Pluijm. *Molecular imaging: An essential tool in preclinical research, diagnostical imaging, and therapy*. Berlin Heidelberg New York: Springer-Verlag, 2005.
- [79] C.H. Contag and M.H. Bachmann. Advances in in vivo bioluminescence imaging of gene expression. *Annu Rev Biomed Eng*, 4:235–260, 2002.
- [80] J.B. Lian, G.S. Stein, J.L. Stein, and A.J. van Wijnen. Osteocalcin gene promoter: unlocking the secrets for regulation of osteoblast growth and differentiation. *J Cell Biochem Suppl*, 30-31:62–72, 1998.

- [81] A.L. Boskey, S. Gadaleta, C. Gundberg, S.B. Doty, P. Ducy, and G. Karsenty. Fourier transform infrared microspectroscopic analysis of bones of osteocalcin-deficient mice provides insight into the function of osteocalcin. *Bone*, 23(3):187–196, 1998.
- [82] T.L. Clemens, H. Tang, S. Maeda, R.A. Kesterson, F. Demayo, J.W. Pike, and C.M. Gundberg. Analysis of osteocalcin expression in transgenic mice reveals a species difference in vitamin D regulation of mouse and human osteocalcin genes. *J Bone Miner Res*, 12(10):1570–1576, 1997.
- [83] B. Iris, Y. Zilberman, E. Zeira, E. Galun, A. Honigman, G. Turgeman, T. Clemens, Z. Gazit, and D. Gazit. Molecular imaging of the skeleton: quantitative real-time bioluminescence monitoring gene expression in bone repair and development. *J Bone Miner Res*, 18(3):570–578, 2003.
- [84] A. Wetterwald, G. van der Pluijm, I. Que, B. Sijmons, J. Buijs, M. Karperien, C.W. Lowik, E. Gautschi, G.N. Thalmann, and M.G. Cecchini. Optical imaging of cancer metastasis to bone marrow: a mouse model of minimal residual disease. *Am J Pathol*, 160(3):1143–1153, 2002.
- [85] F. P. Barry and J. M. Murphy. Mesenchymal stem cells: clinical applications and biological characterization. *Int J Biochem Cell Biol*, 36(4):568–584, 2004.
- [86] I.R. Degano, M. Vilalta, J.R. Bago, A.M. Matthies, J.A. Hubbell, H. Dimitriou, P. Bianco, N. Rubio, and J. Blanco. Bioluminescence imaging of calvarial bone repair using bone marrow and adipose tissue-derived mesenchymal stem cells. *Biomaterials*, 29(4):427–437, 2008.
- [87] V. Ntziachristos, J. Ripoll, L.V. Wang, and R. Weissleder. Looking and listening to light: the evolution of whole-body photonic imaging. *Nat Biotechnol*, 23(3):313–320, 2005.
- [88] M.C. Monier-Faugere. Quality assurance-quality control in bone histopathology and bone histomorphometry. *Bone*, 14(3):559–572, 1993.
- [89] D. C. Brown and K. C. Gatter. The bone marrow trephine biopsy: a review of normal histology. *Histopathology*, 22(5):411–422, 1993.
- [90] L. Dalle Carbonare, M.T. Valenti, F. Bertoldo, M. Zanatta, S. Zenari, G. Realdi, V. Lo Cascio, and S. Giannini. Bone microarchitecture evaluated by histomorphometry. *Micron*, 36(7-8):609–616, 2005.

- [91] P. Chavassieux and P.J. Meunier. Histomorphometric approach of bone loss in men. *Calcif Tissue Int*, 69(4):209–213, 2001.
- [92] A.A. Deodhar and A.D. Woolf. Bone mass measurement and bone metabolism in rheumatoid arthritis: a review. *Br J Rheumatol*, 35(4):309–322, 1996.
- [93] P. Rügsegger, B. Koller, and R. Müller. A microtomographic system for the nondestructive evaluation of bone architecture. *Calcif Tissue Int*, 58(1):24–29, 1996.
- [94] M. Piert, T.T. Zittel, G.A. Becker, M. Jahn, A. Stahlschmidt, G. Maier, H.J. Machulla, and R. Bares. Assessment of porcine bone metabolism by dynamic. *J Nucl Med*, 42(7):1091–1100, 2001.
- [95] S.R. Matteson, S.T. Deahl, M.E. Alder, and P.V. Nummikoski. Advanced imaging methods. *Crit Rev Oral Biol Med*, 7(4):346–395, 1996.
- [96] A.M. Cormack. Reconstruction of densities from their projections, with applications in radiological physics. *Phys Med Biol*, 18(2):195–207, 1973.
- [97] L.A. Feldkamp, S.A. Goldstein, A.M. Parfitt, G. Jesion, and M. Kleerekoper. The direct examination of three-dimensional bone architecture in vitro by computed tomography. *J Bone Miner Res*, 4(1):3–11, 1989.
- [98] G.N. Hounsfield. Computerized transverse axial scanning (tomography).1. Description of system. *Br J Radiol*, 46(552):1016–1022, 1973.
- [99] G. M. Blake and I. Fogelman. Technical principles of dual energy x-ray absorptiometry. *Semin Nucl Med*, 27(3):210–228, 1997.
- [100] M.L. Bouxsein, B.S. Coan, and S.C. Lee. Prediction of the strength of the elderly proximal femur by bone mineral density and quantitative ultrasound measurements of the heel and tibia. *Bone*, 25(1):49–54, 1999.
- [101] J.A. Gasser. Assessing bone quantity by pQCT. *Bone*, 17(4 Suppl):145S–154S, 1995.
- [102] H.N. Rosen, S. Tollin, R. Balena, V.L. Middlebrooks, W.G. Beamer, L.R. Donohue, C. Rosen, A. Turner, M. Holick, and S.L. Greenspan. Differentiating between orchietomized rats and controls using measurements of trabecular bone density: a comparison among DXA, histomorphometry, and peripheral quantitative computerized tomography. *Calcif Tissue Int*, 57(1):35–39, 1995.

- [103] D. Liu, S.L. Manske, S.A. Kontulainen, C. Tang, P. Guy, T.R. Oxland, and H.A. McKay. Tibial geometry is associated with failure load ex vivo: a MRI, pQCT and DXA study. *Osteoporos Int*, 18(7):991–997, 2007.
- [104] S. Kuroda, H. Mukohyama, H. Kondo, K. Aoki, K. Ohya, T. Ohyama, and S. Kasugai. Bone mineral density of the mandible in ovariectomized rats: analyses using dual energy X-ray absorptiometry and peripheral quantitative computed tomography. *Oral Dis*, 9(1):24–28, 2003.
- [105] D.W. Holdsworth and M.D. Thornton. Micro-CT in small animal and specimen imaging. *Trends in Biotechnology*, 20(8 Suppl):S34–S39, 2002.
- [106] J. Damilakis, T.G. Maris, and A.H. Karantanas. An update on the assessment of osteoporosis using radiologic techniques. *Eur Radiol*, 17(6):1591–1602, 2007.
- [107] S. Boutroy, M.L. Bouxsein, F. Munoz, and P.D. Delmas. In vivo assessment of trabecular bone microarchitecture by high-resolution peripheral quantitative computed tomography. *J Clin Endocrinol Metab*, 90(12):6508–6515, 2005.
- [108] J.H. Waarsing, J.S. Day, and H. Weinans. Longitudinal micro-CT scans to evaluate bone architecture. *J Musculoskelet Neuronal Interact*, 5(4):310–312, 2005.
- [109] E.L. Ritman. Micro-computed tomography-current status and developments. *Annu Rev Biomed Eng*, 6:185–208, 2004.
- [110] A. Müller, E. Ruegsegger, and P. Ruegsegger. Peripheral QCT: a low-risk procedure to identify women predisposed to osteoporosis. *Phys Med Biol*, 34(6):741–749, 1989.
- [111] R. Müller, T. Hildebrand, H.J. Hauselmann, and P. Ruegsegger. In vivo reproducibility of three-dimensional structural properties of noninvasive bone biopsies using 3D-pQCT. *J Bone Miner Res*, 11(11):1745–1750, 1996.
- [112] M. Ito, K. Tsurusaki, and K. Hayashi. Peripheral QCT for the diagnosis of osteoporosis. *Osteoporos Int*, 7 Suppl 3:S120–S127, 1997.
- [113] M. Safadi, D. Shapira, I. Leichter, A. Reznick, and M. Silbermann. Ability of different techniques of measuring bone mass to determine vertebral bone loss in aging female rats. *Calcif Tissue Int*, 42(6):375–382, 1988.
- [114] P. Mansfield. Real-time echo-planar imaging by NMR. *Br Med Bull*, 40(2):187–190, 1984.

- [115] P.C. Lauterbur. Image formation by induced local interactions. Examples employing nuclear magnetic resonance. 1973. *Clin Orthop Relat Res*, 244:3–6, 1989.
- [116] W.A. Gibby. Basic principles of magnetic resonance imaging. *Neurosurg Clin N Am*, 16(1):1–64, 2005.
- [117] R. Krug, J. Carballido-Gamio, S. Banerjee, R. Stahl, L. Carvajal, D. Xu, D. Vigneron, D.A. Kelley, T.M. Link, and S. Majumdar. In vivo bone and cartilage MRI using fully-balanced steady-state free-precession at 7 tesla. *Magn Reson Med*, 58(6):1294–1298, 2007.
- [118] F.W. Wehrli, L. Hilaire, M. Fernandez-Seara, B.R. Gomberg, H.K. Song, B. Zemel, L. Loh, and P.J. Snyder. Quantitative magnetic resonance imaging in the calcaneus and femur of women with varying degrees of osteopenia and vertebral deformity status. *J Bone Miner Res*, 17(12):2265–2273, 2002.
- [119] S. Anumula, J. Magland, S. L. Wehrli, H. Ong, H. K. Song, and F. W. Wehrli. Multi-modality study of the compositional and mechanical implications of hypomineralization in a rabbit model of osteomalacia. *Bone*, 42(2):405–413, 2008.
- [120] F.W. Wehrli, B.R. Gomberg, P.K. Saha, H.K. Song, S.N. Hwang, and P.J. Snyder. Digital topological analysis of in vivo magnetic resonance microimages of trabecular bone reveals structural implications of osteoporosis. *J Bone Miner Res*, 16(8):1520–1531, 2001.
- [121] W. Hogler, C.J. Blimkie, C.T. Cowell, A.F. Kemp, J. Briody, P. Wiebe, N. Farpour-Lambert, C.S. Duncan, and H.J. Woodhead. A comparison of bone geometry and cortical density at the mid-femur between prepuberty and young adulthood using magnetic resonance imaging. *Bone*, 33(5):771–778, 2003.
- [122] B.R. Gomberg, F.W. Wehrli, B. Vasilic, R.H. Weening, P.K. Saha, H.K. Song, and A.C. Wright. Reproducibility and error sources of micro-MRI-based trabecular bone structural parameters of the distal radius and tibia. *Bone*, 35(1):266–276, 2004.
- [123] H.J. Woodhead, A.F. Kemp, C.J.R. Blimkie, J.N. Briody, C.S. Duncan, M. Thompson, A. Lam, R. Howman-Giles, and C.T. Cowell. Measurement

- of midfemoral shaft geometry: repeatability and accuracy using magnetic resonance imaging and dual-energy X-ray absorptiometry. *J Bone Miner Res*, 16(12):2251–2259, 2001.
- [124] F.W. Wehrli, G.A. Ladinsky, C. Jones, M. Benito, J. Magland, B. Vasilic, A.M. Popescu, B. Zemel, A.J. Cucchiara, A.C. Wright, H.K. Song, P.K. Saha, H. Peachey, and P.J. Snyder. In vivo magnetic resonance detects rapid remodeling changes in the topology of the trabecular bone network after menopause and the protective effect of estradiol. *J Bone Miner Res*, 23(5):730–740, 2008.
- [125] F.W. Wehrli, M.B. Leonard, P.K. Saha, and B.R. Gomberg. Quantitative high-resolution magnetic resonance imaging reveals structural implications of renal osteodystrophy on trabecular and cortical bone. *J Magn Reson Imaging*, 20(1):83–89, 2004.
- [126] G.J. Kazakia, B. Hyun, A.J. Burghardt, R. Krug, D.C. Newitt, A.E. de Papp, T.M. Link, and S. Majumdar. In vivo determination of bone structure in postmenopausal women: a comparison of HR-pQCT and high-field MR imaging. *J Bone Miner Res*, 23(4):463–474, 2008.
- [127] F.W. Wehrli, H.K. Song, P.K. Saha, and A.C. Wright. Quantitative MRI for the assessment of bone structure and function. *NMR Biomed*, 19(7):731–764, 2006.
- [128] S.R. Cherry. Multimodality in vivo imaging systems: twice the power or double the trouble? *Annu Rev Biomed Eng*, 8:35–62, 2006.
- [129] E.L. Ritman. Molecular imaging in small animals—roles for micro-CT. *J Cell Biochem Suppl*, 39:116–124, 2002.
- [130] D.W. Townsend. Dual-modality imaging: combining anatomy and function. *J Nucl Med*, 49(6):938–955, 2008.
- [131] B.H. Hasegawa, K. Iwata, K.H. Wong, M.C. Wu, A.J. Da Silva, H.R. Tang, W.C. Barber, A.H. Hwang, and A.E. Sakdinawat. Dual-modality imaging of function and physiology. *Acad Radiol*, 9(11):1305–1321, 2002.
- [132] T. Beyer, D. W. Townsend, T. Brun, P. E. Kinahan, M. Charron, R. Roddy, J. Jerin, J. Young, L. Byars, and R. Nutt. A combined PET/CT scanner for clinical oncology. *J Nucl Med*, 41(8):1369–1379, 2000.

- [133] T.F. Lang, B.H. Hasegawa, S.C. Liew, J.K. Brown, S.C. Blankespoor, S.M. Reilly, E.L. Gingold, and C.E. Cann. Description of a prototype emission-transmission computed tomography imaging system. *J Nucl Med*, 33(10):1881–1887, 1992.
- [134] Y. Shao, S.R. Cherry, K. Farahani, K. Meadors, S. Siegel, R.W. Silverman, and P.K. Marsden. Simultaneous PET and MR imaging. *Phys Med Biol*, 42(10):1965–1970, 1997.
- [135] R.B. Slates, K. Farahani, Y. Shao, P.K. Marsden, J. Taylor, P.E. Summers, S. Williams, J. Beech, and S.R. Cherry. A study of artefacts in simultaneous PET and MR imaging using a prototype MR compatible PET scanner. *Phys Med Biol*, 44(8):2015–2027, 1999.
- [136] K. Takahashi, N. Inadama, H. Murayama, T. Yamaya, E. Yoshida, and et al. Preliminary study of a DOI-PET detector with optical imaging capability. *IEEE Nuclear Science Symposium Conference Record*, pages 3318–3321, 2007.
- [137] R.L. Bridges, C.R. Wiley, J.C. Christian, and A.P. Strohm. An introduction to Na(18)F bone scintigraphy: basic principles, advanced imaging concepts, and case examples. *J Nucl Med Technol*, 35(2):64–76, 2007.
- [138] S. Cowey, A.A. Szafran, J. Kappes, K.R. Zinn, G.P. Siegal, R.A. Desmond, H. Kim, L. Evans, and R.W. Hardy. Breast cancer metastasis to bone: evaluation of bioluminescent imaging and microSPECT/CT for detecting bone metastasis in immunodeficient mice. *Clin Exp Metastasis*, 24(5):389–401, 2007.
- [139] K. Strobel, U.E. Exner, K.D. Stumpe, T.F. Hany, B. Bode, K. Mende, P. Veit-Haibach, G.K. von Schulthess, and J. Hodler. The additional value of CT images interpretation in the differential diagnosis of benign vs malignant primary bone lesions with 18F-FDG-PET/CT. *Eur J Nucl Med Mol Imaging*, 35(11):2000–2008, 2008.
- [140] E. Even-Sapir, U. Metser, E. Mishani, G. Lievshitz, H. Lerman, and I. Leibovitch. The detection of bone metastases in patients with high-risk prostate cancer: 99mTc-MDP Planar bone scintigraphy, single- and multi-field-of-view SPECT, 18F-fluoride PET, and 18F-fluoride PET/CT. *J Nucl Med*, 47:287–297, 2006.
- [141] Y.W. Chen, M.Y. Huang, J.S. Hsieh, M.F. Hou, S.H. Chou, and C.L. Lin. Discordant findings of skeletal metastasis between tc 99M MDP bone scans

- and F18 FDG PET/CT imaging for advanced breast and lung cancers—two case reports and literature review. *Kaohsiung J Med Sci*, 23(12):639–646, 2007.
- [142] D.L. Hill, P.G. Batchelor, M. Holden, and D.J. Hawkes. Medical image registration. *Phys Med Biol*, 46(3):R1–R45, 2001.
- [143] C.T. Winkelmann, S.D. Figueroa, T.L. Rold, W.A. Volkert, and T.J. Hoffman. Microimaging characterization of a B16-F10 melanoma metastasis mouse model. *Mol Imaging*, 5(2):105–114, 2006.
- [144] P.L. Chow, D.B. Stout, E. Komisopoulou, and A.F. Chatziioannou. A method of image registration for small animal, multi-modality imaging. *Phys Med Biol*, 51(2):379–390, 2006.
- [145] H. Weinans, P.J. Prendergast, L.M. McNamara, and J.C. Van der Linde. Stress-concentrating effect of resorption lacunae in trabecular bone. *J Biomech*, 39:734–741, 2006.
- [146] R. Huiskes, R. Ruimerman, G.H. van Lenthe, and J.D. Janssen. Effects of mechanical forces on maintenance and adaptation of form in trabecular bone. *Nature*, 405(6787):704–706, 2000.
- [147] K. Kurokawa. How is plasma calcium held constant? Milieu interieur of calcium. *Kidney Int*, 49(6):1760–1764, 1996.
- [148] E. Rubin, F. Gorstein, R. Rubin, R. Schwarting, and D. Strayer. *Rubin's pathology: clinicopathologic foundations of medicine*. USA: Lippincott Williams&Williams, 4th ed. philadelphia edition, 2005.
- [149] M. Sundaram. Founders lecture 2007 : Metabolic bone disease: what has changed in 30 years? *Skeletal Radiol*, 38(9):841–853, 2009.
- [150] C. Messa, W.G. Goodman, C.K. Hoh, Y. Choi, A.R. Nissenson, I.B. Salusky, M.E. Phelps, and R.A. Hawkins. Bone metabolic activity measured with positron emission tomography and [18F]fluoride ion in renal osteodystrophy: correlation with bone histomorphometry. *J Clin Endocrinol Metab*, 77(4):949–955, 1993.
- [151] D. Davidson, J. Pike, D. Garbuz, C.P. Duncan, and B.A. Masri. Intraoperative periprosthetic fractures during total hip arthroplasty. Evaluation and management. *J Bone Joint Surg Am*, 90(9):2000–2012, 2008.

- [152] G. Ullmark, J. Sorensen, B. Langstrom, and O Nilsson. Bone regeneration 6 years after impaction bone grafting: a PET analysis. *Acta Orthop*, 78(2):201–205, 2007.
- [153] A. Schindeler, M.M. McDonald, P. Bokko, and D.G. Little. Bone remodeling during fracture repair: The cellular picture. *Semin Cell Dev Biol*, 19(5):459–466, 2008.
- [154] T.A. Einhorn. The cell and molecular biology of fracture healing. *Clin Orthop Relat Res*, 355 Supl:S7–S21, 1998.
- [155] M. Doblare, J.M. Garcia, and M.J. Gomez. Modelling bone tissue fracture and healing: a review. *Engineering Fracture Mechanics*, 71(13-14):1809–1840, 2004.
- [156] A. Hulth. Current concepts of fracture healing. *Clin Orthop Relat Res*, 249:265–284, 1989.
- [157] T.A. Einhorn. Enhancement of fracture-healing. *J Bone Joint Surg Am*, 77(6):940–956, 1995.
- [158] M. Zlowodzki, W.T. Obrebsky, J.B. Thomison, and P.J. Kregor. Functional outcome after treatment of lower-extremity nonunions. *J Trauma*, 58(2):312–317, 2005.
- [159] N.A. Ebraheim, E.R. Savolaine, A. Patel, M. Skie, and W.T. Jackson. Assessment of tibial fracture union by 35-45 degrees internal oblique radiographs. *J Orthop Trauma*, 5(3):349–350, 1991.
- [160] PF. O’Loughlin, S. Morr, L. Bogunovic, A.D. Kim, B. Park, and J.M. Lane. Selection and development of preclinical models in fracture-healing research. *J Bone Joint Surg Am*, 90 Suppl 1:79–84, 2008.
- [161] P. Lankinen, T.J. Makinen, T.A. Poyhonen, P. Virsu, S. Salomaki, A.J. Hakanen, S. Jalkanen, H.T. Aro, and A. Roivainen. (68)Ga-DOTAVAP-P1 PET imaging capable of demonstrating the phase of inflammation in healing bones and the progress of infection in osteomyelitic bones. *Eur J Nucl Med Mol Imaging*, 35(2):352–364, 2007.
- [162] S.P. Bruder, D.J. Fink, and A.I. Caplan. Mesenchymal stem cells in bone development, bone repair, and skeletal regeneration therapy. *J Cell Biochem*, 56(3):283–294, 1994.

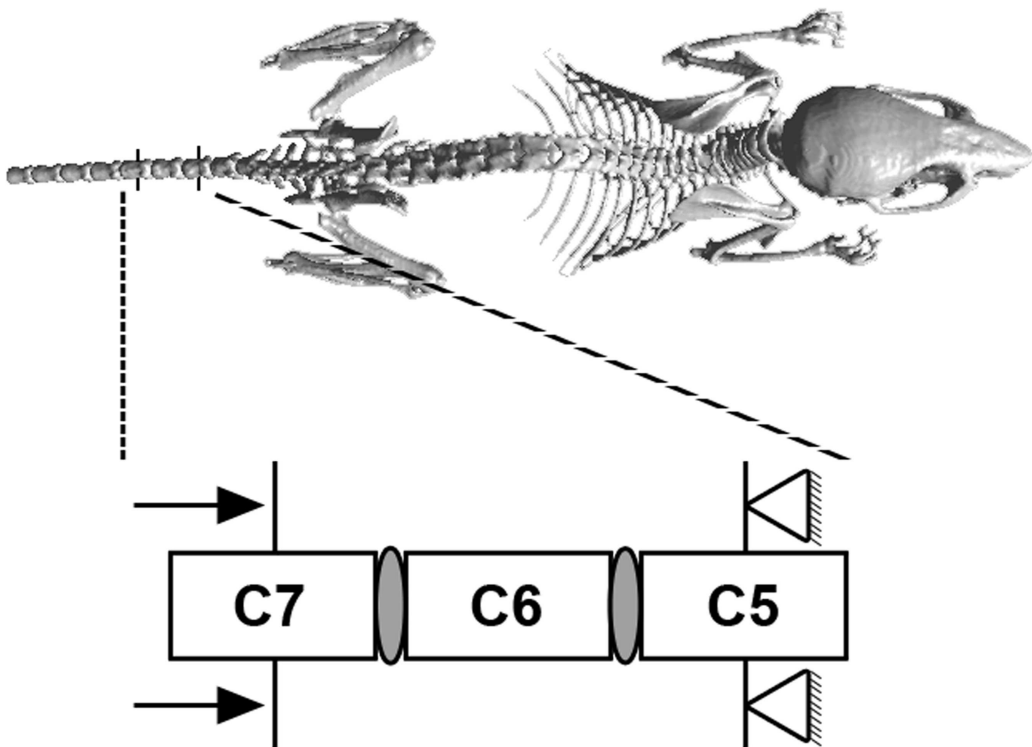
- [163] S.W. Lee, P. Padmanabhan, P. Ray, S.S. Gambhir, T. Doyle, C. Contag, S.B. Goodman, and S. Biswal. Stem cell-mediated accelerated bone healing observed with in vivo molecular and small animal imaging technologies in a model of skeletal injury. *J Orthop Res*, 27(3):295–302, 2009.
- [164] Y. Zilberman, I. Kallai, Y. Gafni, G. Pelled, S. Kossodo, W. Yared, and D. Gazit. Fluorescence molecular tomography enables in vivo visualization and quantification of nonunion fracture repair induced by genetically engineered mesenchymal stem cells. *J Orthop Res*, 26(4):522–530, 2007.
- [165] M.J. Silva, B.A. Uthgenannt, J.R. Rutlin, G.R. Wohl, J.S. Lewis, and M.J. Welch. In vivo skeletal imaging of ^{18}F -fluoride with positron emission tomography reveals damage- and time-dependent responses to fatigue loading in the rat ulna. *Bone*, 39(2):229–236, 2006.
- [166] L. F. Bonewald and M. L. Johnson. Osteocytes, mechanosensing and Wnt signaling. *Bone*, 42(2):606–615, 2008.
- [167] S. Tatsumi, K. Ishii, N. Amizuka, M. Li, T. Kobayashi, K. Kohno, M. Ito, S. Takeshita, and K. Ikeda. Targeted ablation of osteocytes induces osteoporosis with defective mechanotransduction. *Cell Metab*, 5(6):464–475, 2007.
- [168] N. Basso, C. G. Bellows, and J. N. Heersche. Effect of simulated weightlessness on osteoprogenitor cell number and proliferation in young and adult rats. *Bone*, 36(1):173–183, 2005.
- [169] E.R. Morey-Holton and R.K. Globus. Hindlimb unloading rodent model: technical aspects. *J Appl Physiol*, 92(4):1367–1377, 2002.
- [170] T.M. Skerry. The response of bone to mechanical loading and disuse: fundamental principles and influences on osteoblast/osteocyte homeostasis. *Arch Biochem Biophys*, 473(2):117–123, 2008.
- [171] S. Judex, X. Lei, D. Han, and C. Rubin. Low-magnitude mechanical signals that stimulate bone formation in the ovariectomized rat are dependent on the applied frequency but not on the strain magnitude. *J Biomech*, 40(6):1333–1339, 2007.
- [172] Y.F. Hsieh and M.J. Silva. In vivo fatigue loading of the rat ulna induces both bone formation and resorption and leads to time-related changes in bone mechanical properties and density. *J Orthop Res*, 20(4):764–771, 2002.

- [173] Z.A. Dotan. Bone imaging in prostate cancer. *Nat Clin Pract Urol*, 5(8):434–444, 2008.
- [174] R.E. Coleman. Clinical features of metastatic bone disease and risk of skeletal morbidity. *Clin Cancer Res*, 12(20 Pt 2):6243s–6249s, 2006.
- [175] R.E. Coleman. Metastatic bone disease: clinical features, pathophysiology and treatment strategies. *Cancer Treat Rev*, 27(3):165–176, 2001.
- [176] V. Fritz, P. Louis-Plence, F. Apparailly, D. Noel, R. Voide, A. Pillon, J.C. Nicolas, R. Müller, and C. Jorgensen. Micro-CT combined with bioluminescence imaging: a dynamic approach to detect early tumor-bone interaction in a tumor osteolysis murine model. *Bone*, 40(4):1032–1040, 2007.
- [177] A.V. Taira, R.J. Herfkens, S.S. Gambhir, and A. Quon. Detection of bone metastases: assessment of integrated FDG PET/CT imaging. *Radiology*, 243:204–211, 2007.
- [178] T. Hamaoka, J.E. Madewell, D.A. Podoloff, G.N. Hortobagyi, and N.T. Ueno. Bone imaging in metastatic breast cancer. *J Clin Oncol*, 22(14):2942–2953, 2004.
- [179] M.R. Kim, J.L. Roh, J.S. Kim, S.H. Choi, S.Y. Nam, and S.Y. Kim. (18)F-Fluorodeoxyglucose-positron emission tomography and bone scintigraphy for detecting bone metastases in patients with malignancies of the upper aerodigestive tract. *Oral Oncol*, 44(2):148–152, 2007.
- [180] A. Praemer, S. Furner, and D.P. Rice. *Musculoskeletal conditions in the United States*. American academy of orthopaedic surgeons, 1992.
- [181] P. Ducheyne and Q. Qiu. Bioactive ceramics: the effect of surface reactivity on bone formation and bone cell function. *Biomaterials*, 20(23-24):2287–2303, 1999.
- [182] J. Glowacki and J.B. Mulliken. Demineralized bone implants. *Clin Surg*, 12(2):233–241, 1985.
- [183] D.W. Hutmacher. Scaffolds in tissue engineering bone and cartilage. *Biomaterials*, 21(24):2529–2543, 2000.
- [184] J. R. Allport and R. Weissleder. In vivo imaging of gene and cell therapies. *Exp Hematol*, 29(11):1237–1246, 2001.

- [185] J. S. Blum, J. S. Temenoff, H. Park, J. A. Jansen, A. G. Mikos, and M. A. Barry. Development and characterization of enhanced green fluorescent protein and luciferase expressing cell line for non-destructive evaluation of tissue engineering constructs. *Biomaterials* 2, 5(27):5809–5819, 2004.
- [186] B. Johnstone, T.M. Hering, A.I. Caplan, V.M. Goldberg, and J.U. Yoo. In vitro chondrogenesis of bone marrow-derived mesenchymal progenitor cells. *Exp Cell Res*, 238(1):265–272, 1998.
- [187] H.M. Young, S. Torihashi, D. Ciampoli, and K.M. Sanders. Identification of neurons that express stem cell factor in the mouse small intestine. *Gastroenterology*, 115(4):898–908, 1998.
- [188] S.P. Bruder, N. Jaiswal, N.S. Ricalton, J.D. Mosca, K.H. Kraus, and S. Kadiyala. Mesenchymal stem cells in osteobiology and applied bone regeneration. *Clin Orthop Relat Res*, 355 Suppl:S247–S256, 1998.
- [189] S.P. Bruder, A.A. Kurth, M. Shea, W.C. Hayes, N. Jaiswal, and S. Kadiyala. Bone regeneration by implantation of purified, culture-expanded human mesenchymal stem cells. *J Orthop Res*, 16(2):155–162, 1998.
- [190] J. Gao, J.E. Dennis, R.F. Muzic, M. Lundberg, and A.I. Caplan. The dynamic in vivo distribution of bone marrow-derived mesenchymal stem cells after infusion. *Cells Tissues Organs*, 169(1):12–20, 2001.
- [191] C. Olivo, V. Verweij, A. Hagenbeek, W. Dhert, and A. Martens. In vitro tracing of bone marrow stromal cells in tissue engineered scaffolds. *52nd Annual Meeting of the Orthopaedic Research Society*, page Paper No:0987, 2007.
- [192] R.J. Oskouian, G. Pelled, Y. Zilberman, Y. Tal, Z. Gazit, and D. Gazit. Novel, injectable, genetically engineered stem cell-based system for anterior spinal fusion. *Molecular Therapy*, 13:S173–S174, 2006.
- [193] P. Mayer-Kuckuk, T.P. Gade, I.M. Buchanan, M. Doubrovin, L. Ageyeva, J.R. Bertino, A.L. Boskey, R.G. Blasberg, J.A. Koutcher, and D. Banerjee. High-resolution imaging of bone precursor cells within the intact bone marrow cavity of living mice. *Mol Ther*, 12(1):33–41, 2005.
- [194] P. Mayer-Kuckuk, M. Doubrovin, L. Bidaut, T. Budak-Alpdogan, S. Cai, V. Hubbard, O. Alpdogan, M. van den Brink, J.R. Bertino, R.G. Blasberg, D. Banerjee, and J. Gelovani. Molecular imaging reveals skeletal engraftment sites of transplanted bone marrow cells. *Cell Transplant*, 15(1):75–82, 2006.

Chapter 3

Functional bone imaging in an *in vivo* mouse model of bone adaptation



3.1 Mouse tail vertebrae adapt to cyclic mechanical loading by increasing bone formation rate and decreasing bone resorption rate as shown by time-lapsed *in vivo* imaging of dynamic bone morphometry

Floor M. Lambers¹, Friederike A. Schulte¹, Gisela Kuhn¹, Duncan J. Webster¹, and Ralph Müller¹

¹Institute for Biomechanics, ETH Zürich, Zürich, Switzerland

Abstract:

It is known that mechanical loading leads to an increase in bone mass through a positive shift in the balance between bone formation and bone resorption. How the remodeling sites change over time as an effect of loading remains, however, to be clarified. The purpose of this paper was to investigate how bone formation and resorption sites are modulated by mechanical loading over time by using a new imaging technique that extracts three dimensional formation and resorption parameters from time-lapsed *in vivo* micro-computed tomography images. To induce load adaptation, the sixth caudal vertebra of C57BL/6 mice were cyclically loaded through pins in the adjacent vertebrae at either 8N or 0N (control) three times a week for five minutes or 3000 cycles over a total of four weeks. The results showed that mechanical loading significantly increased trabecular bone volume fraction by 20% ($p < 0.001$) and cortical area fraction by 6% ($p < 0.001$). The bone formation rate was on average 23% greater ($p < 0.001$) and the bone resorption rate was on average 25% smaller ($p < 0.001$) for the 8N group than for the 0N group. The increase in bone formation rate for the 8N group was mostly an effect of a significantly increased surface of bone formation sites (on average 16%, $p < 0.001$), while the thickness of bone formation packages was less affected (on average 5% greater, $p < 0.05$). At the same time the surface of bone resorption sites was significantly reduced (on average 15%, $p < 0.001$), while the depth of resorption pits remained the same. For the 8N group, the strength of the whole bone increased significantly by 24% ($p < 0.001$) over the loading period, while the strain energy density in the trabecular bone decreased significantly by

24% ($p < 0.001$). In conclusion, mouse tail vertebrae adapt to mechanical loading by increasing the surface of formation sites and decreasing the surface of resorption sites, leading to an overall increase in bone strength. This new imaging technique will provide opportunities to investigate *in vivo* bone remodeling in the context of disease and treatment options, with the added value that both bone formation and bone resorption parameters can be nondestructively calculated over time.

Keywords:

In vivo micro-computed tomography; bone adaptation; mechanical loading; dynamic bone morphometry; bone strength

3.1.1 Introduction

Bone is continuously remodeled, i.e. old bone is resorbed by osteoclasts and replaced with newly formed bone by osteoblasts [1]. In adults, the skeleton is completely renewed by this process approximately every 10 years [2]. Next to bone remodeling, the skeleton is also shaped by bone modeling. It is assumed that osteocytes can act as mechanosensors by locally promoting bone formation or bone resorption, to maintain bone strength, depending on the local micromechanical environment. It is commonly believed that bone is formed where loads are high and bone is needed, and resorbed where strains and stresses are locally absent or bone is excessive [3–9]. However, fracture incidence is higher in patients with osteoporosis, indicating that affected bone has lost the ability to adapt optimally to external mechanical loads. To understand the underlying mechanism of failure in adaptation during disease, it is imperative to first understand the basic influence of loading on bone adaptation in healthy bone. Load-induced bone adaptation can be explored in animal models [10–20]. In these models adaptation was driven by a load, leading to a change in the distribution of strains of physiological magnitude, instead of supra-physiological strains [21–26]. The magnitude of the response to cyclic loading depends on several variables, including: mechanical strain, strain rate, frequency, strain distribution and number of loading cycles. It is known from such models that bone mass increases with dynamic loading and that bone formation is increased [21, 27, 28] while bone resorption is decreased [28–30]. In these studies, however, the calculation of dynamic bone morphometry parameters and their interpretation have been limited by the reliance on 2D histomorphometric techniques. In using 2D histomorphometric techniques, labels are injected to demarcate the position of the bone surface. To assess dynamic rates longitudinally

multiple labels are possible, but make it difficult to interpret the result, because labels can partially be resorbed over a 4 week period. Therefore, studies have often been limited to cross-sectional designs.

Recently, using a cross-sectional study design, we established an *in vivo* loading model for both cortical and trabecular bone adaptation in the sixth caudal vertebra in C57BL/6 female mice [31]. This mouse tail loading model was adapted from a previous model, where load adaptation was induced in the eight caudal vertebra in rats [28, 32, 33]. By inserting stainless-steel pins into the fifth and seventh caudal vertebrae of mice (see Figure 3.1) we were able to dynamically compress the sixth caudal vertebra (CV6) using a closed-loop force controlled loading device. Following bouts of mechanical stimulation (Amplitude: 8 N, Frequency: 10 Hz, Number of cycles: 3000, 3 times per week for a period of 4 weeks) groups of mice were sacrificed and bone morphometry was assessed using micro-computed tomography (micro-CT). Cortical and trabecular bone volume was shown to increase significantly by 11% and 23% respectively in loaded groups when compared to non-loaded controls.

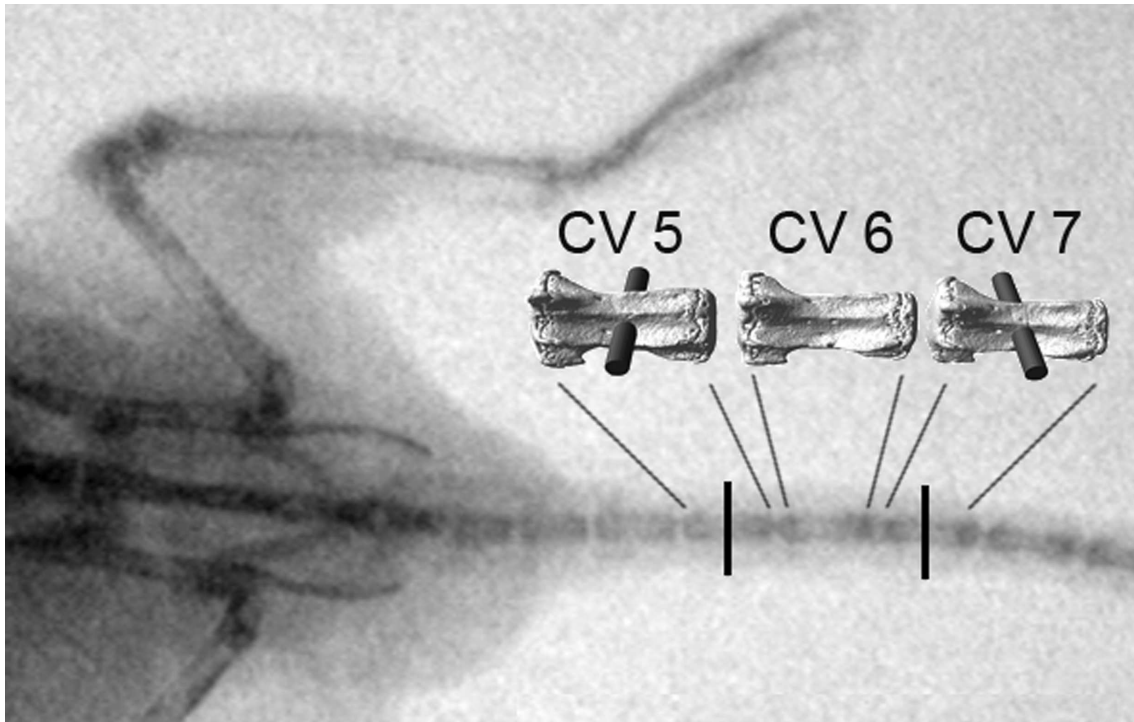


Figure 3.1: Image showing a fluoroscopy image of the mouse, graphically edited to show the locations of the pins, and a 3D representation.

In the study presented here we expand upon the fore mentioned cross-sectional study and calculate bone structural, mechanical, and dynamic formation and resorption parameters in single subjects over time in 3D using *in vivo* micro-CT. In doing so, we apply recently developed techniques to non-invasively extract dynamic bone morphometry parameters from serial *in vivo* micro-CT scans [34]. These dynamic parameters include: bone formation/resorption rate, mineral apposition/resorption rate, mineralizing/eroded surface, and number of formation/resorption sites per bone volume. Shapes of formation sites and resorption sites were visualized and monitored over time in single animals, revealing how these sites are influenced by loading. Furthermore, we performed micro-finite element analysis to investigate changes in strength and mechanical parameters. With this in mind, this study can be divided into three specific aims: firstly, to monitor load-induced changes in the bone microstructure, secondly, to monitor load-induced changes in dynamic bone morphometry parameters, and thirdly, to assess the changes in mechanical parameters as an effect of loading.

3.1.2 Materials and methods

Experimental design

Eighteen 11-week-old female C57BL/6 mice (RCC Ltd, Füllinsdorf, Switzerland) were housed in an environmentally controlled room at a 12-hour light/dark cycle, with free access to a standard diet and tap water. One week of settling was allowed before stainless steel pins (Fine Science Tools, Heidelberg, Germany) were inserted in the fifth and seventh caudal vertebra (Figure 3.1). After pinning, mice were divided into a loaded 8N group (n=9) and a control 0N group (n=9). Three weeks of recovery and in growth time was allowed before the loading regime and weekly *in vivo* micro-CT scans commenced. All procedures were performed under isoflurane anesthesia (2-2.5%, 0.4 L/min, delivered through a nose mask, Provet Medical AG, Lyssach, Switzerland). Approval from the local authorities (Kantonales Veterinäramt Zürich, Zürich, Switzerland) was obtained for all animal procedures.

In vivo loading

Mechanical loading was performed as described previously [31]. Briefly, sinusoidally varying forces (1 N preload, 8 N amplitude) were applied at 10 Hz for 3000 cycles (5 min) to the sixth caudal vertebra (CV6), three times per week for four weeks for the 8N group. As determined previously by strain gauges, loading at 8 N resulted in peak strains of 880 $\mu\epsilon$ on the dorsal side and 820 $\mu\epsilon$ on the ventral side of CV6 [31].

We cannot be sure if the loading regime is physiologically relevant, but this strain was chosen, because it encompasses strains in a physiological range. Strains of 1700 $\mu\epsilon$ have been reported on the ulna of running mice [23]. Similarly, strains on long bones for unrestricted locomotion in rats were shown to be 700-1200 $\mu\epsilon$ [29,35], 1900 $\mu\epsilon$ in wing-flapping of roosters [21], 517 $\mu\epsilon$ for mastication at jaw in rabbits [36], and 61-274 $\mu\epsilon$ in thoracic vertebrae, 49-487 $\mu\epsilon$ in lumbar vertebrae, and 50-376 $\mu\epsilon$ in the calcaneus for trotting sheep [37–39]. Furthermore, the strains applied in our model are in the same strain range as has been applied for other relevant loading models, i.e. 700 $\mu\epsilon$ for rat tail loading [28], 600-2000 $\mu\epsilon$ for axial loading of the tibia [10, 11, 13, 24, 40–44], 1200-2500 $\mu\epsilon$ for four-point-bending [26, 27, 45–47], and 1770-3600 $\mu\epsilon$ for axial loading of the ulna [15, 48–50]. A frequency of 10 Hz was chosen, as it has been shown in other loading models that a frequency between 5 and 10 Hz is more beneficial for the magnitude of the bone formation response to loading than lower frequencies [29, 51]. Furthermore, it has been shown that increasing the frequency above 10 Hz was not more osteogenic than a frequency of 10 Hz [52]. The current setup with loading at 10 Hz and a mean strain of 800 $\mu\epsilon$ leads to a peak strain rate of 40,000 $\mu\epsilon/s$. In mice the peak strain rate was shown to be approximately 30,000 $\mu\epsilon/s$ during unrestricted locomotion and 98,000 $\mu\epsilon/s$ during landing of a fall of 20 cm [23], indicating that our strain rate is in a range that mice would experience physiologically. Loading was applied for 3000 cycles to yield a 5 minute loading period, similar to earlier published loading protocols [24, 25, 53, 54]. For the 0N group the tails were fixed in the loading device, and left in for 5 minutes, but no loading was applied.

***In vivo* micro-computed tomography**

Descriptions and nomenclature in the following sections are in line with a recent review on guidelines for the assessment of bone microstructure with micro-CT [55]. CV6 was scanned weekly with *in vivo* micro-CT (vivaCT 40, Scanco Medical AG, Brüttisellen, Switzerland), with a basal scan before the loading regime started, leading to a total amount of 5 scans. The region of interest was selected from a scout view taken in a dorso-ventral direction. CV6 was measured completely in two connecting stacks, comprising a total length of 4.4 mm. The scanner was operated at 55 kVp and 145 μA , with an integration time of 200 ms, and no frame averaging. 1000 projections were captured per 180 degrees, leading to a nominal isotropic resolution of 10.5 μm . A beam hardening correction algorithm provided by Scanco Medical AG was applied to all scans. The estimated dose rate, as provided by the manufacturer, was 32 mGy/min over a period of 20 minutes. In a radiation control study performed

Table 3.1: Values of the bone structural parameters in the trabecular and cortical region for the 8N and 0N group at the first (week 0) and last (week 4) time point. P-values denote a significant difference between groups for absolute difference between week 0 and 4.

Parameter	Week 0		Week 4		p value
	8N	0N	8N	0N	
Trabecular					
Tb.TV [mm ³]	2.119 ± 0.165	2.13 ± 0.128	2.068 ± 0.165	2.13 ± 0.143	<0.05
BV/TV [%]	19.11 ± 1.647	18.602 ± 2.484	22.962 ± 1.810	19.392 ± 3.123	<0.001
BS/BV [mm ² /mm ³]	35.187 ± 1.568	36.112 ± 3.783	28.909 ± 1.571	33.291 ± 4.240	<0.001
SMI [-]	0.652 ± 0.168	0.612 ± 0.306	0.237 ± 0.189	0.44 ± 0.335	<0.01
Tb.Th [mm]	0.075 ± 0.003	0.073 ± 0.007	0.089 ± 0.005	0.078 ± 0.009	<0.001
Tb.Sp [mm]	0.291 ± 0.031	0.293 ± 0.029	0.292 ± 0.030	0.303 ± 0.035	0.095
Tb.N [1/mm]	3.132 ± 0.299	3.103 ± 0.309	3.057 ± 0.255	2.963 ± 0.340	0.167
Conn.D [1/mm ³]	61.213 ± 13.712	66.431 ± 18.853	46.932 ± 7.920	48.119 ± 15.561	0.289
DA [-]	1.852 ± 0.076	1.828 ± 0.065	1.884 ± 0.069	1.840 ± 0.055	0.210
Cortical					
Ct.TV [mm ³]	5.429 ± 0.331	5.411 ± 0.262	5.504 ± 0.327	5.497 ± 0.320	0.737
Ct.MV [mm ³]	3.209 ± 0.256	3.224 ± 0.180	3.112 ± 0.256	3.222 ± 0.203	<0.01
Ct.Ar/Tt.Ar [%]	40.941 ± 1.659	40.396 ± 2.276	43.512 ± 1.859	41.361 ± 2.292	<0.001
Ct.Th [mm]	0.153 ± 0.006	0.152 ± 0.008	0.165 ± 0.006	0.156 ± 0.009	<0.001

before the start of this experiment no detrimental effects of 5 *in vivo* micro-CT scans on bone development were found (data not shown). The CT scanner was calibrated weekly for mineral equivalent value, and monthly for determining in plane spatial resolution.

Image processing

All raw micro-CT data were reconstructed so that the dorsal side of the vertebra was facing upwards. For the basal scan the long axis of the bone was aligned with the z-axis, to facilitate the conversion of the micro-CT data into micro-finite element (μ FE) models. The follow-up scans were translated and rotated to match the previous measurement using rigid registration [56]. A 3D constrained Gaussian filter (sigma 1.2, support 1) was applied, after which images were segmented by a fixed thresholding procedure (22% of maximum grayscale value).

Static bone morphometry

The trabecular and cortical regions were selected from the thresholded images by automated masks, similar to a procedure described previously [57]. First, an inner mask comprising trabecular bone and the growth plates was produced by using a distance map transformation from a mask which included the complete CV6. For the trabecular mask the growth plates were eliminated by removing the outer 10% of the inner mask, and the space almost void of trabecular bone was taken out by removing the middle 26% (Fig. 3.2a). Within the regions of interest, the bone structural parameters were calculated with a direct 3D model-independent algorithm [58]. The morphological measurements in the trabecular region included

total volume (Tb.TV), bone volume fraction (BV/TV), specific bone surface (BS/BV), structure model index (SMI), trabecular thickness (Tb.Th), trabecular separation (Tb.Sp), trabecular number (Tb.N), connectivity density (Conn.D), and degree of anisotropy (DA). Furthermore a histogram of the trabecular thickness was plotted, to investigate how the thickness distribution changes with loading.

The cortical mask included 75% of the length of the inner mask (Fig. 3.2b). For calculation of the cortical bone structural parameters the trabecular structure was removed from CV6. The morphological measurements in the cortical region included: total volume (Ct.TV), marrow volume (Ct.MV), cortical area fraction (Ct.Ar/Tt.Ar), cortical thickness (Ct.Th). All bone structural parameters were normalized to the first time point for each mouse to calculate percentage changes. The reproducibility of the morphometric parameters was high, with a maximal precision error ($PE_{\%CV}$) of 1.5%.

Dynamic bone morphometry

The dynamic parameters were calculated in the trabecular region. For each mouse, registered binary micro-CT images acquired at consecutive time points were overlaid to calculate bone formation and bone resorption at weekly intervals, i.e. week 0 was overlaid with week 1, week 1 with week 2, week 2 with week 3, and week 3 with week 4 (Fig. 3.2c). This procedure produced small volumes that could be identified as either formed or resorbed bone that could be analyzed morphometrically as described earlier [34] to yield 3D dynamic bone morphometric parameters. These parameters included: bone formation rate (BFR) and bone resorption rate (BRR); mineral apposition rate (MAR) and mineral resorption rate (MRR); mineralizing surface (MS) and eroded surface (ES); and the number of formation sites per bone volume (NFS) and the number of resorption sites per bone volume (NRS). This technique to calculate dynamic parameters was shown to be highly reproducible, with precision errors ranging from 0.92% to 6.58% which is far lower than reproducibility errors reported in histomorphometry. Furthermore, when dynamic parameters were compared to histomorphometric values of the same sample, good agreement was found, with correlations of $R = 0.78$ for MS ($p < 0.01$) and $R = 0.68$ for MAR ($p < 0.001$) [34].

Finite element analysis

Finite element analyses were only performed for the 8N group as we were only interested in changes in mechanical properties due to the loading regimen. For

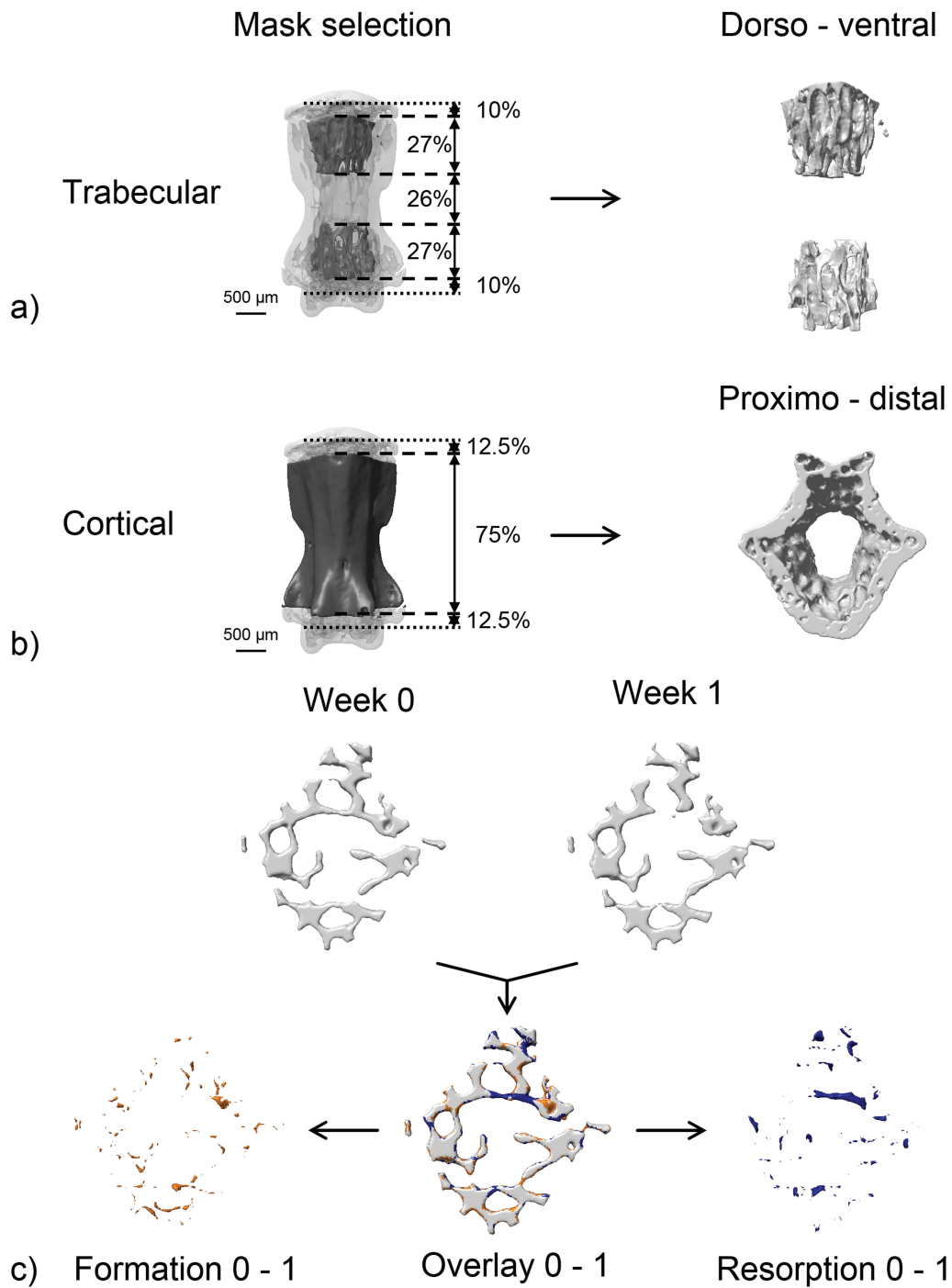


Figure 3.2: Images for clarification of image analysis. a) Selection of the trabecular mask and a representation of the trabecular bone in dorso-ventral direction. b) Selection of the cortical mask and a representation of the cortical bone in proximo-distal direction. c) Representation of volumes from which the dynamic bone morphometry parameters were calculated. Here only cross-sections are shown to enhance understandability of the image. The top row shows the registered thresholded images at two consecutive time points. Below in the middle these thresholded images have been overlaid, in which yellow denotes formed structures, blue resorbed structures, and grey constant bone. The image below on the left side shows the bone formed between week 0 and 1 extracted from the overlaid image, while the right shows the bone resorbed between week 0 and 1.

each mouse at each time point segmented image data were converted into three-dimensional μ FE models, with discs added on both sides to mimic the intervertebral discs. (Fig. 3.6a). All voxels were converted to 8 node brick elements, rendering models of approximately 1,800,000 elements, and were assigned a Young's Modulus of 14.8 GPa, and a poisson's ratio of 0.3. The top was displaced 0.1%, while the bottom was constrained in all directions to simulate the loading condition. The resulting force was calculated and used to scale the output parameters in the model to the actual force. The models were solved using a parallel linear finite element package (ParFE) with an algebraic multigrid preconditioner [59]. The simulations ran on a Cray XT5 super computing system composed of 1844 twelve-core AMD Opteron 2.4 GHz Istanbul processors and 29 TB of physical RAM at the Swiss National Supercomputing Center (CSCS, Manno, Switzerland). The FE model and the accompanying boundary conditions were previously validated [31]. Briefly, following the excision and pinning of mouse tails, micro-strain gages were attached to ventral and dorsal periosteal surfaces of CV6 vertebrae. Upon loading the pinned mouse tails, mechanical strains were recorded and compared to the strains determined by FE models. Strong agreements were found ($R^2 > 0.96$), indicating that loading is purely axial and reproducibly transferred to the bone [31].

To quantify changes in mechanical properties with time, the stiffness, which represents the resistance against deformation in N/mm, was calculated for the whole bone for each mouse at each time point. By using the Pistoia criterion [60] the strength of the whole bone was estimated for each mouse at each time point. This criterion assumes that bone failure is initiated if a certain percentage of the bone tissue (2%) is strained beyond the tissue yield strain ($7000 \mu\epsilon$). It was found that this estimation of bone strength correlates well to bone strength estimated from mechanical tests [60]. Although the Pistoia criterion has been developed for human bone, a yield strain of $7000 \mu\epsilon$ also seems to make sense for these mouse bones, it has been reported that cyclic loading at $6000 \mu\epsilon$ induces fatigue in the ulna in rats [61, 62] and it was predicted from a theoretical framework that failure should occur if the strain is approximately $9000 \mu\epsilon$ [63]. Strain energy density (SED), effective strain (e_{EFF}), and von Mises stress (S_v) were calculated within the trabecular bone. All mechanical parameters were normalized to the first time point for each mouse to calculate percentage changes.

To test how well changes in mechanical parameters were related to changes in trabecular bone microstructure, a regression analysis was performed comparing

percentage changes in structural parameters with percentage changes in mechanical parameters over the whole period of 4 weeks. Furthermore the percentage changes in strength and stiffness were correlated to the percentage changes in apparent volume density of the whole bone.

Statistical analysis

Statistical analysis was performed with the software package R (R: A Language and Environment for Statistical Computing) [64]. A Kolmogorov-Smirnov test was used to verify that the data were normally distributed. To detect significant differences between groups or over time in bone structural parameters, dynamic parameters, and mechanical parameters, repeated measurements ANOVA was performed and implemented as a linear mixed effects model. The absolute differences between last and first time point (week 4 - week 0) for bone structural parameters was compared between groups with an unpaired Student's t-test. Correlations were tested with bivariate regression analysis. P-values smaller than 0.05 were considered significant. All data are shown as mean \pm standard error.

3.1.3 Results

Animals

All mice remained healthy throughout the experiment and had no swollen tails. One mouse was excluded because of a problem with loading at the start of the experiment.

Static bone morphometry

The absolute values of the bone structural parameters in the trabecular bone at the first and last time point are shown in table 3.1. The absolute difference between the first and last time point was significantly greater for the 8N group than for the 0N group for BV/TV ($p < 0.001$), and Tb.Th ($p < 0.001$), and significantly smaller for Tb.TV ($p < 0.05$), BS/BV ($p < 0.001$), and SMI ($p < 0.01$). This indicates that the trabecular structure became thicker and more plate-like. For Tb.Sp, Tb.N, Conn.D, and DA no significant differences were found between groups. The increase in normalized BV/TV of 20.3% for the 8N group was significantly greater than for the 0N group, where the BV/TV did not change significantly over time ($p < 0.001$, Fig. 3.3a). This increase could not be attributed to changes in Tb.N, which decreased 2.3% for the 8N group and 4.6% for the 0N group, but to changes in Tb.Th, which increased 18.5% for the 8N group and 6.8% for 0N group

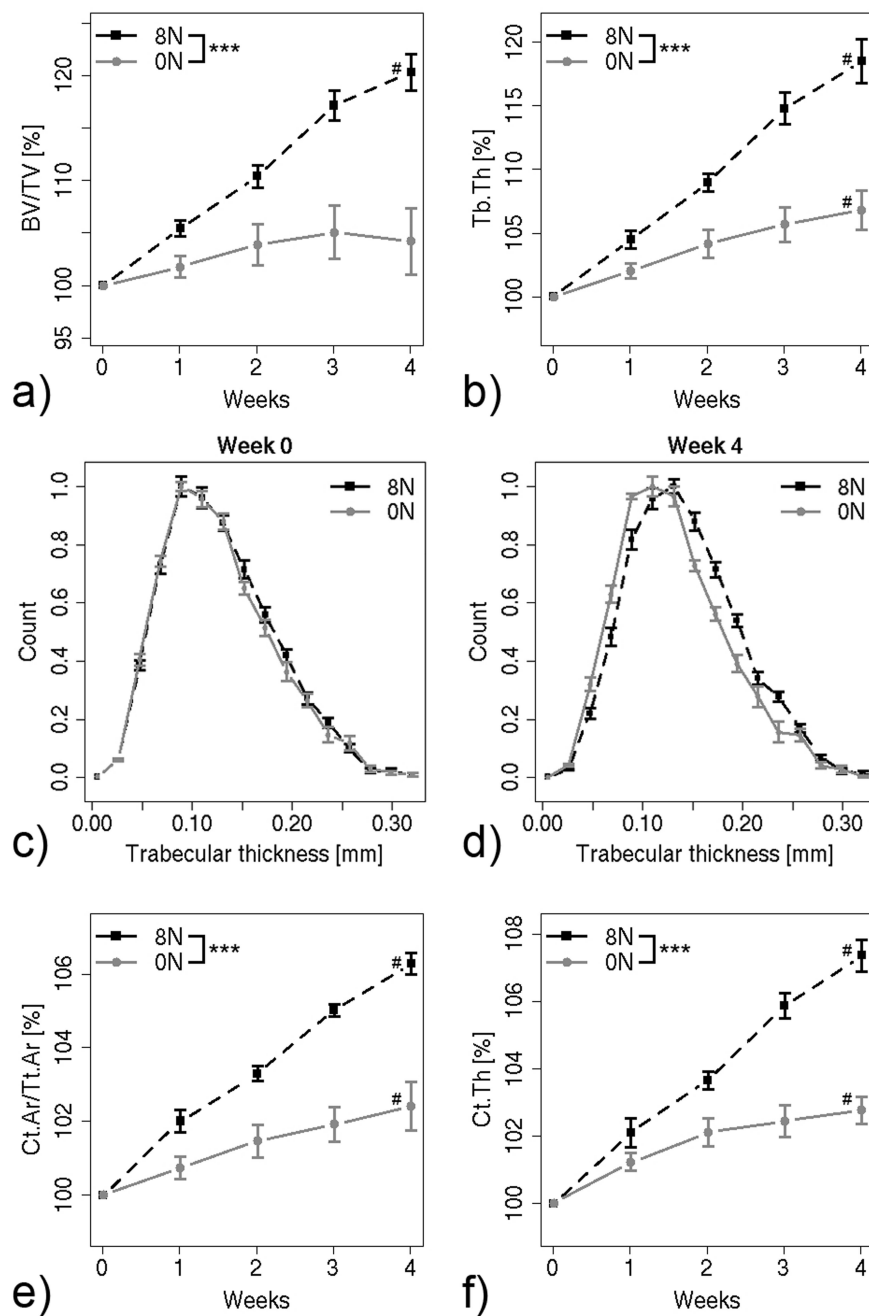


Figure 3.3: Plots of bone structural parameters over four weeks of loading. a) Bone volume fraction, b) Trabecular thickness, c) Histogram of trabecular thickness at week 0, d) Histogram of trabecular thickness at week 4, e) Cortical area fraction, f) Cortical thickness. *** $p < 0.001$ between groups and # $p < 0.05$ over time as tested with repeated measurements ANOVA.

($p < 0.001$, Fig. 3.3b). The thickening of the trabecular structure was also visually apparent from the micro-CT images and can be appreciated when the same cross section is observed at subsequent time points, especially when compared to the 0N group (Fig. 3.4). The increase in Tb.Th was further investigated by histograms of

trabecular thickness, overlapping for both groups at week 0 (Fig. 3.3c), where at week 5, the histogram of the 8N group was shifted to the right compared to the 0N group (Fig. 3.3d). A significant interaction between time and group, indicating the time course developed significantly different between groups, was found for Tb.TV ($p<0.05$), BV/TV ($p<0.001$), BS/BV ($p<0.001$), SMI ($p<0.01$), Tb.Th ($p<0.001$), and Tb.Sp ($p<0.05$).

The absolute values of the bone structural parameters in the cortical bone at the first and last time point are shown in table 3.1. The absolute difference between the first and last time point was significantly greater for the 8N group than for the 0N group for Ct.Ar/Tt.Ar ($p<0.001$), Ct.Th ($p<0.001$), and significantly smaller for Ct.MV ($p<0.01$). No significant difference between groups was seen for Ct.TV. Normalized Ct.Ar/Tt.Ar increased linearly over the four weeks of loading for both groups (Fig. 3.3e). The increase of 6.3% for the 8N group was significantly greater than the increase of 2.4% for the 0N group ($p<0.001$). A similar development was observed for normalized Ct.Th (Fig. 3.3f), where the 7.4% increase for the 8N group was significantly greater than the 2.8% increase for the 0N group ($p<0.001$). Furthermore it was observed that for the 8N group the cortex gained bone volume both on the periosteal and endosteal sides as Ct.TV was increasing, while Ct.MV was decreasing. A significant interaction between time and group, indicating the time course developed significantly different between groups, was found for Ct.MV ($p<0.001$), Ct.Ar/Tt.Ar ($p<0.001$), and Ct.Th ($p<0.001$).

Dynamic bone morphometry

BFR was significantly greater ($p<0.001$) for the 8N group than for the 0N group (Fig. 3.5a), while BRR was significantly smaller ($p<0.001$, Fig. 3.5b). On average BFR was 22.8% greater and BRR 25.2% smaller for the 8N compared to the 0N group. MAR, which represents the thickness of formation packages, was significantly greater ($p<0.05$) for the 8N group than for the 0N group (Fig. 3.5c), while MRR, which represents the depth of resorption pits, was not significantly different between both groups (Fig. 3.5d). On average MAR was 4.9% greater and MRR 3.4% smaller for the 8N group than for the 0N group. MS, which represents the surface of formation sites, was significantly greater ($p<0.001$) for the 8N group than for the 0N group (Fig. 3.5e), while ES, which represents the surface of resorption sites, was significantly smaller ($p<0.001$, Fig. 3.5f). On average MS was 16.0% greater and ES 14.7% smaller for the 8N group than for the 0N group. For the 8N group the average percentage increase in MS was threefold the

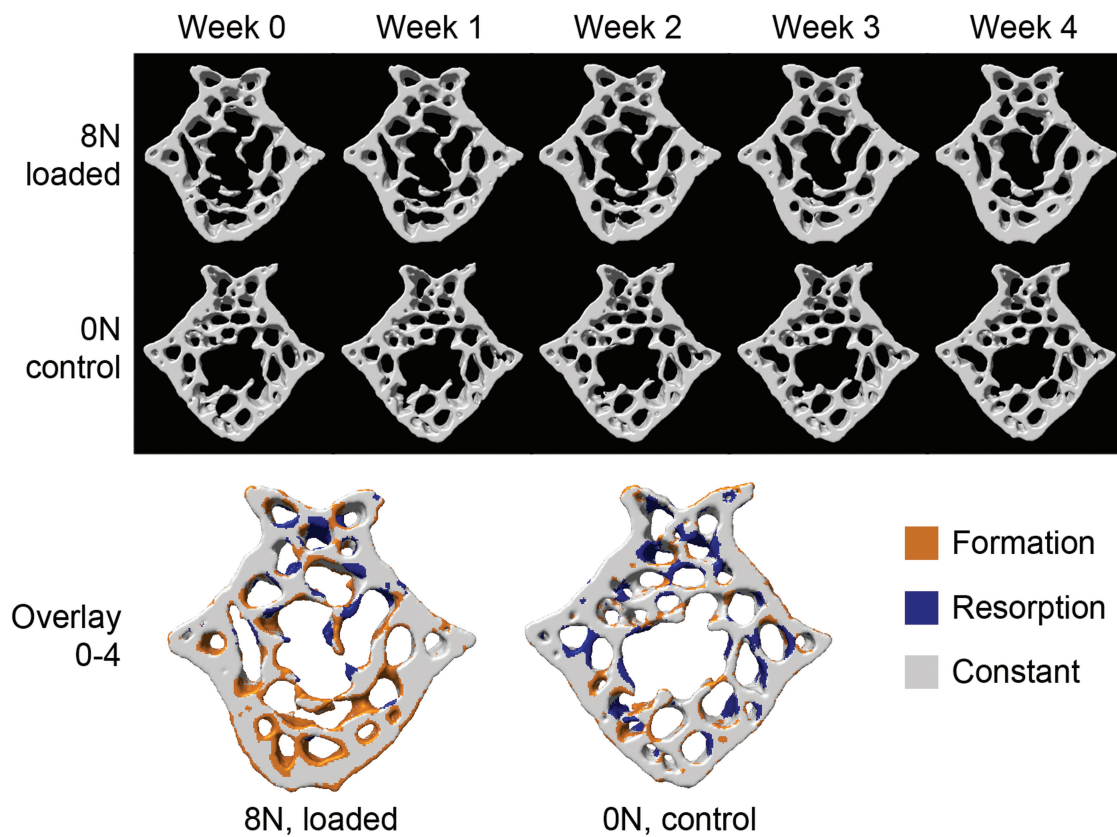


Figure 3.4: Bone microstructure (cross-section) of representative mice of the 8N and 0N group at time points at which *in vivo* micro-CT scans were performed. In the top row (8N group) thickening of the trabecular structure can be observed, while on the bottom row (0N group) little changes in the bone microstructure can be seen between time points. This becomes even clearer when an overlay of the first with the last scan is observed (bottom). For the 8N group many yellow sites, indicating bone formation, can be observed around the trabeculae, while for the 0N mouse formation and resorption are rather balanced (equal amount of blue and yellow structures).

average percentage increase in MAR, indicating that loading had a greater effect on surface than on thickness of formation sites. Similarly, the average decrease in ES was fourfold the average decrease in MRR, indicating that loading modulated the surface of resorption sites more than the depth. NFS or NRS was not significantly different between groups and did not change significantly over time (Fig. 3.5g and h).

When investigating changes over time, a significant effect of time was found for BFR ($p < 0.001$ for both groups), BRR ($p < 0.01$ for 8N), MRR ($p < 0.05$ for 8N and $p < 0.001$ for 0N), MS ($p < 0.01$ for 0N), and ES ($p < 0.01$ for 0N), but the time course only developed significantly different between groups for MS ($p < 0.05$).

When comparing formation with resorption, it can be seen that for the 8N group BFR was on average 1.7 times greater than BRR ($p < 0.001$), where for the

Table 3.2: R values of correlations between percentage change between week 0 and 4 in mechanical parameters and percentage change between week 0 and 4 in bone structural parameters. e_{EFF} = effective strain, S_v = von Mises stress, AVD = apparent volume density, * $p < 0.05$, ** $p < 0.01$, *** $p < 0.001$

	Δ AVD [%]	Δ BV/TV [%]	Δ BS/BV [%]	Δ Tb.Th [%]
Δ SED [%]	-	0.96 ***	0.86 *	0.91 **
Δ e_{EFF} [%]	-	0.93 **	0.85 *	0.93 **
Δ S_v [%]	-	0.92 **	0.85 *	0.93 **
Δ Strength [%]	0.76 *	-	-	-
Δ Stiffness [%]	0.71 *	-	-	-

0N group BFR and BRR were in balance. The ratio between MS and ES was significantly greater for the 8N group than for the 0N group ($p < 0.001$). On average, formation sites occupied up to 1.9 times more surface than resorption sites for the 8N group, and only 1.4 times more for the 0N group. For the 0N group MRR exceeded MAR 1.2 times on average, which was slightly but significantly different to the 8N group, where MRR was on average 1.3 times MAR ($p < 0.05$).

Finite element analysis

In the whole bone, stiffness and strength increased 19.5% and 24% ($p < 0.001$ over time), respectively, for the 8N group (Fig. 3.6a). Changes in stiffness and strength were significantly correlated to percent changes in apparent volume density of the whole bone (table 3.2).

Figure 3.6b shows the region from which the mechanical parameters in the trabecular bone were calculated using colors representing SED. The expanded views on the right side show trabecular structures at week 0 and week 4. Here it can be seen that a high initial SED value leads to thickening of the structural elements, which in turn lowers the SED value in the later time point, hence bone adapted to the mechanical demand. Over the four weeks of loading, SED decreased significantly by 24.3% ($p < 0.001$ over time, Fig. 3.6c). The effective strain decreased 11.5% ($p < 0.001$ over time), and von Mises stress decreased 11.2% ($p < 0.001$ over time). The absolute values for the mechanical parameters in the trabecular bone at the first and last time point for the 8N group are shown in table 3.3.

These mechanical parameters can be seen to revise with changes in trabecular structural indices. From correlations between percentage changes in mechanical parameters and percentage changes in bone structural parameters between week 0 and 4, it was found that the larger the increase in BV/TV and Tb.Th or decrease in

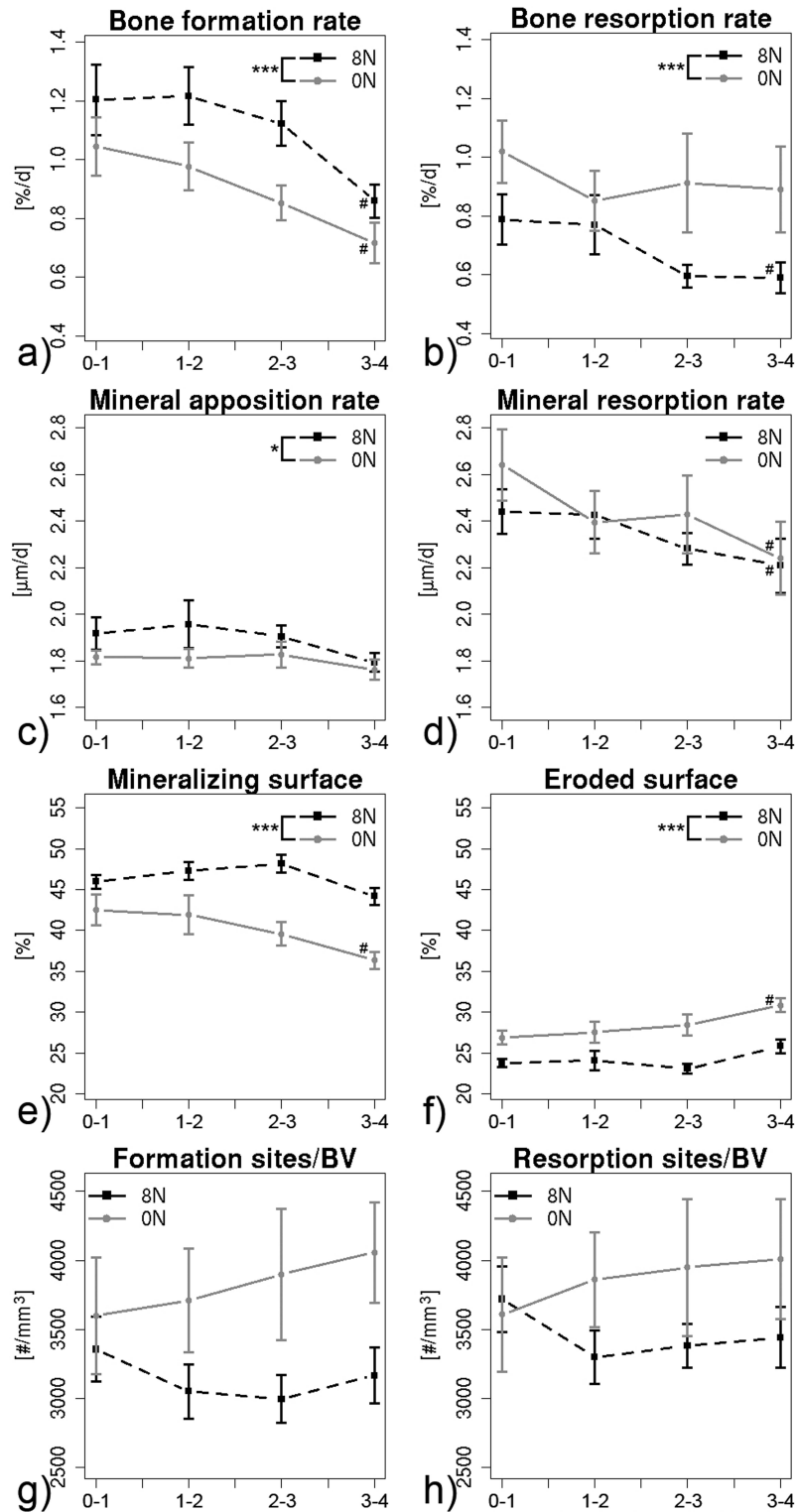


Figure 3.5: Plots of dynamic bone morphometry parameters over time. a) Bone formation rate, b) Bone resorption rate, c) Mineral apposition rate, d) Mineral resorption rate, e) Mineralizing surface, f) Eroded surface, g) Number of formation sites per bone volume, h) Number of resorption sites per bone volume. * $p < 0.05$, ** $p < 0.01$, *** $p < 0.001$ between groups and # $p < 0.05$ over time as tested with repeated measurements ANOVA.

Table 3.3: Mechanical parameters as assessed by finite element analysis in the trabecular region for the 8N group at week 0 and week 4. P-values denote a significant change over time. e_{EFF} = effective strain, S_v = von Mises stress.

	Week 0	Week 4	p value
SED [KPa]	2.024 \pm 0.262	1.525 \pm 0.153	p<0.001
e_{EFF} [$\mu\epsilon$]	821 \pm 57	726 \pm 40	p<0.001
S_v [N/mm ²]	4.17 \pm 0.28	3.70 \pm 0.20	p<0.001
Strength [N]	16.3 \pm 0.90	20.3 \pm 0.77	p<0.001
Stiffness [N/mm]	713 \pm 13	852 \pm 9	p<0.001

Tb.BS/BV, the larger the decrease in SED (R=0.81, R=0.84, R=0.84 respectively, p<0.01, table 3.2 and Fig. 3.6d).

3.1.4 Discussion

In this paper we showed how bone structural, dynamic, and mechanical parameters develop over time as an effect of cyclic mechanical loading. Loading mainly affected the surface of bone formation sites and bone resorption sites, while the thickness of the formation packages was little affected and the resorption depth remained unaltered. The amount of formation and resorption sites per bone volume was similar between the two groups, while the formation sites became wider, and resorption sites became narrower. This indicated that there are not more remodeling sites where osteoblasts are recruited, but that there is a greater net osteoblastic activity per formation site, probably caused by an increase in number of osteoblasts. Similarly, there are not less sites where osteoclasts are recruited, but there is less net osteoclastic activity per resorption site, either through a decrease in number of osteoclasts, or a decrease in activity per osteoclast. The notion that loading leads to an increase in bone formation rate (BFR), a minor increase in thickness of formation packages (MAR), and a major increase in surface of formation sites (MS), is in agreement with previous studies of vertebrae that have shown that loading leads to a greater BFR, double labeled surface, and MAR [20, 25, 28, 32, 65]. Similar to previous studies that have reported a reduction in osteoclast number or surface with loading of trabecular bone [20, 28, 32, 66], a decrease in the surface of resorption sites (ES) was found. Measures for bone resorption rate (BRR) and depth of resorption sites (MRR) were not available previously, which is one of the advantages of the current *in vivo* approach.

A general limitation of the aforementioned studies is that these studies could not show how the dynamic parameters change over time in a longitudinal fashion.

The added value of the data presented here, is that it describes the transient nature of the dynamic parameters themselves. It could be expected that once bone has adapted to the applied load, the formation and resorption parameters return to the values of the 0N group. The fact that the bone formation rate is reducing from two weeks of loading onwards, and is approaching the value of the 0N group, indicates that the bone has almost adapted to the new loading situation. At the last time interval (3-4), the bone formation rate (BFR) for the 8N group is still above the value of the 0N group, and the bone resorption rate (BRR) for the 8N group is still below the value of the 0N group. It seems that after four weeks of loading the thickness of formation packages (MAR) and depth of resorption pits (MRR) are the same for the 8N group and 0N group, while the surface of formation sites (MS) and resorption surface (ES) are still clearly different, but getting closer to the 0N group. Nevertheless, when comparing the ratios between formation and resorption parameters, it is clear that the ratio between MS and ES displays a similar pattern to the ratio between BFR and BRR. Again it follows that bone adaptation mostly influences the covered surface of bone formation sites and bone resorption sites rather than the number of remodeling sites.

In addition to dynamic parameters, load-induced changes in bone structural parameters were monitored over time. As expected, both BV/TV in the trabecular bone and Ct.Ar/Tt.Ar in the cortical bone increased significantly for the 8N group. The increase in BV/TV was accompanied by an increase in Tb.Th. Changes in the bone structural parameters were similar, but lower than changes in a previous cross-sectional study on the same bone with the same loading protocol [20]. However, in that study data were normalized to the 0N group mean, instead of to the first time point of the same vertebra.

Previous studies, in which trabecular bone was mechanically stimulated also reported increases in BV/TV and Tb.Th [14, 24, 42]. An extension here is that we are now also able to analyze the distribution of the local trabecular thickness. The noticed shift in the histogram indicated that the amount of thinner trabeculae decreased, while the amount of thicker trabeculae increased (Fig. 3.3). As Tb.N did not change over time, and the shape of the histogram was similar at week 0 and week4, this also indicated that most trabeculae regardless of their size increase in thickness as an effect of bone adaptation. This can also be seen in the similar profiles for BV/TV and Tb.Th, showing that changes in BV/TV are mainly an effect of changes in Tb.Th, and not Tb.N. Furthermore, not

just for the 8N group but also for the 0N group, significant correlations were found between change in BV/TV and change in Tb.Th ($R=0.76$, and $R=0.74$, $p<0.05$). On the other side, no correlation was found for Tb.N. Nevertheless, this does not necessarily mean no new trabeculae can form. When looking at the time-lapsed images of individual animals it seemed that a few new trabeculae grow, but this is a very small contribution to the total changes in the BV/TV in this model.

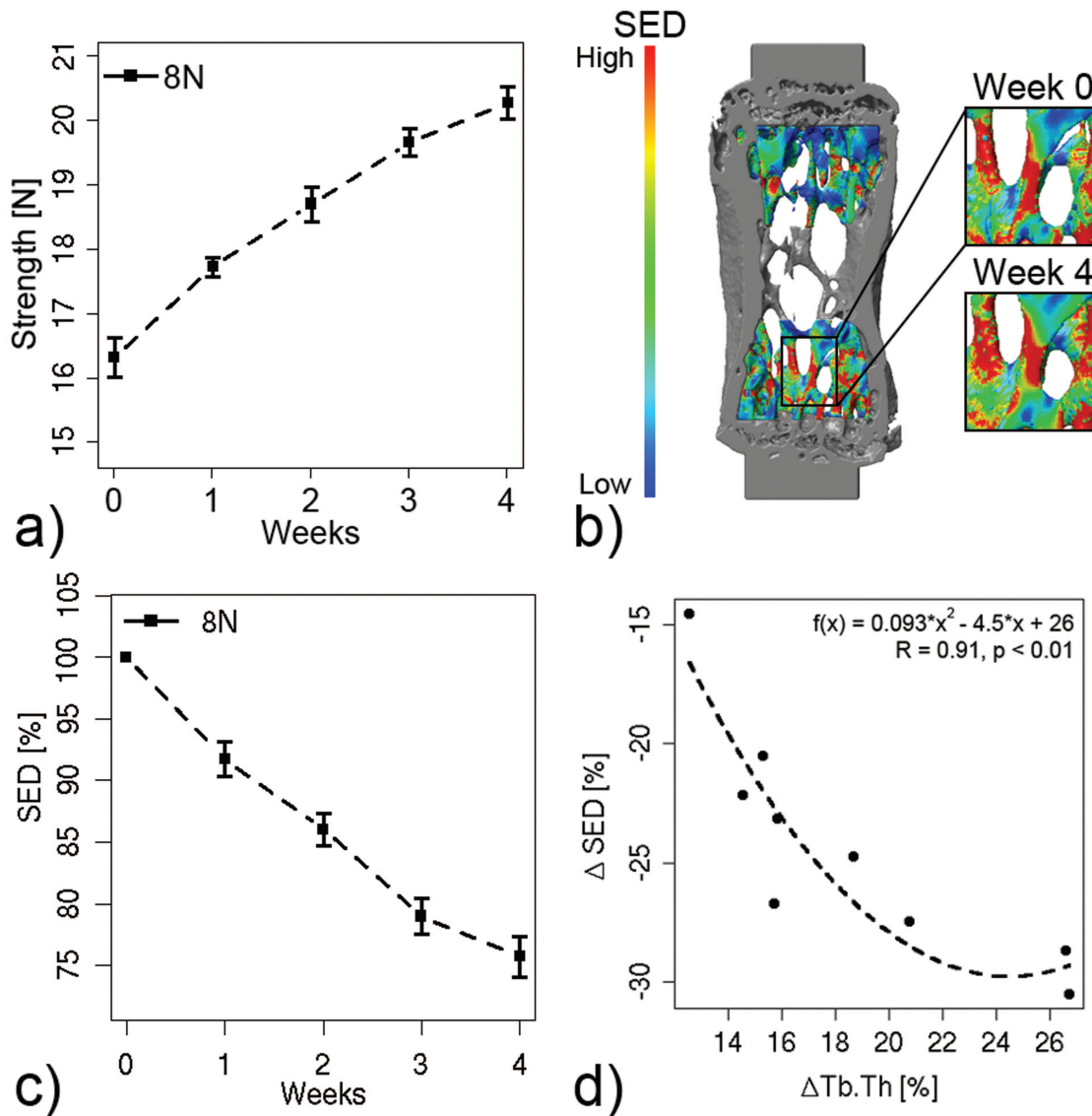


Figure 3.6: Image and plots of micro-finite element data. a) Significant increase in strength for the 8N group ($p<0.001$). b) Representation of finite element model (left). The colored structures indicate the level of strain energy density in the analyzed region of trabecular bone. On the right side is zoomed in on a trabecular detail at week 0 and at week 4, showing an increase in trabecular thickness at a site of high preceding strain energy density. c) Significant reduction in strain energy density for the 8N group ($p<0.001$). d) Negative correlation between percentage change in trabecular thickness and percentage change in strain energy density ($R=0.91$, $p<0.01$).

To examine if the orientation of the strains applied by axial compression differ from the physiological state, and trabeculae would realign, degree of anisotropy (DA) was analyzed in the trabecular bone. DA did not change over time and was not different between groups, indicating that the trabeculae did not change alignment with loading. Therefore, even though the whole surface of the caudal vertebra is covered with tendons that could exert bending forces, the main loading direction physiologically might already be compressive. This could be explained by the axi-symmetrical shape of the vertebra, through which bending components on either side of the vertebra might counteract. Furthermore, also in this loading scenario there might be some bending forces as strains measured *in vitro* using ventral and dorsal strain gauges differed by about 10% [31].

The Ct.Ar/Tt.Ar in the cortical bone increased as an effect of increased Ct.Th, with apposition on both the periosteal and endosteal side. Adding of bone at the cortex on both periosteal and endosteal sides was found in other studies [10, 11, 26, 41, 45], although increases only on the periosteal side [16, 43, 51, 67] or only on the endosteal side [46] have been reported as well.

Finite element analysis showed that the bone strength of the loaded group increased by 24%. Changes in apparent volume density correlated highly significantly to changes in strength and stiffness. This relation would be expected as correlations between bone morphology and bone strength have often been reported [68–70]. Even though bone strength of the whole bone is mostly determined by strength of the cortical bone, no correlations were found between changes in static cortical parameters and changes in bone strength (data not shown). On the other hand, changes in trabecular thickness did contribute to the changes in bone strength ($R = 0.83$, $p < 0.05$), indicating that this mechanical intervention does not only form new bone, but that this new trabecular bone also contributes to an increase in mechanical strength. The fact that correlations were found for changes in trabecular but not changes in cortical bone could be explained by the difference in specific bone surface, which is more than 3 times greater for trabecular than cortical bone, and therefore allows faster adaptation.

The procedure of monitoring load-induced bone adaptation longitudinally with *in vivo* micro-CT had the advantage that changes in the trabecular and cortical bone microstructure could be examined in single mice. This allowed normalization to the first time point for each mouse separately, which in our case

increased the sensitivity to detect changes. Therefore fewer animals are needed to identify alterations in the bone microstructure. Furthermore, these changes could be localized and visualized in trabecular and cortical bone. This emphasizes the importance of performing longitudinal measurements. These data will also provide important input for validation of simulations which predict bone microstructure.

The benefit of serial imaging in mechano-biological research has been shown by others as well. For example, Poliachik et al. showed how botulinum-induced muscle atrophy led to a profound bone loss over time [71]. Furthermore, Brodt et al. could show that loading in 22 month old mice prevented age-related bone loss when mice were scanned longitudinally [72], while Christiansen et al. showed a temporal negative systemic effect of tibial vibration in 6-7 month old mice [17]. In each of these studies, there was a clear benefit from longitudinal imaging, by confirming findings of cross-sectional data, rejecting findings of cross-sectional data, and/or permitting visualization of the bone microstructure at multiple time points within the same animal.

A limitation of our *in vivo* loading model is that it is load rather than strain-controlled. Because of this, the strain-signal imposed to the caudal vertebra differed slightly between animals due to the differences in bone size, which in turn lead to a variation in the subsequent increase in BV/TV. However, this also confirmed the relation that a bone with lower BV/TV but exposed to the same load increased BV/TV to a greater extent. Furthermore, the average axial strain in the vertebra in this model has been shown to be around $800 \mu\epsilon$ for an 8 N load [20], which is similar to values reported previously: $600 \mu\epsilon$ in the tibia [10], $800 \mu\epsilon$ in the tibia [24], and $1200 \mu\epsilon$ in medial surface of the tibia [13]. From histological sections and synchrotron scans (at a resolution of $1.2 \mu\text{m}$), it was found that strains in this range did not cause any fractures, or micro-cracks (data not shown). It is not possible to measure the *in vivo* strain at the caudal vertebrae without altering the forces responsible for the strain, since the complete surface of the vertebral body acts as an insertion surface for muscle or tendon [28]. However, recently a novel bone loading estimation method has been developed to predict external loading conditions [73]. When this method was applied to caudal vertebrae, it was found that the *in vivo* load at the sixth caudal vertebra is around 4N in the axial direction. Therefore, the load applied in this study is approximately twice the average load that mice experience during normal cage activity, and thus can be considered in the physiological range.

An additional concern in our loading model was that the mice had to be surgically operated, which could initiate a systemic effect and influence bone cell metabolism of the neighboring vertebrae including the target vertebra. However, when the bone microstructure in CV6 of pinned mice and age-matched-control mice were compared neither in a cross-sectional, nor in a longitudinal setup differences were found between groups [31], indicating that the pins themselves do not influence the bone metabolism in neighboring vertebrae. Similarly, other researchers using the rat tail loading model found no effect of pinning in vertebrae adjacent to the pinned vertebra [28, 32]. Moreover, trauma due to pinning would lead to increased bone resorption. But the bone resorption rates found in this study for the 0N group have the same value as bone resorption rates found in a pilot study where mice of the same age had no pins (data not shown).

A limitation in our novel approach of extracting bone dynamic parameters directly from *in vivo* images, is that the values before the start of the experiment were unknown. However, the values of the 0N group were in the same range as in mice of the same age without pins (data not shown). Also, the values for the bone formation parameters lie in the same range as values found from histological sections in a previous study with the same loading protocol [20].

A limitation in the FE model presented here was that the same Young's modulus was assigned to all voxel elements uniformly when it is actually reasonable to assume that these properties are not homogeneously distributed in a system that has not finished adapting. To overcome this problem, other researchers have used a voxel conversion technique relating the Young's modulus of each voxel to its mineral density [74]. Locally at bone formation and bone resorption sites the mineralization changes significantly over time [75]. Nevertheless, the mineralization of the whole bone did not change significantly over time (data not shown), likely because the formation and resorption sites make up only a small volume of the whole bone volume. Therefore, we can assume the error coming from the inhomogeneity of the material properties is relatively small, although in the future approaches to directly relating local mechanical properties to measured material properties would be advantageous.

Despite these limitations, we believe there are several advantages of the tail loading model. Firstly, CV6 contains yellow or fatty bone marrow, and is consequently less sensitive for radiation and suitable for future studies investigating aging

or ovariectomy. Secondly, owing to the small size and shape of CV6, realistic finite element analysis can be facilitated more readily. This will enable to characterize the spatial relationship between load induced bone adaptation and the associated micromechanical environment more closely. Thirdly, there is a large trabecular content in CV6, often necessary for gene detection technologies. This will prove useful in future studies which investigate load regulated genes.

To our knowledge, this was the first time that 3D dynamic bone morphometry parameters were calculated at multiple time points within the same animal. The novelty of our technique is that parameters are calculated in 3D, comprise the whole trabecular volume, and most importantly, describe resorption parameters as well. This will be important, especially in future studies where resorption parameters are modulated more than formation parameters, for example in osteoporosis or aging studies. This will also prove useful when validating in silico models that predict bone adaptation. A further novelty is that it could be shown that there was targeted bone adaptation, leading to an increase in bone strength.

In summary, we gained new insights into basic bone remodeling by extracting dynamic bone morphometry parameters in a dynamic loading model over time. Caudal vertebrae adapted to loading mostly by modulating the surface of trabecular formation and resorption sites. This led to an increase of bone strength, which could be well explained by the changes in bone structural parameters. We believe in future 3D dynamic bone morphometry parameters will give invaluable insights into bone remodeling and transient biology for a wide range of disease and treatment regimens.

3.1.5 Acknowledgements

The authors gratefully acknowledge funding from the European Union for the Osteoporotic Virtual Physiological Human project (VPHOP FP7-ICT2008-223865) and computational time from the Swiss National Supercomputing Center (CSCS, Manno, Switzerland). We thank Dr. Thomas Kohler, Dr. Martin Stauber, Dr. Elad Wasserman, David Christen, Dr. Davide Ruffoni, Peter Schwilch, and Marco Hitz of the Institute for Biomechanics, ETH Zürich, Zürich, Switzerland, for technical assistance.

References

- [1] A.G. Robling, A.B. Castillo, and C.H. Turner. Biomechanical and molecular regulation of bone remodeling. *Annu Rev Biomed Eng*, 8:455–498, 2006.
- [2] S. C. Manolagas. Birth and death of bone cells: Basic regulatory mechanisms and implications for the pathogenesis and treatment of osteoporosis. *Endocrine Reviews*, 21(2):115–137, 2000.
- [3] K. Henriksen, A.V. Neutzsky-Wulff, L.F. Bonewald, and M.A. Karsdal. Local communication on and within bone controls bone remodeling. *Bone*, 44(6):1026–1033, 2009.
- [4] C.T. Rubin and L.E. Lanyon. Kappa Delta Award paper. Osteoregulatory nature of mechanical stimuli: function as a determinant for adaptive remodeling in bone. *J Orthop Res*, 5(2):300–310, 1987.
- [5] C.H. Turner, K. Hasegawa, W. Zhang, M. Wilson, Y. Li, and A.J. Dunipace. Fluoride reduces bone strength in older rats. *Journal of Dental Research*, 74(8):1475–1481, 1995.
- [6] C.H. Turner, S.J. Warden, T. Bellido, L.I. Plotkin, N. Kumar, I. Jasiuk, J. Danzig, and A.G. Robling. Mechanobiology of the skeleton. *Sci Signal*, 2(68):pt3, 2009.
- [7] T.M. Skerry. The response of bone to mechanical loading and disuse: fundamental principles and influences on osteoblast/osteocyte homeostasis. *Arch Biochem Biophys*, 473(2):117–123, 2008.
- [8] E.H. Burger, J. Klein-Nulend, A. van der Plas, and P.J. Nijweide. Function of osteocytes in bone—their role in mechanotransduction. *J Nutr*, 125(7 Suppl):2020S–2023S, 1995.
- [9] T.M. Skerry. One mechanostat or many? Modifications of the site-specific response of bone to mechanical loading by nature and nurture. *J Musculoskeletal Neuronal Interact*, 6(2):122–127, 2006.
- [10] R.L. De Souza, M. Matsuura, F. Eckstein, S.C. Rawlinson, L.E. Lanyon, and A.A. Pitsillides. Non-invasive axial loading of mouse tibiae increases cortical bone formation and modifies trabecular organization: a new model to study cortical and cancellous compartments in a single loaded element. *Bone*, 37(6):810–818, 2005.

- [11] T.S. Gross, S. Srinivasan, C.C. Liu, T.L. Clemens, and S.D. Bain. Noninvasive loading of the murine tibia: an *in vivo* model for the study of mechanotransduction. *J Bone Miner Res*, 17(3):493–501, 2002.
- [12] M.P. Akhter, D.M. Raab, C.H. Turner, D.B. Kimmel, and R.R. Recker. Characterization of *in vivo* strain in the rat tibia during external application of a four-point bending load. *J Biomech*, 25(10):1241–1246, 1992.
- [13] A. Moustafa, T. Sugiyama, L.K. Saxon, G. Zaman, A. Sunters, V.J. Armstrong, B. Javaheri, L.E. Lanyon, and J.S. Price. The mouse fibula as a suitable bone for the study of functional adaptation to mechanical loading. *Bone*, 44(5):930–935, 2009.
- [14] M.C.H. van der Meulen, X. Yang, T.G. Morgan, and M.P.G. Bostrom. Bone remodelling algorithms incorporating both strain and microdamage stimuli. *Clin Orthop Relat Res*, 467(8):1381–1391, 2009.
- [15] A.G. Robling, F.M. Hinant, D.B. Burr, and C.H. Turner. Improved bone structure and strength after long-term mechanical loading is greatest if loading is separated into short bouts. *J Bone Miner Res*, 17(8):1545–1554, 2002.
- [16] P. Zhang, S.M. Tanaka, H. Jiang, M. Su, and H. Yokota. Diaphyseal bone formation in murine tibiae in response to knee loading. *J Appl Physiol*, 100(5):1452–1459, 2006.
- [17] B.A. Christiansen, A.A. Kotiya, and M.J. Silva. Constrained tibial vibration does not produce an anabolic bone response in adult mice. *Bone*, 45(4):750–759, 2009.
- [18] A.B. Castillo, I. Alam, S.M. Tanaka, J. Levenda, J. Li, S.J. Warden, and C.H. Turner. Low-amplitude, broad-frequency vibration effects on cortical bone formation in mice. *Bone*, 39(5):1087–1096, 2006.
- [19] C.H. Turner, M.P. Akhter, D.M. Raab, D.B. Kimmel, and R.R. Recker. A noninvasive, *in vivo* model for studying strain adaptive bone modeling. *Bone*, 12(2):73–79, 1991.
- [20] D. Webster, E. Wasserman, M. Ehrbar, F. Weber, I. Bab, and R. Müller. Mechanical loading of mouse caudal vertebrae increases trabecular and cortical bone mass-dependence on dose and genotype. *Biomech Model Mechanobiol*, 9(6):737–747, 2010.

- [21] C.T. Rubin and L.E. Lanyon. Regulation of bone formation by applied dynamic loads. *J Bone Joint Surg Am*, 66(3):397–402, 1984.
- [22] C.T. Rubin and L.E. Lanyon. Regulation of bone mass by mechanical strain magnitude. *Calcif Tissue Int*, 37(4):411–417, 1985.
- [23] K. C. Lee, A. Maxwell, and L. E. Lanyon. Validation of a technique for studying functional adaptation of the mouse ulna in response to mechanical loading. *Bone*, 31(2):407–412, 2002.
- [24] J.C. Fritton, E.R. Myers, T.M. Wright, and M.C. van der Meulen. Loading induces site-specific increases in mineral content assessed by microcomputed tomography of the mouse tibia. *Bone*, 36(6):1030–1038, 2005.
- [25] S.W. Fox, T.J. Chambers, and J.W. Chow. Nitric oxide is an early mediator of the increase in bone formation by mechanical stimulation. *Am J Physiol*, 270(6 Pt 1):E955–E960, 1996.
- [26] D.M. Cullen, R.T. Smith, and M.P. Akhter. Time course for bone formation with long-term external mechanical loading. *J Appl Physiol*, 88(6):1943–1948, 2000.
- [27] S.J. Kuruvilla, S.D. Fox, D.M. Cullen, and M.P. Akhter. Site specific bone adaptation response to mechanical loading. *J Musculoskelet Neuronal Interact*, 8(1):71–78, 2008.
- [28] T.J. Chambers, M. Evans, T.N. Gardner, A. Turner-Smith, and J.W. Chow. Induction of bone formation in rat tail vertebrae by mechanical loading. *Bone Miner*, 20(2):167–178, 1993.
- [29] R.A. Hillam and T.M. Skerry. Inhibition of bone resorption and stimulation of formation by mechanical loading of the modeling rat ulna in vivo. *J Bone Miner Res*, 10(5):683–689, 1995.
- [30] L. Xie, J.M. Jacobson, E.S. Choi, B. Busa, L.R. Donahue, L.M. Miller, C.T. Rubin, and S. Judex. Low-level mechanical vibrations can influence bone resorption and bone formation in the growing skeleton. *Bone*, 39(5):1059–1066, 2006.
- [31] Webster D.J., Morley P.L., van Lenthe G.H., and Müller R. A novel in vivo mouse model for mechanically stimulated bone adaptation—a combined experimental and computational validation study. *Comput Methods Biomech Biomed Engin*, 11(5):435–441, 2008.

- [32] J.W. Chow, C.J. Jagger, and T.J. Chambers. Characterization of osteogenic response to mechanical stimulation in cancellous bone of rat caudal vertebrae. *Am J Physiol*, 265(2 Pt 1):E340–E347, 1993.
- [33] X. E. Guo, M. J. Eichler, E. Takai, and C. H. Kim. Quantification of a rat tail vertebra model for trabecular bone adaptation studies. *J Biomech*, 35(3):363–368, 2002.
- [34] F.A. Schulte, F.M. Lambers, G. Kuhn, and R. Müller. In vivo micro-computed tomography allows direct three-dimensional quantification of both bone formation and bone resorption parameters using time-lapsed imaging. *Bone*, 48:433–442, 2011.
- [35] J. R. Mosley, B. M. March, J. Lynch, and L. E. Lanyon. Strain magnitude related changes in whole bone architecture in growing rats. *Bone*, 20(3):191–198, 1997.
- [36] W. C. de Jong, J. H. Koolstra, J. A. Korfage, L. J. van Ruijven, and G. E. Langenbach. The daily habitual in vivo strain history of a non-weight-bearing bone. *Bone*, 46(1):196–202, 2009.
- [37] L.E. Lanyon. Strain in Sheep Lumbar Vertebrae Recorded during Life. *Acta Orthopaedica Scandinavica*, 42(1):102–112, 1971.
- [38] L.E. Lanyon. In-Vivo Bone Strain Recorded from Thoracic Vertebrae of Sheep. *J Biomech*, 5(3):277–281, 1972.
- [39] L.E. Lanyon. Analysis of Surface Bone Strain in Calcaneus of Sheep during Normal Locomotion - Strain Analysis of Calcaneus. *J Biomech*, 6(1):41–49, 1973.
- [40] K. D. Hankenson, B. J. Ausk, S. D. Bain, P. Bornstein, T. S. Gross, and S. Srinivasan. Mice lacking thrombospondin 2 show an atypical pattern of endocortical and periosteal bone formation in response to mechanical loading. *Bone*, 38(3):310–316, 2006.
- [41] S.L. Poliachik, D. Threet, S. Srinivasan, and T.S. Gross. 32 wk old C3H/HeJ mice actively respond to mechanical loading. *Bone*, 42(4):653–659, 2008.
- [42] T. Sugiyama, L.K. Saxon, G. Zaman, A. Moustafa, A. Sunters, J.S. Price, and L.E. Lanyon. Mechanical loading enhances the anabolic effects of intermittent parathyroid hormone (1-34) on trabecular and cortical bone in mice. *Bone*, 43(2):238–248, 2008.

- [43] S. Srinivasan, D.A. Weimer, S.C. Agans, S.D. Bain, and T.S. Gross. Low-magnitude mechanical loading becomes osteogenic when rest is inserted between each load cycle. *J Bone Miner Res*, 17(9):1613–1620, 2002.
- [44] M.A. Lynch, M.D. Brodt, and M.J. Silva. Skeletal effects of whole-body vibration in adult and aged mice. *J Orthop Res*, 28(2):241–247, 2010.
- [45] H. Hagino, M. Kuraoka, Y. Kameyama, T. Okano, and R. Teshima. Effect of a selective agonist for prostaglandin E receptor subtype EP4 (ONO-4819) on the cortical bone response to mechanical loading. *Bone*, 36(3):444–453, 2005.
- [46] A.G. Robling, D.B. Burr, and C.H. Turner. Partitioning a daily mechanical stimulus into discrete loading bouts improves the osteogenic response to loading. *J Bone Miner Res*, 15(8):1596–1602, 2000.
- [47] J.A. Robinson, M. Chatterjee-Kishore, P.J. Yaworsky, D.M. Cullen, W. Zhao, C. Li, Y. Kharode, L. Sauter, P. Babij, E.L. Brown, A.A. Hill, M.P. Akhter, M.L. Johnson, R.R. Recker, B.S. Komm, and F.J. Bex. Wnt/beta-catenin signaling is a normal physiological response to mechanical loading in bone. *J Biol Chem*, 281(42):31720–31728, 2006.
- [48] A. Feher, A. Koivunemi, M. Koivunemi, R. K. Fuchs, D. B. Burr, R. J. Phipps, S. Reinwald, and M. R. Allen. Bisphosphonates do not inhibit periosteal bone formation in estrogen deficient animals and allow enhanced bone modeling in response to mechanical loading. *Bone*, 46(1):203–207, 2010.
- [49] A.G. Robling and C.H. Turner. Mechanotransduction in bone: genetic effects on mechanosensitivity in mice. *Bone*, 31(5):562–569, 2002.
- [50] S.J. Warden, J.A. Hurst, M.S. Sanders, C.H. Turner, D.B. Burr, and J. Li. Bone adaptation to a mechanical loading program significantly increases skeletal fatigue resistance. *J Bone Miner Res*, 20(5):809–816, 2005.
- [51] Y.F. Hsieh and C.H. Turner. Effects of loading frequency on mechanically induced bone formation. *J Bone Miner Res*, 16(5):918–924, 2001.
- [52] S. J. Warden and C. H. Turner. Mechanotransduction in the cortical bone is most efficient at loading frequencies of 5-10 Hz. *Bone*, 34(2):261–270, 2004.
- [53] P. J. Fox, T. R. Mackin, L. D. Turner, I. Colton, K. A. Nugent, and R. E. Scholten. Noninterferometric phase imaging of a neutral atomic beam. *Journal of the Optical Society of America B-Optical Physics*, 19(8):1773–1776, 2002.

- [54] T.J. Chambers, S. Fox, C.J. Jagger, J.M. Lean, and J.W. Chow. The role of prostaglandins and nitric oxide in the response of bone to mechanical forces. *Osteoarthritis Cartilage*, 7(4):422–423, 1999.
- [55] M.L. Bouxsein, S.K. Boyd, B.A. Christiansen, R.E. Guldborg, K.J. Jepsen, and R. Müller. Guidelines for assessment of bone microstructure in rodents using micro-computed tomography. *J Bone Miner Res*, 25(7):1468–1486, 2010.
- [56] P. Thevenaz, U.E. Ruttimann, and M. Unser. A pyramid approach to subpixel registration based on intensity. *IEEE Trans Image Process*, 7(1):27–41, 1998.
- [57] T. Kohler, M. Stauber, L.R. Donahue, and R. Müller. Automated compartmental analysis for high-throughput skeletal phenotyping in femora of genetic mouse models. *Bone*, 41(4):659–667, 2007.
- [58] T. Hildebrand, A. Laib, R. Müller, J. Dequeker, and P. Ruegsegger. Direct three-dimensional morphometric analysis of human cancellous bone. *J Bone Miner Res*, 14(7):1167–1174, 1999.
- [59] P. Arbenz, G.H. van Lenthe, U. Mennel, R. Müller, and M. Sala. A scalable multi-level preconditioner for matrix-free micro-finite element analysis of human bone structures. *Int J Numer Methods Eng*, 73:927–949, 2008.
- [60] W. Pistoia, B. van Rietbergen, E.M. Lochmuller, C.A. Lill, F. Eckstein, and P. Ruegsegger. Estimation of distal radius failure load with micro-finite element analysis models based on three-dimensional peripheral quantitative computed tomography images. *Bone*, 30(6):842–848, 2002.
- [61] P. Muir, S. J. Sample, J. G. Barrett, J. McCarthy, Jr. Vanderby, R., M. D. Markel, L. J. Prokuski, and V. L. Kalscheur. Effect of fatigue loading and associated matrix microdamage on bone blood flow and interstitial fluid flow. *Bone*, 40(4):948–956, 2007.
- [62] J. G. Barrett, S. J. Sample, J. McCarthy, V. L. Kalscheur, P. Muir, and L. Prokuski. Effect of short-term treatment with alendronate on ulnar bone adaptation to cyclic fatigue loading in rats. *J Orthop Res*, 25(8):1070–1077, 2007.
- [63] H. Chen, X. Zhou, S. Emura, and S. Shoumura. Site-specific bone loss in senescence-accelerated mouse (SAMP6): a murine model for senile osteoporosis. *Exp Gerontol*, 44(12):792–798, 2009.

- [64] R Development Core Team. R: A Language and Environment for Statistical Computing. *R Foundation for Statistical Computing, Vienna, Austria*, 2010.
- [65] J.M. Lean, C.J. Jagger, T.J. Chambers, and J.W. Chow. Increased insulin-like growth factor I mRNA expression in rat osteocytes in response to mechanical stimulation. *Am J Physiol*, 268(2 Pt 1):E318–E327, 1995.
- [66] R. Garman, C. Rubin, and S. Judex. Small oscillatory accelerations, independent of matrix deformations, increase osteoblast activity and enhance bone morphology. *PLoS ONE*, 2(7):e653, 2007.
- [67] S. Srinivasan, S.C. Agans, K.A. King, N.Y. Moy, S.L. Poliachik, and T.S. Gross. Enabling bone formation in the aged skeleton via rest-inserted mechanical loading. *Bone*, 33(6):946–955, 2003.
- [68] R. Voide, G.H. van Lenthe, and R. Müller. Bone morphometry strongly predicts cortical bone stiffness and strength, but not toughness, in inbred mouse models of high and low bone mass. *J Bone Miner Res*, 23(8):1194–1203, 2008.
- [69] P. Ammann and R. Rizzoli. Bone strength and its determinants. *Osteoporos Int*, 14(Suppl 3):S13–S18, 2003.
- [70] R. Müller, M. Hannan, S.Y. Smith, and F. Bauss. Intermittent ibandronate preserves bone quality and bone strength in the lumbar spine after 16 months of treatment in the ovariectomized cynomolgus monkey. *J Bone Miner Res*, 19(11):1787–1796, 2004.
- [71] S. L. Poliachik, S. D. Bain, D. Threet, P. Huber, and T. S. Gross. Transient muscle paralysis disrupts bone homeostasis by rapid degradation of bone morphology. *Bone*, 46(1):18–23, 2010.
- [72] M.D. Brodt and M.J. Silva. Aged mice have enhanced endocortical response and normal periosteal response compared with young-adult mice following 1 week of axial tibial compression. *J Bone Miner Res*, 25(9):2006–2015, 2010.
- [73] B. Christen, B. van Rietbergen, F.M. Lambers, R. Müller, and K. Ito. Bone morphology allows estimation of loading history in a murine model of bone adaptation. *Biomech Model Mechanobiol*, accepted, 2011.
- [74] J. Homminga, R. Huiskes, B. Van Rietbergen, P. Ruegsegger, and H. Weinans. Introduction and evaluation of a gray-value voxel conversion technique. *J Biomech*, 34(4):513–517, 2001.

- [75] C. Lukas, F. Lambers, D. Ruffoni, F.A. Schulte, G. Kuhn, P. Kollmannsberger, R. Weinkamer, and R. Müller. Quantification of the interplay between mineralization and remodeling in trabecular bone assessed by in vivo micro-computed tomography. *Bone*, 48:S250, 2011.

3.2 Optimization of *in vivo* response to mechanical loading

3.2.1 Effect of number of loading bouts

To investigate whether the amount of loading bouts could be reduced, but still produce an anabolic response, an experiment was performed in which one group of mice was loaded once per week (1X, n=10), while the other group was loaded three times per week (3X, n=6). The reasoning for this was, that if a similar anabolic response would be seen with loading only once per week, this would reduce the amount of stress for the mice, and contribute to the replace, reduce, and refine guidelines for laboratory animal study planning. Loading, scanning, and data analysis was performed the same as described in chapter 3.1. No group without loading was included in this experiment.

For both groups there was a significant increase in BV/TV over time (Fig. 3.7a), with a significantly greater increase for 3x (+21%) than for 1x (+8.4%). This was accompanied by a significant increase in Tb.Th of +18% for 3x and +12% for 1x, with a tendency for greater values for 3x, but no significant difference between groups (Fig. 3.7b). Nevertheless, Th.Sp, which is the inverse of Tb.Th, only increased significantly for 1x by 6%, suggesting that 3x did influence Tb.Th more positively than 1x. Similarly, Tb.N decreased significantly by -6% for 1x, but only a non significant decrease of -3% was found for 3x (Fig. 3.7c). Furthermore, BS was stable for 3x, but decreased significantly by 6% for 1x (Fig. 3.7d), with a significant difference between groups. This indicated that 3 times per week loading was more anabolic for the trabecular bone than once per week loading.

In the cortical bone significant increases over time were found for several parameters, but no significant differences between groups for any of the cortical static bone parameters. Ct.Ar/Tt.Ar increased +3.2% for 3x and +3.6% for 1x (Fig. 3.7e) as an effect of Ct.Th, which increased +5.2% for 3x and +4.3% for 1x (Fig. 3.7f). These increases resulted in an increase in TV (+1.6% for 3x and +1.9% for 1x), while for MV no significant changes were observed (-0.6% for 3x and -0.5% for 1x). Furthermore, for both groups significant increases were found in I_{max} (+8.3% for 3x and +7.4% for 1x) and I_{min} (+5.2% for 3x and +6.9% for 1x). This indicated that loading once per week was as anabolic on the cortical bone as loading three times per week.

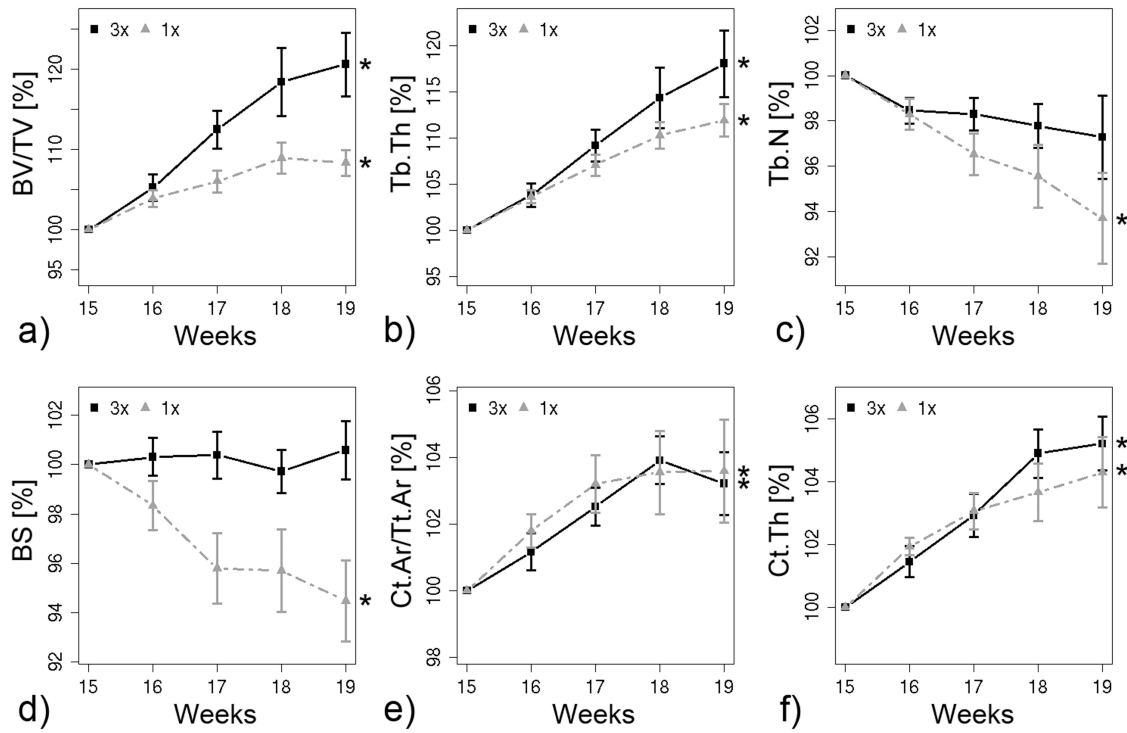


Figure 3.7: Static bone parameters over time. a) BV/TV, b) Tb.Th, c) CtAr/TtAr, d) Ct.Th. * indicates significant difference over time as tested with repeated measurements anova.

No significant differences between 3x and 1x were found for any of the dynamic bone parameters. Nevertheless, there was a tendency for 3x to have lower resorption rates, while formation rates were almost exactly the same (Fig. 3.8). On average BFR was 0.5% greater, MAR 0.8% smaller, and MS 1.2% smaller for 3x than 1x. On the other hand, BRR was on average 24% lower for 3x than 1x, with a smaller depth of resorption pits, as indicated by the on average 8.4% lower value for MRR, and with a smaller surface occupied by resorption sites, as indicated by the on average 7.2% smaller ES for 3x than to 1x. For both groups BFR was greater than BRR, with significantly greater depth for resorption pits than thickness of formation packets ($MRR > MAR$), and significantly greater surface occupied by formation sites than resorption sites ($MS > ES$). This indicated that when loading is applied once per week, bone formation is already enhanced, while bone resorption is reduced more for three times per week loading than for one time per week loading.

Bone strength increased 23% for 3x and 20% for 1x with no significant difference between groups. Eventhough little significant differences were found between 1x and 3x, the values of the 3x had a tendency to show better anabolic response in the trabecular static bone parameters, dynamic parameters and bone

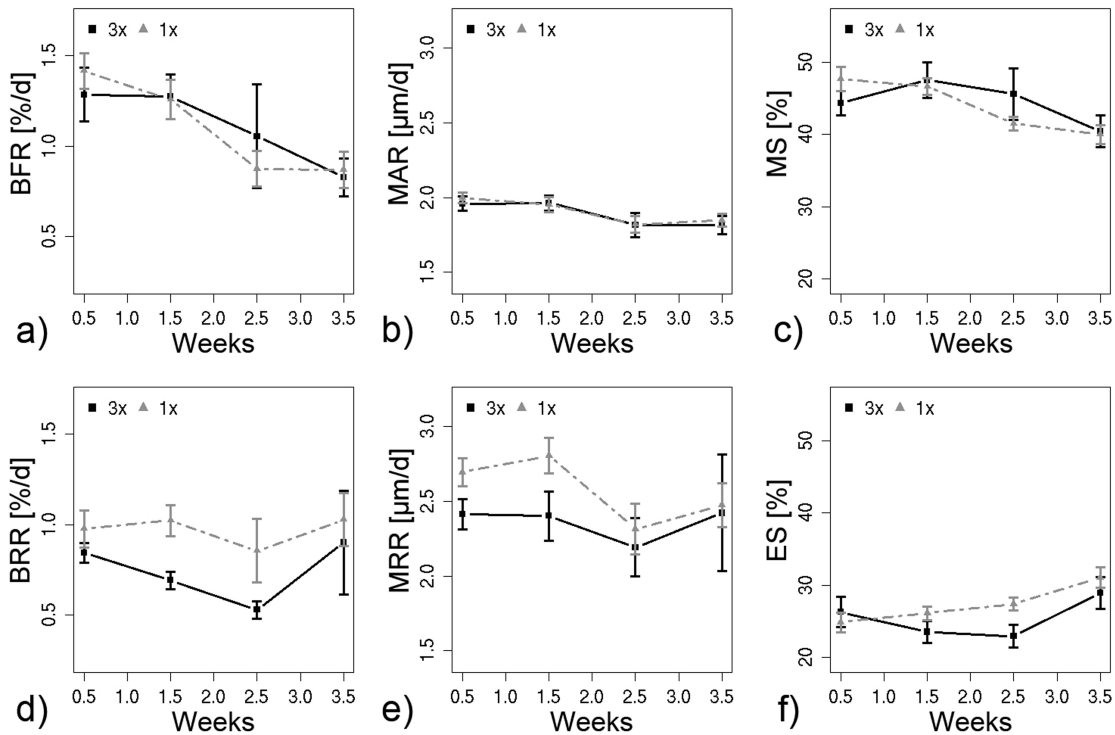


Figure 3.8: Dynamic bone parameters over time. a) BFR, b) MAR, c) MS, d) BRR, e) MAR, and f) ES.

strength. Therefore, it was concluded that 3 times loading per week seemed more anabolic and was used for all following studies.

3.2.2 Effect of load

To investigate whether the load could be reduced, but still produce an anabolic response, an experiment was performed in which mice were loaded at 0 N (n=6), 4 N (n=6) or 8 N (n=6) three times per week for 4 weeks. Scanning and data analysis was performed as described in the previous chapter.

For most static parameters a dose response was observed with changes for 8N greater than for 4N, and changes for 4N greater than changes for 0N. BV/TV increased significantly over time for 8N (+17%) and 4N (+6.1%), but not for 0N (+3.6%), with a significant difference between 8N and 0N (Fig. 3.9a). Similarly, the increase in Tb.Th of 17.7% for 8N was significantly greater than the increase of 8.9% for 4N and than the increase of 6.3% for 0N (Fig. 3.9b). Tb.N, which was not significantly different between groups, decreased significantly for 8N (-5.6%), 4N (-4%), and 0N (-5.3%). Also Conn.D decreased significantly over time for 8N (-22%), 4N (-18%), and 0N (-23%).

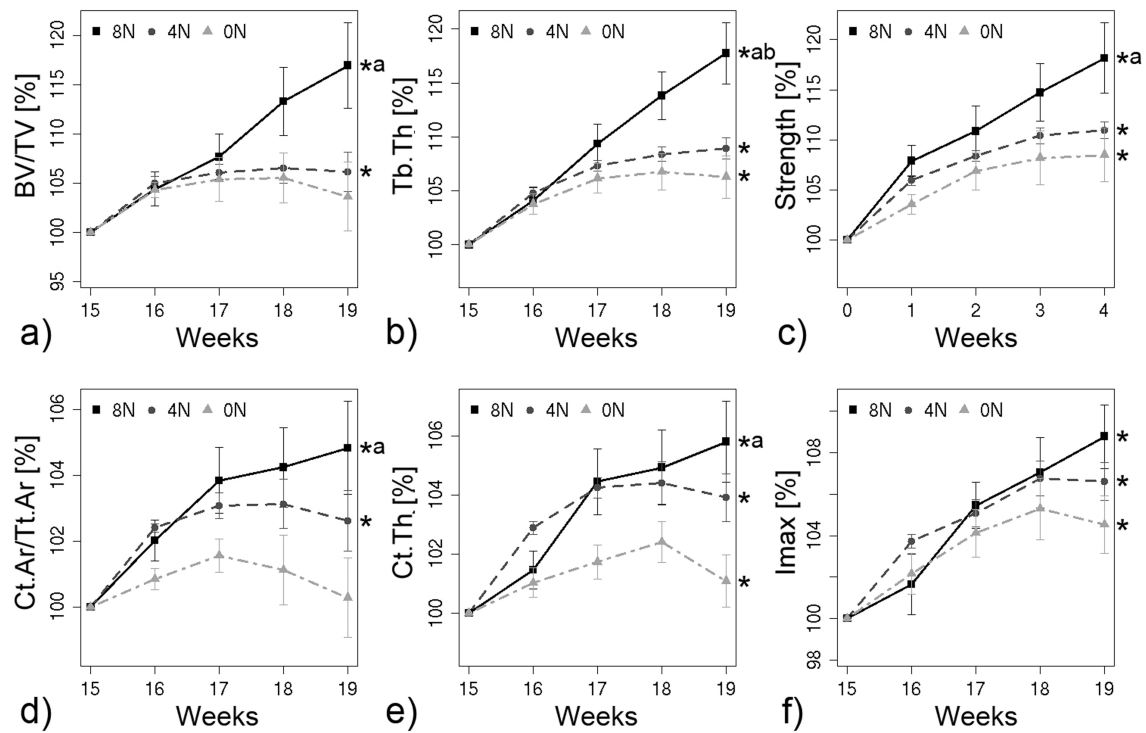


Figure 3.9: Static and mechanical bone parameters over time. a) BV/TV, b) Tb.Th, c) Bone strength, d) Ct.Ar/Tt.Ar, e) Ct.Th, and f) Imax. * indicates significant difference over time, ^a significantly different compared to 0N, and ^b significantly different compared to 4N as tested with repeated measurements anova.

The increases in Ct.Ar/Tt.Ar and Ct.Th were significantly greater for 8N than 0N, but not significantly different between the other groups. A significant increase in Ct.Ar/Tt.Ar was only observed for 8N (+4.8%) and 4N (+2.6%), but not for 0N (Fig. 3.9d). Ct.Th increased significantly over time for all three groups, with an increase of 5.8% for 8N, of 3.9% for 4N, and of +1.1% for 0N (Fig. 3.9e). The increase in Ct.Th was characterized by addition of bone on the periosteal side, as indicated by a significant increase in TV for all three groups (+2.5% for 8N, +2.8% for 4N, and +3.2% for 0N). At the same time, the volume of the marrow space was maintained for the loaded groups (4N and 8N), while this increased significantly by 3% for 0N. These changes in the cortex resulted in a total increase in resistance against bending (Fig. 3.9f), as indicated by Imax (+8.8% for 8N, +6.6% for 4N, +4.5% for 0N) and Imin (+6.3% for 8N, +6.6% for 4N, +5.1% for 0N). Also the strength of the whole bone increased significantly over time by 18% for 8N, 11% for 4N, and 8% for 0N, with a significant difference between 8N and 0N (Fig. 3.9c).

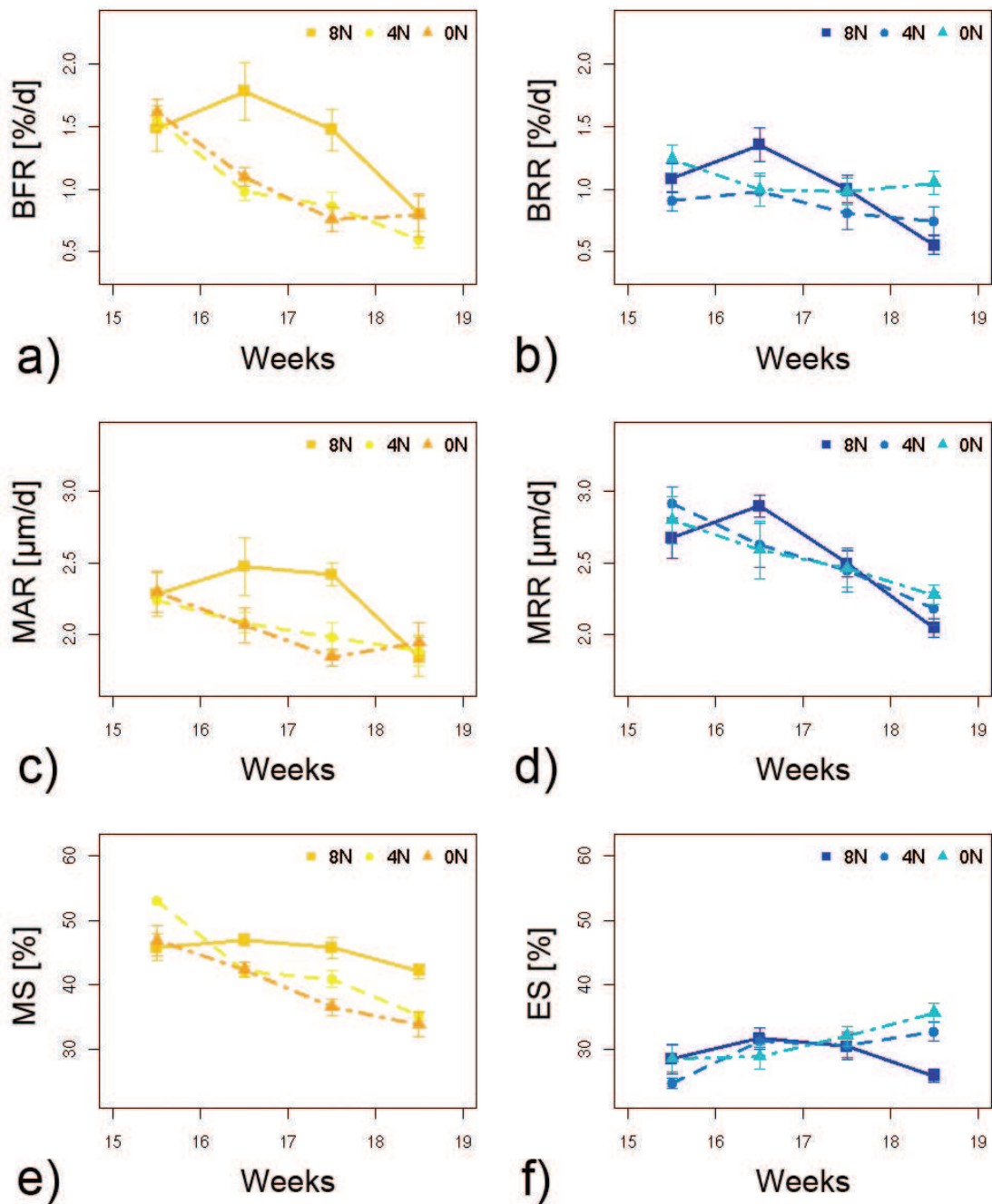


Figure 3.10: Dynamic bone parameters over time. a) BFR, b) BRR, c) MAR, d) MRR, e) MS, f) ES.

There was a tendency that 8N had greater bone formation and lower bone resorption than 0N (Fig. 3.10a and b). BFR was on average 37.5% greater and BRR on average 4.8% smaller for 8N than for 0N. Strangely, BFR was on average 6.4% smaller for 4N than for 0N. Nevertheless, also BRR was on average 18.7% smaller for 4N than for 0N (Fig. 3.10b). A dose response in the ratio between BFR and BRR could be

observed. On average BFR was 39% greater than BRR for 8N, while this ratio was 14.5% for 4N, and -1.8% for 0N. When regarding the shape of the remodeling sites, it was found that loading mostly had an effect on MS, where 8N was significantly greater than 4N, and 4N was significantly greater than 0N (Fig. 3.10e). The surface occupied by formation sites (MS) was significantly greater than the surface occupied by resorption sites (ES), with a difference of 53% for 8N, of 48% for 4N, and of 30% for 0N (Fig. 3.10f). For both 0N and 4N the depth of the resorption pits (MRR) was on average about 25% greater than the thickness of the formation packets (MAR), while for 8N this difference was only on average 12% (Fig. 3.10c and d). The fact that loading affected the surface occupied by remodeling sites more than the thickness of formation sites or depth of resorption sites is in agreement to a previous study (chapter 3.1). Even if not many significant differences were observed between groups, a dose response was present for most parameters, with 8N showing the largest anabolic response, and with the 4N group between the 8N and 0N group. Very little differences were found between 4N and 0N, indicating that 4N might not be enough to elicit an anabolic response. Therefore, it would be recommended to keep the force (for this mouse strain and age) at at least 8 N for future studies.

3.3 Longitudinal effects on bone strength and dynamic morphometry during 14 weeks of cyclic loading in a mouse model of bone adaptation

Floor M. Lambers¹, Kathleen M. Koch¹, Gisela Kuhn¹, Claudia Weigt¹, Friederike A. Schulte¹, and Ralph Müller¹

¹Institute for Biomechanics, ETH Zürich, Zürich, Switzerland

Abstract:

The aim of this study was to assess the long-term effect of loading on bone microstructure, bone strength, and bone remodeling rates. Mice were subjected to cyclic loading at the sixth caudal vertebra with 8N or 0N (control) three times per week for a total period of 14 weeks. Structural bone parameters were determined from *in vivo* micro-computed tomography (micro-CT) scans performed at week 0, 4, 6, 8, 10, 12, and 14. Mechanical parameters were derived from micro-finite element analysis. Dynamic bone morphometry was calculated using registration of serial micro-CT scans. Results showed that the cortex adapted to 8N in about 6 weeks, after which very little changes occurred. The trabecular bone needed 8 weeks to adapt to 8N. The bone strength achieved at 8 weeks was maintained until the end of the experiment. In the first 4 weeks of the experiment, bone formation rate was 32% greater and bone resorption rate 22% smaller for 8N than 0N. This difference reduced as the bone became adapted with remodeling rates of 8N returning to control levels. Together these data suggest that once bone has adapted to a new load, the remodeling rates return to normal levels while maintaining bone strength.

Keywords:

In vivo micro-computed tomography; long-term load adaptation; mechanical loading; bone microstructure; dynamic bone morphometry; bone strength

3.3.1 Introduction

Bone remodeling is important for maintaining mechanical integrity of bone. Changes in the mechanical environment are assumed to induce alterations in bone remodeling effects, with the general rule that bone mass is increased upon a greater mechanical demand, while bone mass is decreased in absence of mechanical forces. There have been numerous *in vivo* loading studies that focused on immediate effects of loading [1–10], but only a few studies continued monitoring until bone had adapted completely. In one study, four-point-bending was applied to the tibia of rats for 6, 12 or 18 weeks. In the loaded leg bone formation rate was elevated on both periosteal and endosteal side of the cortex up to 12 weeks of loading, but only the endocortical mineral apposition rate remained elevated compared to contra lateral leg after 18 weeks of loading [11]. Another study reported that after 14 weeks of four-point-bending at the tibia in rats no periosteal bone label was observed, suggesting that bone formation rate was arrested and bone was fully adapted to the new load [12]. Similarly, when bone remodeling rates were compared after 5 and 10 weeks of loading at the ulna in rats, it was found that formation rates were greater in loaded than control leg at 5 weeks of loading, but after 10 weeks of loading, the rates had returned to control levels, indicating complete adaptation [13]. These studies focused on cortical adaptation only.

To our knowledge, no studies have assessed the long-term effect of loading on structural parameters and dynamic remodeling rates in the trabecular bone. With the advent of *in vivo* micro-CT it has become easier to investigate over which time frame bone adapts to loading. With this imaging technique the bone microstructure can be visualized within a single animal at multiple time points. Furthermore, dynamic bone parameters can be extracted from serial *in vivo* micro-CT scans [14], enabling to assess how formation and resorption rates are evolving over time.

With a recently developed *in vivo* loading model [2, 15] it was shown that the trabecular bone in caudal vertebrae of mice actively responds to mechanical loading, with a linear increase in bone volume fraction up to 4 weeks of loading [16]. Here, the same loading model was used to monitor at which time point the bone is fully adapted to the load and to investigate the effect of long-term loading on structural changes and remodeling rates in trabecular bone. We hypothesized that bone remodeling rates are elevated until the bone is strong enough for the new loading condition, and that once the bone has fully adapted, dynamic bone

Table 3.4: Percent difference to previous time point in bone structural parameters.

		0-4	4-6	6-8	8-10	10-12	12-14
Whole bone							
AVD [%]	8N	8.50 ± 0.92	1.53 ± 0.21	0.72 ± 0.23	0.57 ± 0.24	-0.29 ± 0.37	0.48 ± 0.45
	0N	3.41 ± 0.94	0.87 ± 0.42	0.26 ± 0.37	0.95 ± 0.27	0.43 ± 0.18	0.59 ± 0.23
Cortical bone							
Ct.Ar/Tt.Ar [%]	8N	4.46 ± 1.02	1.07 ± 0.31	0.06 ± 0.22	0.67 ± 0.32	-0.63 ± 0.17	0.30 ± 0.59
	0N	1.92 ± 1.06	0.55 ± 0.50	-0.19 ± 0.39	0.05 ± 0.38	0.39 ± 0.32	0.11 ± 0.24
Ct.Th [%]	8N	5.33 ± 0.93	1.48 ± 0.60	0.55 ± 0.19	0.61 ± 0.24	-0.24 ± 0.13	0.73 ± 0.47
	0N	2.21 ± 0.98	0.25 ± 0.50	0.32 ± 0.38	-0.07 ± 0.44	0.36 ± 0.34	0.53 ± 0.34
TV [%]	8N	2.02 ± 0.59	1.05 ± 0.48	0.92 ± 0.30	0.77 ± 0.42	0.74 ± 0.30	0.27 ± 0.48
	0N	2.34 ± 0.46	0.85 ± 0.39	0.42 ± 0.10	0.86 ± 0.10	0.34 ± 0.44	1.10 ± 0.24
MV [%]	8N	-0.82 ± 0.74	0.34 ± 0.50	0.88 ± 0.38	0.30 ± 0.60	1.17 ± 0.29	0.10 ± 0.77
	0N	0.98 ± 0.68	0.44 ± 0.56	0.56 ± 0.31	0.85 ± 0.31	0.08 ± 0.54	1.03 ± 0.18
Trabecular bone							
BV/TV [%]	8N	23.7 ± 4.78	5.47 ± 1.53	1.98 ± 0.94	-1.89 ± 1.24	-1.39 ± 1.32	0.23 ± 2.02
	0N	10.7 ± 2.87	-0.28 ± 1.50	-0.63 ± 0.85	0.80 ± 0.77	-1.06 ± 0.57	2.06 ± 1.18
BS/BV [%]	8N	-16.6 ± 2.26	-4.66 ± 0.76	-1.89 ± 0.82	-0.35 ± 1.21	1.18 ± 1.33	-1.20 ± 1.57
	0N	-9.44 ± 1.39	-0.85 ± 1.01	-0.37 ± 0.68	-1.77 ± 0.62	-1.17 ± 0.62	-1.76 ± 0.67
Tb.Th [%]	8N	16.5 ± 2.00	3.79 ± 0.36	1.58 ± 0.77	1.09 ± 1.14	0.03 ± 1.12	1.35 ± 1.25
	0N	6.82 ± 1.39	1.21 ± 0.93	0.80 ± 0.79	1.42 ± 0.46	0.98 ± 0.60	1.05 ± 0.41
Tb.Sp [%]	8N	-1.52 ± 0.66	-1.18 ± 0.67	-0.98 ± 0.78	1.00 ± 0.58	0.43 ± 0.64	0.65 ± 0.50
	0N	-1.59 ± 1.24	1.32 ± 1.03	0.31 ± 0.55	0.91 ± 0.56	0.93 ± 0.43	1.26 ± 0.40
Tb.N [%]	8N	0.21 ± 0.71	-0.76 ± 0.71	1.13 ± 0.83	-1.37 ± 0.62	-0.09 ± 0.73	-0.17 ± 0.90
	0N	-0.49 ± 1.40	-1.11 ± 0.90	-0.18 ± 0.39	-0.80 ± 0.46	-1.24 ± 0.39	-0.89 ± 0.36
Conn.D [%]	8N	-16.9 ± 2.70	1.00 ± 3.76	-9.27 ± 2.95	-11.43 ± 3.85	10.27 ± 3.26	-3.16 ± 4.30
	0N	-20.1 ± 4.04	-2.92 ± 4.90	-4.26 ± 3.99	-9.88 ± 3.11	-9.38 ± 6.20	0.91 ± 6.04

parameters return to control levels, with maintenance of bone strength at a higher level. The study can be subdivided into three aims: (1) to investigate microstructural changes in bone in response to long-term mechanical loading, (2) to investigate the effect of long-term loading on bone strength, and (3) to investigate the effect of complete load adaptation on bone remodeling rates.

3.3.2 Materials and methods

Animals

Twenty 11-week-old female C57BL/6 mice (RCC Ltd, Füllinsdorf, Switzerland) were housed in an environmentally controlled room at a 12-hour light/dark cycle, with free access to a standard diet and tap water. To enable loading of the sixth caudal vertebra (CV6), stainless steel pins (Fine Science Tools, Heidelberg, Germany) were inserted in the fifth and seventh caudal vertebrae after one week of settling [2]. Based on the weights, mice were divided into a loaded 8N group and a control 0N group. Due to swollen tissue around the pins several mice had to be excluded during the experiment, eventually leading to group size of 5 for the 8N group and 6 for the 0N group. Three weeks after insertion of the pins the scanning and loading regime was started. All procedures were performed under isoflurane anesthesia (2-2.5%, 0.4 L/min, delivered through a nose mask, Provet Medical AG, Lyssach, Switzerland).

Approval from the local ethics committee (Kantonales Veterinäramt Zürich, Zürich, Switzerland) was obtained for all animal procedures.

***In vivo* loading**

For mechanical loading, pins were fixed in a previously developed caudal vertebral axial compression device [2]. The proximal pin was clamped tightly, while the distal pin was connected to a load cell which applied sinusoidally varying forces at 8N, 10 Hz for 3000 cycles (5 min) to CV6. This load protocol was applied three times per week for 14 weeks for the 8N group. As determined previously by strain gauges, loading at 8 N resulted in peak strains of 880 $\mu\epsilon$ on the dorsal side and 820 $\mu\epsilon$ on the ventral side of CV6 [2]. These strains encompass strains in a physiological range and are similar to other loading protocols. For the 0N group (control) the mice were placed in the loading device, but no loading was applied.

***In vivo* micro-computed tomography**

The descriptions below are according to guidelines for the assessment of bone microstructure with micro-CT [17]. During *in vivo* micro-CT measurements, the mice were positioned in a warmed holder (35°C) to prevent them from cooling down. The tail was extending from the holder and tightly fixed. Scans of CV6 were performed at the start of loading, after 4 weeks, and thereafter every two weeks up to 14 weeks at a resolution of 10.5 μm with an *in vivo* micro-CT scanner (vivaCT 40, Scanco Medical AG, Brüttisellen, Switzerland). No scan was performed at two weeks to reduce radiation, and since it was found in a previous experiment that the loading response was linear in the first 4 weeks [16]. CV6 was selected from a scoutview, and scanned completely in two connecting stacks, with a total length of 4.4 mm. The following settings were used for the scanner: 55 kVp, 145 μA , integration time of 200 ms, and 1000 projections per 180 degrees. A beam hardening correction algorithm provided by Scanco Medical AG was applied to all scans. The micro-CT scanner was calibrated weekly for mineral equivalent value, and monthly for determining in plane spatial resolution.

All raw micro-CT data were reconstructed with the dorsal side of the vertebra facing upwards. For the first scan the long axis of the bone was aligned along the z-axis, to facilitate the conversion of the micro-CT data into micro-finite element (μFE) models. The follow-up scans were translated and rotated to match the previous measurement using rigid registration [18]. A 3D constrained Gaussian filter

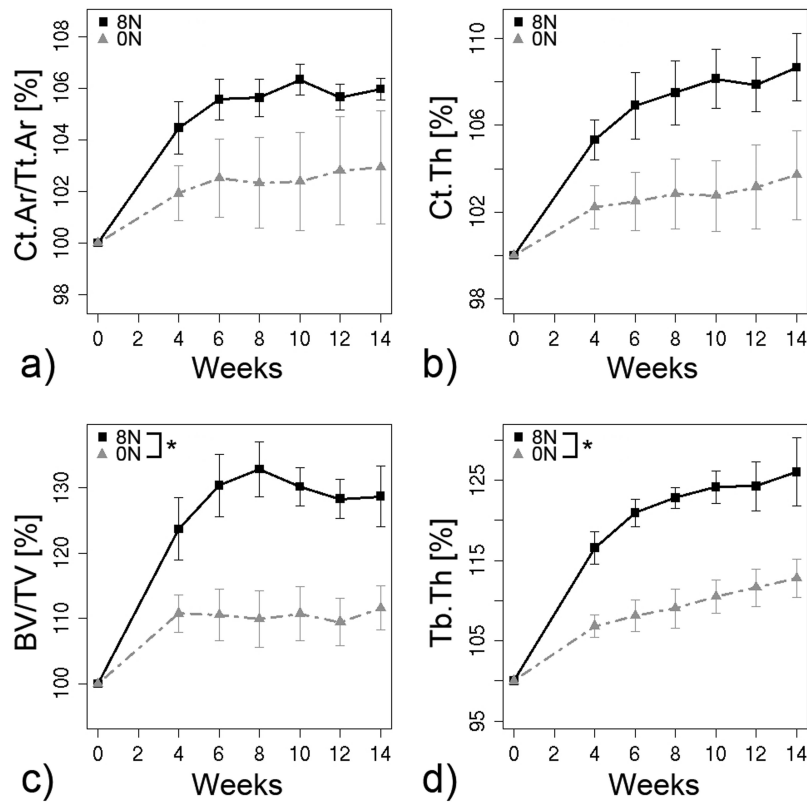


Figure 3.11: Changes in bone microstructure over time. a) Cortical area fraction (Ct.Ar/Tt.Ar), b) Cortical thickness (Ct.Th), c) Bone volume fraction (BV/TV), d) Trabecular thickness (Tb.Th). * indicates significant difference between groups.

(sigma 1.2, support 1) was applied, after which images were segmented by a fixed thresholding procedure (22% of maximum gray scale value).

Bone structural parameters

Static bone morphometry was calculated in the whole bone, cortical bone, and trabecular bone, by using masks that automatically selected these regions [16]. For the whole bone, apparent volume density (AVD) was calculated. The parameters in the cortical bone included cortical area fraction (Ct.Ar/Tt.Ar), cortical thickness (Ct.Th), tissue volume (TV), and marrow volume (MV). For calculation of these parameters, the trabecular bone was removed, and the mask was cut at 70% of the length of the whole bone (depending on the size of an inner mask). The parameters in the trabecular bone included bone volume density (BV/TV), trabecular thickness (Tb.Th), trabecular number (Tb.N), trabecular spacing (Tb.Sp), connectivity density (Conn.D), and specific bone surface (BS/BV). For the trabecular mask 72% of the length of the bone was kept to exclude the growth plates from analysis, and the

middle one third of the remainder was removed, as this region was almost void of trabecular bone.

Mechanical parameters

Three-dimensional μ FE models were created from micro-CT data for each mouse at each time point by converting all voxels to 8 node brick elements, and by adding discs on both sides of the vertebra to mimic the intervertebral discs. The μ FE models consisted of approximately 1,800,000 elements, and were assigned a Young's Modulus of 14.8 GPa, and a Poisson's ratio of 0.3 as previously validated [2]. The top was displaced to simulate 0.1% compression, while the bottom was constrained in all directions to enable the calculation of bone strength, strain energy density (SED), effective strain (e_{EFF}), and von mises stress (S_v). The resulting force was calculated and used to scale the output parameters in the model to the same force. The models were solved using a parallel linear finite element package (ParFE) with an algebraic multigrid preconditioner. The simulations ran on a Cray XT5 super computing system composed of 1844 twelve-core AMD Opteron 2.4 GHz Istanbul processors and 29 TB of physical RAM at the Swiss National Supercomputing Center (CSCS, Manno, Switzerland).

Dynamic bone morphometry

Dynamic bone morphometry was calculated in the trabecular bone. First, registered follow-up scans were superimposed to create an image in which volumes could be described as only present at the initial time point (indicating resorbed bone), only present at the follow-up time point (indicating formed bone), or present at both time points (indicating constant bone). This was done for each of the follow-up time intervals (see figure 3.14a). Second, these volumes were morphometrically analyzed, as validated previously [14], to calculate dynamic morphometric indices. These included bone formation rate (BFR); representative of the volume of formed bone, bone resorption rate (BRR); representative of the volume of resorbed bone, mineral apposition rate (MAR); indicative of the thickness of formation packets, mineral resorption rate (MRR); indicative of the depth of resorption cavities, mineralizing surface (MS); the percentage surface occupied by formation sites, and eroded surface (ES); the percentage surface occupied by resorption sites. For these parameters, the value was calculated from the preceding weeks, e.g. the value at week 4 was calculated from the overlay between week 0 and 4.

Statistical analysis

Statistical analysis was performed with the software package R [19]. To detect significant differences between groups or over time in bone structural parameters, dynamic parameters, and mechanical parameters, repeated measurements ANOVA was performed. Correlations were tested with bivariate exponential regression analysis. P-values smaller than 0.05 were considered significant. All data are shown as mean \pm standard error.

3.3.3 Results

Bone microstructure

AVD of the whole bone increased significantly over time by 12% and 7% for 8N and 0N respectively, with a significant difference between groups ($p < 0.01$).

In the cortical bone Ct.Ar/Tt.Ar increased significantly by 6% for 8N, while there was no significant change (+3%) for 0N (Fig. 3.11a). After 14 weeks of loading Ct.Th, which increased significantly by 9% for 8N, was significantly greater than for 0N, where Ct.Th increased by 4% (Fig. 3.11b). The greatest load adaptation response for 8N was observed in the first 6 weeks, after which there was less than 1% change with respect to previous time points in both Ct.Ar/Tt.Ar and Ct.Th (Table 3.4).

In the trabecular bone BV/TV increased by 29% for 8N and 12% for 0N, with a significant difference between groups ($p < 0.01$, Fig. 3.11c). The increase in BV/TV was mostly an effect of increases in Tb.Th, for which the increase of 26% for 8N was significantly greater ($p < 0.01$) than the increase of 13% for 0N (Fig. 3.11d). Most load adaptation in the trabecular bone occurred until week 8, with only small changes afterwards for both BV/TV and Tb.Th (Table 3.4).

Mechanical properties

Bone strength of the whole bone increased 37% for 8N and 22% for 0N, with almost a significant difference between groups ($p = 0.050$, Fig. 3.12a). The greatest increase in bone strength occurred in the first 8 weeks, after which it was maintained at the level that was reached after 8 weeks. Similarly, the greatest change in mechanical properties in the trabecular bone occurred in the first 8 weeks for the loaded group, and deviated only slightly afterwards. SED decreased by 33% for 8N in the first 8 weeks, and deviated less than 1% afterwards. On the contrary, SED decreased by

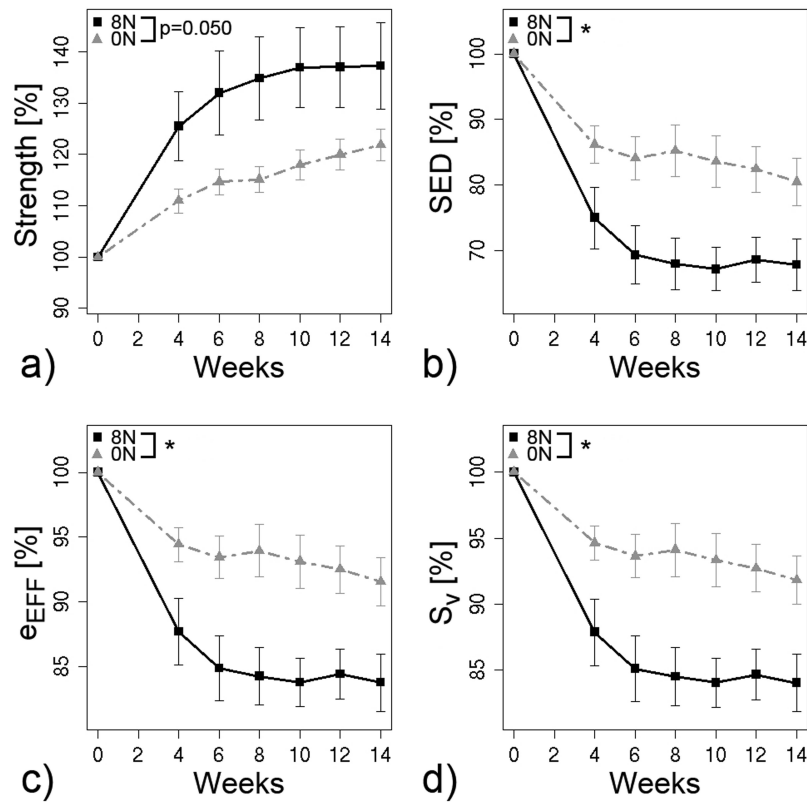


Figure 3.12: Changes in mechanical properties over time. a) Bone strength, b) Strain energy density (SED), c) Effective strain (e_{EFF}), d) Von mises stress (S_v). * indicates significant difference between groups.

15% in the first 8 weeks for 0N, and decreased another 5% in the following weeks, with a significant difference between groups ($p < 0.05$, Fig. 3.12b). Both e_{EFF} and S_v decreased 16% for 8N and 8% for 0N, with a significant difference between groups ($p < 0.05$, Fig. 3.12c and d).

Dynamic bone morphometry

Figure 3.13 shows how bone dynamic parameters changed over time. No significant differences between groups were found when the complete loading period was taken into account. Nevertheless, when only the first 4 or 6 weeks were taken into account BFR and MS were significantly greater for 8N than for 0N. The largest difference between groups was present at week 4, where BFR was 32% greater, MAR was 5.9% greater, and MS was 15% greater for 8N than for 0N, while BRR was 22% smaller, MRR was 5% smaller, and ES was 22% smaller for 8N than for 0N (Table 3.5). The difference between 8N and 0N decreased over time for most parameters, indicating that the dynamic parameters of the loaded group returned to control levels. A visual

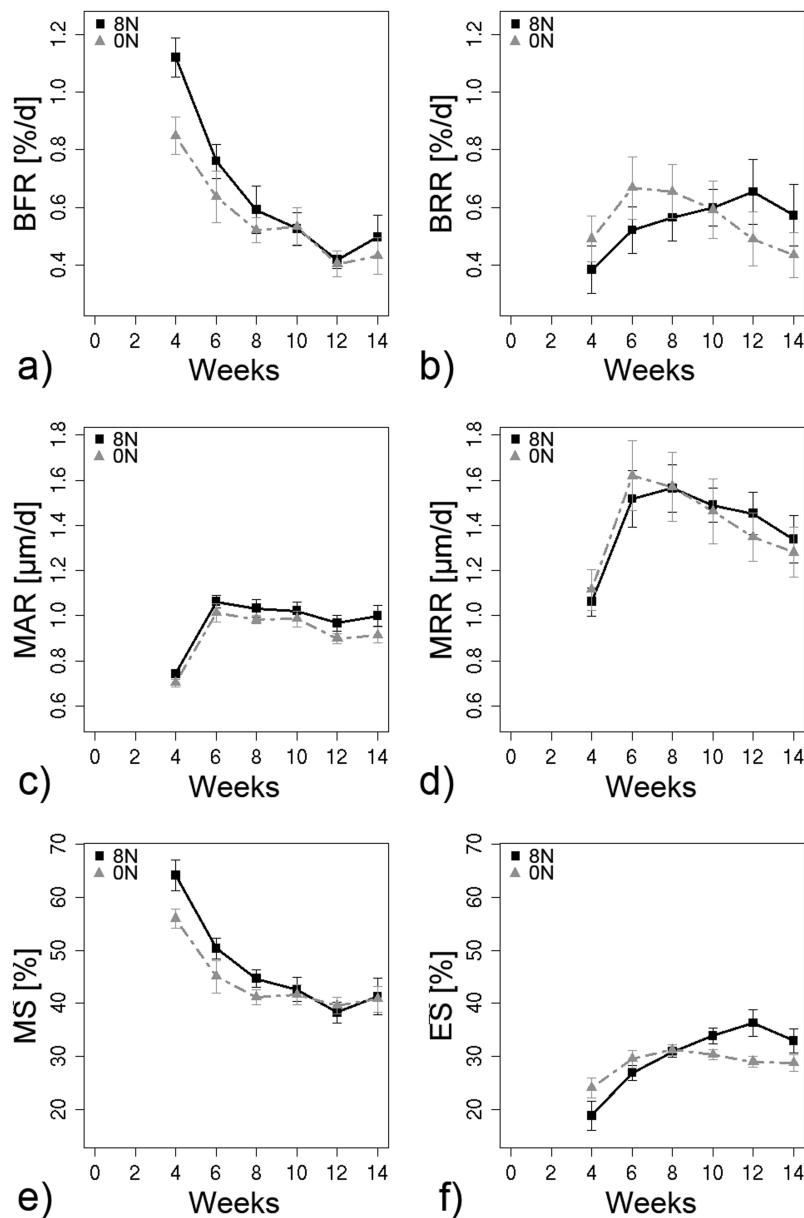


Figure 3.13: Changes in dynamic bone parameters over time. a) Bone formation rate (BFR), b) Bone resorption rate (BRR), c) Mineral apposition rate (MAR), d) Mineral resorption rate (MRR), e) Mineralizing surface (MS), f) Eroded surface (ES).

representation of this notion is shown in figure 3.14a. It can be seen that bone formation, shown in yellow, was the largest at the first time interval, and decreased for the later time intervals for a representative mouse of the 8N group. It can also be perceived that bone resorption, represented by blue volumes, increased over time. For the first overlays bone formation exceeded bone resorption largely, which can be noticed by the fact that much more yellow than blue volumes are present, while for the later overlays bone formation and resorption are more balanced, with resorption

Table 3.5: Percentage difference between 8N and 0N for each time interval.

	BFR	BRR	MAR	MRR	MS	ES
15-19	32.2	-21.9	5.9	-4.8	14.6	-21.8
19-21	19.4	-22.0	4.9	-6.2	11.8	-8.9
21-23	13.7	-13.8	5.1	-0.4	8.4	-1.2
23-25	-1.3	1.2	3.6	1.8	2.5	11.6
25-27	3.6	33.6	7.5	7.9	-3.2	25.2
27-29	15.3	32.0	9.3	4.6	1.2	14.5

exceeding formation slightly. It seems that more bone was formed and less bone was resorbed for 8N than 0N when comparing overlays between groups (Fig. 3.14b).

3.3.4 Discussion

In the present study the long-term effect of mechanical loading on bone microstructure, bone strength, and dynamic bone remodeling rates was investigated. It was found that as bone is adapting to the new loading configuration, dynamic bone remodeling rates return to control levels, with maintenance of greater bone strength.

Interestingly, load adaptation in the cortical bone, which took about 6 weeks, was faster than load adaptation in the trabecular bone, where up to 8 weeks changes in BV/TV and Tb.Th were observed. This could indicate that the necessity for cortical adaptation is greater, as the cortex is more important for mechanical stability, and consequently reacts faster. Another explanation could be that the surface available for remodeling at the cortex was larger than the surface available for remodeling in the trabecular bone. BS in trabecular bone was approximately 14 mm², while BS in cortical bone was about 23 mm², almost double the trabecular surface. In agreement with this, the absolute increase in bone volume was 0.27 mm³ for 8N and 0.19 mm³ for 0N for the cortical bone, which was greater than the absolute increase in bone volume in the trabecular bone, which was 0.12 mm³ for 8N and 0.06 mm³ for 0N over the complete duration of the experiment. Nevertheless, the trabecular bone is per bone volume more metabolically active, due to a higher specific bone surface (BS/BV). The increase in bone volume per initial bone volume was almost three times larger in the trabecular than cortical bone. But, since the geometry of trabecular bone is more specialized, it might take longer to complete shaping of the optimal geometry to preserve mechanical integrity with the least bone mass. This is in agreement with a computational simulation of the femur

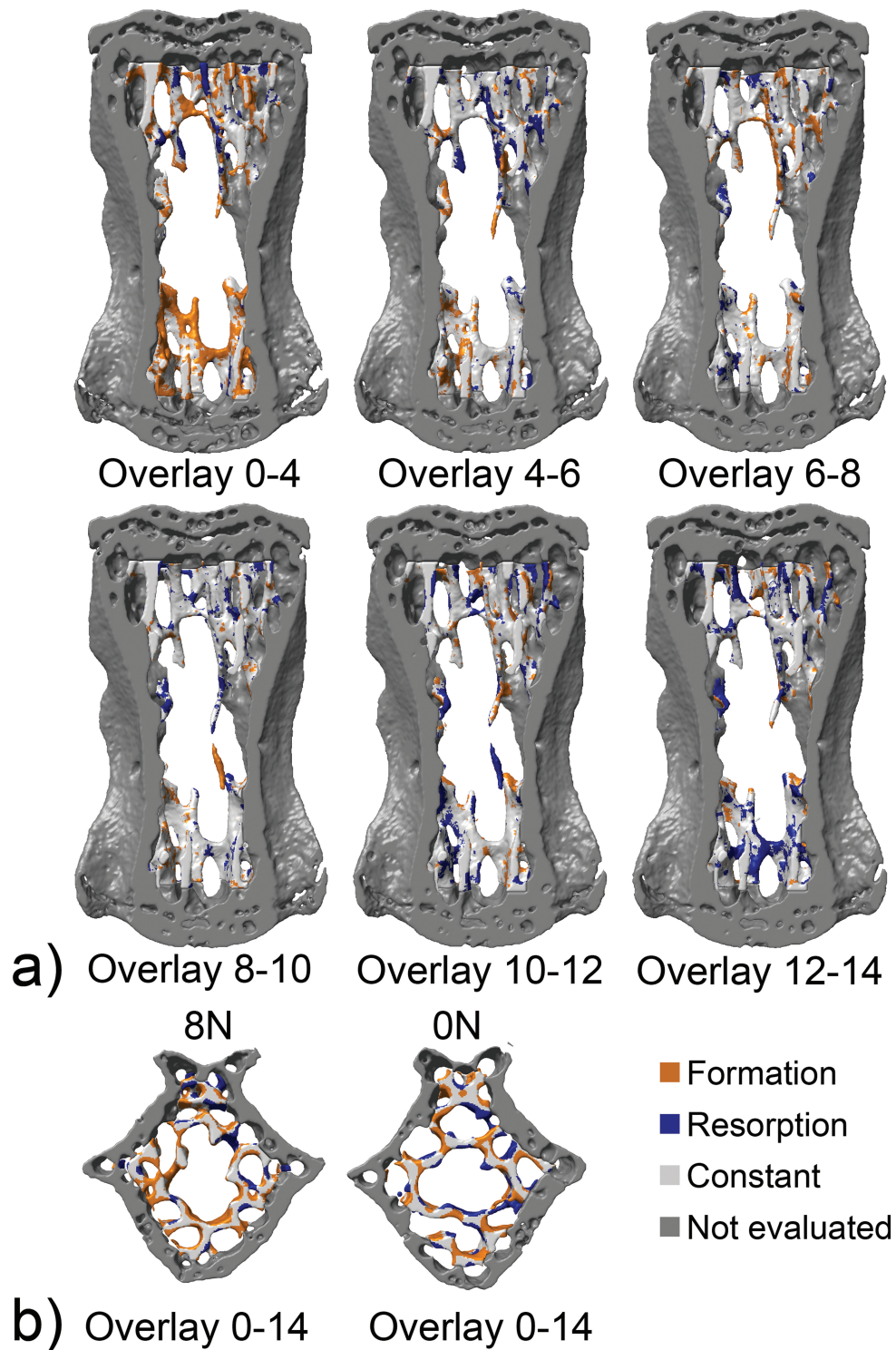


Figure 3.14: Visual representation of changes in dynamic bone parameters over time of a representative 8N mouse. Bone formation is represented by yellow volumes, and bone resorption by blue volumes. b) Overlay of a representative 0N and 8N mouse between first and last time point.

where loading to the bone was simulated and both cortical and trabecular bone was taken into account. At the start of the simulation more load was carried by

the cortex, while with load adaptation more and more load became carried by the trabecular bone, indicating that optimization of trabecular bone took longer than optimization of cortical bone [20].

The novelty of our study was that dynamic bone remodeling rates could be calculated three-dimensionally within single subjects at multiple time points. This enabled to monitor the remodeling transient of complete load adaptation. It was shown that dynamic bone remodeling rates decreased slowly over time to approach the control levels, rather than an abrupt change as soon as the optimal geometry was reached. This makes sense, as bone formation and resorption are assumed to be controlled for a large part by the mechanical environment. As the bone is adapted, but the load remains the same, the strain signal for the cells reduces, leading to a gradual reduction in bone formation rate and a gradual increase in bone resorption rate back to normal levels. In agreement with this, in studies of the cortex, where finite element models were compared with histology, correlations were found between strain gradient and periosteal sites of bone formation [21, 22].

As is typical for biological systems, there seemed to be a slight over-adaptation in the trabecular bone. BRR was lower for 8N than for 0N and approached the 0N value up to week 10, exceeded the value of 0N at week 12, and reduced again during the last time interval to approach the level of 0N. Compared to BRR, a slightly delayed response was observed in BFR, which decreased continuously over time, reached the 0N value, and increased scantily for the last time interval. It seems to make sense that the response in BFR was somewhat delayed compared to the increase in BRR, as in a bone remodeling unit osteoclasts are followed by osteoblasts. Furthermore, this slight delay could also arise from the fact that we can scan mineralized bone only and no osteoid, leading to a delayed observation of osteoblastic effects.

Profiles for MS and ES resembled the profiles of BFR and BRR, indicating most of the adaptation occurred through modulation in the remodeling surface, rather than the thickness of formation packets (MAR) and depth of resorption pits (MRR), which were quite similar between groups over all time points. In agreement, similar observations were reported in previous studies, where load induced increases in MS were greater than load-induced changes in MAR [1, 15, 23–25].

A limitation in the calculation of the dynamic parameters was that the time for the first interval was 4 weeks rather than the 2 weeks for all later time intervals (to reduce the radiation dose). Because of this, intermediate remodeling was not captured during this time, leading to a lower than actual value. This is especially apparent in the profiles of MAR and MRR which hardly change over time, but show a jump between the first and second time interval, which is probably mostly due to this difference in time frame. The fact that BFR is underestimated at week 4, further substantiates the effect that formation rate is greater over the first time interval. Another limitation of the study is that it is unknown how long the bone strength would remain once the mechanical loading scheme is abandoned. It could be speculated, however, that - as bone formation and resorption seem to be governed by the mechanical environment - the bone mass and strength would adapt again and return to original bone mass and strength.

In summary, the longitudinal imaging approach enabled to monitor complete adaptation of trabecular bone, and allowed to determine the time course needed for the bone to adapt to 8N load. In future this will be valuable input for computational models that try to reach homeostasis.

3.3.5 Acknowledgements

The authors gratefully acknowledge funding from the European Union for the Osteoporotic Virtual Physiological Human project (VPHOP FP7-ICT2008-223865), funding from the Whitaker foundation and computational time granted from the Swiss National Supercomputing Center (CSCS, Manno, Switzerland).

References

- [1] T.J. Chambers, M. Evans, T.N. Gardner, A. Turner-Smith, and J.W. Chow. Induction of bone formation in rat tail vertebrae by mechanical loading. *Bone Miner*, 20(2):167–178, 1993.
- [2] Webster D.J., Morley P.L., van Lenthe G.H., and Müller R. A novel in vivo mouse model for mechanically stimulated bone adaptation—a combined experimental and computational validation study. *Comput Methods Biomech Biomed Engin*, 11(5):435–441, 2008.
- [3] T.S. Gross, S. Srinivasan, C.C. Liu, T.L. Clemens, and S.D. Bain. Noninvasive

- loading of the murine tibia: an *in vivo* model for the study of mechanotransduction. *J Bone Miner Res*, 17(3):493–501, 2002.
- [4] A. Moustafa, T. Sugiyama, L.K. Saxon, G. Zaman, A. Sunter, V.J. Armstrong, B. Javaheri, L.E. Lanyon, and J.S. Price. The mouse fibula as a suitable bone for the study of functional adaptation to mechanical loading. *Bone*, 44(5):930–935, 2009.
- [5] C.H. Turner, K. Hasegawa, W. Zhang, M. Wilson, Y. Li, and A.J. Dunipace. Fluoride reduces bone strength in older rats. *Journal of Dental Research*, 74(8):1475–1481, 1995.
- [6] R.A. Hillam and T.M. Skerry. Inhibition of bone resorption and stimulation of formation by mechanical loading of the modeling rat ulna *in vivo*. *J Bone Miner Res*, 10(5):683–689, 1995.
- [7] A.G. Robling, F.M. Hinant, D.B. Burr, and C.H. Turner. Improved bone structure and strength after long-term mechanical loading is greatest if loading is separated into short bouts. *J Bone Miner Res*, 17(8):1545–1554, 2002.
- [8] B.A. Christiansen, A.A. Kotiya, and M.J. Silva. Constrained tibial vibration does not produce an anabolic bone response in adult mice. *Bone*, 45(4):750–759, 2009.
- [9] R.L. De Souza, M. Matsuura, F. Eckstein, S.C. Rawlinson, L.E. Lanyon, and A.A. Pitsillides. Non-invasive axial loading of mouse tibiae increases cortical bone formation and modifies trabecular organization: a new model to study cortical and cancellous compartments in a single loaded element. *Bone*, 37(6):810–818, 2005.
- [10] M.C.H. van der Meulen, X. Yang, T.G. Morgan, and M.P.G. Bostrom. Bone remodelling algorithms incorporating both strain and microdamage stimuli. *Clin Orthop Relat Res*, 467(8):1381–1391, 2009.
- [11] D.M. Cullen, R.T. Smith, and M.P. Akhter. Time course for bone formation with long-term external mechanical loading. *J Appl Physiol*, 88(6):1943–1948, 2000.
- [12] C. H. Turner, T. A. Woltman, and D. A. Belongia. Structural changes in rat bone subjected to long-term, *in vivo* mechanical loading. *Bone*, 13(6):417–422, 1992.

- [13] L.K. Saxon, A.G. Robling, I. Alam, and C.H. Turner. Mechanosensitivity of the rat skeleton decreases after a long period of loading, but is improved with time off. *Bone*, 36(3):454–464, 2005.
- [14] F.A. Schulte, F.M. Lambers, G. Kuhn, and R. Müller. In vivo micro-computed tomography allows direct three-dimensional quantification of both bone formation and bone resorption parameters using time-lapsed imaging. *Bone*, 48:433–442, 2011.
- [15] D. Webster, E. Wasserman, M. Ehrbar, F. Weber, I. Bab, and R. Müller. Mechanical loading of mouse caudal vertebrae increases trabecular and cortical bone mass-dependence on dose and genotype. *Biomech Model Mechanobiol*, 9(6):737–747, 2010.
- [16] F.M. Lambers, F.A. Schulte, G. Kuhn, D.J. Webster, and R. Müller. Mouse tail vertebrae adapt to cyclic mechanical loading by increasing bone formation rate and decreasing bone resorption rate as shown by time-lapsed *in vivo* imaging of dynamic bone morphometry. *Bone*, accepted, 2011.
- [17] M.L. Bouxsein, S.K. Boyd, B.A. Christiansen, R.E. Guldborg, K.J. Jepsen, and R. Müller. Guidelines for assessment of bone microstructure in rodents using micro-computed tomography. *J Bone Miner Res*, 25(7):1468–1486, 2010.
- [18] P. Thevenaz, U.E. Ruttimann, and M. Unser. A pyramid approach to subpixel registration based on intensity. *IEEE Trans Image Process*, 7(1):27–41, 1998.
- [19] R Development Core Team. R: A Language and Environment for Statistical Computing. *R Foundation for Statistical Computing, Vienna, Austria*, 2010.
- [20] I. G. Jang and I. Y. Kim. Computational simulation of simultaneous cortical and trabecular bone change in human proximal femur during bone remodeling. *J Biomech*, 43(2):294–301, 2010.
- [21] T. S. Gross, J. L. Edwards, K. J. McLeod, and C. T. Rubin. Strain gradients correlate with sites of periosteal bone formation. *J Bone Miner Res*, 12(6):982–988, 1997.
- [22] S. Judex and R.F. Zernicke. High-impact exercise and growing bone: relation between high strain rates and enhanced bone formation. *J Appl Phys*, 88(6):2183–2191, 2000.

- [23] S.W. Fox, T.J. Chambers, and J.W. Chow. Nitric oxide is an early mediator of the increase in bone formation by mechanical stimulation. *Am J Physiol*, 270(6 Pt 1):E955–E960, 1996.
- [24] J. M. Lean, A. G. Mackay, J. W. Chow, and T. J. Chambers. Osteocytic expression of mRNA for c-fos and IGF-I: an immediate early gene response to an osteogenic stimulus. *Am J Physiol*, 270(6 Pt 1):E937–E945, 1995.
- [25] J.W. Chow, C.J. Jagger, and T.J. Chambers. Characterization of osteogenic response to mechanical stimulation in cancellous bone of rat caudal vertebrae. *Am J Physiol*, 265(2 Pt 1):E340–E347, 1993.

3.4 Multimodality imaging of load-induced bone adaptation

Floor M. Lambers^{1,*}, Florian Stucker^{2,*}, Claudia Weigt¹, Gisela Kuhn¹, Kathleen Koch¹, Friederike A. Schulte¹, Jorge Ripoll³, Markus Rudin², and Ralph Müller¹

¹Institute for Biomechanics, ETH Zürich, Zürich, Switzerland

²Institute for Biomedical Engineering, University and ETH Zürich, Zürich, Switzerland

³Institute of Electronic Structure and Laser, Foundation for Research and Technology-Hellas (FORTH), Heraklion, Crete, Greece

* F. M. Lambers and F. Stucker contributed equally to this work.

Abstract:

Micro-computed tomography (micro-CT) is a widely used imaging modality in bone research to investigate bone microstructure. Nevertheless, to gain a better understanding in how bone remodeling is modulated through interventions, not only the bone microstructure, but also the cellular activity underlying these anatomical changes should be monitored over time. Therefore, the purpose of this study was to establish a longitudinal *in vivo* imaging approach of osteoblast and osteoclast activity using fluorescence molecular tomography (FMT). The reproducibility of FMT was assessed by measuring mice multiple times. The precision error, expressed as coefficient of variation, was smaller than 1%, indicating high reproducibility. The accuracy of FMT was verified by correlating osteoblast and osteoclast activity obtained from longitudinal FMT measurements with dynamic formation and resorption parameters calculated from *in vivo* micro-computed tomography (micro-CT) with a recently established technique. Good agreement for osteoclast activity and dynamic resorption parameters were found ($R = 0.8$, $p < 0.05$). The sensitivity of FMT was tested by comparing osteoblast and osteoclast activity in a group where the caudal vertebra was mechanically loaded to a control group. The osteoblast activity was 26% greater and osteoclast activity 14% lower for loaded than control group, but did not reach significance between groups. In conclusion, the *in vivo* imaging approach with FMT is feasible and is a promising technique for future orthopedic research.

Keywords:

multimodality imaging, fluorescence molecular tomography, *in vivo* micro-computed tomography, load adaptation, mechanical loading

3.4.1 Introduction

Bone is important for protection of organs, calcium and phosphate storage, and for allowing locomotion. Locomotion is granted through mechanical integrity of the skeleton, which is optimized by bone remodeling, through which old bone is replaced by new bone. Also, bone has the ability to adapt to new mechanical environments, by adding bone at sites where needed, and removing bone at sites where loads are no longer transferred. In bone diseases and disorders, this mechanism, however, is disturbed, and it is to date not exactly understood what the underlying cellular pathways are. Load adaptation can be investigated using animal models in combination with very controlled loading regimes [1–6]. Previously, we found that by using the caudal vertebra loading model, four weeks of loading at 8 N resulted in an increase in bone volume density of 20%, with increased bone formation rate and decreased bone resorption rate in loaded compared to control animals [7]. To gain a better understanding of the cellular and molecular processes underlying bone remodeling, multimodality imaging strategies should be used, combining structural with molecular readouts. Recently, the fluorescent probe OsteoSense[®] (PerkinElmer, Boston, MA, USA) was developed for measuring bone formation. It is composed of a bisphosphonate ligand (pamidronate) and a near-infrared fluorochrome (IRDye 78), and binds with great affinity to newly mineralizing bone surfaces [8]. In the bone remodeling process, osteoblasts are the cells that form the bone by production of the bone matrix (collagen and osteoid), which later mineralizes by precipitation of calcium salts that together with phosphate form hydroxyapatite crystals (bone mineral). Thus, because OsteoSense[®] binds with great affinity to newly mineralizing bone surfaces, the fluorochrome distribution indicates osteoblast activity and can be visualized and quantified *in vivo* in 3D by fluorescence molecular tomography (FMT) [9–11]. In the bone remodeling process, osteoclasts are the bone resorbing cells that dissolve the mineral matrix of bone by secretion of proteolytic enzymes and acids. Thus, as OsteoSense[®] binds to the bone mineral, the decrease in fluorescence intensity, caused by resorption of the label, might be considered an indicator of osteoclast activity.

The aim of this study was to establish a longitudinal *in vivo* imaging approach of osteoblast and osteoclast activity using fluorescence molecular tomography (FMT).

To achieve this goal, the reproducibility and accuracy of FMT measurements were investigated. Furthermore, multimodality imaging was used to monitor load-induced bone adaptation and to test the sensitivity of FMT measurements. Here, mice in which the caudal vertebra was loaded at 8 N, were compared to a control group. We hypothesized that for mice loaded at 8 N the fluorescence intensity would be greater, indicative of the increased bone formation rate, and that fluorescence intensity would decrease less between subsequent measurements compared to control subjects, as bone resorption rate was shown to be lower [7].

3.4.2 Methods

Experimental design

Twenty female C57BL/6 mice (RCC Ltd, Füllinsdorf, Switzerland) were ordered at an age of 11 weeks and housed in an environmentally controlled room at a 12-hour light/dark cycle and free access to a standard diet and water. To enable *in vivo* loading, stainless steel pins (Fine Science Tools, Heidelberg, Germany) were inserted manually in the fifth and seventh caudal vertebrae, with a previously designed device [2], after one week of settling. Based on the weight, mice were divided into a loaded (8N) and a control group (0N). Due to swollen tissue around the tails, several mice had to be excluded during the experiment, eventually leading to a group size of 5 for 8N and 8 for 0N. Recovery and in growth time of three weeks was allowed before *in vivo* loading and imaging started. Imaging included *in vivo* micro-CT scans at day 0, 7, 14, 21 and 28, and FMT measurements at day 0, 13, 14, 27 and 28. All procedures were performed under isoflurane anesthesia (2-2.5%, 0.4 L/min, delivered through a nose mask, Provet Medical AG, Lyssach, Switzerland). Approval of the local authorities (Kantonales Veterinäramt Zürich, Zürich, Switzerland) was obtained for all animal procedures.

In vivo loading

For the 8N group, mechanical loading was applied at 8 N, 10 Hz, for 3000 cycles, three times per week for a total of 4 weeks. The proximal pin was clamped tightly, while the distal pin was attached to the actuator, and moved sinusoidally, resulting in 800 microstrain on the sixth caudal vertebra (CV6) [2]. For the 0N group, tails were placed in the loading device but no loading was applied.

***In vivo* micro-CT**

CV6 was scanned weekly with *in vivo* micro-CT (vivaCT 40, Scanco Medical AG, Brüttisellen, Switzerland), with a basal scan before the loading regime started, leading to a total of 5 scans. A total length of 4.4 mm was scanned to include CV6 completely. Scans were performed at 55 kVp, 145 μ A, 200 ms integration time, and 1000 projections per 180 degrees, leading to a nominal isotropic resolution of 10.5 μ m. The micro-CT scanner was calibrated weekly for mineral equivalent value, and monthly for determining in plane spatial resolution. For all scans a beam hardening correction was applied. All raw micro-CT data were reconstructed such that CV6 had a similar orientation, to enable better visual comparison between mice. Follow-up scans were registered on the previous time point in order to have matching orientations of the bone microstructure over time [12]. A 3D constrained Gaussian filter (sigma 1.2, support 1) was applied, after which images were segmented by a fixed thresholding procedure (22% of maximum grayscale value). In the whole bone the apparent volume density (AVD), bone surface (BS), and tissue mineral density (TMD) were calculated.

Dynamic bone morphometry

When thresholded initial and registered follow-up scans were superimposed, this allowed visualization of locations of bone formation (only present in the follow-up scan) and locations of bone resorption (only present in the initial scan). An example of this procedure is shown in figure 3.16d. A cross-section of a vertebra at the initial time point (day 0) is shown on the left and in the middle a registered cross-section of the last time point (day 28). On the right side these cross-sections are superimposed, showing in blue the locations where bone was resorbed between day 0 and 28, and in yellow the locations where bone was formed between day 0 and 28. From these superimposed images, sites of formation and resorption could be morphometrically analyzed in 3D, as described previously [13]. The dynamic bone formation parameters included bone formation rate (BFR); the volume of the formed bone divided by the bone volume at the initial time point and days between scans, mineralizing surface (MS); the surface of the formed bone divided by the bone surface at the initial time point, and mineral apposition rate (MAR); the mean thickness of all formation sites divided by the days between scans. In analogy, the bone resorption parameters included bone resorption rate (BRR); representative of the volume of resorbed bone, eroded surface (ES); representative of the percentage surface occupied by resorption sites, and mineral resorption rate (MRR); representative of the thickness of resorption cavities. To enable comparison between dynamic bone morphometry

and fluorescence intensity of FMT measurements, the time frames over which the dynamic formation and resorption parameters were calculated from follow-up scans was two weeks: The thresholded imaged data at day 14 were registered and superimposed on the thresholded image data at day 0, and the thresholded imaged data at day 28 were registered and superimposed on the thresholded imaged data at day 14.

In vivo FMT

Twenty-four hours before the FMT measurement on day 0, 14 and 28, OsteoSense[®] 680 was injected intraperitoneally (thus at a different time point for each mouse). OsteoSense[®] 680 was diluted in saline to 2 nmol/300 μ l, and injected based on weight of the mouse at 2 nmol/25 g. In a pilot study we found that OsteoSense[®] 680 remains bound to the bone, with still a detectable signal after 4 weeks (data not shown). Therefore, in this study OsteoSense[®] 680 was injected on a 2 weeks basis, with a FMT measurement performed directly before and 24 hours after OsteoSense[®] 680 injection, to control for background fluorescence intensity. During each measurement, which took about 5 minutes, the mice were anesthetized and placed on a temperature controlled animal bed to maintain the body temperature.

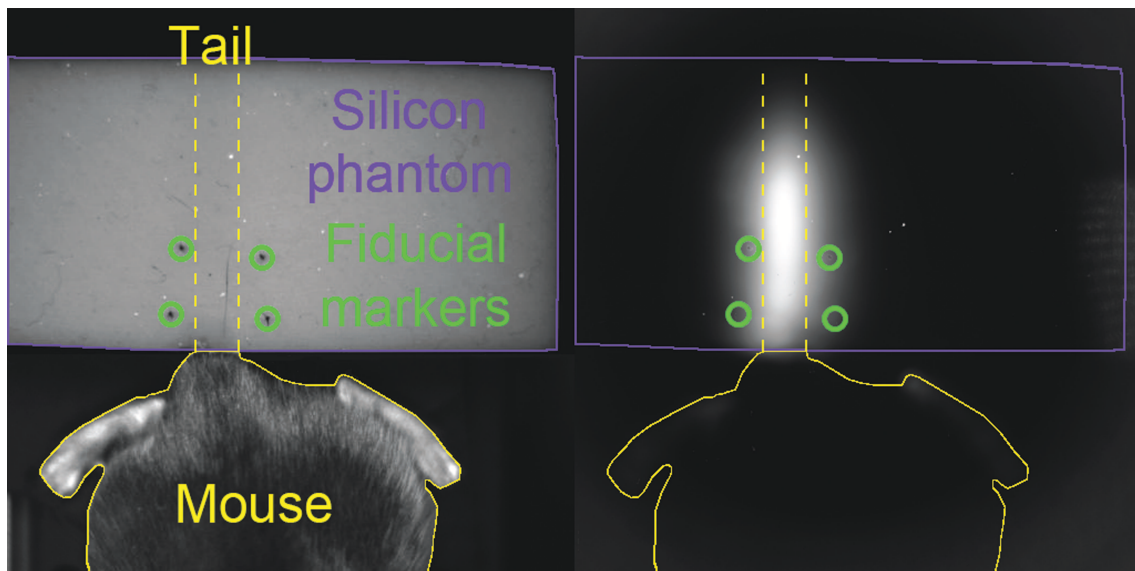


Figure 3.15: Contrast-enhanced white light and fluorescence image showing details for FMT measurements. On the white light image on the left side is shown how the mouse was positioned. The silicon phantom (marked in purple) in which the tail was embedded (marked in yellow) had fiducial markers (marked in green) to enable reproducible fixing of the tail in the phantom, and reproducible selecting of the region of interest. The corresponding fluorescence image is shown on the right, with the same colored markings to indicate the location of the mouse, phantom, tail, and markers.

FMT measurements were performed on day 0, 13, 14, 27 and 28 on an in-house built system at the animal imaging center, ETH Zurich [11, 14]. Before each session, a reference black and white image was acquired and a system calibration was performed. For each measurement a grid of 7x8 points separated by a constant distance (2.5 mm) was scanned with a 671 nm continuous wave laser source (B&W Tek, Newark, DE, USA) by using galvomirrors (Scancube, Scanlab, Germany) which was directed towards the sample in reflectance mode by the aid of a mirror (first surface mirror, Edmund Optics, Barrington, USA). For each illuminated grid point, the fluorescent and the excitation intensities were captured with appropriate band pass filters at 660 nm and 720 nm with 30nm bandwidth (Semrock, Rochester NY, USA) by a cooled high sensitive charge-coupled device (CCD) (DV-434, Andor Technology, Belfast, Northern Ireland) focused onto the sample with a 50mm f/1.4 camera objective (Nikon 50mm f/1.4D AF, Nikkor, Japan). All elements of the setup were controlled using custom software developed in Labview (National Instruments). For both wavelengths, an image without laser excitation was taken and used as background to assess the effect of the detector noise and possible ambient light entering the measurement housing. In order to provide an adequate illumination, the mouse tail was surrounded by a silicone phantom with tissue-like optical properties (scattering coefficient $\mu_s'=10 \text{ cm}^{-1}$, attenuation coefficient $\mu_a=0.2 \text{ cm}^{-1}$) to mimic slab geometry of the sample. The phantom included fiducial markers at the locations of the pins. These markers were used for reproducible positioning of the tail in the phantom and for reproducible positioning of the grid on the region of interest (figure 3.15) in the field of view of the CCD camera. The region of interest included approximately the region from the fifth to the ninth caudal vertebrae.

Reproducibility

To test reproducibility of the FMT measurements, each mouse was measured three times per time point. For each measurement the mouse was repositioned, and the tail taken out of the phantom and fixed again. The reproducibility was defined by the precision error (PE), expressed in absolute values (PE_{SD}), or as coefficient of variation ($PE_{\%CV}$) as proposed by others [13, 15–17]. 95%-Confidence intervals ($CI_{95\%}$) were determined for all of the $PE_{\%CV}$ values using a chi-squared distribution. Furthermore, intra-class correlation coefficients (ICC) were calculated, which are defined as the inter-subject variance divided by the population variance, where a value of 0 denotes no and a value of 1 perfect reproducibility.

Fluorescence intensity

For FMT image reconstruction the normalized Born approximation was applied, which removes the effects of non-uniform tissue properties [18]. This approximation uses the ratio of the measured fluorescence and excitation images accounting for the fluorescence signal on the sample surface. In the so-called forward model, this surface intensity distribution is computed both at the excitation and fluorescent wavelengths based on an assumed distribution of the fluorescent sources within the sample [19]. Image reconstruction was then performed through a custom software developed in Matlab (The Mathworks, Natick, MA) by inverting this forward model using an algebraic reconstruction technique (ART) which results in a three dimensional map of the fluorescent probe distribution within the subject. The mean fluorescence intensity (FI) over the ROI, which depends on the reconstructed fluorophore concentration, was used for analysis. For evaluation of FI over time and between groups the mean of the three reproducibility measurements was used. First, the complete region of interest, including all vertebrae was analyzed. Second, the region of interest was split in a proximal part, approximately containing the loaded and both pinned vertebrae, and a distal part, containing the vertebrae distal to the pinned vertebra. Since the values were very small, FI was multiplied by a constant factor to set at a maximum of 1.

Accuracy

Correlations between dynamic bone parameters and percentage change in FI were performed to investigate if osteoblast and osteoclast activity measured with FMT were related to dynamic bone formation and resorption parameters measured with micro-CT. To test whether the initial FI was related to the initial bone microstructure, correlations were performed between the FI and AVD and BS.

Statistical analysis

Statistical analysis was performed with the software package R (R: A Language and Environment for Statistical Computing) [20]. To detect significant differences between groups or over time in bone structural parameters, dynamic parameters, and fluorescence intensities, repeated measurements ANOVA was performed and implemented as a linear mixed effects model. Correlations were tested with bivariate regression analysis. P-values smaller than 0.05 were considered significant. All data are shown as mean \pm standard error.

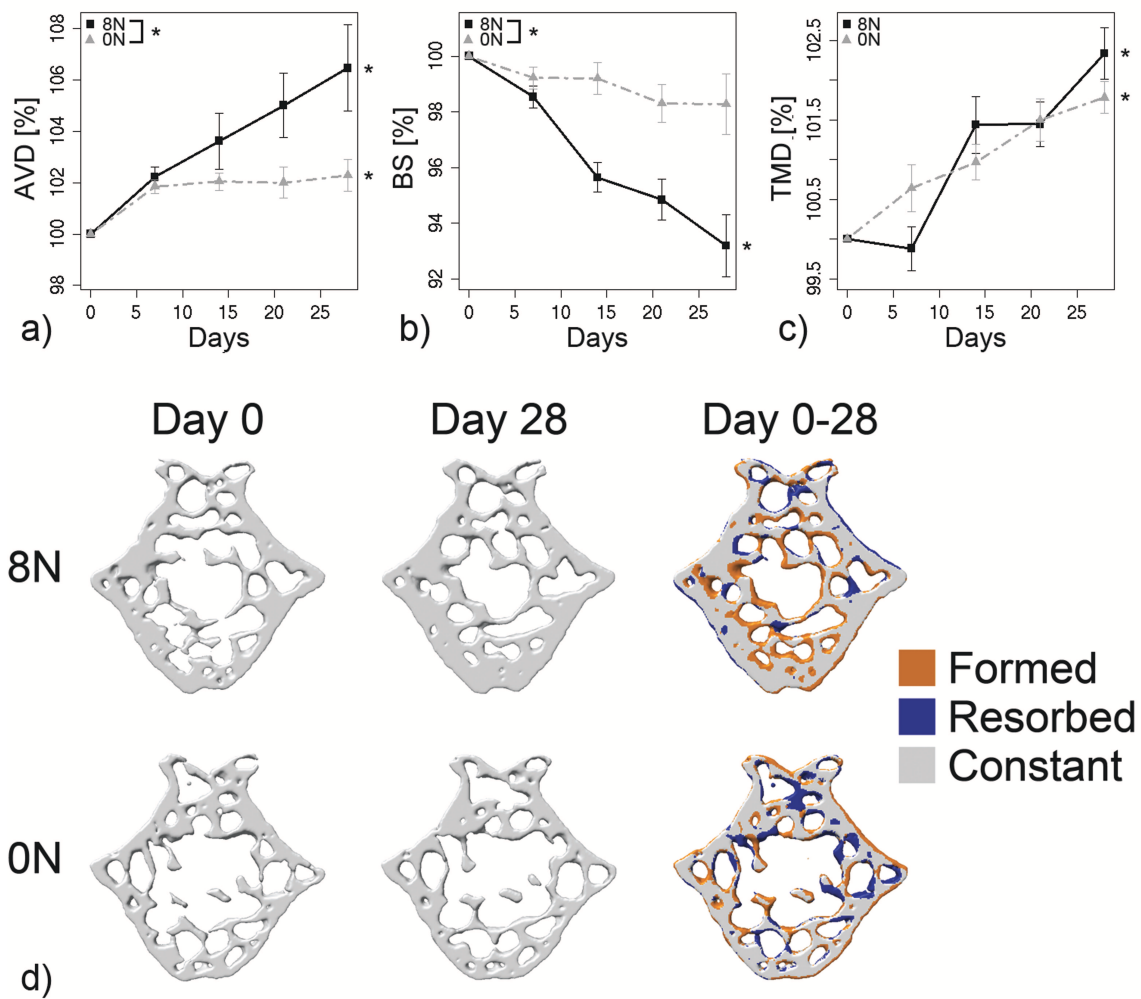


Figure 3.16: Changes in static bone parameters over time. a) Apparent volume density (AVD), b) Bone surface (BS), c) Tissue mineral density (TMD). Significant differences between groups or over time, as tested with repeated measures ANOVA, are shown with an asterisk. d) Cross-section of CV6 of average mouse of 8N and 0N group. On the left the thresholded image at day 0 is shown, in the middle the thresholded image at day 28, and on the right the superimposed image of day 28 on day 0, revealing the sites of bone formation (yellow) and resorption (blue).

3.4.3 Results

Static bone parameters

AVD increased significantly by 6.5% for 8N and by 2.3% for 0N, with a significantly greater increase for the 8N compared to the 0N group (figure 3.16a). At the same time BS did not change significantly over time for the 0N group, but decreased significantly by 6.8% for the 8N group, with a significant difference between groups (figure 3.16b). TMD increased significantly for both groups, but without difference between groups (figure 3.16c). This indicated that loading did influence the bone microstructure, but not the mineral density of the bone.

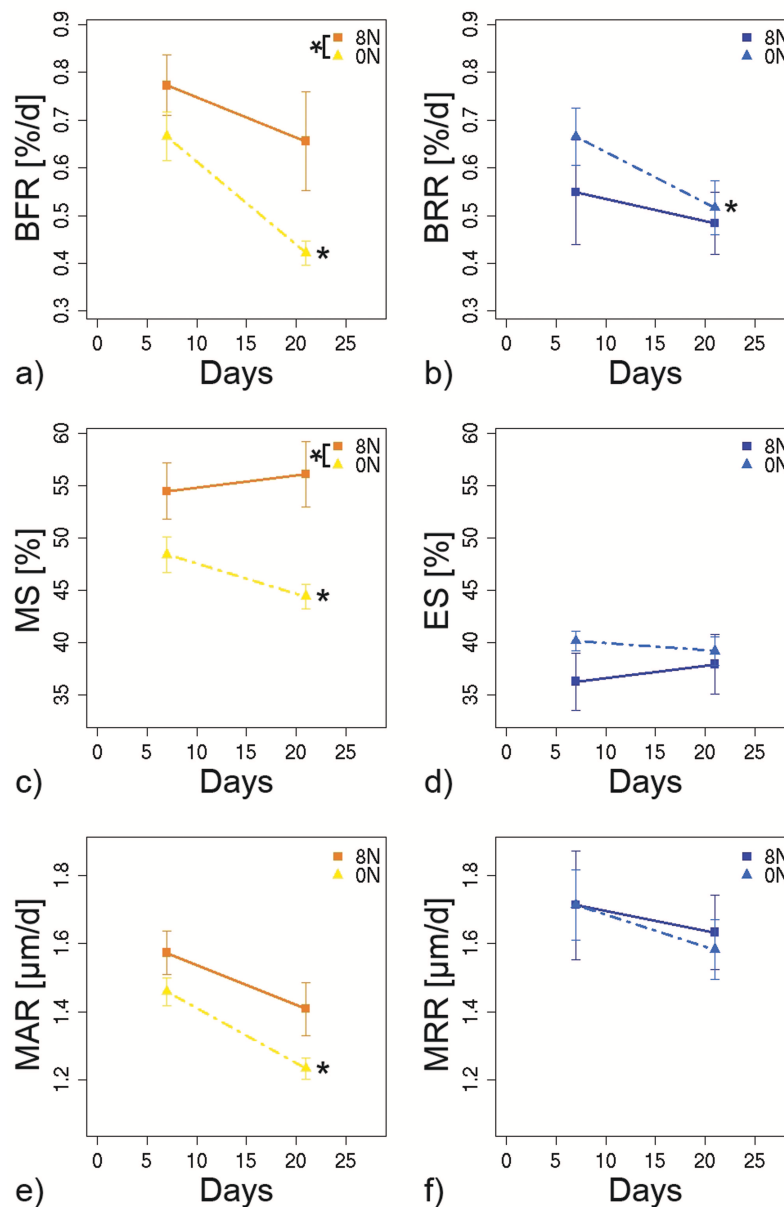


Figure 3.17: Changes in dynamic bone parameters over time. a) Bone formation rate (BFR), b) Bone resorption rate, c) Mineralizing surface (MS), d) Eroded surface (ES), e) Mineral apposition rate (MAR), f) Mineral resorption rate (MRR). Significant differences between groups or over time, as tested with repeated measures ANOVA, are shown with an asterisk.

Dynamic bone morphometry

Dynamic bone formation and resorption parameters were calculated by superimposing registered thresholded image data between week 0 and week 14, and between week 14 and week 28, and morphometrically analyzing them. BFR was significantly greater for the 8N group than for the 0N group ($p < 0.05$), with a significant decrease for the 0N group over time ($p < 0.01$, figure 3.17a). For the 0N group also BRR decreased significantly over time ($p < 0.05$). BRR tended to be lower for 8N

than 0N group, but this was not significant (figure 3.17b). Nevertheless, for the 8N group BFR was significantly (on average 1.4 times) greater than BRR ($p < 0.001$), while for the 0N group BFR and BRR were balanced and not significantly different. Figure 3.16d shows a cross-section of CV6 indicating bone formation and resorption sites between day 0 and 28. It is clear that for the 8N mouse there is greater bone formation (represented in yellow) and less bone resorption (represented in blue).

MS, the percent surface occupied by formation sites, was significantly greater for the 8N than 0N group ($p < 0.01$), with a significant decrease over time for the 0N group ($p < 0.05$, figure 3.17c). On average MS was 19% greater for the 8N group than 0N group. ES, the percent of the surface occupied by resorption sites, was not significantly different between groups (figure 3.17d). Still, for the 8N group, MS was significantly greater than ES ($p < 0.001$), while for the 0N group ES was significantly greater than MS ($p < 0.001$). MAR, the thickness of formation packets, decreased significantly for the 0N group ($p < 0.001$), but not 8N group. On average MAR was 11% greater for the 8N than 0N group, but this was not significantly different ($p = 0.050$, figure 3.17e). Also MRR, which describes the depth of resorption pits, was not significantly different between groups (figure 3.17f).

These results indicate that loading mainly had a positive effect on bone formation, by significantly increasing the surface of formation sites and slightly increasing the thickness of formation packets. There was a tendency that loading reduced bone resorption (by reducing the surface of resorption sites), while the depth of resorption pits remained the same, but this was not significant.

Reproducibility

FMT measurements were highly reproducible, with precision errors, expressed as coefficient of variation, ranging between 0.21% and 0.45% (table 3.6). Also the intra-class correlations, which ranged between 0.699 and 0.869, showed that the single animals could be reproducibly measured.

Fluorescence intensity

For all mice FI increased within 24 h after injection, i.e. on day 0, 14, and 28, while FI decreased in the following two weeks, i.e. between day 0 and 13, and between day 14 and 27 (figure 3.18a). Specifically, increases in FI were an effect of OsteoSense[®] 680 injection and its binding to bone remodeling sites, indicative of osteoblast activity. On the other hand, the decrease in FI was caused by resorption

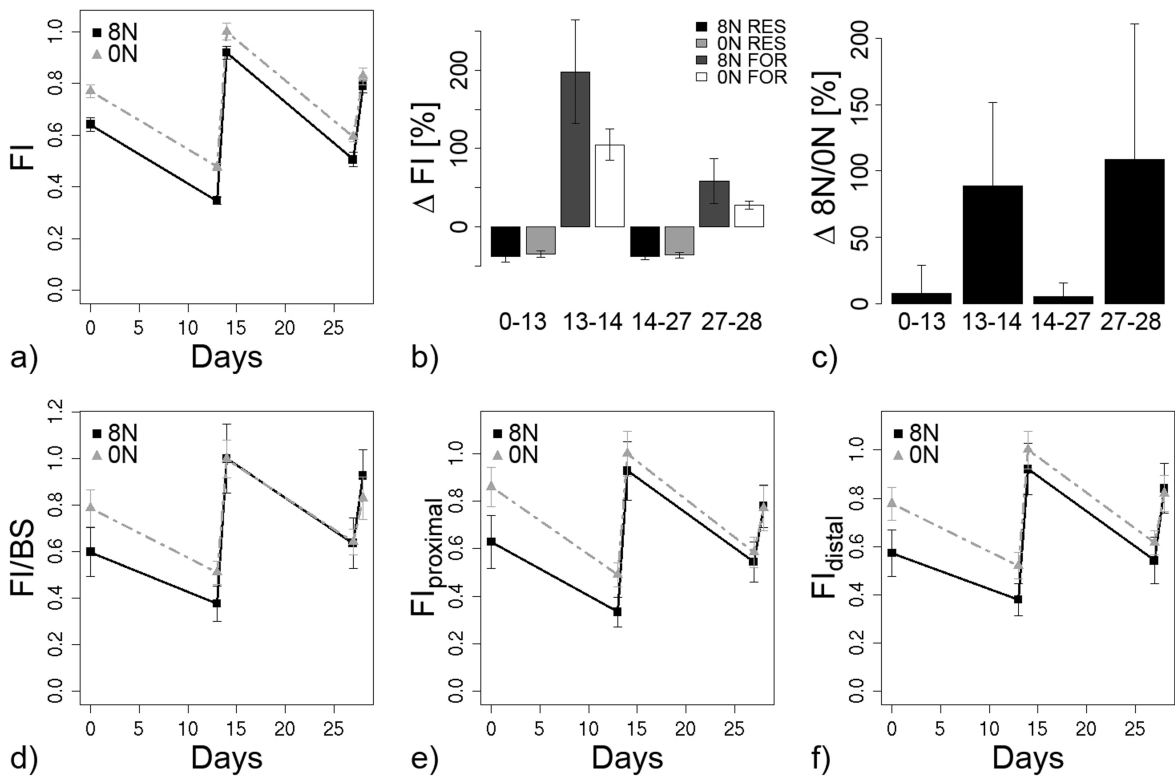


Figure 3.18: Changes in fluorescence intensity over time. a) Fluorescence intensity, b) Percentage differences in fluorescence intensity between time points, c) Percentage differences between time points normalized to the percentage difference of 0N. d) Fluorescence intensity divided by bone surface, e) Fluorescence intensity in proximal sub region, f) Fluorescence intensity in distal sub region. RES = decrease in FI, FOR = increase in FI.

of the OsteoSense[®] 680 labels, and indicative of osteoclast activity. No significant difference in FI was found between the 8N and 0N group. Nevertheless, there seemed to be a trend for a greater increase in FI after OsteoSense[®] 680 injection for the 8N than 0N group (figure 3.18b). The decrease in FI between day 0 and 13 and between day 14 and 27 was very similar for both groups. On the other hand, the increase in FI between day 13 and 14 was 89% greater for the 8N than 0N group, and the increase between day 27 and 28 109% greater (figure 3.18c). To determine FI per surface available for OsteoSense[®] 680 to bind, FI was divided by BS. There was a greater increase in FI between day 13 and 14 and between 27 and 28 for the 8N group than 0N group, but this was not significantly different (figure 3.18d). To further investigate the origin of the fluorescence signal, the region of interest was divided into 2 sub regions: a proximal, containing the loaded vertebra and both pinned vertebrae (figure 3.18e), and a distal region, containing approximately the eighth and ninth caudal vertebrae (figure 3.18f). It was expected that the proximal region would have a greater FI, because this included the loaded vertebra, however the contrary was true. Nevertheless, differences between 8N and 0N groups were

Table 3.6: Reproducibility of FMT measurements expressed as precision error of the standard deviation (PE_{SD}), coefficient of variation ($PE_{\%CV}$) and intra-class correlations (ICC). Also the 95% confidence intervals for the ($PE_{\%CV}$) are shown.

Time	Mean	PE_{SD}	$PE_{\%CV}$ (%)	$CI_{95\%} PE_{\%CV}$	ICC
0	5.55E-04	7.38E-05	0.31%	0.24% - 0.42%	0.869
13	3.52E-04	4.75E-05	0.25%	0.19% - 0.34%	0.852
14	7.60E-04	1.18E-04	0.41%	0.32% - 0.56%	0.699
27	4.82E-04	5.04E-05	0.21%	0.17% - 0.29%	0.873
28	6.47E-04	7.81E-05	0.30%	0.24% - 0.41%	0.852

more pronounced in the proximal region, but still not significantly different.

Accuracy

Correlations between dynamic formation and resorption parameters and percentage change in FI were performed to investigate the accuracy of FMT measurements. The decrease in FI between day 0 and 13, as an effect of osteoclast activity, was significantly related to BRR ($R = 0.81$) and MRR ($R = 0.8$), with the general rule: the larger the resorption rates the greater the decrease in FI (figure 3.19). Also, a greater ES seemed related to a greater decrease in FI ($R = 0.43$), but this was not significantly correlated. Correlations between increase in FI and dynamic formation parameters were not significant. To determine whether fluorescence intensity was related to the initial bone microstructure, correlations between initial bone microstructure and initial fluorescence intensity were performed. The correlations between fluorescence intensity and BS or AVD were not significant.

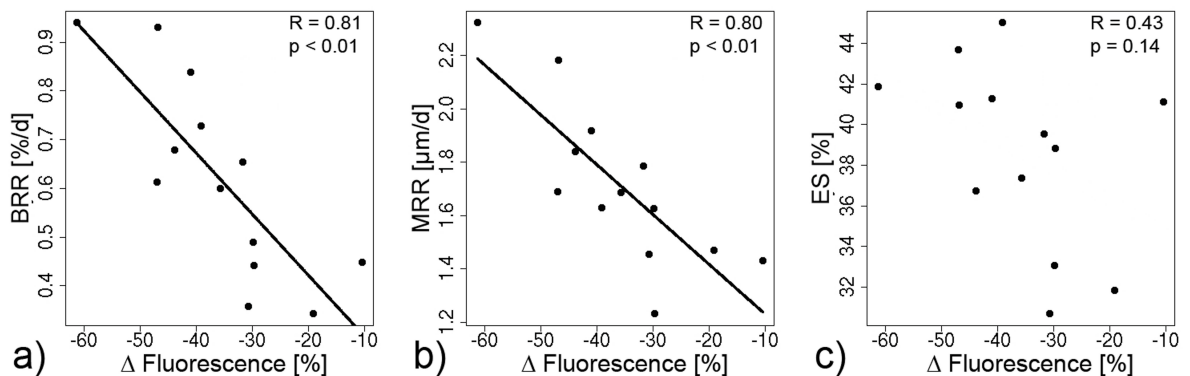


Figure 3.19: Correlations between dynamic resorption parameters and decrease in fluorescence intensity between day 0 and 13. a) BRR, b) MRR, c) ES.

3.4.4 Discussion

In this study, a longitudinal *in vivo* imaging approach of osteoblast and osteoclast activity using fluorescence molecular tomography (FMT) was established. Furthermore, multimodality imaging was used to monitor load-induced bone adaptation. It was found that the combination of *in vivo* micro-CT and FMT is feasible, and can be performed reproducibly at multiple time points throughout a study to gain information about changes in bone microstructure and also in the underlying osteoblast and osteoclast activity. *In vivo* micro-CT had the advantage of monitoring changes in the bone microstructure and dynamic bone parameters, which gave insight in the outcomes of remodeling activity. FMT had the advantage of imaging osteoblast activity more directly than micro-CT and enabled inferring on osteoclast activity. The osteoblast activity was measured accurately in a time span of 24 h, while the osteoclast activity was calculated similar to calculation of BRR from the micro-CT data. In agreement, good correlations between bone resorption rates as determined from micro-CT, and osteoclast activity as determined from a loss in the reconstructed fluorophore concentration between time points using FMT, was found. The correlations between bone formation rates and osteoblast activity were not significant, probably as an effect of the difference in time frame between measures. Nevertheless, this underpins that FMT constitutes a complimentary technique for measuring osteoblast activity.

An extension of this study compared to previous studies, was that the animals were monitored over time, and measured at multiple time points with FMT. With FMT and OsteoSense[®] 680, osteoblast activity could be measured accurately over a time span of 24 h at multiple time points. This is different in comparison to histology, where there should be about 4-7 days between administration of different labels, a time frame that cannot be extended unlimitedly, as the label would be resorbed. Also the FMT readout is faster when compared to the assessment of dynamic parameters from micro-CT scans, for which a difference of 7 days between scans is considered optimal. Thus, in a study where instant osteoblast activity should be measured at several time points, FMT measurements appear very useful, quick (about 5 minutes per measurement) and can be used as a complementary technique. The principal advantage of the tomographic information provided by FMT is quantitative analysis of the fluorescence signal, providing a reliable measure of osteoblast and osteoclast activity. This is an extension to planar fluorescence imaging, where possibilities for quantitative analysis are limited.

In agreement with previous *in vivo* loading studies [1, 21–24], mice, in which a bone was loaded, had an increased bone formation rate and a decreased bone resorption rate compared to control mice, with a greater effect on bone formation. This was observed from both dynamic parameters and FMT measurements. While a significant difference in BFR was found between groups, the difference in osteoblast activity as derived from FMT measurements did not reach significance. One explanation could be that OsteoSense[®] 680 was injected 24 h before measurement, and thus also 24 h before loading was applied (and also 24 h after loading for the second and third OsteoSense[®] 680 injection). It is conceivable that a stimulus on the bone formation rate is already reduced 24 h after loading, which might diminish the effect of loading on osteoblast activity, rendering the difference between loaded and control group not significant. Injections of OsteoSense[®] 680 right before loading might enhance the sensitivity of FMT. Alternatively, one might argue that the time frame over which BFR was calculated included 14 days resulting in a cumulative effect of multiple remodeling sites. On the other hand, fluorescent based measurements of osteoblast activity occurred over a 24 h time frame only, which was maybe not long enough to pick up the difference. Another reason could be that for the calculation of BFR, only CV6 was analyzed, while osteoblast activity with FMT was calculated from a region of interest that included approximately the fifth through the ninth caudal vertebra, which likely obscured the fluorescence intensity of the loaded vertebra. Additionally, multiple injections often result in more non-specific binding of the probe, leading to autofluorescence, which reduces the sensitivity.

A surprising observation was that the bone adaptation response in the trabecular bone was about half the response we found in previous studies where loading was applied to CV6 (data not shown). This might have been an effect of OsteoSense[®] 680, as bisphosphonates are known to reduce bone turnover, and may therefore interfere with the response to loading. However, this explanation appears unlikely in view of the fact that the amount of OsteoSense[®] 680 injected corresponds to less than 1% of the therapeutic dose. If it were to have an effect, one would expect bone to become more mineralized, as with bisphosphonates bone resorption is slowed down. Nevertheless, the increase in TMD for both groups was in the same range as in mice of the same age without OsteoSense[®] 680 injection (data not shown). Also, it has recently been shown that OsteoSense[®] 680 does not interfere with normal bisphosphonate binding [25], indicating that also the loading response should not be arrested. Furthermore, in a pilot study where mice were

injected only once with OsteoSense[®] 680 normal, load adaptation in the same range as in previous studies was found [7]. Thus it remains unclear why the mice in this study did not respond as actively to loading.

The most serious limitation of FMT is the low spatial resolution, on the order of 1 mm; therefore it is difficult to exactly determine the accurate location from which the fluorescence signal originates. Also, it is not possible to measure only the loaded/control vertebra, because this would limit the excitation pattern to too few grid sources (points where the laser excites the ROI), which would compromise the quality of data reconstruction and thus for quantification of the fluorescence signal. A further consideration of longitudinal FMT measurements with OsteoSense[®] 680 is that the probe remains bound to the bone for a long time, which might reduce the signal to background ratio in subsequent studies. Therefore, background images have to be collected prior to each OsteoSense[®] 680 injection. On the positive side: analyzing the background intensity allows estimating osteoclast activity. Also, bound probe molecules will inhibit the label binding at follow-up injections: the fact that the increase in fluorescence intensity (I) following OsteoSense[®] 680 administration decreased in the order day -1/0 < day 13/14 ($\Delta FI_{day13/14}/\Delta FI_{day0} = 85\%$) < day 27/28 ($\Delta FI_{day27/28}/\Delta FI_{day0} = 35\%$) may indicate that the additional binding of the probe is reduced. Nevertheless, osteoblast related fluorescence increase might also depend on the time between probe injections. At a shorter time frame it might be that the locations of the bone remodeling units remain largely unchanged, leaving fewer surfaces for the label to bind. Over a longer time frame, the bone remodeling units may affect larger spatial domains offering additional surface binding sites. Also BFR and BRR as calculated from micro-CT data reduced over time (for the 0N group), which indicates reduced bone turnover. Thus, whether the increase in fluorescence signal was caused by a slowdown in the bone metabolism, or by inhibition of further binding of the probe, cannot be distinguished.

Several recent studies have shown the advantage of registering CT and FMT imaging modalities [26–29]. In this study, FMT and micro-CT images were not registered due to the large difference in spatial resolution provided by the two modalities: the resolution of the FMT measurement is approximately 1 mm, compared to 10.5 μm for micro-CT. Thus one FMT voxel would include about 10^6 micro-CT voxels. Also, only the loaded vertebra was scanned with micro-CT. Scanning of the adjacent vertebrae would have been a challenge, because the metallic pins in the fifth and seventh caudal vertebrae would have caused significant

image artifacts when included in the volume of interest. Moreover, the image acquisition time would become very long (on the order of hours) and yielded large data sets (approximately 20 GB). The length of the measurement and size of the image data could have been overcome by scanning at a lower resolution, but in that case it would not have been possible to resolve the trabecular structure.

To monitor osteoclast activity over time, biochemical markers of bone resorption (e.g. collagen telopeptides) can be sampled from blood or urine and analyzed. Nevertheless, these readouts are systemic, and cannot be used to determine local osteoclast activity. Recently, a fluorescent probe has been developed that allows to monitor osteoclast activity *in vivo*, by probing cathepsin K activity, which is a protease associated with collagen degradation and osteoclast activity [30]. This probe is, however, not commercially available. The procedure described in this study to estimate osteoclast activity is less direct, but was shown to be accurate, and can be implemented from a commercially available probe.

In conclusion, we have shown the advantage of performing complementary FMT and micro-CT measurements: the combination providing anatomical and dynamic information from *in vivo* micro-CT and molecular readouts on cell activity from FMT is promising for further research in orthopedics where the relation between osteoblast activity, osteoclast activity and bone microstructure should be investigated.

3.4.5 Acknowledgement

The authors gratefully acknowledge funding from the European Union for the Osteoporotic Virtual Physiological Human project (VPHOP FP7-ICT2008-223865). We thank Dr. Michaela Kneissel, Head of Bone Metabolism Research in the Musculoskeletal Disease Area at Novartis for support and time to show how planar fluorescence measurements were performed at their lab. We thank Katerina Dikaiou for support with the FMT measurements.

References

- [1] T.J. Chambers, M. Evans, T.N. Gardner, A. Turner-Smith, and J.W. Chow. Induction of bone formation in rat tail vertebrae by mechanical loading. *Bone Miner*, 20(2):167–178, 1993.

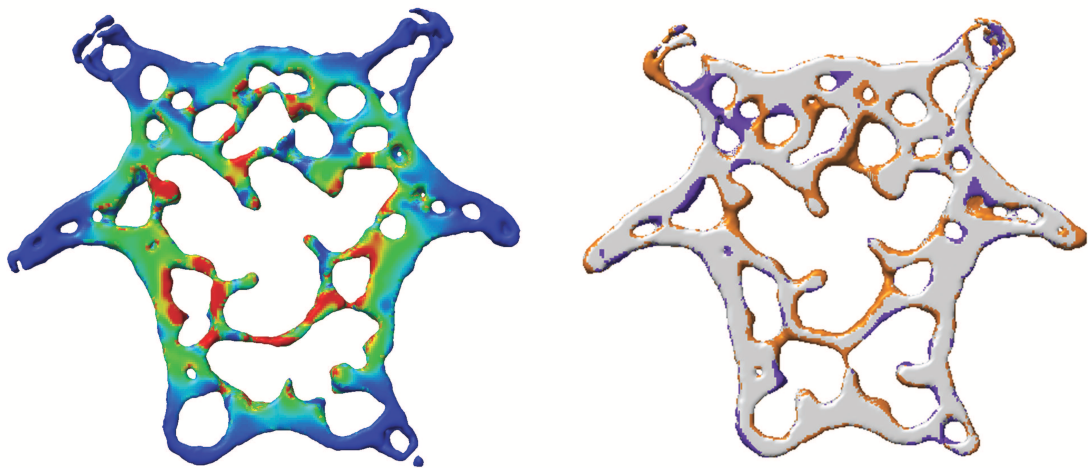
- [2] Webster D.J., Morley P.L., van Lenthe G.H., and Müller R. A novel in vivo mouse model for mechanically stimulated bone adaptation—a combined experimental and computational validation study. *Comput Methods Biomech Biomed Engin*, 11(5):435–441, 2008.
- [3] T.S. Gross, S. Srinivasan, C.C. Liu, T.L. Clemens, and S.D. Bain. Noninvasive loading of the murine tibia: an in vivo model for the study of mechanotransduction. *J Bone Miner Res*, 17(3):493–501, 2002.
- [4] A. Moustafa, T. Sugiyama, L.K. Saxon, G. Zaman, A. Sunters, V.J. Armstrong, B. Javaheri, L.E. Lanyon, and J.S. Price. The mouse fibula as a suitable bone for the study of functional adaptation to mechanical loading. *Bone*, 44(5):930–935, 2009.
- [5] M.C.H. van der Meulen, X. Yang, T.G. Morgan, and M.P.G. Bostrom. Bone remodelling algorithms incorporating both strain and microdamage stimuli. *Clin Orthop Relat Res*, 467(8):1381–1391, 2009.
- [6] A.G. Robling, D.B. Burr, and C.H. Turner. Partitioning a daily mechanical stimulus into discrete loading bouts improves the osteogenic response to loading. *J Bone Miner Res*, 15(8):1596–1602, 2000.
- [7] F.M. Lambers, F.A. Schulte, G. Kuhn, D.J. Webster, and R. Müller. Mouse tail vertebrae adapt to cyclic mechanical loading by increasing bone formation rate and decreasing bone resorption rate as shown by time-lapsed *in vivo* imaging of dynamic bone morphometry. *Bone*, accepted, 2011.
- [8] A. Zaheer, R.E. Lenkinski, A. Mahmood, A.G. Jones, L.C. Cantley, and J.V. Frangioni. In vivo near-infrared fluorescence imaging of osteoblastic activity. *Nat Biotechnol*, 19(12):1148–1154, 2001.
- [9] E.E. Graves, D. Yessayan, G. Turner, R. Weissleder, and V. Ntziachristos. Validation of in vivo fluorochrome concentrations measured using fluorescence molecular tomography. *J Biomed Opt*, 10(4):44019, 2005.
- [10] V. Ntziachristos, C. Bremer, E.E. Graves, J. Ripoll, and R. Weissleder. In vivo tomographic imaging of near-infrared fluorescent probes. *Mol Imaging*, 1(2):82–88, 2002.
- [11] A. Martin, J. Aguirre, A. Sarasa-Renedo, D. Tsoukatou, A. Garofalakis, H. Meyer, C. Mamalaki, J. Ripoll, and A. M. Planas. Imaging changes in

- lymphoid organs *in vivo* after brain ischemia with three-dimensional fluorescence molecular tomography in transgenic mice expressing green fluorescent protein in t lymphocytes. *Mol Imaging*, 7(4):157–167, 2008.
- [12] P. Thevenaz, U.E. Ruttimann, and M. Unser. A pyramid approach to subpixel registration based on intensity. *IEEE Trans Image Process*, 7(1):27–41, 1998.
- [13] F.A. Schulte, F.M. Lambers, G. Kuhn, and R. Müller. *In vivo* micro-computed tomography allows direct three-dimensional quantification of both bone formation and bone resorption parameters using time-lapsed imaging. *Bone*, 48:433–442, 2011.
- [14] F. Stuker. *Hybrid Imaging: Combining Fluorescence Molecular Tomography with Magnetic Resonance Imaging*. DISS. ETH NO. 19664, 2011.
- [15] C. C. Gluer, G. Blake, Y. Lu, B. A. Blunt, M. Jergas, and H. K. Genant. Accurate assessment of precision errors: how to measure the reproducibility of bone densitometry techniques. *Osteoporos Int*, 5(4):262–270, 1995.
- [16] T. L. Mueller, M. Stauber, T. Kohler, F. Eckstein, R. Müller, and G. H. van Lenthe. Non-invasive bone competence analysis by high-resolution pQCT: an *in vitro* reproducibility study on structural and mechanical properties at the human radius. *Bone*, 44(2):364–371, 2009.
- [17] T. Kohler, M. Beyeler, D. Webster, and R. Müller. Compartmental bone morphometry in the mouse femur: reproducibility and resolution dependence of microtomographic measurements. *Calcif Tissue Int*, 77(5):281–290, 2005.
- [18] V. Ntziachristos and R. Weissleder. Experimental three-dimensional fluorescence reconstruction of diffuse media by use of a normalized Born approximation. *Opt Lett*, 26(12):893–895, 2001.
- [19] J. Ripoll and V. Ntziachristos. Imaging scattering media from a distance: theory and applications of noncontact optical tomography. *Modern Physics Letters B*, 18(28-29):1403–1431, 2004.
- [20] R Development Core Team. R: A Language and Environment for Statistical Computing. *R Foundation for Statistical Computing, Vienna, Austria*, 2010.
- [21] D. Webster, E. Wasserman, M. Ehrbar, F. Weber, I. Bab, and R. Müller. Mechanical loading of mouse caudal vertebrae increases trabecular and cortical bone mass-dependence on dose and genotype. *Biomech Model Mechanobiol*, 9(6):737–747, 2010.

- [22] S.W. Fox, T.J. Chambers, and J.W. Chow. Nitric oxide is an early mediator of the increase in bone formation by mechanical stimulation. *Am J Physiol*, 270(6 Pt 1):E955–E960, 1996.
- [23] J.M. Lean, C.J. Jagger, T.J. Chambers, and J.W. Chow. Increased insulin-like growth factor I mRNA expression in rat osteocytes in response to mechanical stimulation. *Am J Physiol*, 268(2 Pt 1):E318–E327, 1995.
- [24] J.W. Chow, C.J. Jagger, and T.J. Chambers. Characterization of osteogenic response to mechanical stimulation in cancellous bone of rat caudal vertebrae. *Am J Physiol*, 265(2 Pt 1):E340–E347, 1993.
- [25] K. M. Kozloff, L. I. Volakis, J. C. Marini, and M. S. Caird. Near-infrared fluorescent probe traces bisphosphonate delivery and retention in vivo. *J Bone Miner Res*, 25(8):1748–1758, 2010.
- [26] M. Nahrendorf, P. Waterman, G. Thurber, K. Groves, M. Rajopadhye, P. Panizzi, B. Marinelli, E. Aikawa, M.J. Pittet, F.K. Swirski, and R. Weissleder. Hybrid in vivo fnt-ct imaging of protease activity in atherosclerosis with customized nanosensors. *Arterioscler Thromb Vasc Biol*, 29(10):1444–1451, 2009.
- [27] X. Guo, X. Liu, X. Wang, F. Tian, F. Liu, B. Zhang, G. Hu, and J. Bai. A combined fluorescence and microcomputed tomography system for small animal imaging. *IEEE Trans Biomed Eng*, 57(12):2876–2883, 2010.
- [28] R.B. Schulz, A. Ale, A. Sarantopoulos, M. Freyer, E. Soehngen, M. Zientkowska, and V. Ntziachristos. Hybrid system for simultaneous fluorescence and x-ray computed tomography. *IEEE Trans Med Imaging*, 29(2):465–473, 2010.
- [29] X. Zhang, C.T. Badea, and G.A. Johnson. Three-dimensional reconstruction in free-space whole-body fluorescence tomography of mice using optically reconstructed surface and atlas anatomy. *J Biomed Opt*, 14(6):064010, 2009.
- [30] K.M. Kozloff, L. Quinti, S. Patntirapong, P.V. Hauschka, C.H. Tung, R. Weissleder, and U. Mahmood. Non-invasive optical detection of cathepsin K-mediated fluorescence reveals osteoclast activity in vitro and in vivo. *Bone*, 44(2):190–198, 2009.

Chapter 4

Functional bone imaging in an *in vivo* mouse model of aging and disease



4.1 Transient bone morphometry in a mouse tail model of postmenopausal osteoporosis

Floor M. Lambers¹, Gisela Kuhn¹, Friederike A. Schulte¹, Kathleen Koch¹, and Ralph Müller¹

¹Institute for Biomechanics, ETH Zürich, Zürich, Switzerland

Abstract:

Recently, it has been shown that transient bone biology can be observed *in vivo* using time-lapsed micro-computed tomography (micro-CT) in the mouse tail bone. Nevertheless, in order for the mouse tail bone to be a model for human disease, the hallmarks of any disease must be mimicked by this model. The aim of this study was to investigate whether postmenopausal osteoporosis could be modeled in caudal vertebrae of C57BL/6J mice, considering static and dynamic bone morphometry as well as mechanical properties, and to describe temporal changes in bone remodeling rates. Twenty C57BL/6J mice were ovariectomized (OVX, n=11) or sham operated (SHM, n=9) and monitored with *in vivo* micro-CT on the day of surgery and every two weeks after, up to 12 weeks. There was a significant decrease in bone volume fraction for OVX (-35%) compared to SHM (+16%) in the trabecular bone (p<0.001). For OVX, high turnover bone loss was observed with bone resorption rate exceeding bone formation rate (p<0.001). Furthermore there was a significant decrease in whole bone strength for OVX (-18%) compared to SHM (+13%, p<0.001). From these results we conclude that the mouse tail vertebra mimics postmenopausal bone loss with respect to these parameters and therefore might be a suitable model for postmenopausal osteoporosis. When evaluating temporal changes in remodeling rates it was found that OVX caused an immediate increase in bone resorption rate (p < 0.001) and a delayed increase in bone formation rate (p<0.001). Monitoring transient bone biology is a promising method for future research.

Keywords:

Bone resorption, osteoporosis, ovariectomy, *in vivo* micro computed tomography, high turnover

4.1.1 Introduction

Osteoporosis, the most common bone disease, has become a major health problem worldwide [1]. Preclinical studies using animal models that approximate the progression of (postmenopausal) osteoporosis in humans are essential for the development of safer and more effective prevention and treatment of osteoporosis [2]. Removal of the ovaries (ovariectomy) in rats is a well-established model in postmenopausal osteoporosis research [3, 4]. Ovariectomy leads to estrogen depletion, which in turn causes bone loss. With this technique, osteoporosis-related bone loss has often been investigated in the proximal tibia of rats [5, 6]. A smaller effect of ovariectomy-induced bone loss has been seen in the distal tibia [7, 8] and lumbar vertebra [9], while no bone loss has been observed in caudal (tail) vertebrae of rats [10, 11].

In the past decade ovariectomy of mice has emerged as a model for osteoporosis, because mouse models have several advantages over rat models. The accessibility of the mouse genome facilitates gene identification and deletion for the study of modifying molecular mechanisms of osteoporosis [12]. Also the costs are lower due to cheaper housing of mice and smaller amounts of drugs that are needed for mice. Furthermore by using an inbred strain, the mice are all genetically identical, leading to high reproducibility and the ability to replicate experiments [12]. In mice the most frequently investigated site is the distal femur, where large amounts of bone loss occur after ovariectomy [13, 14]. At other sites there are some conflicting results. Nevertheless, in mice, ovariectomy-induced bone loss is strain- and skeletal-site-dependent [15–18].

Recently, it has been shown that transient bone biology can be observed *in vivo* using time-lapsed micro-computed tomography (micro-CT) in the mouse tail bone. Nevertheless, in order for the mouse tail bone to be a model for human disease, the hallmarks of any disease must be mimicked by this model. To our knowledge, ovariectomy-induced bone loss has not been investigated in caudal vertebrae of mice. However, it would be very convenient if, instead of the distal femur, a caudal vertebra could be used as an osteoporosis model, because this would have several advantages: (1) it is more easily accessible for high resolution imaging, (2) the whole bone can be imaged within an acceptable scan time and dose, (3) both cortical and trabecular bone can be imaged, (4) the amount of trabecular bone is relatively high in vertebrae, (5) the caudal vertebrae are non-weight-bearing, thus less dependent on rodent activity, and (6) it is accessible for mechanical loading [19].

In order to have a valid postmenopausal osteoporosis model, several main requirements have to be fulfilled [2,3]. First, there should be a large amount of bone loss, as women can lose up to 20% of their bone mass in the first 5-7 years that follow menopause [20]. Second, the model should demonstrate high turnover bone loss, as typically postmenopausal bone deterioration progresses by an increased bone formation rate, and an increased bone resorption rate, with bone resorption exceeding bone formation [21]. Third, as a result of the bone loss, fragility fractures should be present in the bone. Fragility fractures are uncommon in rodents [22], but the strength of the bone must decrease. Therefore, it has been established that bone strength can be assessed with mechanical testing [23,24] or finite element analysis [25] as a surrogate for bone fragility.

We hypothesized ovariectomy would induce bone loss in caudal vertebrae of C57Bl/6J mice, since this vertebra was shown to increase bone mass upon cyclic loading [19], and thus seemed responsive to interventions. Furthermore, when osteoporosis related bone loss was evaluated in caudal vertebrae of SAMP6 mice, a senescence-accelerated mouse strain, the bone mass at 4 and 12 months of age was significantly lower than in controls [26]. To investigate whether the above mentioned requirements were achieved for caudal vertebrae of C57Bl/6J mice, several methods were used. First, to monitor the extent of bone loss and changes in the bone microstructure after ovariectomy, the sixth caudal vertebra was scanned with *in vivo* micro-computed tomography (micro-CT) at multiple time points. Second, to investigate the presence of high turnover bone loss, bone dynamic morphometry parameters were calculated with a recently validated *in vivo* technique [27]. This technique allows the quantification of dynamic bone formation and resorption parameters in 3D over time from serial micro-CT scans. Third, to investigate changes in strength of the bones, micro-finite element (μ FE) analysis was performed.

Previous reports have described temporal patterns in the bone microstructure or mineralization as an effect of ovariectomy in rats or mice. Nevertheless, to better understand how ovariectomy influences osteoblast and osteoclast activity, the transient patterns of bone remodeling rates should be described as well. Little attention has been given to this as until recently it was challenging to determine how bone remodeling rates change over time using histomorphometry (loss of label) or biochemical markers (not site specific). The recently validated *in vivo* technique to extract dynamic bone morphometry parameters from serial *in vivo*

micro-CT scans [27], on the other hand, allows to investigate temporal changes in remodeling rates, giving an accurate indication how formation and resorption sites are modulated by ovariectomy. This information is essential for gaining a better understanding of ovariectomy-induced bone loss.

Summarized, the aim of this study was to investigate whether caudal vertebrae of C57BL/6J mice are a valid model for postmenopausal osteoporosis, taking into account the bone microstructure, dynamic morphometry parameters and mechanical properties. A further objective was to provide a more detailed description of temporal patterns in dynamic bone remodeling rates induced by ovariectomy.

4.1.2 Methods

Animals

Twenty 14-week-old female C57BL/6J mice (RCC Ltd, Füllinsdorf, Switzerland) were housed in an environmentally controlled room at a 12-hour light/dark cycle, with free access to standard diet and tap water. After one week of settling the mice were ovariectomized bilaterally (OVX, n=11) or sham-operated (SHM, n=9). The analgesic buprenorphin (Temgesic, 0.1 mg/kg) was injected twice daily on the day of surgery and for the following 2 days to avoid pain. The mice were monitored closely and weighed 3-4 times per week in the first two weeks post-operation and before each micro-CT scan thereafter. All procedures were performed under isoflurane anaesthesia (2-2.5%, 0.4 L/min) delivered through a nose mask. All experimental procedures were approved by the local laboratory animal care and use committee (Kantonales Veterinäramt Zürich, Zürich, Switzerland).

In vivo micro-computed tomography

Descriptions and nomenclature in the following sections are in line with a recent review on guidelines for the assessment of bone microstructure with micro-CT [28]. The sixth caudal vertebra (CV6) was scanned with *in vivo* micro-CT (vivaCT 40, Scanco Medical AG, Brüttisellen, Switzerland), on the day of surgery and consecutively every two weeks for 12 weeks, resulting in a total of 7 images per mouse. The mice were scanned under isoflurane anaesthesia in a holder heated at just below body temperature (35°C). Vitamine A cream was applied to the eyes to prevent desiccation. The region of interest was selected by counting the vertebrae from the first caudal vertebra (at the sacrum) in a dorso-ventrally taken scoutview. CV6 was measured completely in two connecting stacks, comprising a length of 4.4 mm. The

Table 4.1: Bone structural parameters in the trabecular and cortical bone at all time points for both groups. P-value denotes significant difference between groups as tested with repeated measurements ANOVA. SE = standard error.

Trabecular		Week 0	Week 2	Week 4	Week 6	Week 8	Week 10	Week 12	Pval
Tb.TV [mm ³]	OVX	1.91 ± 0.16	1.98 ± 0.15	2.05 ± 0.15	2.15 ± 0.17	2.20 ± 0.19	2.20 ± 0.18	2.24 ± 0.20	<0.001
	SHM	2.11 ± 0.30	2.12 ± 0.30	2.12 ± 0.29	2.11 ± 0.30	2.12 ± 0.29	2.12 ± 0.30	2.13 ± 0.30	
BV/TV [%]	OVX	22.1 ± 2.4	23.7 ± 2.4	21.5 ± 2.3	17.9 ± 2.3	15.7 ± 2.0	14.5 ± 1.9	14.4 ± 1.7	<0.001
	SHM	19.9 ± 3.6	20.9 ± 3.1	21.4 ± 3.2	22.0 ± 3.2	22.4 ± 3.1	22.6 ± 3.0	22.8 ± 3.1	
BS/BV [mm ² /mm ³]	OVX	32.1 ± 2.1	30.7 ± 1.8	33.2 ± 2.2	37.6 ± 3.1	39.6 ± 3.0	40.1 ± 3.0	39.7 ± 2.3	<0.001
	SHM	34.6 ± 5.7	33.2 ± 4.9	32.5 ± 5.0	32.0 ± 4.9	31.6 ± 4.7	31.3 ± 4.6	31.1 ± 4.5	
SMI [1]	OVX	0.276 ± 0.240	0.129 ± 0.250	0.379 ± 0.180	0.755 ± 0.210	0.958 ± 0.200	1.138 ± 0.280	1.034 ± 0.140	0.3731
	SHM	0.504 ± 0.380	0.364 ± 0.350	0.286 ± 0.350	0.241 ± 0.330	0.179 ± 0.340	0.139 ± 0.320	0.124 ± 0.300	
Tb.Th [mm]	OVX	0.0790 ± 0.0000	0.0820 ± 0.0000	0.0780 ± 0.0000	0.0720 ± 0.0000	0.0700 ± 0.0000	0.0690 ± 0.0000	0.0700 ± 0.0000	<0.001
	SHM	0.0760 ± 0.0100	0.0780 ± 0.0100	0.0790 ± 0.0100	0.0790 ± 0.0100	0.0800 ± 0.0100	0.0800 ± 0.0100	0.0800 ± 0.0100	
Tb.Sp [mm]	OVX	0.281 ± 0.020	0.275 ± 0.020	0.278 ± 0.020	0.286 ± 0.030	0.300 ± 0.030	0.314 ± 0.030	0.324 ± 0.030	<0.001
	SHM	0.288 ± 0.020	0.287 ± 0.020	0.287 ± 0.020	0.283 ± 0.020	0.282 ± 0.020	0.282 ± 0.020	0.281 ± 0.020	
Tb.N [1/mm]	OVX	3.21 ± 0.19	3.26 ± 0.19	3.23 ± 0.23	3.17 ± 0.24	3.06 ± 0.24	2.95 ± 0.27	2.87 ± 0.23	<0.001
	SHM	3.15 ± 0.25	3.13 ± 0.24	3.12 ± 0.22	3.13 ± 0.24	3.15 ± 0.21	3.14 ± 0.22	3.14 ± 0.22	
Conn.D [1/mm ³]	OVX	63.2 ± 12.0	63.0 ± 10.9	59.6 ± 8.0	58.8 ± 10.4	51.5 ± 11.3	47.6 ± 13.3	44.6 ± 9.7	0.3159
	SHM	59.4 ± 9.7	57.4 ± 11.8	55.2 ± 9.5	55.3 ± 10.6	54.4 ± 9.6	51.8 ± 11.4	52.5 ± 10.1	
Cortical		Week 0	Week 2	Week 4	Week 6	Week 8	Week 10	Week 12	Pval
Ct.TV [mm ³]	OVX	5.22 ± 0.38	5.39 ± 0.35	5.46 ± 0.36	5.54 ± 0.34	5.55 ± 0.37	5.54 ± 0.35	5.60 ± 0.37	<0.001
	SHM	5.44 ± 0.39	5.47 ± 0.39	5.49 ± 0.40	5.50 ± 0.40	5.52 ± 0.40	5.54 ± 0.41	5.55 ± 0.41	
Ct.MV [mm ³]	OVX	2.92 ± 0.26	3.02 ± 0.24	3.11 ± 0.24	3.25 ± 0.26	3.30 ± 0.28	3.30 ± 0.27	3.35 ± 0.30	<0.001
	SHM	3.21 ± 0.42	3.22 ± 0.42	3.21 ± 0.41	3.21 ± 0.42	3.22 ± 0.41	3.22 ± 0.43	3.23 ± 0.43	
Ct.Ar/Tt.Ar [%]	OVX	44.2 ± 1.8	44.0 ± 1.7	43.1 ± 1.5	41.5 ± 1.8	40.7 ± 1.8	40.6 ± 1.9	40.2 ± 2.1	<0.001
	SHM	41.0 ± 4.7	41.3 ± 4.6	41.7 ± 4.4	41.8 ± 4.5	41.9 ± 4.4	42.1 ± 4.5	42.1 ± 4.4	
Ct.Th [mm]	OVX	0.161 ± 0.010	0.161 ± 0.010	0.160 ± 0.010	0.158 ± 0.010	0.156 ± 0.010	0.156 ± 0.010	0.154 ± 0.010	<0.001
	SHM	0.152 ± 0.010	0.154 ± 0.010	0.155 ± 0.010	0.156 ± 0.010	0.156 ± 0.010	0.157 ± 0.010	0.156 ± 0.010	
Tt.Ar [mm ²]	OVX	497 ± 36	513 ± 33	520 ± 34	528 ± 32	529 ± 35	528 ± 33	533 ± 35	<0.001
	SHM	518 ± 37	521 ± 37	523 ± 38	523 ± 38	525 ± 38	528 ± 39	529 ± 39	
Ct.Ar [mm ²]	OVX	220 ± 15	226 ± 14	224 ± 14	219 ± 12	215 ± 13	214 ± 14	214 ± 13	<0.05
	SHM	211 ± 22	214 ± 21	217 ± 20	218 ± 21	219 ± 21	221 ± 21	221 ± 20	

scanner was operated at 55 kVp and 145 μ A, with an integration time of 200 ms, and no frame averaging. 1000 projections were captured per 180 degrees, leading to a nominal isotropic resolution of 10.5 μ m. A beam hardening correction algorithm provided by Scanco Medical AG was applied to all scans. The estimated dose rate was 32 mGy/min over a period of 20 minutes. The CT scanner was calibrated weekly for mineral equivalent value and monthly for determining in-plane spatial resolution. All raw micro-CT data were reconstructed with the dorsal side of the vertebra facing upwards. For the basal scan, the long axis of the bone was aligned with the z-axis, to facilitate the conversion of the micro-CT data into micro-finite element (μ FE) models. The follow-up scans were translated and rotated to match the previous measurement using rigid registration. A 3D constrained Gaussian filter (sigma 1.2, support 1) was applied, after which images were segmented by a fixed thresholding procedure (22% of maximum grayscale value).

Static bone morphometry

The trabecular and cortical regions were selected from the thresholded images by automated masks. For the trabecular mask, the growth plates were eliminated (top and bottom 10%) and the space almost void of trabecular bone (the middle 26%) was excluded from the analysis. Within the regions of interest, the bone structural parameters were calculated with a direct 3D model-independent algorithm, including total volume (Tb.TV), bone volume fraction (BV/TV), specific bone surface (BS/BV), structure model index (SMI), trabecular thickness (Tb.Th), trabecular separation (Tb.Sp), trabecular number (Tb.N), and connectivity density (Conn.D).

For the calculation of cortical bone, morphometrical indices the trabecular structure was removed and 12.5% from top and bottom were eliminated to exclude the regions close to the growth plates. The morphological indices in the cortical region included: total volume (Ct.TV), marrow volume (Ct.MV), cortical area fraction (Ct.Ar/Tt.Ar), average cortical thickness (Ct.Th), total cross-sectional area inside the periosteal envelope (Tt.Ar), and cortical bone area (Ct.Ar). All bone structural parameters were normalized to the first time point for each mouse to calculate percentage changes.

Dynamic bone morphometry

The dynamic bone morphometry parameters were calculated in the trabecular region with a recently validated technique [27]. For this procedure scans of follow-up time points were rotated and translated (registered) to match the orientation of

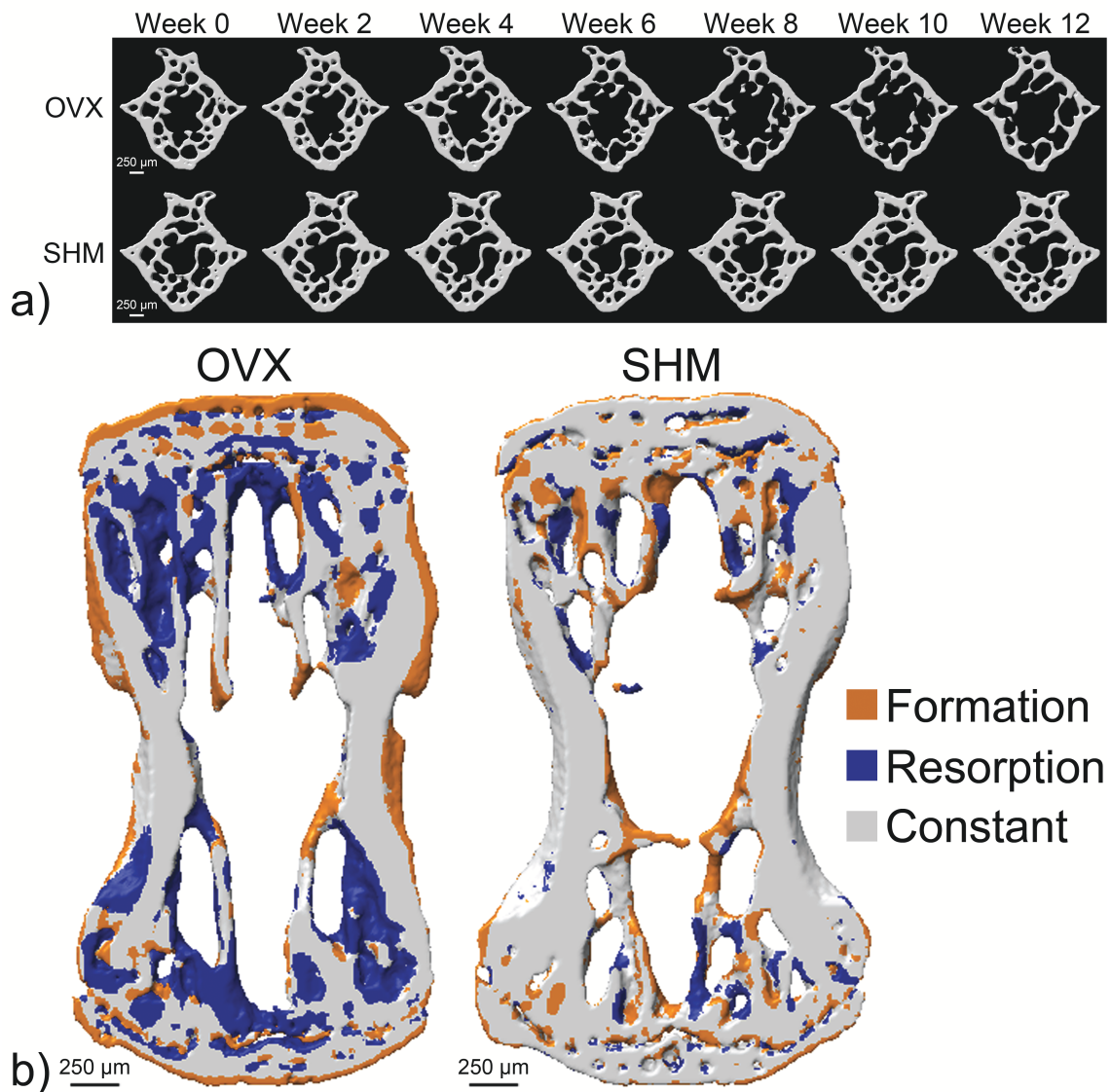


Figure 4.1: Visualization of bone loss. a) Bone microstructure (cross-section) of representative vertebrae of the OVX and SHM group for all time points at which *in vivo* micro-CT scans were performed. b) Images of overlaid bone microstructure (cross-section) of week 0 and 12 of representative vertebrae of the OVX and SHM group. Structures in yellow denote bone was formed between week 0 and 12 (only present at week 12). Structures in blue indicate bone was resorbed between week 0 and 12 (only present at week 0). Grey structures were present at both time points.

the previous scan. Thus, the same cross-section (or bone volume) can be visualized at serial time points, which allows observation of the changing bone microstructure over time (see Fig. 4.1a). From these images it is then possible to visually observe where bone was formed or resorbed between time points, but to better localize these sites of formation and resorption and to allow morphometric analysis of remodeling sites, follow-up scans were superimposed on each other. With this step, sites present only at the initial time point, sites only present at the subsequent time point, and sites present at both time points can be colored differently (see Fig. 4.1b).

The voxels only present at the initial time point must have been removed between scans and are considered resorbed bone (blue). Similarly, voxels only present at the subsequent time point must have been added and therefore are representative of formed bone (yellow). Furthermore, for voxels present at both time points no measurable changes occurred, and these sites are regarded as constant bone (gray). To explain this technique in comparison to dynamic histomorphometry: the complete surface of the bone at the initial time point can be considered as the first label, while the complete surface of the following time point can be considered as the second label. The volume between these bone surface labels can then be considered resorbed or formed bone. When the second label resides within the bone of the initial time point, bone resorption occurred, while when the second label is where the bone marrow would have been at the initial time point, bone was formed between scans. The difference of our approach compared to histomorphometry is that labels cannot be lost, labels are also existent for resorbed sites, and parameters describing the volume, thickness, and surface of remodeling sites are calculated directly in 3D.

In our approach, for each mouse, registered binary micro-CT images acquired at consecutive time points were overlaid to calculate bone formation and bone resorption for each interval (i.e. week 0-2, week 2-4, week 4-6, week 6-8, week 8-10, and week 10-12). Similar as in histomorphometry the rates calculated over a time interval were considered the value at the later time point (i.e. the value at week 2 is calculated from the overlay of week 0-2). With this procedure, volumes of bone formation or resorption could be identified and analyzed morphometrically. These parameters were defined in analogy to histomorphometric indices and included bone formation rate (BFR), bone resorption rate (BRR), mineral apposition rate (MAR), mineral resorption rate (MRR), mineralizing surface (MS), eroded surface (ES), the number of formation sites per bone volume (NFS) and the number of resorption sites per bone volume (NRS). A full description of the procedure to calculate the dynamic morphometric properties has been presented and validated earlier [27].

Finite element analysis

For each mouse at each time point segmented image data were converted into three dimensional μ FE models, with discs added on both sides to mimic the intervertebral discs. All voxels were converted to 8-node brick elements, rendering models of approximately 1.8 million elements. A Young's Modulus of 14.8 GPa,

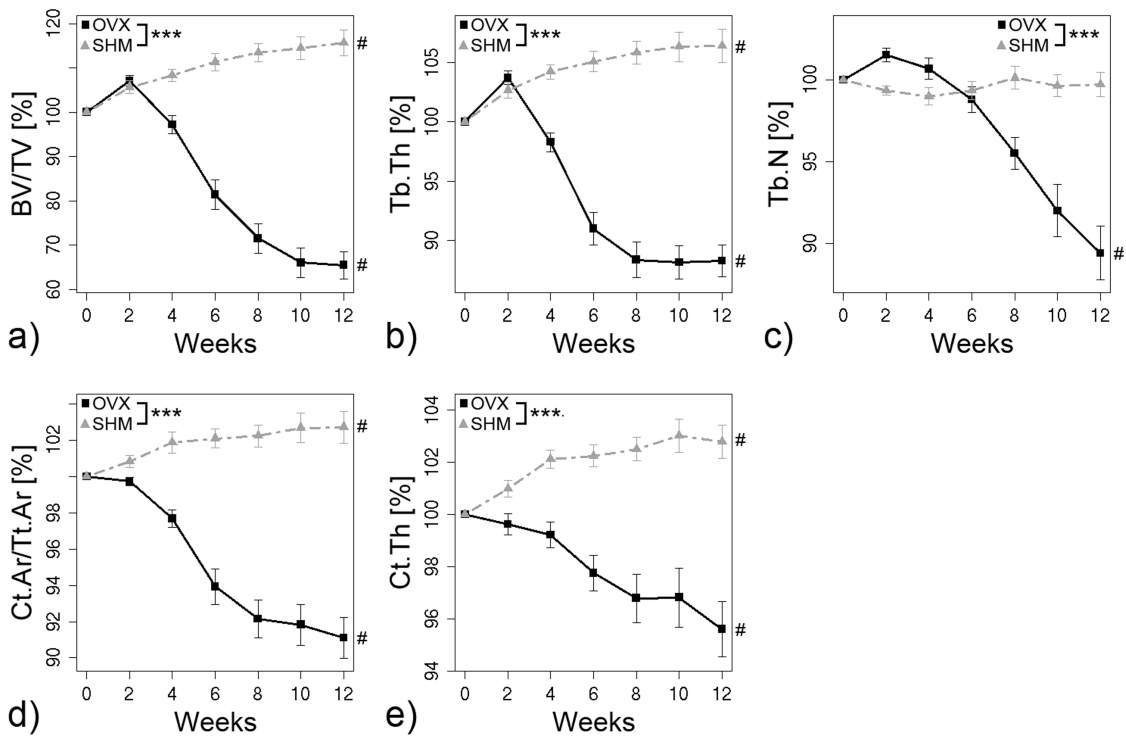


Figure 4.2: Static bone morphometry parameters over time. a) Trabecular bone volume fraction (BV/TV), b) Trabecular thickness (Tb.Th), c) Trabecular number (Tb.N), d) Cortical area fraction (Ct.Ar/Tt.Ar), e) Cortical thickness (Ct.Th). *** $p < 0.001$ between groups and # $p < 0.001$ over time as tested with repeated measurements ANOVA.

and a poisson's ratio of 0.3 were assigned to each element, as previously validated for caudal vertebrae [29]. The top was displaced 0.1%, while the bottom was constrained in all directions. The models were solved using a parallel finite element package (ParFE) with an algebraic multigrid preconditioner. The simulations ran on a Cray XT5 super computing system composed of 22,128 CPU cores and 29 TB of RAM at the Swiss National Supercomputing Center (CSCS, Manno, Switzerland).

The resulting force was calculated and used to scale the output parameters to the same force (4N). The real force that CV6 is subjected to under physiological conditions is unknown, but it has recently been found by using a novel bone loading estimation method that external loading conditions of CV6 are in the range of 4N [30]. By using the Pistoia criterion the strength of the whole bone was estimated for each mouse at each time point [31].

The change in strain energy density (SED) was calculated in the trabecular and cortical bone in three regions: the proximal region, the middle region, and the distal region (Fig. 4.5). In each of these regions the fraction of load carried

by the cortical bone was calculated, by calculating the strain energy dissipated in the cortex as a fraction of the total strain energy [32]. To quantify changes in mechanical properties over time, the data were normalized to the first time point for each mouse.

Statistical analysis

Statistical analysis was performed with the software package R (R: A Language and Environment for Statistical Computing). A Kolmogorov-Smirnov test verified that the data were normally distributed. Repeated measurements ANOVA, implemented as a linear mixed effects model, was performed to detect significant differences in bone parameters between groups and over time. With this test, significant differences were determined for effect of time, effect of group, and the interaction between time and group, which indicated whether the time course developed differently between groups. P-values smaller than 0.05 were considered significant. All data are shown as mean \pm standard error.

4.1.3 Results

Animals

All animals remained healthy and gained weight throughout the experiment. There was a trend that OVX mice gained more weight than SHM mice. Four mice were excluded, because the wrong vertebra was scanned at one of the time points (2 SHM, 2 OVX).

Static bone morphometry

As can visually be seen in Figure 4.1a, for OVX the bone microstructure deteriorated over time, while for the SHM the bone microstructure remained relatively constant. The change in BV/TV over time was significantly different between groups ($p < 0.001$); it increased 16% for SHM ($p < 0.001$ over time) and decreased 35% for OVX ($p < 0.001$ over time) as compared to the baseline (Fig. 4.2a). Both groups showed a similar increase in BV/TV in the first two weeks, after which there was a clear difference between groups. The decrease in BV/TV for OVX was mainly caused by thinning and perforation of trabeculae, leading to a somewhat delayed decrease in the number of trabeculae. Tb.Th decreased 12% for OVX ($p < 0.001$ over time), which was significantly different from SHM ($p < 0.001$) where Tb.Th increased 6% ($p < 0.001$ over time, Fig. 4.2b). Tb.N started to decrease roughly two weeks later, resulting in an 11% decrease for OVX at 12 weeks ($p < 0.001$ over

time), which was significantly different ($p < 0.001$) from SHM, where Tb.N remained constant (Fig. 4.2c). Significant differences between OVX and SHM were also found for Tb.TV ($p < 0.001$), BS/BV ($p < 0.001$), and Tb.Sp ($p < 0.001$), but not for SMI or Conn.D (Table 4.1).

In the cortex, a similar progression of bone loss was observed: Ct.Ar/Tt.Ar developed significantly different over time between groups ($p < 0.001$): for SHM, Ct.Ar/Tt.Ar increased 3% ($p < 0.001$ over time), while for OVX it decreased 9% ($p < 0.001$ over time, Fig. 4.2d). This came with a concomitant decrease in Ct.Th of 5% for OVX ($p < 0.001$ over time), while for SHM this increased by 3% ($p < 0.001$ over time and $p < 0.001$ between groups, Fig. 4.2e). The cortex was reduced mostly on the endosteal side, while some apposition was present at the periosteal side. This was also confirmed by a significantly greater increase of 15% in Ct.MV for OVX ($p < 0.001$ over time) compared to no change for SHM ($p < 0.001$ between groups), and a significantly greater increase of 7% in Ct.TV for OVX ($p < 0.001$ over time) compared to a 2% increase for SHM ($p < 0.001$ over time and $p < 0.001$ between groups, Table 4.1).

Dynamic bone morphometry

BFR was elevated for OVX compared to SHM starting from 8 weeks (Fig. 4.3a), while BRR was greater for OVX than for SHM over the whole time range (Fig. 4.3b). On average BFR was 1.6 times greater for OVX than SHM ($p < 0.05$), and BRR 3.7 times greater for OVX than SHM ($p < 0.001$). This is also visually evident in figure 4.1b, where for OVX there are more yellow structures (indicating BFR) and many more blue structures (indicating BRR) than for SHM. MAR, which represents the thickness of formation sites, was significantly greater for OVX than SHM ($p < 0.01$, Fig. 4.3c). Also MRR, which represents the depth of resorption sites, was significantly greater for OVX than SHM ($p < 0.001$, Fig. 4.3d). On average MAR was 1.2 times greater and MRR 1.7 times greater for OVX than SHM. MS, which represents the surface of formation sites, was significantly smaller for OVX than SHM ($p < 0.001$, Fig. 3e). ES, which represents the surface of resorption sites, was significantly greater for OVX than SHM ($p < 0.001$, Fig 4.3f). For OVX the profiles of MS and ES had the opposite shape: when MS seemed the smallest at week 6 (on average 1.5 times smaller than for SHM), ES seemed the largest (on average 1.4 times larger than for SHM).

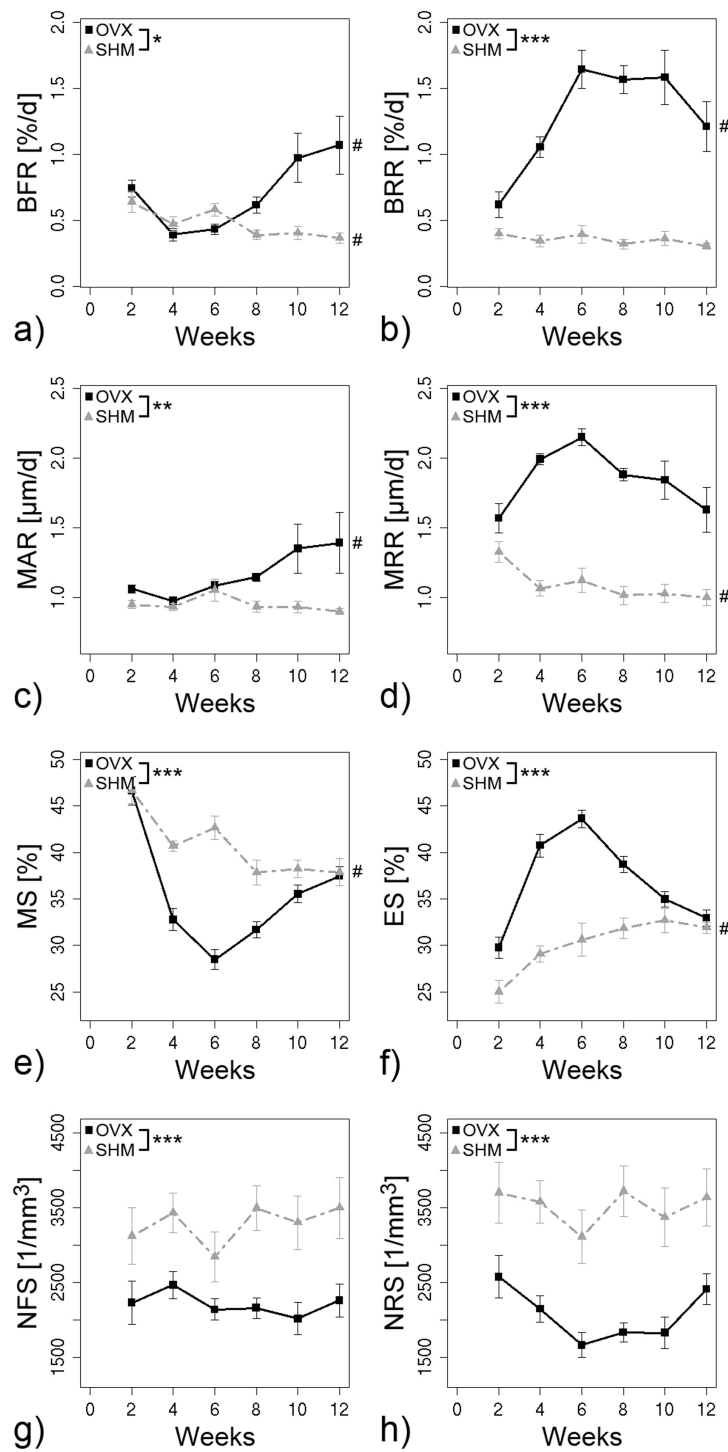


Figure 4.3: Dynamic bone morphometry over time. a) Bone formation rate (BFR), b) Bone resorption rate (BRR), c) Mineral apposition rate (MAR), d) Mineral resorption rate (MRR), e) Mineralizing surface (MS), f) Eroded surface (ES), g) Number of formation sites per bone volume (NFS), h) Number of resorption sites per bone volume (NRS). The x-axis indicates between which time points the dynamic parameters were determined, e.g. 0-2 indicates from an overlay of week 2 on week 0. * $p < 0.05$, ** $p < 0.01$, *** $p < 0.001$ between groups and # $p < 0.01$ over time as tested with repeated measurements ANOVA.

To investigate whether the profiles for ES and MS were an effect of changes in the amount of sites or an effect of changes in shape of formation and resorption sites, the number of formation and resorption sites per bone volume were calculated. NFS was significantly smaller for OVX than for SHM ($p < 0.001$, Fig. 4.3g), and also NRS was significantly smaller for OVX than for SHM ($p < 0.001$, Fig. 4.3h). No changes were seen for NFS and NRS over time, indicating that when MS decreased, this was mostly because the surface of formation sites decreased, rather than that the number of formation sites decreased. Similarly, a change in ES was mainly caused by a change in surface of resorption sites.

This gives evidence that both the shape and the number of formation and resorption sites were modulated by OVX. Formation sites were smaller in number, with a smaller surface, but an increased thickness. At the same time the quantity of resorption sites was less, with sites showing a broader surface, greater thickness, and becoming more massive. Even though the number of formation and resorption sites was smaller for OVX than SHM, the thicknesses were so much increased, and the surface increased to such an extent for resorption sites, that the volumes of formation and resorption were larger for OVX than for SHM.

When the ratios between formation and resorption were explored it could be seen that BFR was greater than BRR for SHM, while BRR was greater than BFR for OVX. The ratio was significantly smaller for OVX than for SHM ($p < 0.001$). Similarly, the ratio between MS and ES was significantly smaller for OVX than for SHM ($p < 0.001$), and the ratio between MAR and MRR was significantly smaller for OVX than for SHM ($p < 0.001$), but on the contrary the ratio between NFS and NRS was significantly greater for OVX than for SHM ($p < 0.001$). On average MRR was greater than MAR for OVX, and ES was greater than MS for OVX, while NRS was smaller than NFS for OVX. This indicates that for OVX the sites of resorption were less numerous, but more massive, or that multiple sites had merged into fewer, but larger sites.

Finite element analysis

From μ FE analysis it was found that the strength of CV6 reduced 18% for OVX ($p < 0.001$ over time), which was significantly different from SHM ($p < 0.001$), where the strength increased 13% ($p < 0.001$ over time, Fig. 4.4a). As can be seen in figure 4.5, for both the cortical and trabecular bone, SED increased for OVX ($p < 0.001$ over time), while it decreased for SHM ($p < 0.001$ over time), with significant differences

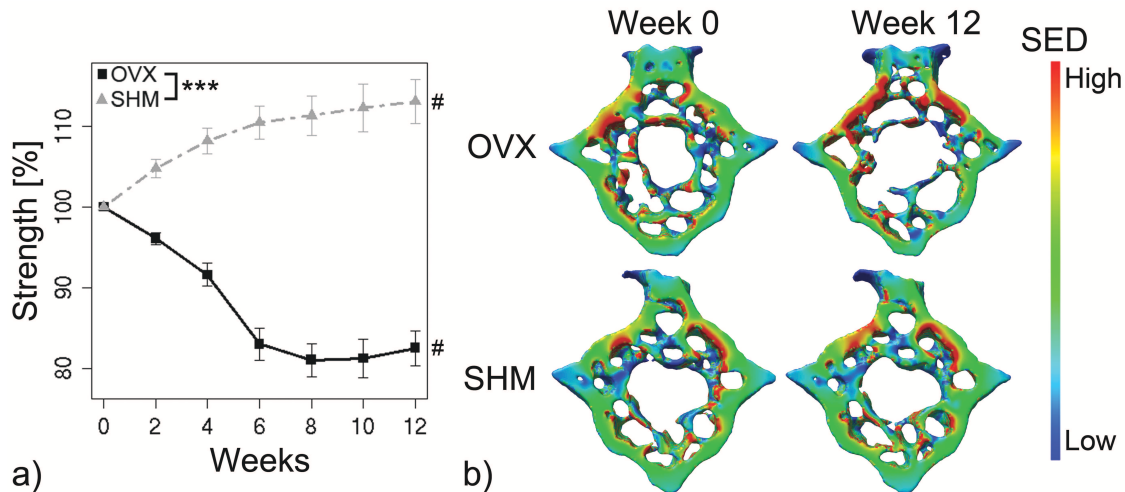


Figure 4.4: a) Strength of the whole bone over time. *** $p < 0.001$ between groups and # $p < 0.001$ over time as tested with repeated measurements ANOVA. b) Visualization of SED in cross-sections of representative mice at first and last time point. Red denotes high SED, while blue represents low SED (see scale bar).

between groups ($p < 0.01$) in the proximal and distal region. The increase in SED for OVX in both trabecular and cortical region was also visually apparent (Fig. 4.4b). In the middle region, no significant differences were found between OVX and SHM. As there were only a few trabeculae in the center of the trabecular middle region that show non-consistent changes, the error bars were comparatively large. The fraction of load carried by the trabecular bone (Fig. 4.5, last column) was much smaller than the load carried by the cortical bone in all of the regions, especially in the middle region. With the decrease in bone volume fraction for OVX, significantly less load was carried by the trabecular bone in region 1 ($p < 0.01$ over time) and region 3 ($p < 0.001$ over time). On the contrary for SHM the fraction of load carried by the trabecular bone increased significantly over time in all 3 regions ($p < 0.001$ over time).

4.1.4 Discussion

In this study we showed that the sixth caudal vertebra of C57BL/6 mice is a valid model for studying osteoporosis-related bone loss, by showing that ovariectomy led to high turnover bone loss, with a subsequent reduction in the bone strength. Consequently, it is proposed that the caudal vertebrae of ovariectomized mice can be used as an alternative model for to study postmenopausal osteoporosis. With regard to bone structural parameters, we confirmed that ovariectomy caused a significant decrease in BV/TV and a significant decrease in Ct.Ar/Tt.Ar, with a

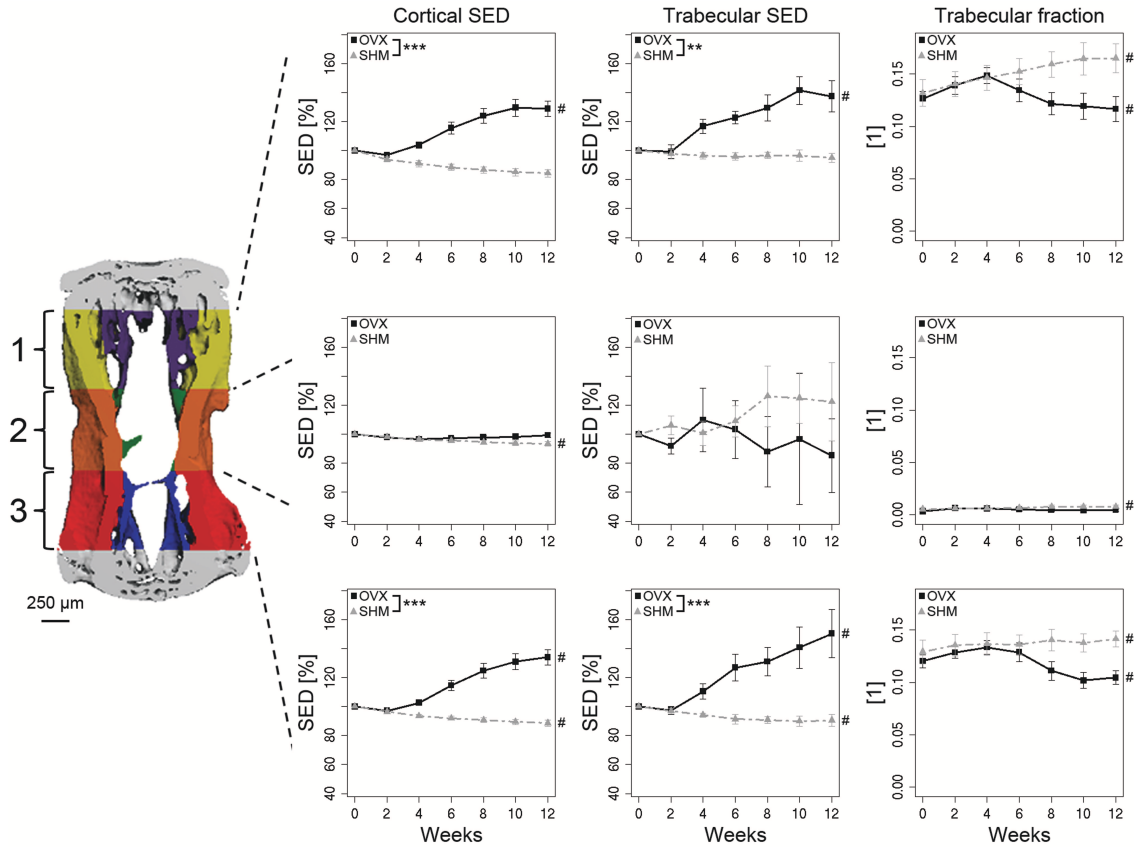


Figure 4.5: SED in cortical (left) and trabecular (middle) region, and fraction of load carried by the trabecular bone (right) in the proximal region (upper), middle region (middle), and distal region (lower). The selection of the regions is shown in the colored image on the left. ** $p < 0.01$, *** $p < 0.001$ between groups and # $p < 0.001$ over time as tested with repeated measurements ANOVA.

greater bone loss in the trabecular than cortical region, as has been reported in previous studies at other skeletal sites in mice [15, 18, 33, 34]. The greater loss in the trabecular bone can be explained by the fact that the cortical bone is more important for mechanical stability of the bone, while the trabecular bone, as it has a larger surface, is more important for homeostasis [35]. This observation was also confirmed by the fact that, in the sixth caudal vertebra, the cortical bone carried relatively more load, and that this fraction became even larger after ovariectomy.

Unexpectedly, the trabecular volume fraction showed a delayed decrease starting only 2 weeks post ovariectomy. This trend has not been shown by others. In a study with time-lapsed images of the tibia in C57BL/6J mice up to 5 weeks after surgery, no significant effect of OVX was found [18]. In cross-sectional studies, several others found significant decreases in BV/TV 2 weeks after OVX in the tibia in C3H/Hen mice [34] and 4 weeks after OVX in lumbar vertebrae, the proximal tibia, and the distal femur in C57BL/6J mice [15, 17]. Additionally, in rats where

time-lapsed images of the proximal tibia were available, an initial delay in the decrease has not been described [5,6]. A finding that coincides with this initial lack of response to OVX, however, is that in rats, skeletal sites with fatty (yellow) bone marrow content react slower to OVX than sites with hematopoietic (red) bone marrow [9]. It has also been shown that, in rats, the fifth caudal vertebra consists of fatty bone marrow [11]. Thus, it might be that in mice, the sixth caudal vertebra contains fatty (yellow) bone marrow and that this influences the response to OVX, leading to a delayed bone loss. Often times the presence of yellow marrow in the tail of the mouse has been regarded as a negative effect. Nevertheless, in elderly osteoporotic subjects, bone marrow is also predominantly yellow [36]. Furthermore yellow bone marrow is less sensitive to radiation effects. Therefore the presence of yellow bone marrow may also be seen as an advantage over other models of postmenopausal bone loss.

When investigating bone dynamic parameters, it was found that both bone formation rate and bone resorption rate were elevated for OVX compared to SHM, with the bone resorption rate exceeding bone formation rate in OVX, indicating high turnover bone loss. Similarly, Bain et al. [33] found an increase in bone resorption determined from [³H]tetracycline assay in the femur and thoracic vertebra, but failed to show an increase in bone formation rate between OVX and SHM in the tibia four weeks after OVX. In our study, differences in BFR between OVX and SHM were also not present at this time point. Likewise, Kimble et al. [34] found an increase in bone resorption, as assessed by an increased osteoclast number per surface and percentage of bone covered by resorption surfaces in the tibia 2 weeks after ovariectomy. In contrast to our study, Okada et al. [37] reported increases in bone formation rate and bone resorption rate already at 2 weeks after ovariectomy as determined from biochemical markers in blood, with the bone resorption rate exceeding bone formation rate, as determined from a decrease in BV/TV. Iwaniec et al. [17] did not find significant differences in BFR or osteoclast surface in either femur or lumbar vertebra between ovariectomy or sham groups. The differences in these findings might lie in the differences between skeletal sites and the sensitivity of the methods. An improvement in our analysis, as compared to previous studies, is that bone formation and resorption parameters could be evaluated within the same bone at multiple time points, increasing statistical power. A further advantage is that the parameters are calculated in 3D, and thus include more bone, through which the analysis picks up differences more readily.

Regarding the mechanical properties, we observed that the strength of the sixth caudal vertebra was significantly reduced in OVX compared to SHM. In agreement several other investigators have reported similar reductions in mechanical properties after OVX [16,38]. Interestingly, an additional observation of our study was that the load carrying capacity of the trabecular bone reduced drastically, confirming the importance of cortical bone for mechanical stability.

There were several limitations associated with our study. The general disadvantages of a mouse model, including the lack of fragility fractures, the continuation of growth, and speed of bone loss, also apply to our study. However, even though fragility fractures were not present, as in any rodent models of osteoporosis, the strength of the bone did reduce significantly. Furthermore, the speed of bone loss in the mouse is faster than seen in rats or humans, but is very predictable and similar for all mice (as they have the same genetic background), which is a requirement for a relevant model. Thus, in our eyes these disadvantages are surmounted by the advantages of the mouse model.

A limitation of our technique in the extraction of dynamic parameters is that only active sites of formation and resorption are captured, unlike in histology where the total amount of sites can be seen, with a distinction between active and non-active sites. Furthermore, dynamic parameters were investigated at two-week intervals. While this allowed investigating changes in dynamic parameters over time within the same animal, intermediate changes within the 2 week time-span could not be captured, leading to a reduction of the actual values for formation and resorption.

A drawback of the longitudinal setup in our study is the effect of radiation. However, in a radiation control study performed before the start of this experiment, no detrimental effects of radiation were found on the bone micro-structure or biochemical markers (data not shown). Analogously, it has been shown that multiple scans did not have a detectable radiation effect in proximal tibia in C57BL/6J mice [18] and wistar rats [39]. Also, if the radiation would have had an effect, a decrease in bone mass for the sham mice would be anticipated but did not occur.

In conclusion, we showed that ovariectomy led to 1) decreased bone mass, 2) high turnover bone loss, and 3) reduced bone strength in the sixth caudal vertebra of C57BL/6J mice. The added value of our study was that dynamic parameters

were calculated over time within single animals, allowing monitoring transient progression in remodeling rates, and included bone resorption rates. From our findings, we conclude that the sixth caudal vertebra of C57BL/6J mice is a suitable model for postmenopausal osteoporosis. Firstly, it shows similarities to the human progression of osteoporosis in static, dynamic, and mechanical parameters, and secondly, is accessible for high resolution imaging and non-destructive strength analysis.

4.1.5 Acknowledgements

The authors gratefully acknowledge funding from the European Union for the Osteoporotic Virtual Physiological Human project (VPHOP FP7-ICT2008-223865) and computational time from the Swiss National Supercomputing Center (CSCS, Manno, Switzerland). We thank Peter Schwilch and Marco Hitz for technical assistance with the mouse holder.

References

- [1] O. Ström, F. Borgström, J.A. Kanis, J. Compston, C. Cooper, E.V. McCloskey, and B. Jönsson. Osteoporosis: burden, health care provision and opportunities in the EU. *Arch Osteoporos*, DOI 10.1007/s11657-011-0060-1, 2011.
- [2] S. Reinwald and D. Burr. Review of nonprimate, large animal models for osteoporosis research. *J Bone Miner Res*, 23(9):1353–1368, 2008.
- [3] D.B. Kimmel. *Osteoporosis*. Academic Press, San Diego, 1996.
- [4] D.N. Kalu. The ovariectomized rat model of postmenopausal bone loss. *Bone Miner*, 15(3):175–191, 1991.
- [5] J.E.M. Brouwers, F.M. Lambers, J.A. Gasser, B. van Rietbergen, and R. Huiskes. Bone degeneration and recovery after early and late bisphosphonate treatment of ovariectomized wistar rats assessed by *in vivo* micro-computed tomography. *Calcif Tissue Int*, 82(3):202–211, 2008.
- [6] S.K. Boyd, P. Davison, R. Müller, and J.A. Gasser. Monitoring individual morphological changes over time in ovariectomized rats by *in vivo* micro-computed tomography. *Bone*, 39(4):854–862, 2006.

- [7] T.J. Wronski, L.M. Dann, K.S. Scott, and M. Cintron. Long-term effects of ovariectomy and aging on the rat skeleton. *Calcif Tissue Int*, 45(6):360–366, 1989.
- [8] X.Y. Tian, X.Q. Liu, H.Y. Chen, R.B. Setterberg, M. Li, and W.S. Jee. Greater efficacy of alfacalcidol in the red than in the yellow marrow skeletal sites in adult female rats. *J Musculoskelet Neuronal Interact*, 8(3):257–266, 2008.
- [9] T.J. Wronski, L.M. Dann, and S.L. Horner. Time course of vertebral osteopenia in ovariectomized rats. *Bone*, 10(4):295–301, 1989.
- [10] N. Miyakoshi, K. Sato, T. Abe, T. Tsuchida, Y. Tamura, and T. Kudo. Histomorphometric evaluation of the effects of ovariectomy on bone turnover in rat caudal vertebrae. *Calcif Tissue Int*, 64(4):318–324, 1999.
- [11] M. Li, Y. Shen, H. Qi, and T.J. Wronski. Comparative study of skeletal response to estrogen depletion at red and yellow marrow sites in rats. *Anat Rec*, 245(3):472–480, 1996.
- [12] R.F. Klein. Genetics of osteoporosis—utility of mouse models. *J Musculoskelet Neuronal Interact*, 8(4):287–290, 2008.
- [13] J.M. Alexander, I. Bab, S. Fish, R. Müller, T. Uchiyama, G. Gronowicz, M. Nahounou, Q. Zhao, D.W. White, M. Chorev, D. Gazit, and M. Rosenblatt. Human parathyroid hormone 1-34 reverses bone loss in ovariectomized mice. *J Bone Miner Res*, 16(9):1665–1673, 2001.
- [14] A. Cano, S. Dapia, I. Noguera, B. Pineda, C. Hermenegildo, R. del Val, J.R. Caeiro, and M.A. Garcia-Perez. Comparative effects of 17beta-estradiol, raloxifene and genistein on bone 3D microarchitecture and volumetric bone mineral density in the ovariectomized mice. *Osteoporos Int*, 19(6):793–800, 2008.
- [15] M.L. Bouxsein, K.S. Myers, K.L. Shultz, L.R. Donahue, C.J. Rosen, and W.G. Beamer. Ovariectomy-induced bone loss varies among inbred strains of mice. *J Bone Miner Res*, 20(7):1085–1092, 2005.
- [16] C.Y. Li, M.B. Schaffler, H.T. Wolde-Semait, C.J. Hernandez, and K.J. Jepsen. Genetic background influences cortical bone response to ovariectomy. *J Bone Miner Res*, 20(12):2150–2158, 2005.
- [17] U.T. Iwaniec, D. Yuan, R.A. Power, and T.J. Wronski. Strain-dependent variations in the response of cancellous bone to ovariectomy in mice. *J Bone Miner Res*, 21(7):1068–1074, 2006.

- [18] J. Klinck and S.K. Boyd. The magnitude and rate of bone loss in ovariectomized mice differs among inbred strains as determined by longitudinal *in vivo* micro-computed tomography. *Calcif Tissue Int*, 83(1):70–79, 2008.
- [19] D. Webster, E. Wasserman, M. Ehrbar, F. Weber, I. Bab, and R. Müller. Mechanical loading of mouse caudal vertebrae increases trabecular and cortical bone mass-dependence on dose and genotype. *Biomech Model Mechanobiol*, 9(6):737–747, 2010.
- [20] J.Y. Reginster, N. Sarlet, and M.P. Lecart. Fractures in osteoporosis: the challenge for the new millennium. *Osteoporos Int*, 16 Suppl 1:S1–S3, 2005.
- [21] J.P. Bilezikian, T. Matsumoto, T. Bellido, S. Khosla, J. Martin, R.R. Recker, R. Heaney, E. Seeman, S. Papapoulos, and S.R. Goldring. Targeting bone remodeling for the treatment of osteoporosis: summary of the proceedings of an ASBMR workshop. *J Bone Miner Res*, 24(3):373–385, 2009.
- [22] M. Egermann, J. Goldhahn, and E. Schneider. Animal models for fracture treatment in osteoporosis. *Osteoporos Int*, 16(Suppl 2):S129–S138, 2005.
- [23] L. Mosekilde, C.C. Danielsen, and U.B. Knudsen. The effect of aging and ovariectomy on the vertebral bone mass and biomechanical properties of mature rats. *Bone*, 14(1):1–6, 1993.
- [24] D. Fonseca and W.E. Ward. Daidzein together with high calcium preserve bone mass and biomechanical strength at multiple sites in ovariectomized mice. *Bone*, 35(2):489–497, 2004.
- [25] J.E.M. Brouwers, B. van Rietbergen, R. Huiskes, and K. Ito. Effects of PTH treatment on tibial bone of ovariectomized rats assessed by *in vivo* micro-CT. *Osteoporos Int*, 20(11):1823–1835, 2009.
- [26] M.J. Silva, M.D. Brodt, and B.A. Uthgenannt. Morphological and mechanical properties of caudal vertebrae in the SAMP6 mouse model of senile osteoporosis. *Bone*, 35(2):425–431, 2004.
- [27] F.A. Schulte, F.M. Lambers, G. Kuhn, and R. Müller. *In vivo* micro-computed tomography allows direct three-dimensional quantification of both bone formation and bone resorption parameters using time-lapsed imaging. *Bone*, 48:433–442, 2011.

- [28] M.L. Bouxsein, S.K. Boyd, B.A. Christiansen, R.E. Guldberg, K.J. Jepsen, and R. Müller. Guidelines for assessment of bone microstructure in rodents using micro-computed tomography. *J Bone Miner Res*, 25(7):1468–1486, 2010.
- [29] Webster D.J., Morley P.L., van Lenthe G.H., and Müller R. A novel in vivo mouse model for mechanically stimulated bone adaptation—a combined experimental and computational validation study. *Comput Methods Biomech Biomed Engin*, 11(5):435–441, 2008.
- [30] B. Christen, B. van Rietbergen, F.M. Lambers, R. Müller, and K. Ito. Bone morphology allows estimation of loading history in a murine model of bone adaptation. *Biomech Model Mechanobiol*, accepted, 2011.
- [31] W. Pistoia, B. van Rietbergen, E.M. Lochmuller, C.A. Lill, F. Eckstein, and P. Ruegsegger. Estimation of distal radius failure load with micro-finite element analysis models based on three-dimensional peripheral quantitative computed tomography images. *Bone*, 30(6):842–848, 2002.
- [32] L.J.3rd Melton, D. Christen, B.L. Riggs, S.J. Achenbach, R. Müller, G.H. van Lenthe, S. Amin, E.J. Atkinson, and S. Khosla. Assessing forearm fracture risk in postmenopausal women. *Osteoporos Int*, 21(7):1161–1169, 2010.
- [33] S.D. Bain, M.C. Bailey, D.L. Celino, M.M. Lantry, and M.W. Edwards. High-dose estrogen inhibits bone resorption and stimulates bone formation in the ovariectomized mouse. *J Bone Miner Res*, 8(4):435–442, 1993.
- [34] R.B. Kimble, S. Bain, and R. Pacifici. The functional block of TNF but not of IL-6 prevents bone loss in ovariectomized mice. *J Bone Miner Res*, 12(6):935–941, 1997.
- [35] A.M. Parfitt. Osteonal and hemi-osteonal remodeling: the spatial and temporal framework for signal traffic in adult human bone. *J Cell Biochem*, 55(3):273–286, 1994.
- [36] B. C. Vande Berg, J. Malghem, F. E. Lecouvet, and B. Maldaque. [Normal bone marrow: dynamic aspects in magnetic resonance imaging]. *J Radiol*, 82(2):127–135, 2001.
- [37] Y. Okada, I. Morimoto, K. Ura, Y. Nakano, Y. Tanaka, S. Nishida, T. Nakamura, and S. Eto. Short-term treatment of recombinant murine interleukin-4 rapidly inhibits bone formation in normal and ovariectomized mice. *Bone*, 22(4):361–365, 1998.

- [38] W.E. Ward and D. Fonseca. Soy isoflavones and fatty acids: effects on bone tissue postovariectomy in mice. *Mol Nutr Food Res*, 51(7):824–831, 2007.
- [39] J.E.M. Brouwers, B. van Rietbergen, and R. Huiskes. No effects of in vivo micro-CT radiation on structural parameters and bone marrow cells in proximal tibia of wistar rats detected after eight weekly scans. *J Orthop Res*, 25(10):1325–1332, 2007.

4.2 Bone strength but not microstructure is retained in aging mice

Floor M. Lambers¹, Gisela Kuhn¹, Claudia Weigt¹, Kathleen Koch¹, Friederike A. Schulte¹, and Ralph Müller¹

¹Institute for Biomechanics, ETH Zürich, Zürich, Switzerland

Abstract:

Many reports exist that characterize how bone microstructure changes with age in mice. For a better understanding of the etiology of age related changes in bone, however, a thorough characterization of all three static, dynamic, and mechanical parameters in a longitudinal fashion is imperative. For this purpose, the sixth caudal vertebra and tibia of female C57Bl/6 mice were scanned at multiple time points between an age of 16 and 88 weeks using *in vivo* micro-computed tomography (micro-CT). From these scans, static, dynamic and mechanical properties were analyzed longitudinally. Over time, bone formation rate decreased 78%, while bone resorption rate (which was low at all time points) increased 20% between the first and last time point in the caudal vertebra. This did not influence the vertebra negatively; the bone volume fraction and bone strength increased throughout the study and reached values of 136% and 127% of their initial value, respectively. In the tibia, a reduction of 18% in cortical area fraction was found, caused by a relatively large bone resorption rate on the endosteal side of the cortex, which was compensated by a relatively large bone formation rate on the periosteal side of the cortex. Therefore, the mechanical properties were not influenced negatively; the resistance against bending and torsion was unaltered. In conclusion, we found that even with age the bone optimizes its microstructure to enable the bone to carry the forces that it is subjected to.

Keywords:

Bone development, bone remodeling, bone microstructure, bone strength, *in vivo* micro-computed tomography

4.2.1 Introduction

The mechanism of how bone develops over a lifetime and the etiology of age-related changes in bone remain poorly understood. To gain a better understanding of this, it is necessary to establish bone development and aging patterns. It is often difficult to investigate the effect of bone development and aging in the bone of human subjects; therefore, murine models have become increasingly important. Although bone development in an animal model is not directly comparable to human bone progression, it serves as a useful tool to complement our knowledge on changes in bone dynamics, bone microstructure and mechanical properties of bone with age.

In mice, it has most often been shown that in the cortex of long bones, like the femur, tibia, or radius, the bone mineral density, cortical area, and moment of inertia in the diaphysis increase up to an age of 4 months, remain stable up to 12 months [1–3], and decrease mildly or severely until end of life [4–8]. Furthermore, Halloran et al. [6] reported a continuous decrease in the trabecular bone volume fraction in the proximal metaphysis of the tibia from age of 1.5 months on up to 24 months, with a constant increase in trabecular thickness up to 12 months, and a stable value afterwards. On the other hand, Willingham et al. [8] found the trabecular bone mass in the tibial metaphyses to increase up to 4 months, and decrease afterwards, but, similarly, found an incessant increase in trabecular thickness. At another site with larger volumes of trabecular bone, i.e. the fifth lumbar vertebra, the trabecular bone volume fraction has been reported to increase up to 12 months, and decrease up to 20 months of age [8]. But, in disagreement, another study showed that the bone volume fraction continued to decrease in the fifth lumbar vertebra from an age of 2 months on [5].

Differences in the manifestation of bone loss with age between studies might lie in differences in mouse strains, or more likely, in the cross-sectional nature of these experiments, where differences between groups cannot be accounted for, as starting values are unknown. Thus, although a substantial amount of data is available on changes in bone with age, there is a lack of longitudinal studies to investigate this. In one longitudinal study, the bone microstructure of the tibia and the third lumbar vertebra were monitored over time with *in vivo* micro-CT up to 48 weeks of age. In both vertebra and tibia minimal decreases in trabecular bone volume density were observed between 12 and 48 weeks of age [9]. However, to gain better insight in how bone remodeling is influenced with age, also bone dynamics should be investigated and include data over a substantial part of the life span of a

mouse. Therefore, in this study, we evaluated the static, dynamic, and mechanical properties of a caudal vertebra and tibia in mice during an age of 20 to 88 weeks, by using *in vivo* micro-computed tomography (micro-CT). This enabled us to monitor changes in the bone microstructure, extract 3D dynamic bone morphometry parameters over time [10], and to calculate changes in mechanical properties from micro-CT data and micro-finite element (μ FE) models longitudinally.

4.2.2 Material and methods

Experimental design

Thirty six female C57BL/6J mice were acquired at 15 weeks of age (n=12) or 18 weeks of age (n=24) from RCC Ltd (Füllinsdorf, Switzerland). The mice were maintained in an environmentally controlled animal facility with a 12-hour light/dark cycle and fed standard rodent diet and water ad libitum. The mice were randomly divided into three groups (A, B, and C). Each group was scanned approximately every 12 weeks, with an offset of 4 weeks, up to 88 weeks, leading to six alternating measurements per mouse (at an age of 16, 28, 41, 52, 63 and 78 weeks for group A; at an age of 20, 32, 44, 56, 68 and 82 weeks for group B; and at an age of 24, 36, 48, 59, 73 and 88 weeks for group C). This setup was chosen to enable scanning over a substantial part of the life span of a mouse, while keeping the radiation dose per animal minimal. From week 20 on, the weights were recorded after CT-scans and monthly in the last 3 months.

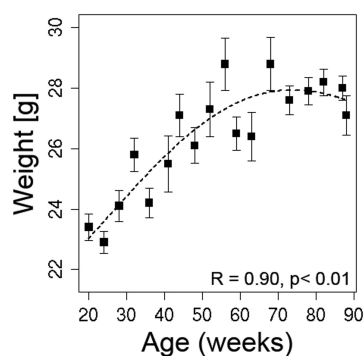


Figure 4.6: Weight of mice over time. The dotted line shows the polynomial fit. The R and p value indicate how well the fit represents the data.

***In vivo* micro-computed tomography**

The sixth caudal vertebra and a cortical slab of the tibia were measured with an *in vivo* micro-CT scanner (vivaCT40, Scanco Medical AG, Brüttisellen, Switzerland) on two consecutive days, for each time point, at a resolution of 10.5 μm . The vertebra and tibia were chosen, because these represent two bones with different loading conditions (mostly compression and mostly bending, respectively) and different bone microstructure (with large amounts of trabecular bone and mainly cortical bone, respectively). Mice were positioned in custom-built animal beds during the measurements, while anesthetized with isoflurane. For vertebra measurements, the tail was extended from a heated (just below body temperature) holder, and tightly fixed. For tibia measurements, the left tibia was stretched outside of the holder, with tissues around the leg in the opening to prevent motion-artifacts. Scans of the tibia were available from 20 weeks of age on, as the holder for scanning the tibia was only completed then.

The starting position for each scan was determined from a scout view. For the sixth caudal vertebra, the correct vertebra was counted from the first caudal vertebra, which is connected to the sacrum. The scanned region included the whole vertebra, and had a length of 4.4 mm. For the tibia, the location of the most distal and proximal side of the tibia were used to calculate the position to scan a length of 2.2 mm in the center of the tibia.

For both bones, 1000 projections per 180 degrees were acquired at 55 kVp, 145 μA , with an integration time of 200 ms. A beam hardening correction algorithm, provided by Scanco Medical AG, was applied to all scans. Calibration hydroxyapatite (HA) phantoms (Scanco Medical AG) were scanned weekly to facilitate the conversion of the linear attenuation of a given voxel to mineral content (mgHA/cm^3) and monthly for determination of in plane spatial resolution.

To enable visual comparison between subjects, all image data were reconstructed such that the orientation in the xy-plane (slice) was the same. The image data of the first time point of each animal was rotated, such that the centerline of the bone and z-axis (long axis) coincided. Follow-up scans were registered on the previous time point [11]. To smooth the data, a 3D constrained Gaussian filter (sigma 1.2, support 1) was applied. Next, segmentation was performed by thresholding the data at 22% of the maximum grayscale value. For the scans of the tibia, the fibula was excluded by component labeling.

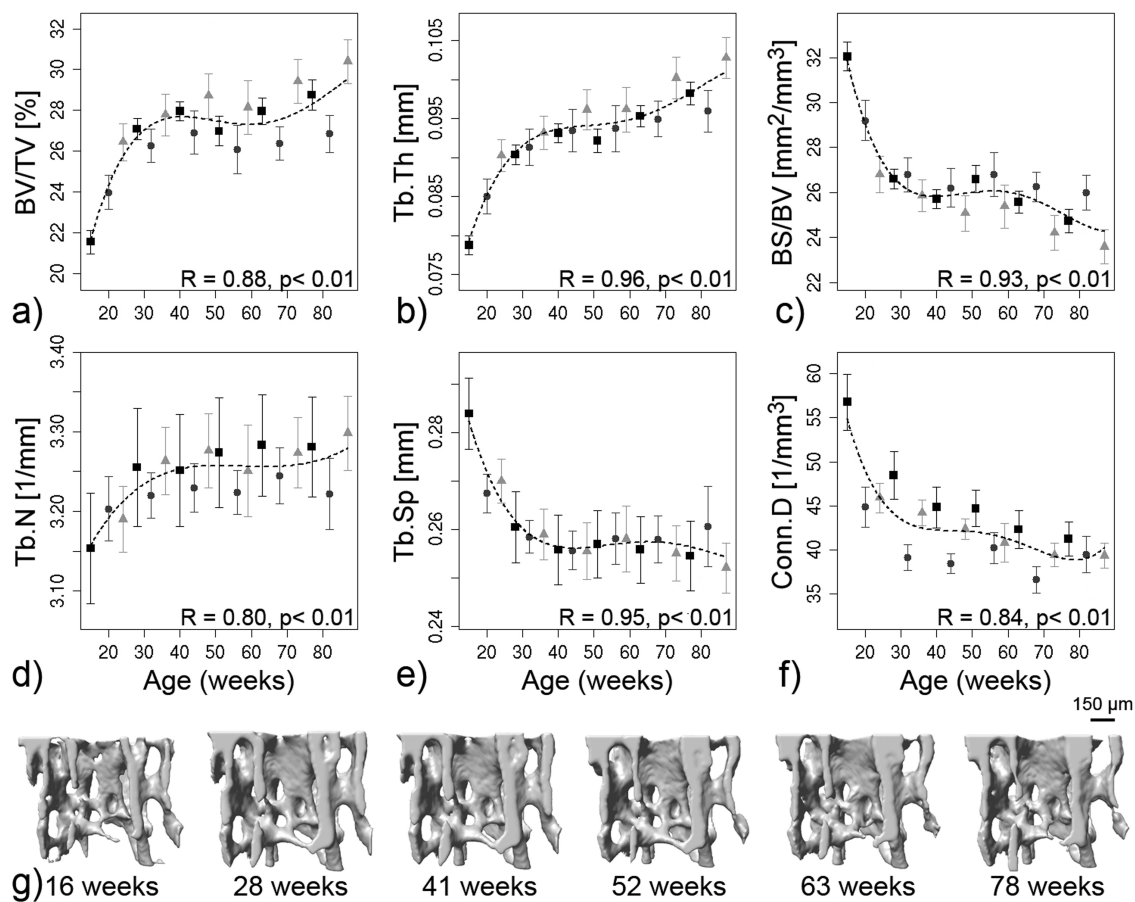


Figure 4.7: Figures of trabecular analysis in the sixth caudal vertebra. a) Bone volume fraction (BV/TV), b) Trabecular thickness (Tb.Th), c) Specific bone surface (BS/BV), d) Trabecular number (Tb.N), e) Trabecular separation (Tb.Sp) and f) Connectivity density (Conn.D). The different symbols are for the three different groups. The dotted line shows the polynomial fit. The R and p value indicate how well the fit represents the data. g) Section of trabecular bone of a representative mouse of group A. The numbers below the images indicate the age in weeks.

Bone microstructure

Static bone morphometry was calculated in either whole, trabecular or cortical bone, with a direct 3D model-independent algorithm [12]. Regions of interest were defined by automatic masks, as described previously [13]. Within the whole bone, apparent volume density (AVD) was calculated.

The trabecular mask of the vertebra excluded the growth plates and the center almost void of trabecular bone. The trabecular parameters included total volume (Tb.TV), bone volume fraction (BV/TV), specific bone surface (BS/BV), trabecular thickness (Tb.Th), trabecular separation (Tb.Sp), trabecular number (Tb.N), and connectivity density (Conn.D).

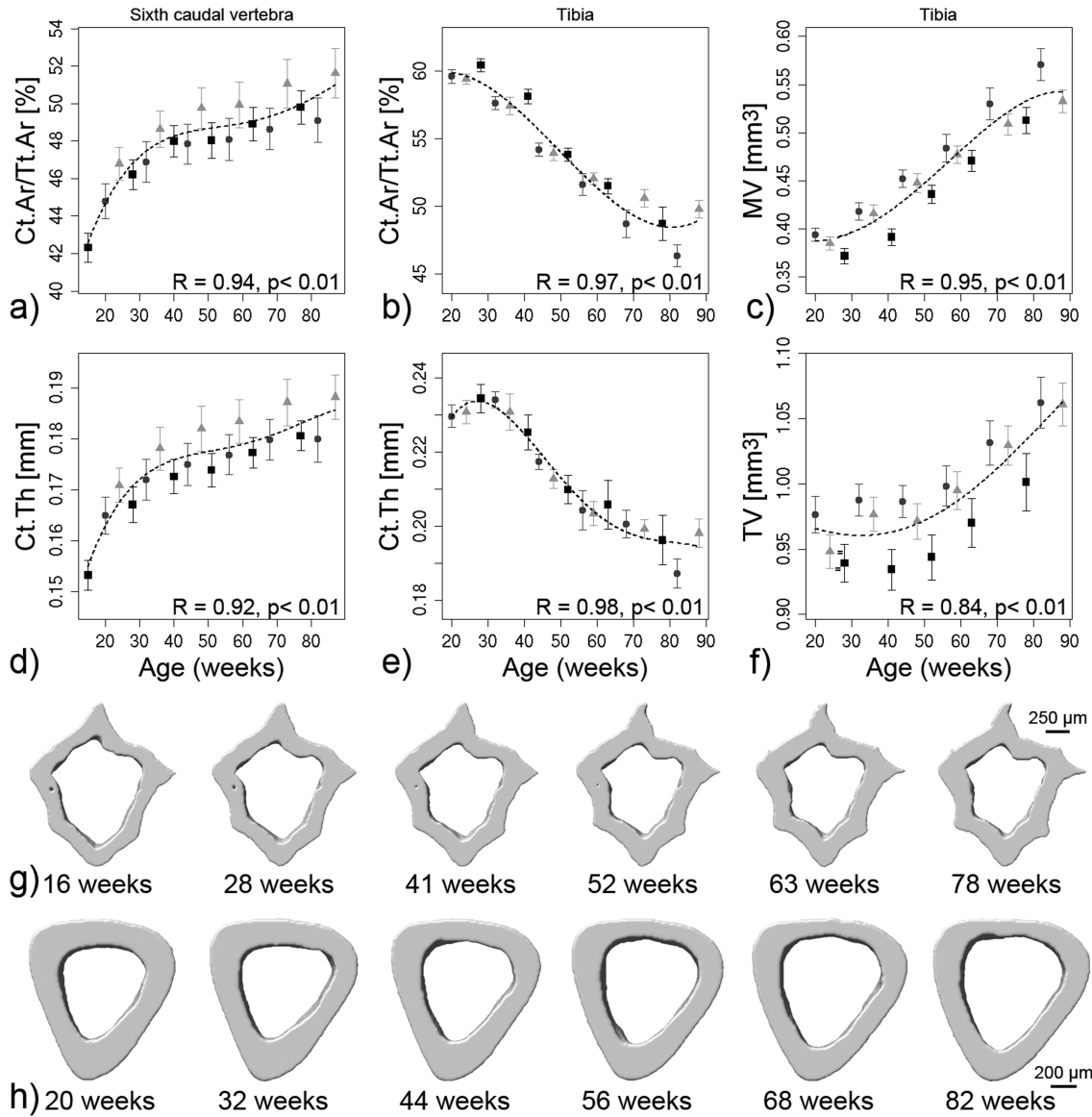


Figure 4.8: Figures of cortical analysis in sixth caudal vertebra and tibia. a) Cortical area fraction (Ct.Ar/Tt.Ar) of vertebra, b) Ct.Ar/Tt.Ar of tibia, c) Marrow volume (MV) of tibia, d) Cortical thickness (Ct.Th) of vertebra, e) Ct.Th of tibia, and f) Tissue volume (TV) of tibia. The different symbols are for the three different groups. The dotted line shows the polynomial fit. The R and p value indicate how well the fit represents the data. g) Cross-section of cortical bone of the vertebra of a representative mouse of group A. h) Cross-section of cortical bone in the tibia of a representative mouse of group B. The numbers below the images g) and h) indicate the age in weeks.

The vertebral cortical mask comprised 70% of the length of the whole vertebra, and for calculation of cortical parameters the complete trabecular structure was removed from the bone. Even though the center of the tibia was calculated for each scan, the scanned volumes at follow-up times were not exactly the same. Therefore, to ensure the same region of the tibia was analyzed for the serial scans, the center 80 slices present at all time points (as determined from registration) were analyzed. The cortical masks included the cortical bone and marrow space.

Within the cortical masks, total volume (Ct.TV), marrow volume (Ct.MV), cortical area fraction (Ct.Ar/Tt.Ar), and average cortical thickness (Ct.Th) were calculated.

The tissue mineral density (TMD) was calculated in the trabecular and cortical region of the vertebra and in the tibia, by using the thresholded files as a mask for the grayscale image.

Bone remodeling

Dynamic bone morphometry parameters were calculated with a recently validated technique [10]. For this procedure, scans of follow-up time points were rotated and translated (registered) to match the orientation of the previous scan. Thus, the same cross-section (or bone volume) can be visualized at serial time points, which allows observation of the changing bone microstructure over time (see Fig. 4.7g). From these images it is then possible to visually observe where bone was formed or resorbed between time points, but to better localize these sites of formation and resorption and to allow morphometric analysis of remodeling sites, follow-up scans were superimposed on each other. With this step, sites present only at the initial time point, sites only present at the subsequent time point, and sites present at both time points can be colored differently (see Fig. 4.9c). The voxels only present at the initial time point must have been removed between scans and are considered resorbed bone (blue). Similarly, voxels only present at the subsequent time point must have been added and therefore are representative of formed bone (yellow). Furthermore, for voxels present at both time points no measureable changes occurred, and these sites are regarded as constant bone (gray). With this procedure, volumes of bone formation or resorption between time points could be identified and analyzed morphometrically. The dynamic bone morphometry parameters included bone formation rate (BFR), bone resorption rate (BRR), mineral apposition rate (MAR), mineral resorption rate (MRR), mineralizing surface (MS), and eroded surface (ES). For the vertebra, these parameters were calculated in the trabecular bone, while for the tibia the analysis was split up in an examination of the remodeling sites at the endosteal- and periosteal-side of the cortex.

Bone mechanics

To test how mechanical properties of the bone changed with age, three-dimensional μ FE models, consisting of approximately 1,800,000 elements, were created of the vertebra, with simplified discs added on top and bottom to mimic intervertebral discs (Fig. 4.10e). All voxels were converted to 8 node brick elements, and assigned

Table 4.2: R and p-values of correlations between percentage change in bone strength and percentage change in apparent volume density in sixth caudal vertebra.

	Δ AVD [%]		
	Weeks	R	p
Δ Strength [%]	15-28	0.95	<0.001
	20-32	0.89	<0.01
	24-36	0.91	<0.01
	28-40	0.86	<0.01
	32-44	0.84	<0.05
	36-48	0.91	<0.01
	40-51	0.91	<0.01
	44-56	0.89	<0.01
	48-59	0.90	<0.01
	51-63	0.91	<0.001
	56-68	0.94	<0.001
	59-73	0.91	<0.01
	63-77	0.78	<0.05
	68-82	0.92	<0.01
	73-87	0.84	<0.05

a Young's Modulus of 14.8 Gpa and poisson's ratio of 0.3, as previously validated for caudal vertebrae [14]. The top was displaced 0.1%, while the bottom was constrained in all directions. The force resulting from this displacement was used to scale strain energy density (SED) in the cortical and trabecular region to a force of 4N, which was recently shown to be the average force to which caudal vertebrae are subjected physiologically [15]. With the Pistoia criterion, from which bone strength can be defined by simulating compression such that 2% of all elements have an effective strain larger than 7000 microstrain [16], the strength of the whole bone was estimated for each mouse at each time point. Also, the fraction of load carried by the cortical bone was approximated, by calculating the strain energy dissipated in the cortex as a fraction of the total strain energy [17]. Furthermore, to test whether the changes in bone mass had an effect on mechanical properties of the whole bone, correlations between changes in AVD and changes in bone strength were performed.

The μ FE models were solved using a parallel finite element solver (ParFE) with an algebraic multigrid preconditioner [18]. The simulations ran on a Cray XT5 super computing system composed of 22,128 cores and 29 TB of physical RAM at the Swiss National Supercomputing Center (CSCS, Manno, Switzerland).

As for the tibia only a slab of cortical bone was available, it was not possible to create realistic μ FE models which should include the whole bone. Instead,

the resistance against bending was investigated in the center 80 slices, by calculating the properties maximal and minimal moment of inertia (I_{max} , I_{min}). Furthermore, the ability to withstand torsional load was calculated from the polar moment of inertia (J). To allow comparison, these properties were also derived for the cortex of the vertebra.

Data analysis

Statistical analysis was performed with the software package R (R: A Language and Environment for Statistical Computing) [19]. For all parameters a polynomial curve (fourth order) was fitted to the averaged data. Percent changes in static, dynamic, and mechanical parameters were calculated from these fits, unless otherwise indicated. P-values smaller than 0.05 were considered significant. All data are shown as mean \pm standard error.

4.2.3 Results

Body mass

The mice gained on average 20% weight throughout the study (Fig. 4.6). At week 20 the weight ranged from 21 to 28 gram, while on the day of sacrifice the weight ranged from 23-32 gram. Five mice died or were sacrificed prior to the end of the experiment due to aging disabilities (4 out of 5 were sacrificed in the last 3 months of the experiment).

Bone microstructure

In the trabecular bone of the vertebra, BV/TV increased 27% between week 16 and 41, declined 2% thereafter, but recovered again, and increased up to 88 weeks by 36% of the initial value (Fig. 4.7a). Tb.Th showed a similar temporal curve as BV/TV. Tb.Th had a value of 0.080 mm at week 16 and increased rapidly by 18% up to week 41, stabilized between week 40 and 59 (<1% change), and increased further by 7% between week 59 and 88 to a value of 0.101 mm (Fig. 4.7b). The profile of BS/BV over time was opposite compared to Tb.Th, and decreased by 23% between week 16 and 88 (Fig. 4.7c). Similar to an increase in Tb.Th, a decrease in BS/BV indicates that less bone surface is present per bone volume, and, consequently, that bone structures become thicker. This is also implied by the decrease of 9% in Tb.Sp observed between week 16 and 41 (Fig. 4.7e). On the contrary, Tb.N increased slightly by 3% between week 16 and 41, but was constant for the remainder of the experiment (Fig. 4.7d). This suggests, as has

Table 4.3: Dynamic parameters in trabecular region of the sixth caudal vertebra, and on endosteal and periosteal side of the cortex for the tibia.

Average over weeks	BFR [%/d]	BRR [%/d]	MAR [$\mu\text{m}/\text{d}$]	MRR [$\mu\text{m}/\text{d}$]	MS [%]	ES [%]
Caudal vertebra						
15-28	0.363 \pm 0.10	0.042 \pm 0.02	0.27 \pm 0.03	0.25 \pm 0.06	68 \pm 4.6	16 \pm 3.9
20-32	0.165 \pm 0.08	0.051 \pm 0.03	0.21 \pm 0.04	0.20 \pm 0.06	53 \pm 9.3	24 \pm 6.2
24-36	0.140 \pm 0.06	0.067 \pm 0.04	0.22 \pm 0.05	0.22 \pm 0.08	49 \pm 5.7	29 \pm 6.6
28-40	0.097 \pm 0.05	0.050 \pm 0.02	0.18 \pm 0.03	0.19 \pm 0.04	47 \pm 6.4	29 \pm 4.6
32-44	0.074 \pm 0.04	0.052 \pm 0.06	0.16 \pm 0.03	0.16 \pm 0.06	42 \pm 5.2	30 \pm 5.1
36-48	0.107 \pm 0.04	0.078 \pm 0.04	0.20 \pm 0.04	0.24 \pm 0.07	46 \pm 7.2	32 \pm 5.4
40-51	0.084 \pm 0.03	0.129 \pm 0.06	0.20 \pm 0.02	0.28 \pm 0.06	38 \pm 7.9	42 \pm 7.5
44-56	0.064 \pm 0.05	0.096 \pm 0.10	0.17 \pm 0.03	0.24 \pm 0.08	37 \pm 8.0	36 \pm 6.4
48-59	0.082 \pm 0.04	0.106 \pm 0.05	0.20 \pm 0.02	0.26 \pm 0.06	39 \pm 8.4	40 \pm 5.6
51-63	0.125 \pm 0.03	0.075 \pm 0.03	0.22 \pm 0.02	0.21 \pm 0.03	47 \pm 5.9	32 \pm 5.5
56-68	0.091 \pm 0.07	0.066 \pm 0.02	0.19 \pm 0.04	0.20 \pm 0.05	41 \pm 8.7	34 \pm 7.5
59-73	0.120 \pm 0.06	0.056 \pm 0.02	0.20 \pm 0.04	0.18 \pm 0.04	50 \pm 6.8	31 \pm 5.5
63-77	0.075 \pm 0.02	0.053 \pm 0.02	0.16 \pm 0.02	0.17 \pm 0.07	44 \pm 4.1	33 \pm 3.5
68-82	0.079 \pm 0.05	0.071 \pm 0.06	0.16 \pm 0.04	0.19 \pm 0.08	42 \pm 4.8	35 \pm 3.1
73-87	0.071 \pm 0.02	0.046 \pm 0.02	0.16 \pm 0.03	0.16 \pm 0.04	44 \pm 4.5	33 \pm 4.8
Tibia endocortical						
20-32	0.018 \pm 0.01	0.064 \pm 0.02	0.34 \pm 0.09	0.38 \pm 0.06	15 \pm 7.5	44 \pm 8.5
24-36	0.009 \pm 0.01	0.068 \pm 0.02	0.28 \pm 0.09	0.36 \pm 0.05	9 \pm 4.0	44 \pm 9.2
28-40	0.012 \pm 0.01	0.046 \pm 0.02	0.28 \pm 0.06	0.30 \pm 0.08	20 \pm 10.0	53 \pm 9.0
32-44	0.006 \pm 0.01	0.066 \pm 0.02	0.25 \pm 0.08	0.33 \pm 0.06	11 \pm 4.8	66 \pm 11.9
36-48	0.009 \pm 0.01	0.069 \pm 0.02	0.23 \pm 0.08	0.37 \pm 0.05	15 \pm 7.2	66 \pm 11.7
40-51	0.006 \pm 0.01	0.102 \pm 0.02	0.29 \pm 0.08	0.44 \pm 0.05	7 \pm 5.3	68 \pm 18.3
44-56	0.008 \pm 0.01	0.072 \pm 0.04	0.23 \pm 0.05	0.32 \pm 0.06	12 \pm 10.5	57 \pm 12.0
48-59	0.013 \pm 0.02	0.075 \pm 0.03	0.28 \pm 0.14	0.37 \pm 0.06	13 \pm 8.3	49 \pm 12.2
51-63	0.007 \pm 0.01	0.088 \pm 0.02	0.25 \pm 0.05	0.38 \pm 0.05	8 \pm 4.3	51 \pm 8.6
56-68	0.003 \pm 0.00	0.098 \pm 0.02	0.20 \pm 0.06	0.36 \pm 0.04	4 \pm 2.8	51 \pm 5.6
59-73	0.010 \pm 0.01	0.068 \pm 0.03	0.21 \pm 0.07	0.31 \pm 0.08	11 \pm 8.7	43 \pm 6.1
63-77	0.006 \pm 0.01	0.084 \pm 0.04	0.20 \pm 0.06	0.32 \pm 0.08	7 \pm 5.0	51 \pm 12.5
68-82	0.006 \pm 0.01	0.079 \pm 0.04	0.19 \pm 0.04	0.31 \pm 0.13	9 \pm 7.9	48 \pm 9.1
73-87	0.016 \pm 0.01	0.054 \pm 0.03	0.24 \pm 0.09	0.29 \pm 0.09	16 \pm 9.8	38 \pm 13.6
Tibia periosteal						
20-32	0.013 \pm 0.01	0.010 \pm 0.01	0.21 \pm 0.03	0.23 \pm 0.07	38 \pm 8.0	20 \pm 16.1
24-36	0.029 \pm 0.03	0.004 \pm 0.00	0.23 \pm 0.05	0.19 \pm 0.05	44 \pm 5.6	10 \pm 7.1
28-40	0.006 \pm 0.01	0.011 \pm 0.01	0.18 \pm 0.07	0.20 \pm 0.07	21 \pm 12.2	37 \pm 22.1
32-44	0.006 \pm 0.01	0.006 \pm 0.01	0.17 \pm 0.06	0.18 \pm 0.08	19 \pm 11.4	25 \pm 10.5
36-48	0.001 \pm 0.00	0.006 \pm 0.01	0.15 \pm 0.03	0.17 \pm 0.03	17 \pm 9.7	35 \pm 27.0
40-51	0.008 \pm 0.01	0.006 \pm 0.01	0.19 \pm 0.05	0.20 \pm 0.10	30 \pm 11.2	13 \pm 9.7
44-56	0.006 \pm 0.01	0.002 \pm 0.00	0.17 \pm 0.03	0.15 \pm 0.03	30 \pm 14.2	11 \pm 9.3
48-59	0.011 \pm 0.02	0.000 \pm 0.00	0.19 \pm 0.04	0.14 \pm 0.01	38 \pm 9.7	4 \pm 4.3
51-63	0.019 \pm 0.02	0.003 \pm 0.01	0.22 \pm 0.06	0.17 \pm 0.06	41 \pm 8.5	6 \pm 9.1
56-68	0.022 \pm 0.02	0.001 \pm 0.00	0.21 \pm 0.03	0.14 \pm 0.03	45 \pm 4.6	3 \pm 4.1
59-73	0.020 \pm 0.02	0.000 \pm 0.00	0.19 \pm 0.05	0.12 \pm 0.01	45 \pm 4.6	2 \pm 1.9
63-77	0.020 \pm 0.02	0.003 \pm 0.01	0.18 \pm 0.05	0.17 \pm 0.14	44 \pm 6.5	3 \pm 3.4
68-82	0.022 \pm 0.03	0.003 \pm 0.01	0.19 \pm 0.06	0.15 \pm 0.06	40 \pm 9.2	5 \pm 4.8
73-87	0.017 \pm 0.01	0.000 \pm 0.00	0.17 \pm 0.02	0.11 \pm 0.01	42 \pm 4.9	3 \pm 2.7

often been hypothesized, that no new trabeculae form after the bone has reached maturity. Furthermore, Conn.D decreased 26% between week 16 and 88, with the steepest decrease between week 16 and 41 (Fig. 4.7f). Visually, these changes can be appreciated in figure 4.7g, where a section of a vertebra scanned at week 16, 28, 41, 52, 63, and 78 (group A) is presented.

In the cortical bone of the vertebra a continuous increase in Ct.Ar/Tt.Ar of up to 19% (Fig. 4.8a), and Ct.Th of up to 19% (Fig. 4.8d) could be observed, with a slowdown in gain from week 40 on. MV decreased 10% over time, while TV increased 6%, indicating that the increase in Ct.Th was through apposition on both endosteal and periosteal side of the cortex. This is also apparent in a diaphyseal cross-section of a vertebra (Fig. 4.8g).

In the tibia, the temporal changes in the cortical bone were quite different from the vertebra. Ct.Ar/Tt.Ar decreased from 60% at week 20 to 49% at week 88 (Fig. 4.8b). This reduction was caused by a continuous decrease in Ct.Th of 15% (Fig. 4.8e). The cortex was resorbed on the endosteal side, as indicated by the 40% increase in MV (Fig. 4.8c), while it was gaining on the periosteal side, as pointed out by the 10% increase in TV (Fig. 4.8f). Expansion of the cortex on the periosteal side, with removal of bone on the endosteal side can clearly be seen in figure 4.8h.

Bone mineral density

The mineralization increased 9% in the trabecular bone and 8% in the cortical bone of the caudal vertebra between week 16 and 88. In the trabecular bone TMD was 522 mgHA/cm³ at week 16 and 567 mgHA/cm³ at week 88. The mineralization in the cortical bone was 13-14% higher than the mineralization in the trabecular bone at all time points, indicating similar speed of mineralization for both compartments. For both trabecular and cortical bone there was a more rapid increase in mineralization between week 16 and 40, and a more constant value between week 40 and 88. In the cortical bone of the tibia, the mineralization was greater than in the vertebra, and even more constant; the mineralization deviated only by 1.5% from 775 mgHA/cm³ throughout the study.

Bone remodeling

Figure 4.9a shows overlays of vertebral cross-sections at follow-up time points. In this image, yellow indicates bone formation between time points, while blue

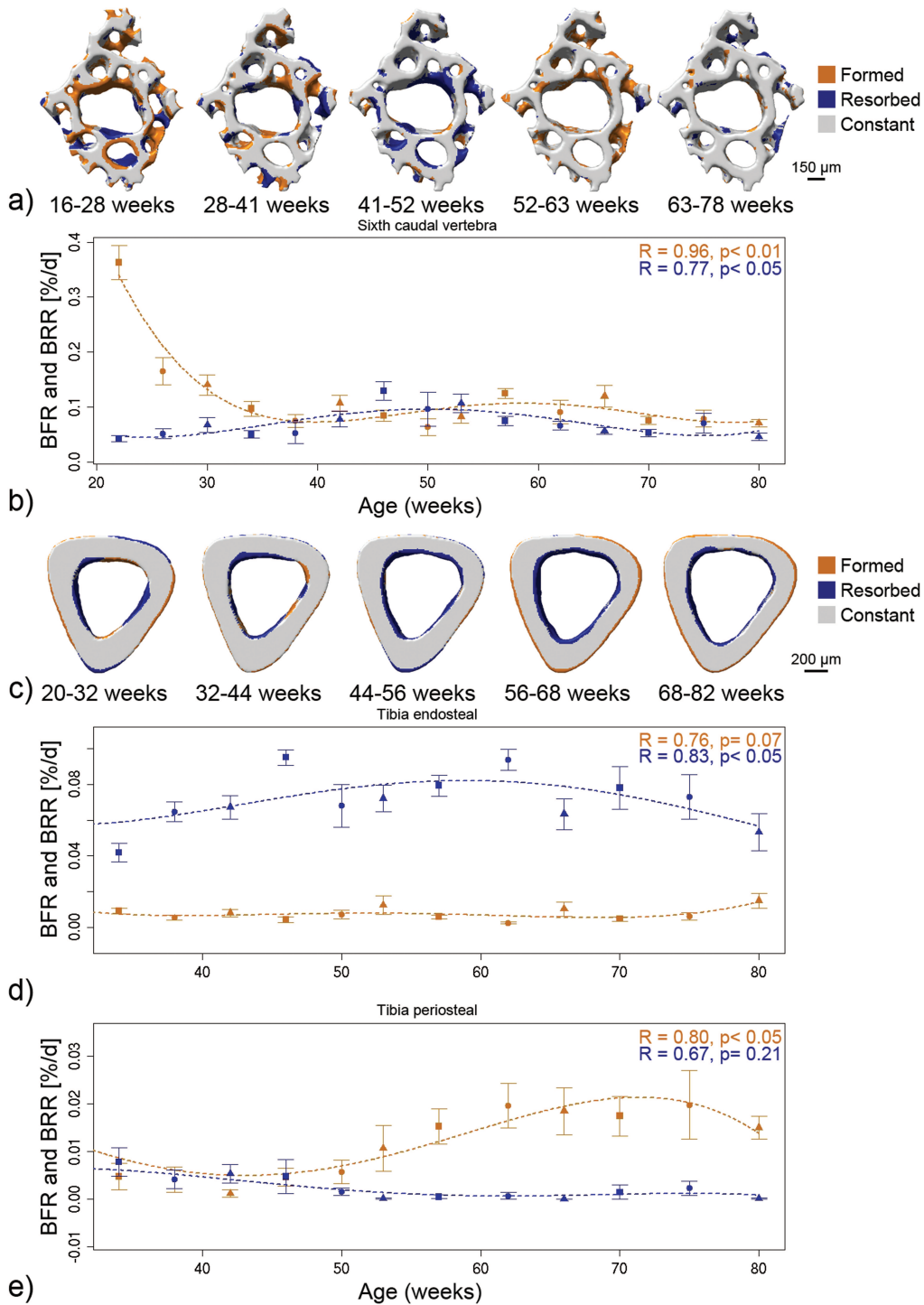


Figure 4.9: Figures of dynamic bone morphometry. a) Visual representation of overlaid vertebral cross-sections at follow-up time points. b) Bone formation rate (BFR, in yellow) and bone resorption rate (BRR, in blue) in the vertebra. c) Visual representation of overlaid tibial cross-sections at follow-up time points. d) BFR (in yellow) and BRR (in blue) on the endosteal side of cortical bone in the tibia. e) BFR (in yellow) and BRR (in blue) on the periosteal side of cortical bone in the tibia. Numbers below the images a and c indicate the age from which the overlays were created. The different symbols in figures b, d and e are for the three different groups. The dotted line shows the polynomial fit. The R and p value indicate how well the fit represents the data.

represents bone resorption. Thus, as the number of yellow sites is greater in the first image than in the following ones, this implies bone formation reduces at older ages (Fig. 4.9a). This was also quantified, and it was found that BFR at week 88 was only 22% of the value at week 16. On the contrary, BRR increased by 20% between week 16 and 88, but at most time points (not between week 40 and 59) had a lower value than BFR (Fig. 4.9b). Furthermore, it was observed that there was a peak in BRR (205% of value at week 16) at week 50, at which time point a drop in BV/TV occurred. This was followed by a peak in BFR at week 57, with 144% of the value at week 38. These peaks were a result of increased thickness of resorption cavities (MRR) around week 50, and increased thickness of formation packets (MAR) around week 57 (Table 4.3). The peaks in BRR and BFR were less reflected by MS or ES. The surface occupied by formation sites, MS, decreased 38% between week 16 and 46 and afterwards increased slightly by 5% up to week 88. The surface occupied by resorption sites, ES, increased by 113% between week 16 and 50, after which a minor decrease of 7% occurred.

In the tibia, cortical expansion on the periosteal side and resorption on the endosteal side was clear from overlaid follow-up images (Fig. 4.9c). Alike, BFR was greater than BRR on the periosteal side (Fig. 4.9d), while BRR was greater than BFR on the endosteal side (Fig. 4.9e). On average, BFR was 1.5 times greater on the periosteal side than endosteal side, while BRR was 25 times larger on the endosteal side than on the periosteal side (BRR was close to 0 on the periosteal side).

Bone mechanics

In the vertebra the strength increased rapidly between week 16 and 41 by 21%, and slowly increased another 5% up to week 88 (Fig. 4.10a). Significant correlations were found between percent change in AVD and percent change in bone strength ($R > 0.78$, $p < 0.05$), with the rule that the greater the increase in AVD, the greater the increase in bone strength (Table 4.2). This indicated that formed bone contributed to bone strength throughout age. As the bone became stronger, SED in both cortical (Fig. 4.10b) and trabecular region (Fig. 4.10c) decreased by 38% and 37% respectively. The fraction of load carried by the cortex was on average 82% and did not change with age (Fig. 4.10d).

The cortex of the vertebra became stronger against bending and torsional forces, as indicated by the continuous increase in I_{min} (Fig. 4.10f), I_{max} (Fig. 4.10g), and

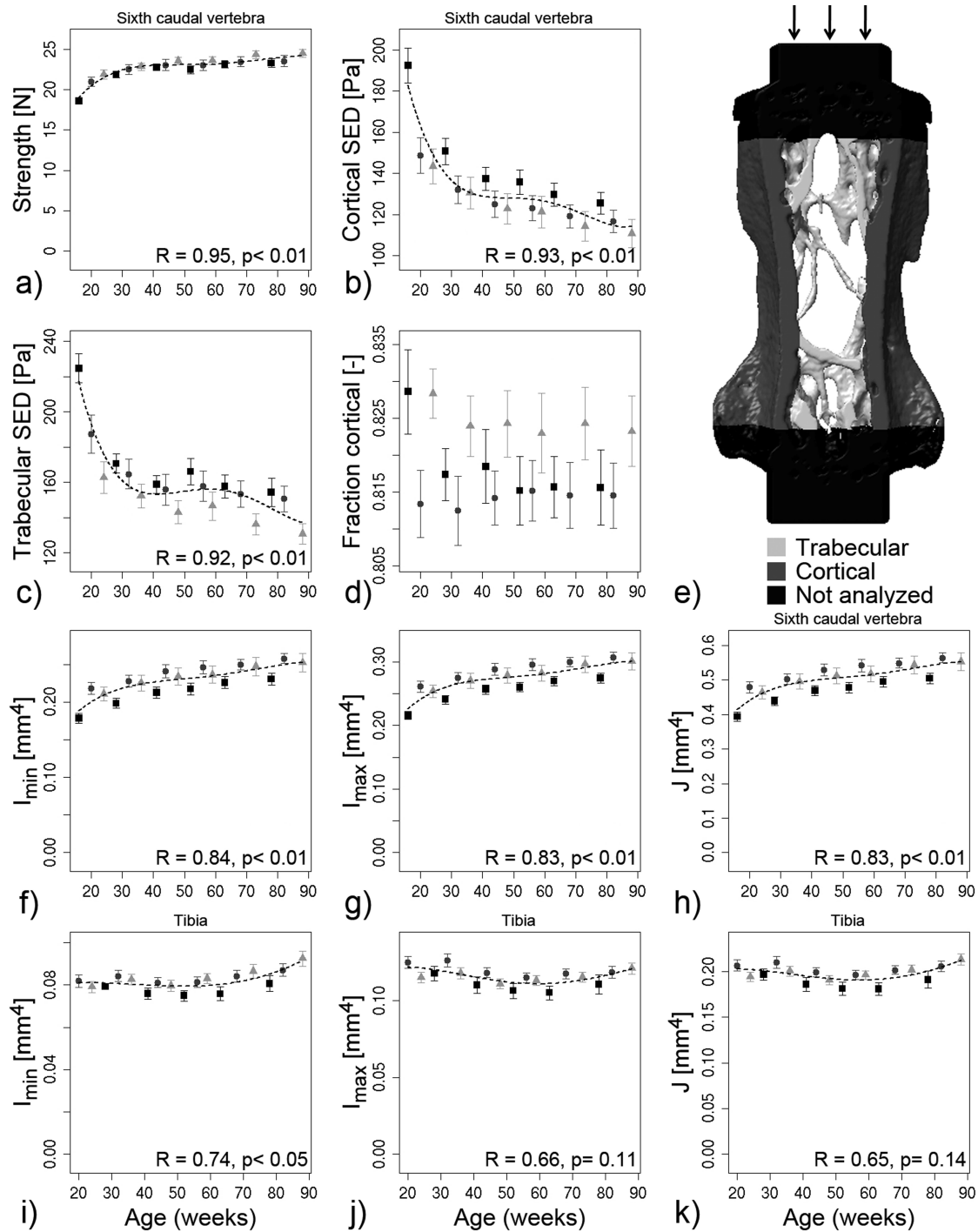


Figure 4.10: Figures of mechanical properties. a) Strength of vertebra, b) Strain energy density (SED) in cortical bone, c) SED in trabecular bone, and d) Fraction of load carried by the cortex of the vertebra. e) Representation of the FE model with different gray colors for trabecular and cortical bone which were analyzed to calculate the fraction of load carried by the cortex. f) Minimal moment of inertia (I_{min}), g) Maximal moment of inertia (I_{max}), and h) polar moment of inertia (J) in the vertebra. i) Minimal moment of inertia (I_{min}), g) Maximal moment of inertia (I_{max}), and h) polar moment of inertia (J) in the tibia.

J (Fig. 4.10h), which reached 134%, 133% and 133% of their initial value by week 88 respectively.

Even though in the tibia there was a large decrease in Ct.Th, the resistance against bending remained at an equal level, as indicated by I_{min} (Fig. 4.10i) and I_{max} (Fig. 4.10j), which did not change significantly over time for either group. Furthermore, J did not change significantly, showing that the tibia remained strong against torsional loads (Fig. 4.10k).

4.2.4 Discussion

This paper describes how bone microstructure, bone remodeling, and bone mechanical properties were modulated by age in the sixth caudal vertebra and tibia in mice in a longitudinal fashion. It was found that with age, bone architecture and dynamics changed, but did not influence the mechanical properties negatively. In the sixth caudal vertebra, the strength of the vertebra increased up to the end of the study, and in the tibia the resistance against bending and torsion remained unaltered, as well as the mineralization of the bone. One study that investigated the effect of age on bone at several skeletal sites included a caudal vertebra, and found, in agreement with our data, that BV/TV in the seventh caudal vertebra increases up to 20 months of age in BALB/C mice [8]. Also, the notion that in the tibia Ct.Th decreases with age, with an increase in the medullary cavity and increase in the periosteal dimension, is supported by a study in male C57Bl/6 mice, where the same trend is shown up to an age of 24 months [6]. Furthermore, others have found the resistance against bending and torsional loads to remain at the same level up to 12 months of age in the diaphysis of the tibia of C57Bl/6 mice [3, 9]. On the contrary, Buie et al. did not find changes in Ct.Th and decreases in TV and MV [9]. However, when examining the representative images of this study, it appeared that the location at the diaphysis from which the data were taken differed between time points. This drawback was taken care of in our study by using registration to ensure the same region was analyzed and visualized at follow-up time points and thus represents, next to the longitudinal setup, an advantage over previous long-term studies.

Interestingly, the apposition on the cortices with age was different between the caudal vertebra and tibia. This is probably related to the main loading direction the bone is subjected to. In the tibia, loading at the diaphysis is mainly through bending, for which apposition on the periosteal side is beneficial. On the other hand, a caudal vertebra is mainly loaded by compression, in which case

apposition on both endosteal and periosteal side is advantageous. This might indicate that even with age bones adapted to their mechanical environment.

Comparable results to the tibia have been presented for the femur, another appendicular bone. Increases on the periosteal side and decreases on the endosteal side of the cortex at the diaphysis of the femur have been reported, often associated with a decrease in Ct.Th, but also preservation of resistance against bending and torsional forces [2,4,5,8], indicating that in the femur also the bone strength in the main loading direction is preserved with age.

Although dynamic rates calculated in our study cannot be directly compared to histomorphometric values gained in other studies, the trends can be compared. A reduction in BFR with age was found in the fourth lumbar vertebra in CW-1 mice [20], which is in agreement with our results. Glatt et al. [5] could not examine remodeling rates in mice over 12 months of age, since labels were too few in metaphysis of femur. This phenomenon is reflected in the low remodeling rates from 40 weeks on in our study. This illustrates the advantage of extracting dynamic rates from micro-CT data, where longer time intervals can be chosen and results are not dependent on a few labels.

Unexpectedly, for all mice a drop in BV/TV was observed between an age of 40 and 60 weeks, which recovered afterwards. The reason for this is unclear. One explanation could be that the physical activity of mice reduces with age, as in humans, leading to a lower demand on the bones with a result of lower BV/TV around an age of 40 weeks. Nevertheless, in this case no recovery would have been expected afterwards. The decline in BV/TV from week 40 on was reflected by an increase in BRR, while the following recovery was mostly an effect of increased BFR. The bone adaptation during the decline was mostly influenced by the thickness of resorption pits (MRR), while the surface occupied by resorption sites (ES) remained largely unaffected. Similarly, the recovery phase originated from an increase in thickness of formation packets (MAR), more than that the surface occupied by formation sites (MS) was affected. It is interesting to note that this is a different effect as we saw in load adaptation, where changes in BFR and BRR were mostly an effect of changes in MS and ES. Changes in MAR and MRR are likely related to changes in osteoblast and osteoclast activity. In agreement with this, it was found in cell cultures of different age populations of mice, that with age the osteoclastogenesis is promoted, and that the relationship between osteoblast and

osteoclasts is altered [21, 22]. Also, in the fourth lumbar vertebra in CW-1 female mice, acid phosphatase, which is a marker for bone resorption, increased between 3 and 30 months of age, indicating cell activity changes with age [23].

A limitation of the study design was that the three groups were scanned consecutively, rather than in parallel over the complete time range (to prevent radiation effects). On the other hand, since all three groups showed the same evolution over time, the results seem reproducible, and allowed to scan up to an age of 88 weeks. Furthermore, a longitudinal setup is still considered more reliable than a cross-sectional design (e.g. in a cross-sectional design we could have found that BV/TV at week 82 (group B) was lower than BV/TV at week 73 (group C), and would have concluded that the bone volume fraction decreases with age).

A shortcoming in the FE model was that homogeneous properties were assumed across ages. Nevertheless, when investigating tissue mineral density with age, which has been shown to be correlated to the elastic modulus [24], it was found that the increase (up to 9%) was rather small compared to the increase in BV/TV (up to 30%), or Ct.Ar/Tt.Ar (up to 17%). Furthermore, when greater mineralization would have been assumed in the FE model at later time points, the strength would have had an even greater increase, and is currently slightly under-estimated.

In conclusion, we have provided an extensive long-term study on the effect of age on a caudal vertebra and tibia in mice. We have shown that even during aging, bone is able to optimize its strength. In the sixth caudal vertebra this concept was supported by an increase in bone strength, a slight increase in mineralization, and significant correlations between changes in bone strength and changes in apparent volume density between all time points, up to 88 weeks of age. In the tibia this notion was emphasized by sustained resistance against bending and torsion, and a constant mineralization. In future, it could be investigated if anabolic treatment, like loading, could further enhance bone strength in aged mice.

4.2.5 Funding source

The authors gratefully acknowledge funding from the European Union for the Osteoporotic Virtual Physiological Human project (VPHOP FP7-ICT2008-223865) and computational time from the Swiss National Supercomputing Center (CSCS, Manno, Switzerland).

References

- [1] W.G. Beamer, L.R. Donahue, C.J. Rosen, and D.J. Baylink. Genetic variability in adult bone density among inbred strains of mice. *Bone*, 18(5):397–403, 1996.
- [2] C. Price, B.C. Herman, T. Lufkin, H.M. Goldman, and K.J. Jepsen. Genetic variation in bone growth patterns defines adult mouse bone fragility. *J Bone Miner Res*, 20(11):1983–1991, 2005.
- [3] J.M. Somerville, R.M. Aspden, K.E. Armour, K.J. Armour, and D.M. Reid. Growth of C57BL/6 mice and the material and mechanical properties of cortical bone from the tibia. *Calcif Tissue Int*, 74(5):469–475, 2004.
- [4] V.L. Ferguson, R.A. Ayers, T.A. Bateman, and S.J. Simske. Bone development and age-related bone loss in male C57BL/6J mice. *Bone*, 33(3):387–398, 2003.
- [5] V. Glatt, E. Canalis, L. Stadmeier, and M.L. Bouxsein. Age-related changes in trabecular architecture differ in female and male C57BL/6J mice. *J Bone Miner Res*, 22(8):1197–1207, 2007.
- [6] B.P. Halloran, V.L. Ferguson, S.J. Simske, A. Burghardt, L.L. Venton, and S. Majumdar. Changes in bone structure and mass with advancing age in the male C57BL/6J mouse. *J Bone Miner Res*, 17(6):1044–1050, 2002.
- [7] A. Weiss, I. Arbell, E. Steinhagen-Thiessen, and M. Silbermann. Structural changes in aging bone: osteopenia in the proximal femurs of female mice. *Bone*, 12(3):165–172, 1991.
- [8] M.D. Willingham, M.D. Brodt, K.L. Lee, A.L. Stephens, J. Ye, and M.J. Silva. Age-related changes in bone structure and strength in female and male BALB/c mice. *Calcif Tissue Int*, 86(6):470–483, 2010.
- [9] H.R. Buie, C.P. Moore, and S.K. Boyd. Postpubertal architectural developmental patterns differ between the L3 vertebra and proximal tibia in three inbred strains of mice. *J Bone Miner Res*, 23(12):2048–2059, 2008.
- [10] F.A. Schulte, F.M. Lambers, G. Kuhn, and R. Müller. In vivo micro-computed tomography allows direct three-dimensional quantification of both bone formation and bone resorption parameters using time-lapsed imaging. *Bone*, 48:433–442, 2011.
- [11] P. Thevenaz, U.E. Ruttimann, and M. Unser. A pyramid approach to subpixel registration based on intensity. *IEEE Trans Image Process*, 7(1):27–41, 1998.

- [12] T. Hildebrand, A. Laib, R. Müller, J. Dequeker, and P. Ruegsegger. Direct three-dimensional morphometric analysis of human cancellous bone. *J Bone Miner Res*, 14(7):1167–1174, 1999.
- [13] F.M. Lambers, F.A. Schulte, G. Kuhn, D.J. Webster, and R. Müller. Mouse tail vertebrae adapt to cyclic mechanical loading by increasing bone formation rate and decreasing bone resorption rate as shown by time-lapsed *in vivo* imaging of dynamic bone morphometry. *Bone*, accepted, 2011.
- [14] Webster D.J., Morley P.L., van Lenthe G.H., and Müller R. A novel in vivo mouse model for mechanically stimulated bone adaptation—a combined experimental and computational validation study. *Comput Methods Biomech Biomed Engin*, 11(5):435–441, 2008.
- [15] B. Christen, B. van Rietbergen, F.M. Lambers, R. Müller, and K. Ito. Bone morphology allows estimation of loading history in a murine model of bone adaptation. *Biomech Model Mechanobiol*, accepted, 2011.
- [16] W. Pistoia, B. van Rietbergen, E.M. Lochmuller, C.A. Lill, F. Eckstein, and P. Ruegsegger. Estimation of distal radius failure load with micro-finite element analysis models based on three-dimensional peripheral quantitative computed tomography images. *Bone*, 30(6):842–848, 2002.
- [17] S. Kirmani, D. Christen, G.H. van Lenthe, P.R. Fischer, M.L. Bouxsein, L.K. McCready, L.J.3rd Melton, B.L. Riggs, S. Amin, R. Müller, and S. Khosla. Bone structure at the distal radius during adolescent growth. *J Bone Miner Res*, 24(6):1033–1042, 2009.
- [18] P. Arbenz, G.H. van Lenthe, U. Mennel, R. Müller, and M. Sala. A scalable multi-level preconditioner for matrix-free micro-finite element analysis of human bone structures. *Int J Numer Methods Eng*, 73:927–949, 2008.
- [19] R Development Core Team. R: A Language and Environment for Statistical Computing. *R Foundation for Statistical Computing, Vienna, Austria*, 2010.
- [20] B. Bar-Shira-Maymon, R. Coleman, A. Cohen, E. Steinhagen-Thiessen, and M. Silbermann. Age-related bone loss in lumbar vertebrae of CW-1 female mice: a histomorphometric study. *Calcif Tissue Int*, 44(1):36–45, 1989.
- [21] J. Cao, L. Venton, T. Sakata, and B.P. Halloran. Expression of RANKL and OPG correlates with age-related bone loss in male C57BL/6 mice. *J Bone Miner Res*, 18(2):270–277, 2003.

- [22] J.J. Cao, T.J. Wronski, U. Iwaniec, L. Phleger, P. Kurimoto, B. Boudignon, and B.P. Halloran. Aging increases stromal/osteoblastic cell-induced osteoclastogenesis and alters the osteoclast precursor pool in the mouse. *J Bone Miner Res*, 20(9):1659–1668, 2005.
- [23] B. Bar-Shira-Maymon, R. Coleman, E. Steinhagen-Thiessen, and M. Silbermann. Correlation between alkaline and acid phosphatase activities and age-related osteopenia in murine vertebrae. *Calcif Tissue Int*, 44(1):99–107, 1989.
- [24] L.M. Miller, W. Little, A. Schirmer, F. Sheik, B. Busa, and S. Judex. Accretion of bone quantity and quality in the developing mouse skeleton. *J Bone Miner Res*, 22(7):1037–1045, 2007.

4.3 Caudal vertebrae of mice remain mechanosensitive with age after cyclic loading

Floor M. Lambers¹, Claudia Weigt¹, Kathleen M. Koch¹, Friederike A. Schulte¹, Gisela Kuhn¹, and Ralph Müller¹

¹Institute for Biomechanics, ETH Zürich, Zürich, Switzerland

Abstract:

For developing treatment strategies against age-related bone loss, it is important to know whether bones remain responsive to mechanical stimuli with age. To investigate whether caudal vertebrae of mice remain mechanosensitive with age, load-induced bone adaptation was analyzed longitudinally in mice aged 15, 52, and 82 weeks at the start of loading. Results showed that for each age group there was a beneficial effect of loading. In the bone microstructure in 15- and 82-week-old mice, this was most pronounced in the trabecular bone, where the increase in bone volume density on top of the control groups was 20% and 18% respectively. In 52-week-old mice, on the other hand, the greatest effect of loading was observed in the cortical bone, where the cortical thickness decreased for the control group, but remained for the loaded group. For all ages, bone formation was greater in loaded groups, while bone resorption was smaller, with the largest effect on the surface of remodeling sites. Mineralizing surface was significantly greater for loaded than control group in 15- and 82-week-old mice (by 13%). For 52-week-old control mice, eroded surface exceeded mineralizing surface, while these were in balance for the loaded group. When investigating mechanosensitivity, it was found that bone formation occurred at sites with about 16% higher preceding strain energy density than at quiescent surfaces, while resorption occurred at sites where strain energy density was about 17% lower. Taken together, these results proof that mechanosensitivity is maintained with age in caudal vertebrae of mice.

Keywords:

Aging, mechanosensitivity, mechanical loading, *in vivo* micro-computed tomography, animal model

4.3.1 Introduction

The pathology that causes changes in bone microstructure with age is poorly understood. One common thought is that with age mechanosensitivity of bone is lost, leading to untargeted and unbalanced bone remodeling, and consequently loss of bone strength. The most common strategy to investigate whether mechanosensitivity is lost with age is through animal loading models, which provide a useful tool for exploring load-induced changes in bone remodeling with age. Results of animal studies are conflicting; several report no effect of loading [1–4], while others do see a benefit of loading or physical exercise [5–10]. These differences might be explained by different skeletal site, exact age, differences in loading protocol, and species or mouse strain. Furthermore, most previous studies had a cross-sectional design, which might obscure results, as starting points are not available. For example Brodt et al. did not see difference between loaded and control groups when only endpoints were used, but when scanning over time significant differences between groups were found [5]. Additionally, previous studies assessed mechanosensitivity on a global level only, by evaluating load-induced changes in the bone microstructure or remodeling rates. However, a comparison between local strains and the subsequent local remodeling response would give a better indication of mechanosensitivity, as this would indicate whether the bone remains mechanosensitive locally.

Therefore, the aim of this study was to longitudinally analyze load-induced bone adaptation in the sixth caudal vertebra of mice of three age groups, by evaluating effects on bone microstructure, bone remodeling and bone strength. Furthermore, to more accurately assess mechanosensitivity, strain energy density (SED) at surfaces where remodeling followed were compared to SED levels at quiescent surfaces.

4.3.2 Materials and methods

Study design

Female C57BL/6 mice (RCC Ltd, Füllinsdorf, Switzerland) at an age of 15 weeks (W15, n=5 8N, n=6 0N), 52 weeks (W52, n=6 8N, n=11 0N), and 82 weeks (W82, n=6 8N, n=5 0N) at the start of loading were enrolled in this experiment. Mice had free access to a standard diet and tap water, and were housed in an environmentally controlled room at a 12-hour light/dark cycle. To enable loading of the sixth caudal vertebra (CV6), pins were surgically inserted in the fifth and seventh caudal vertebrae three to six weeks before the start of loading. Three times per

week for six weeks the tails were fixed in a caudal axial compression device [11], and mechanical loading was applied either at 0N (control) or at 8N (loaded) at 10 Hz for 3000 cycles (5 min). *In vivo* micro-CT scans of CV6 were obtained at the start of loading for each group, and subsequently at week 4 and 6 for W15, at week 1, 2, 4, and 6 for W52, and at week 2, 4 and 6 for W82. During loading and micro-CT scans mice were anesthetized with isoflurane (2-2.5%, Provet Medical AG, Lyssach, Switzerland). For each CT-scan cooling down of the mice was prevented by heating the mouse bed at 35°C, and eye cream was applied to avoid desiccation of the cornea. All animal procedures were approved by the local authorities (Kantonales Veterinärämte Zürich, Zürich, Switzerland).

Bone microstructure

CV6 was scanned at a nominal isotropic resolution of 10.5 μm with an *in vivo* micro-CT scanner (vivaCT 40, Scanco Medical AG, Brüttisellen, Switzerland). Settings of the scanner were 55 kVp, 145 μA , 200 ms integration time, and 1000 projections per 180 degrees. From scoutviews taken in dorso-ventral direction CV6 was selected, and comprised a length of 4.4 mm. To correct for beam hardening, a correction algorithm provided by Scanco Medical AG was applied to all scans. Weekly, the scanner was calibrated for mineral equivalent value, and monthly for in place spatial resolution. The estimated dose, as provided by the manufacturer, was 640 mGy per scan.

Image data were Gauss filtered (sigma=1, support=1.2) and thresholded at 22% of maximum grayscale value. Bone static parameters were calculated within masks that automatically selected trabecular or cortical bone with a direct 3D approach [12]. In the whole bone apparent volume density (AVD) was calculated. In the cortical region, tissue volume (Ct.TV), bone volume (Ct.BV), marrow volume (MV), cortical area fraction (Ct.Ar/Tt.Ar), average cortical thickness (Ct.Th), maximum moment of inertia (I_{max}), and minimum moment of inertia (I_{min}) were calculated. The trabecular parameters included tissue volume (Tb.TV), bone volume (Tb.BV), bone volume fraction (BV/TV), specific bone surface (BS/BV), trabecular thickness (Tb.Th), trabecular spacing (Tb.Sp), trabecular number (Tb.N), and connectivity density (Conn.D). For all mice the bone static parameters were normalized to the first time point, to assess the changes in bone microstructure in percentage values. Furthermore, to elucidate the additive effect of loading, differences between the mean of the 8N and 0N groups were calculated.

Table 4.4: Absolute static bone morphometrical parameters in cortical bone at week 0 and 6 and percentage change between time points. Absolute values shown in bold indicate significant change over time between week 0 and 6 for the group, while bold percentage values indicate significant difference between both groups for percentage change as tested with repeated measures ANOVA.

	Ct.TV [mm ³]	Ct.BV [mm ³]	MV [mm ³]	Ct.Ar/Tt.Ar [%]	Ct.Th [mm]	I _{max} [mm ⁴]	I _{min} [mm ⁴]
3.5 Months							
8N Week 0	5.69 ± 0.11	2.18 ± 0.05	3.51 ± 0.07	38.4 ± 0.5	0.146 ± 0.002	0.23 ± 0.010	0.20 ± 0.009
8N Week 6	5.86 ± 0.12	2.37 ± 0.05	3.49 ± 0.09	40.5 ± 0.5	0.156 ± 0.001	0.26 ± 0.010	0.21 ± 0.009
Percentage	103 %	109 %	100 %	106 %	107 %	111 %	107 %
0N Week 0	5.34 ± 0.21	2.12 ± 0.08	3.22 ± 0.16	39.8 ± 1.1	0.151 ± 0.002	0.21 ± 0.016	0.18 ± 0.013
0N Week 6	5.51 ± 0.22	2.24 ± 0.10	3.26 ± 0.16	40.8 ± 1.4	0.154 ± 0.004	0.23 ± 0.019	0.20 ± 0.016
Percentage	103 %	106 %	101 %	103 %	102 %	106 %	106 %
12 Months							
8N Week 0	5.43 ± 0.06	2.60 ± 0.05	2.83 ± 0.08	47.9 ± 1.1	0.172 ± 0.005	0.27 ± 0.008	0.24 ± 0.008
8N Week 6	5.61 ± 0.10	2.66 ± 0.05	2.95 ± 0.09	47.4 ± 0.9	0.174 ± 0.004	0.30 ± 0.010	0.26 ± 0.009
Percentage	103 %	103 %	104 %	99 %	101 %	109 %	107 %
0N Week 0	5.48 ± 0.12	2.68 ± 0.06	2.80 ± 0.08	48.9 ± 0.8	0.176 ± 0.003	0.29 ± 0.010	0.25 ± 0.010
0N Week 6	5.65 ± 0.13	2.65 ± 0.07	3.01 ± 0.09	46.8 ± 0.9	0.174 ± 0.003	0.29 ± 0.012	0.25 ± 0.011
Percentage	103 %	99 %	107 %	96 %	99 %	103 %	101 %
19 Months							
8N Week 0	5.71 ± 0.18	2.65 ± 0.17	3.06 ± 0.07	46.2 ± 1.7	0.169 ± 0.006	0.30 ± 0.019	0.26 ± 0.018
8N Week 6	5.73 ± 0.18	2.73 ± 0.15	3.00 ± 0.10	47.5 ± 1.7	0.175 ± 0.006	0.31 ± 0.019	0.26 ± 0.017
Percentage	100 %	103 %	98 %	103 %	104 %	102 %	101 %
0N Week 0	5.64 ± 0.10	2.81 ± 0.09	2.83 ± 0.12	49.9 ± 1.6	0.179 ± 0.005	0.31 ± 0.009	0.26 ± 0.008
0N Week 6	5.65 ± 0.10	2.76 ± 0.10	2.89 ± 0.12	48.9 ± 1.8	0.178 ± 0.006	0.31 ± 0.010	0.26 ± 0.009
Percentage	100 %	98 %	102 %	98 %	100 %	99 %	99 %

Bone turnover

To assess bone turnover, dynamic bone parameters were calculated in the trabecular bone by overlaying the thresholded (registered) image data of consecutive time points. With this procedure the exact sites of formation and resorption could be identified and described morphometrically, as validated previously [13]. The bone dynamic parameters included bone formation rate (BFR), bone resorption rate (BRR), mineral apposition rate (MAR), mineral resorption rate (MRR), mineralizing surface (MS), and eroded surface (ES). Furthermore, this procedure allowed to visualize the sites of formation, presented in yellow, and resorption, presented in purple (Figure 4.12d).

Finite element analysis

Three dimensional micro-finite element (μ FE) models were created by adding discs, mimicking intervertebral discs, on both sides of the vertebrae, and converting the voxels into 8 node brick elements, which were assigned a Young's Modulus of 14.8 GPa and Poisson ratio of 0.3 [11]. To calculate the strain energy density (SED), the top of the model was displaced 0.1% while the bottom nodes were constrained in all directions. The resulting forces were used to scale SED values. Furthermore, the strength of the whole bone was calculated by using the Pistoia criterion [14]. Each model consisted of approximately 1.8 million elements and was solved using a parallel linear finite element package (ParFE) with an algebraic multigrid preconditioner. The simulations ran on a Cray XT5 super computing system composed of 1844 twelve-core AMD Opteron 2.4 GHz Istanbul processors and 29 TB of physical RAM at the Swiss National Supercomputing Center (CSCS, Manno, Switzerland). For each mouse, the strength was normalized to the first time point, and subsequently, the mean difference of the 0N group was subtracted from the mean difference of the 8N group, to calculate the additive effect of loading on bone strength.

Mechanosensitivity

To test mechanosensitivity, the initial mean SED in the trabecular bone was correlated with the percent change in BV/TV. To more closely investigate whether bone was formed at sites subjected to high strains, and bone was resorbed at sites subjected to low strains, the mean surface SED was calculated at sites where subsequently formation, resorption, or no remodeling occurred (Figure 4.14a). This was done as follows: The surface between the bone and the formed sites was projected on the initial SED to calculate the mean SED at surfaces where formation followed.

Similarly, the surface between background and resorbed sites was projected on the initial SED to calculate the mean SED at surfaces where subsequently bone resorption occurred. Furthermore, the surface between bone and background (quiescent surfaces) was projected on the initial SED to calculate the mean SED at quiescent surfaces. For each mouse and each time point, the mean SED value at surfaces of formation and resorption was normalized to the mean SED at quiescent surfaces.

Statistical analysis

Significant differences in bone structural parameters, dynamic parameters, bone strength, or mechanosensitivity, between 0N and 8N groups or over time, were tested with repeated measurements ANOVA. Correlations were tested with bivariate regression analysis. P-values below 0.05 were considered significant. All data are shown as mean \pm standard error. Statistical analysis was performed with the software package R (R: A Language and Environment for Statistical Computing) [15].

4.3.3 Results

Whole bone

In the whole bone, the change in AVD was significantly different between loaded and control groups at all ages, with a positive effect of loading (Fig. 4.11a). This positive effect originated from different trends between the groups, which were observed for most static bone morphometrical parameters. For W15, AVD increased significantly over time for both groups, while for W52, AVD decreased significantly over time for both groups. For W82, AVD was stable for the control group and increased significantly over time for the loaded group. When investigating the strength of the whole bone, there was an additive effect of loading on the bone strength (Fig. 4.11b), with only a significant difference between loaded and control group for W82. In this age group, the strength remained constant for the 0N group and increased significantly by 9% for the 8N group. For W52, the bone strength decreased significantly over time for both groups, with a tendency for larger loss in the 0N group (-9%) compared to the 8N group (-3.5%). For W15 the strength increased significantly over time by 15% for the 0N group and 32% for the 8N group, with almost a significant difference between groups ($p=0.050$).

Cortical bone

A positive effect of loading was also apparent in the cortical bone. For Ct.Ar/Tt.Ar a significant increase over time was found for the 8N, but not 0N groups of W15 and

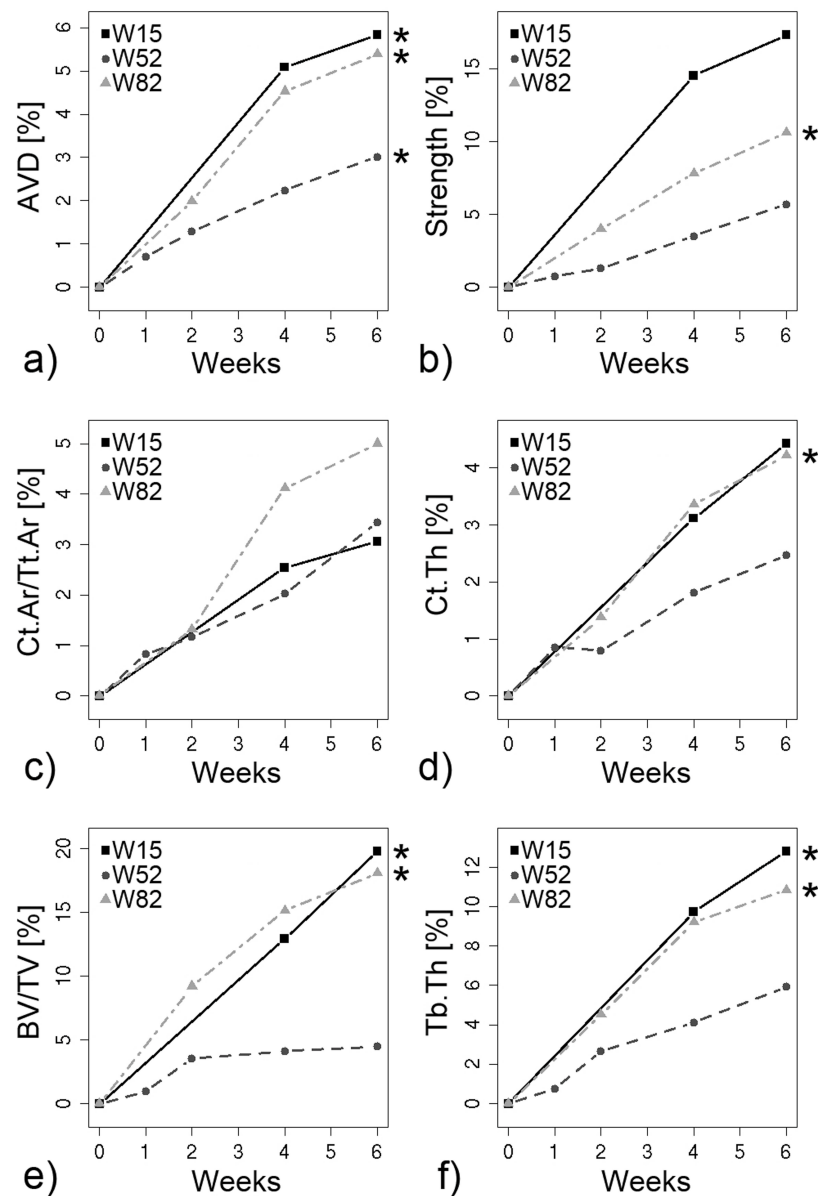


Figure 4.11: Beneficial effect of loading on the bone microstructure and bone strength. Values shown are mean percent difference between 8N and 0N groups. a) Average volume density (AVD), b) Bone strength, c) Cortical area fraction (Ct.Ar/Tt.Ar), d) Cortical thickness (Ct.Th), e) Bone volume fraction (BV/TV), f) Trabecular thickness (Tb.Th). Asterisk indicates significant difference between 8N and 0N group of respective age.

W82, while for W52 there was no change in Ct.Ar/Tt.Ar over time for the 8N group, and a significant decrease for the 0N group (Table 4.4). Thus, for each age group there was an additive effect of loading on Ct.Ar/Tt.Ar (Figure 4.11c). Similarly, Ct.Th only increased significantly for the 8N groups of W15 and W82 by 7% and 3.6% respectively, but was not significantly different over time for the 0N groups of those ages. Furthermore, a non significant increase of 1.1% was observed in Ct.Th

in the 8N group of W52, while it decreased significantly by 1.5% for the 0N group, with almost a significant difference between groups ($p=0.051$). The additive effect of loading on Ct.Th of the 8N group compared to the 0N group ranged between 2.6% and 4.5% (Figure 4.11d). The resistance against bending, as indicated by I_{min} and I_{max} , increased significantly for the 8N groups, but not 0N groups, of W15 and W52. The values for W82 were already quite high for both groups, and remained stable over time (Table 4.4).

Trabecular bone

In table 4.5 the absolute values of the static bone morphometrical parameters in the trabecular bone are shown. Significantly greater increases in multiple trabecular parameters were observed for the 8N groups than 0N groups of W15 and W82. On the contrary, for W52 a significant decrease in almost all parameters was seen for both 0N and 8N group. Nevertheless, Tb.Th only decreased significantly for the 0N group of W52. Thus an additive effect of loading on Tb.Th was apparent for all age groups (Figure 4.11f). This additive effect was reflected in BV/TV, with percent difference between 8N and 0N group ranging between 4.5% and 20% (Figure 4.11e). These results suggest that loading has a beneficial effect on trabecular bone, with greater beneficial effects for W15 and W82, than for W52.

Bone turnover

Loading had a positive effect on bone remodeling, as can be seen by the higher values for formation parameters and lower values for the resorption parameters for the 8N compared to the 0N groups at all ages (Figure 4.12). On average, BFR was 26% ($p<0.05$), 10% and 16% greater for the 8N group than the 0N group for W15, W52, and W82 respectively. At the same time, BRR was on average 22%, 11%, and 43% lower for the 8N group than the 0N group for W15, W52, and W82 respectively (Figure 4.12a). For both groups of W15 and for the 8N group of W82, BFR was significantly greater than BRR, while for both groups of W52, BRR was significantly greater than BFR. For all groups the depth of the resorption cavities, as represented by MRR, was significantly greater than the thickness of the formation packets, as represented by MAR, with slightly greater values for MRR for the 0N groups (Figure 4.12b). The surface of the formation sites, as depicted by MS, was significantly greater for the 8N than 0N group for W15 and W82, and not significantly different for W52. Similarly, the surface of the resorption sites, as shown by ES, was significantly smaller for the 8N group of W82, and showed a tendency for smaller values for the 8N groups of W15 and W52 (Figure 4.12c).

Table 4.5: Absolute static parameters in trabecular bone at week 0 and 6 and percentage change between time points. Absolute values shown in bold indicate significant change over time between week 0 and 6 for the group, while bold percentage values indicate significant difference between both groups for percentage change as tested with repeated measures ANOVA.

	Tb.TV [mm ³]	Tb.BV [mm ³]	BV/TV [%]	BS/BV [mm ² /mm ³]	Tb.Th [mm]	Tb.Sp [mm]	Tb.N [1/mm]	Conn.D [1/mm ³]
3.5 Months								
8N Week 0	2.30 ± 0.04	0.38 ± 0.03	16.7 ± 0.79	38 ± 1.1	0.071 ± 0.002	0.32 ± 0.008	2.91 ± 0.082	58 ± 2.6
8N Week 6	2.29 ± 0.06	0.50 ± 0.02	21.6 ± 0.60	30 ± 0.8	0.086 ± 0.002	0.31 ± 0.005	2.89 ± 0.050	49 ± 2.0
Percentage	100 %	130 %	130 %	79 %	121 %	97 %	99 %	84 %
0N Week 0	2.14 ± 0.10	0.36 ± 0.03	16.6 ± 1.00	36 ± 1.0	0.073 ± 0.002	0.32 ± 0.013	2.84 ± 0.103	54 ± 5.4
0N Week 6	2.16 ± 0.11	0.40 ± 0.04	18.3 ± 1.04	32 ± 1.1	0.079 ± 0.003	0.32 ± 0.010	2.79 ± 0.088	41 ± 4.4
Percentage	101 %	112 %	111 %	90 %	108 %	100 %	98 %	78 %
12 Months								
8N Week 0	1.83 ± 0.06	0.50 ± 0.01	27.2 ± 1.20	27 ± 1.0	0.092 ± 0.002	0.25 ± 0.007	3.44 ± 0.069	51 ± 3.2
8N Week 6	1.93 ± 0.06	0.44 ± 0.01	23.1 ± 0.59	29 ± 0.7	0.090 ± 0.002	0.28 ± 0.008	3.17 ± 0.061	43 ± 2.6
Percentage	105 %	90 %	85 %	107 %	99 %	114 %	92 %	85 %
0N Week 0	1.81 ± 0.05	0.52 ± 0.02	28.8 ± 0.78	26 ± 0.5	0.092 ± 0.001	0.24 ± 0.006	3.52 ± 0.075	50 ± 3.1
0N Week 6	1.98 ± 0.06	0.46 ± 0.02	23.3 ± 1.00	30 ± 0.8	0.085 ± 0.002	0.27 ± 0.008	3.31 ± 0.075	53 ± 3.3
Percentage	109 %	88 %	81 %	115 %	93 %	112 %	94 %	109 %
19 Months								
8N Week 0	2.01 ± 0.04	0.46 ± 0.04	22.9 ± 1.99	31 ± 1.7	0.085 ± 0.003	0.27 ± 0.013	3.34 ± 0.114	56 ± 4.3
8N Week 6	1.97 ± 0.07	0.52 ± 0.03	26.4 ± 1.88	27 ± 1.2	0.094 ± 0.003	0.27 ± 0.012	3.30 ± 0.109	45 ± 2.2
Percentage	98 %	114 %	117 %	86 %	111 %	100 %	99 %	82 %
0N Week 0	1.85 ± 0.08	0.50 ± 0.02	27.3 ± 1.36	27 ± 1.4	0.093 ± 0.004	0.27 ± 0.010	3.43 ± 0.105	60 ± 6.7
0N Week 6	1.90 ± 0.09	0.50 ± 0.02	26.6 ± 1.12	27 ± 1.2	0.093 ± 0.003	0.27 ± 0.010	3.28 ± 0.094	53 ± 3.5
Percentage	103 %	101 %	98 %	100 %	100 %	103 %	96 %	90 %

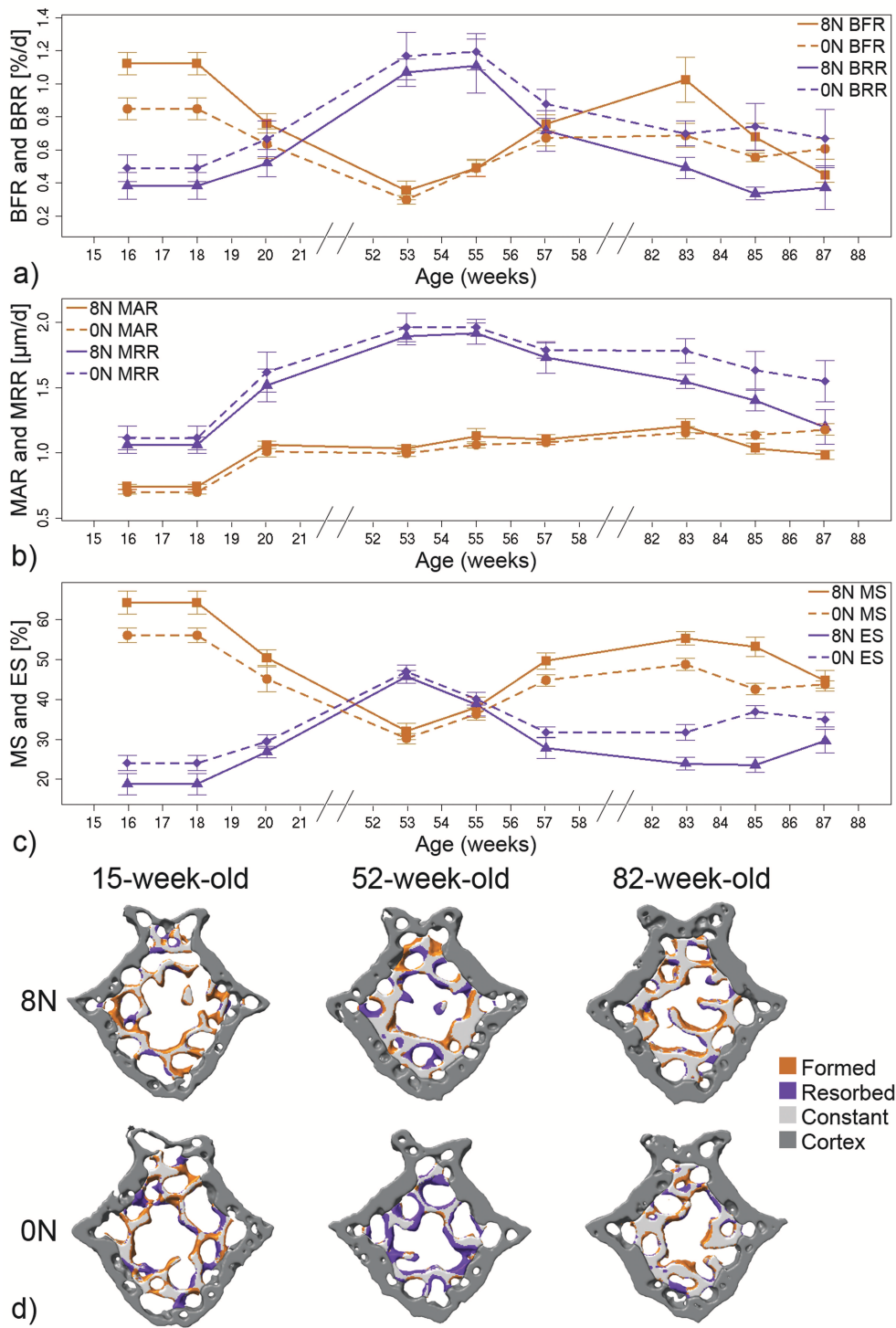


Figure 4.12: Bone remodeling. For all plots the 8N group is shown with continuous lines, while the 0N group is shown with dashed lines. a) Bone formation rate (BFR) in yellow and bone resorption rate (BRR) in purple, b) Mineral apposition rate (MAR) in yellow and mineral resorption rate (MRR) in purple, c) Mineralizing surface (MS) in yellow and eroded surface (ES) in purple. d) Cross-sections of the average mouse of each group showing bone formation between week 0 and 6 in yellow, bone resorption between week 0 and 6 in purple, and structures unchanged between time points in light gray. Cortical bone, which is not included in the analysis, is shown in dark gray.

For both 0N and 8N groups of W15 and W82, MS was significantly greater than ES. For the 0N group of W52, ES was significantly greater than MS, while for the 8N group, MS and ES were balanced. This indicated that loading increased the surface of formation sites, and decreased the surface of resorption sites, but did not modulate thickness of remodeling sites.

Differences between 8N and 0N groups in dynamic bone parameters at all ages are visualized in figure 4.12d, where a cross-section of an overlay between week 0 and 6 of the average mouse of each group is shown. It is clear that for W15 loading acts both on formation and resorption, as there are more yellow and less purple sites in the cross section of the 8N group. On the other hand, for W52, the 8N group has depressed bone resorption, with a balance between formation and resorption, while resorption exceeds bone formation for the 0N group, which is apparent as very little yellow and many purple sites are present. For W82 again a similar trend as for W15 can be observed, with more bone formation and less bone resorption for the 8N than 0N group.

Mechanosensitivity

Global mechanosensitivity was tested by correlating the initial average SED in the trabecular bone, which indicated the need for adaptation, with the subsequent change in BV/TV. For both 0N and 8N groups the change in BV/TV between week 0 and 6 could be predicted from the initial SED value, with a much stronger correlation for the 8N groups ($R = 0.86$, $p < 0.0001$), than for the 0N groups ($R = 0.67$, $p < 0.001$). Furthermore, when correlations between initial SED and subsequent change in BV/TV were calculated per age group, significant correlations were found for all of the 8N groups ($R = 0.92$ for W15, $R = 0.83$ for W52, and $R = 0.83$ for W82), while no correlations were found for the 0N groups, which is also clear from figure 4.13, where for the 8N groups the dots are on a line for each age group, while for the 0N groups the dots are like a cloud for each age group. This was a first indicator that CV6 remains mechanosensitive. To investigate whether mechanosensitivity remained locally, initial surface SED at sites where remodeling followed was compared to initial surface SED at quiescent surfaces (figure 4.14a). For each age group, SED at sites where formation followed was significantly greater than at quiescent surfaces, and also sites where resorption followed had significantly lower initial SED values (figure 4.14b). The SED was on average 15%, 14% and 20% greater at sites where formation followed than at quiescent sites for W15, W52, and W82 respectively. Likewise, SED was on average 17% lower at sites where resorption

occurred than at constant sites for W15, 15% for W52, and 20% for W82. This indicated that CV6 of mice not only actively responded to the strains they were subjected to, but also added bone at sites subjected to higher strains and resorbed bone at sites subjected to lower strains.

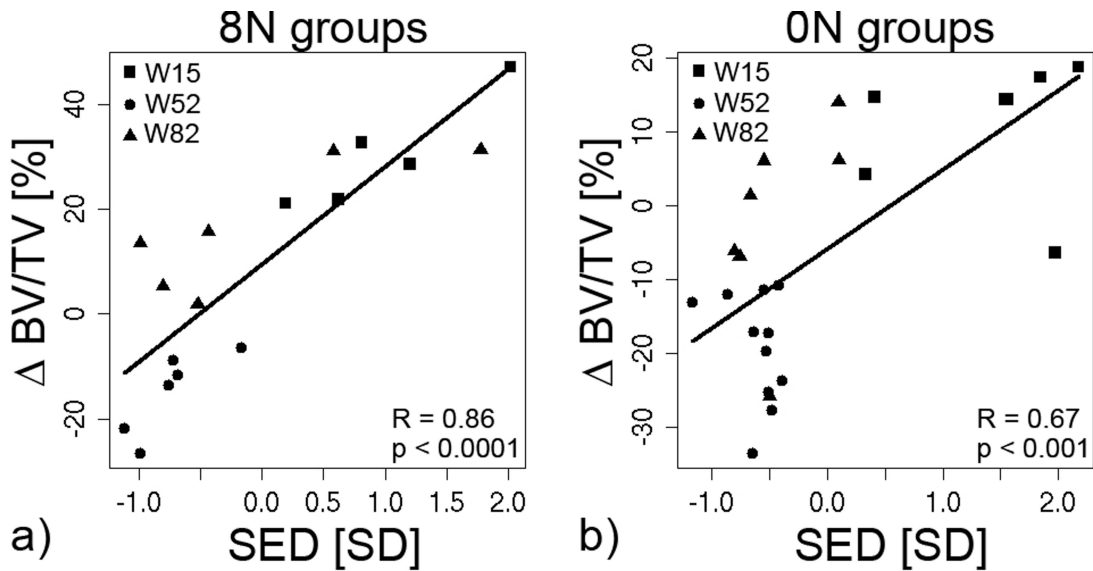


Figure 4.13: Significant correlations between initial strain energy density (SED), expressed as standard deviations from mean, and following percentage change in bone volume fraction (BV/TV) in trabecular bone for a) 8N groups, and b) 0N groups.

4.3.4 Discussion

In the present study, we found that mechanosensitivity of the sixth caudal vertebra in mice remains with age. This was verified by four observations. Firstly, loading had a beneficial effect on the bone microstructure, by either increasing bone volume density and/or cortical area fraction, or by counteracting the bone loss. This was most obvious in the trabecular and cortical thickness. Secondly, loading had a beneficial effect on bone turnover. In the loaded groups the bone formation rate was greater, while the bone resorption rate was lower than in the non-loaded groups, leading to as described above, a net gain in bone mass, or prevention from bone loss. Thirdly, loading had a beneficial effect on the bone strength. In the loaded groups, strength increased significantly greater than in control groups, or the strength remained constant in the loaded group, while in the control group bone strength decreased. Fourthly, for the loaded groups the initial strain energy density (SED) could predict the change in BV/TV, with the observation that the sites where formation followed had significantly greater initial SED value than sites

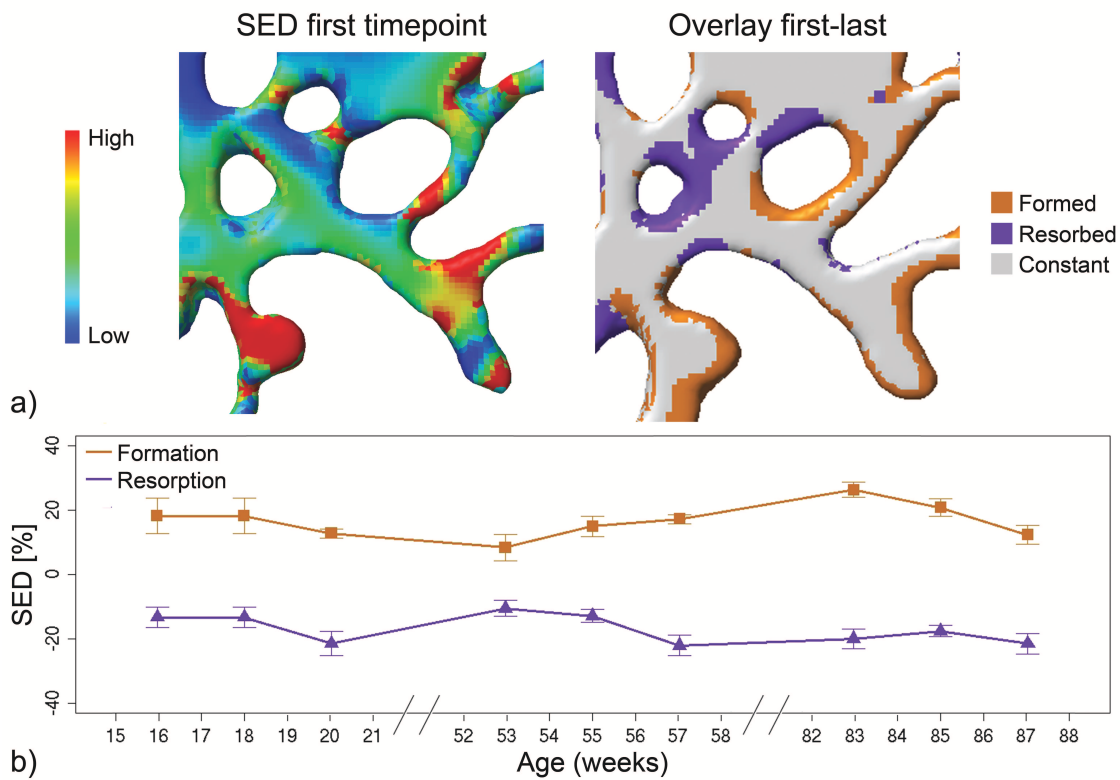


Figure 4.14: Mechanosensitivity. a) By projecting initial surface SED (left) on a superimposed image showing the sites of formation and resorption (right), and normalizing to surfaces where no remodeling followed, the mean SED at formation and resorption sites could be calculated. b) Mean SED at sites where formation or resorption followed.

where bone remained constant, and also the sites with significantly lower initial strain energy density subsequently led to bone resorption in all of the age groups. This indicated that not only globally, but also locally the bone of aged mice was still mechanosensitive, and formed bone at sites where necessary for mechanical integrity (high SED), while bone was resorbed at sites where load was no longer transferred through the bone, with a global positive effect of loading.

The trend of bone loss in the trabecular bone at an age of 52 weeks was also observed in a previous study in the same bone [aging paper]. Similarly, in other bones, it was often found that peak bone mass is reached at an age of about 52 weeks, and stabilizes or decreases thereafter, depending on the skeletal site [16–20]. Interestingly, loading had the largest additive effect on the trabecular bone in the 15- and 82-week-old mice, while for the 52-week-old mice the positive effect was mostly through cortical adaptation. This could be explained by the fact that the 52-week-old mice had the highest absolute trabecular bone parameters, leading to too low SED values to induce a positive remodeling balance in the trabecular bone. The cortical bone of the 52-week-old mice, on the other hand, did respond

to loading by thickening of the cortex in this 8N group, through apposition on the periosteal side, while the bone was even resorbed on the endosteal site, as indicated by the increase in MV and TV.

A difference between our results and previous studies is that no clear loss of bone was evident in 82-week-old mice compared to 52-week-old mice, whereas in studies of tibia-loading often a loss of trabecular bone between these ages is found. Nevertheless, in previous studies of caudal or lumbar vertebrae, also no age-related bone loss was observed [19, 21]. This difference could also indicate that the mechanosensitivity of bones is regulated locally, and remains in caudal vertebrae, but might be lost at other skeletal sites. On the other hand, this would not be very likely, because a positive effect of loading was found in tibia of aged mice [5] and rats [7] or ulna of aged rats [6].

In 82-week-old (19-month-old) mice the bone responded to loading by significantly increasing cortical and trabecular thickness, whereas the values for the 0N group remained constant. Similar to our study, Brodt et al. [5] reported a beneficial effect of loading on BV/TV in 22 month old mice. In contrast to our study, however, a loss in BV/TV was found for control mice, which was prevented by loading (similar to our 52-week-old mice). This discrepancy can be explained by the use of a different mouse strain (BALB/c), because when the tibia was loaded in C57Bl/6 mice, bone formation was induced in 22 month old mice [7].

The fact that mechanosensitivity remains with age, is thus also supported by other animal experiments. Nevertheless, it is in contrast with some cellular based findings. For example, it was found that the number of living osteocytes reduces by half, between the age of 3 and 32 months in CW-1 mice [22], which would be expected to have an effect on the mechanosensitivity. Furthermore, osteoblasts regulate the recruitment and activity of osteoclasts through expression of RANKL, osteoprotegerin (OPG), and macrophage-colony stimulation factor (M-CSF), and it was found that there were age-related differences in the expression of these molecules [23, 24], indicating unbalanced remodeling with age, and a lack of response to mechanical demand. Nevertheless, it was found that only immature pre-osteoblasts show age-related differences in RANKL and OPG expression, but mature cells were not different [23].

Of note, in 15-week-old mice the difference in bone strength between the 8N

and 0N group was the largest, although the difference between 8N and 0N was similar for BV/TV and even greater in Ct.Ar/Tt.Ar for 82-week-old than 15-week-old mice. This inconsistency can be explained by absolute values. Here, the absolute value of the 82-week-old group was greater. Thus, the percentage value, even if in absolute terms the same increase, is smaller for the 82-week-old mice than 15-week-old mice, leading to a percentage-wise smaller difference between 8N and 0N mice in bone strength.

An extension of this study compared to previous studies, was that dynamic bone parameters were assessed in 3D and at multiple time points throughout the loading period. The dynamic bone parameters changed over time and between age groups, with reductions in BFR and MS with age. MAR, on the other hand, hardly deviated between age groups. This would make sense, because when MAR increases this would indicate that the activity per osteoblast is increased, which is unlikely. On the other hand, osteoclasts are more mobile and a change in MRR can be caused by a change in per osteoclast activity or osteoclast number. For each age group the depth of the resorption pits was larger than the thickness of the formation packets. Nevertheless, the percent surface occupied by formation sites was significantly greater than the surface occupied by resorption sites for both loaded and control groups of 15- and 82-week-old mice, while for the loaded 52-week-old mice MS and ES were balanced, and for the 0N group of the 52-week-old mice ES even exceeded MS significantly. The fact that the surface of the remodeling sites was modulated more by loading than the thickness is in agreement with a previous loading study, where MS and ES were modulated more than MAR or MRR [25].

A novel observation in our study was that the mechanosensitivity of the caudal vertebra remained with age. It is interesting to see that the percent change needed to result in a remodeling response remained the same over age, because this would indicate that the osteocytes start a signaling cascade at a similar percentage change in SED at old or young ages, even though the amount of living osteocytes reduces with age. For each age, an increase in SED of about 16% led to bone formation, while a decrease in SED of about 17% led to bone resorption, indicating there is a similar percentage change in SED or threshold to start bone resorption or bone formation. The absolute SED values, on the contrary, deviated largely between mice and groups, indicating that a change in SED is more important than absolute SED to induce bone remodeling.

A limitation in our study design is that the initial bone structural parameters were not exactly the same between the 0N and 8N groups at the start of the experiment, with a smaller BV/TV for the 8N than 0N group for 15- and 52-week-old mice (not significantly different), even though this was attempted by matching the groups by weight. As can be seen from the correlations, a higher SED value (corresponding to a lower BV/TV or AVD) is more likely to result in a greater increase in BV/TV upon loading. Thus had the groups been the other way around, maybe the results would have been different, responses would maybe not have been the same. Also the absolute BV/TV was greater at 52 and 82 weeks of age than at 15 weeks of age. Therefore, an improvement in the study design would have been to adapt the applied loads to the initial bone volume densities to result in the same strains between mice. Nevertheless, when bone structural parameters were normalized to SED values (data not shown), the differences between the 0N and 8N groups became clearer, with significant differences between groups for most parameters, indicating that if groups would have been switched the same outcome would have been found.

A further limitation of the study was that the time points that the mice were scanned for the three age groups were not exactly the same. This was, because the 15- and 82-week-old mice were scanned at later time points as well, but to enable better comparison between age groups, only the first 6 weeks of each experiment are shown here.

In conclusion, it was shown that caudal vertebrae of mice retain mechanosensitivity with age at a local level, and form bone at sites subjected to higher strains, and resorb bone at sites subjected to lower strains. This led to beneficial effects of loading at a global scale on the bone microstructure, bone remodeling, and bone strength for each age group. Data of mice cannot be directly compared to humans, but this data and data of other studies [8, 26–28] support the fact that physical exercise could be beneficial for elderly to retain bone mass and bone strength.

4.3.5 Acknowledgement

The authors gratefully acknowledge funding from the European Union for the Osteoporotic Virtual Physiological Human project (VPHOP FP7-ICT2008-223865) and computational time from the Swiss National Supercomputing Center (CSCS, Manno, Switzerland).

References

- [1] B.A. Christiansen, A.A. Kotiya, and M.J. Silva. Constrained tibial vibration does not produce an anabolic bone response in adult mice. *Bone*, 45(4):750–759, 2009.
- [2] M.A. Lynch, M.D. Brodt, and M.J. Silva. Skeletal effects of whole-body vibration in adult and aged mice. *J Orthop Res*, 28(2):241–247, 2010.
- [3] C.T. Rubin, S.D. Bain, and K.J. McLeod. Suppression of the osteogenic response in the aging skeleton. *Calcif Tissue Int*, 50(4):306–313, 1992.
- [4] M. Silbermann, B. Bar-Shira-Maymon, R. Coleman, A. Reznick, Y. Weisman, E. Steinhagen-Thiessen, H. von der Mark, and K. von der Mark. Long-term physical exercise retards trabecular bone loss in lumbar vertebrae of aging female mice. *Calcif Tissue Int*, 46(2):80–93, 1990.
- [5] M.D. Brodt and M.J. Silva. Aged mice have enhanced endocortical response and normal periosteal response compared with young-adult mice following 1 week of axial tibial compression. *J Bone Miner Res*, 25(9):2006–2015, 2010.
- [6] L.K. Saxon, A.G. Robling, I. Alam, and C.H. Turner. Mechanosensitivity of the rat skeleton decreases after a long period of loading, but is improved with time off. *Bone*, 36(3):454–464, 2005.
- [7] S. Srinivasan, S.C. Agans, K.A. King, N.Y. Moy, S.L. Poliachik, and T.S. Gross. Enabling bone formation in the aged skeleton via rest-inserted mechanical loading. *Bone*, 33(6):946–955, 2003.
- [8] M.R. Forwood and D.B. Burr. Physical activity and bone mass: exercises in futility? *Bone Miner*, 21(2):89–112, 1993.
- [9] K.H. Wenger, J.D. Freeman, S. Fulzele, D.M. Immel, B.D. Powell, P. Moliator, Y.J. Chao, H.S. Gao, M. Elsalanty, M.W. Hamrick, C.M. Isales, and J.C. Yu. Effect of whole-body vibration on bone properties in aging mice. *Bone*, 47(4):746–755, 2010.
- [10] C.H. Turner, K. Hasegawa, W. Zhang, M. Wilson, Y. Li, and A.J. Dunipace. Fluoride reduces bone strength in older rats. *Journal of Dental Research*, 74(8):1475–1481, 1995.

- [11] Webster D.J., Morley P.L., van Lenthe G.H., and Müller R. A novel *in vivo* mouse model for mechanically stimulated bone adaptation—a combined experimental and computational validation study. *Comput Methods Biomech Biomed Engin*, 11(5):435–441, 2008.
- [12] T. Hildebrand, A. Laib, R. Müller, J. Dequeker, and P. Ruegsegger. Direct three-dimensional morphometric analysis of human cancellous bone. *J Bone Miner Res*, 14(7):1167–1174, 1999.
- [13] F.A. Schulte, F.M. Lambers, G. Kuhn, and R. Müller. *In vivo* micro-computed tomography allows direct three-dimensional quantification of both bone formation and bone resorption parameters using time-lapsed imaging. *Bone*, 48:433–442, 2011.
- [14] W. Pistoia, B. van Rietbergen, E.M. Lochmuller, C.A. Lill, F. Eckstein, and P. Ruegsegger. Estimation of distal radius failure load with micro-finite element analysis models based on three-dimensional peripheral quantitative computed tomography images. *Bone*, 30(6):842–848, 2002.
- [15] R Development Core Team. R: A Language and Environment for Statistical Computing. *R Foundation for Statistical Computing, Vienna, Austria*, 2010.
- [16] B.P. Halloran, V.L. Ferguson, S.J. Simske, A. Burghardt, L.L. Venton, and S. Majumdar. Changes in bone structure and mass with advancing age in the male C57BL/6J mouse. *J Bone Miner Res*, 17(6):1044–1050, 2002.
- [17] H.R. Buie, C.P. Moore, and S.K. Boyd. Postpubertal architectural developmental patterns differ between the L3 vertebra and proximal tibia in three inbred strains of mice. *J Bone Miner Res*, 23(12):2048–2059, 2008.
- [18] J.M. Somerville, R.M. Aspden, K.E. Armour, K.J. Armour, and D.M. Reid. Growth of C57BL/6 mice and the material and mechanical properties of cortical bone from the tibia. *Calcif Tissue Int*, 74(5):469–475, 2004.
- [19] M.D. Willinghamm, M.D. Brodt, K.L. Lee, A.L. Stephens, J. Ye, and M.J. Silva. Age-related changes in bone structure and strength in female and male BALB/c mice. *Calcif Tissue Int*, 86(6):470–483, 2010.
- [20] V. Glatt, E. Canalis, L. Stadmeier, and M.L. Bouxsein. Age-related changes in trabecular architecture differ in female and male C57BL/6J mice. *J Bone Miner Res*, 22(8):1197–1207, 2007.

- [21] T.J. Wronski, L.M. Dann, K.S. Scott, and M. Cintron. Long-term effects of ovariectomy and aging on the rat skeleton. *Calcif Tissue Int*, 45(6):360–366, 1989.
- [22] B. Bar-Shira-Maymon, R. Coleman, A. Cohen, E. Steinhagen-Thiessen, and M. Silbermann. Age-related bone loss in lumbar vertebrae of CW-1 female mice: a histomorphometric study. *Calcif Tissue Int*, 44(1):36–45, 1989.
- [23] J. Cao, L. Venton, T. Sakata, and B.P. Halloran. Expression of RANKL and OPG correlates with age-related bone loss in male C57BL/6 mice. *J Bone Miner Res*, 18(2):270–277, 2003.
- [24] J.J. Cao, T.J. Wronski, U. Iwaniec, L. Phleger, P. Kurimoto, B. Boudignon, and B.P. Halloran. Aging increases stromal/osteoblastic cell-induced osteoclastogenesis and alters the osteoclast precursor pool in the mouse. *J Bone Miner Res*, 20(9):1659–1668, 2005.
- [25] F.M. Lambers, F.A. Schulte, G. Kuhn, D.J. Webster, and R. Müller. Mouse tail vertebrae adapt to cyclic mechanical loading by increasing bone formation rate and decreasing bone resorption rate as shown by time-lapsed *in vivo* imaging of dynamic bone morphometry. *Bone*, accepted, 2011.
- [26] S.J. Warden, R.K. Fuchs, and C.H. Turner. Steps for targeting exercise towards the skeleton to increase bone strength. *Eura Medicophys*, 40(3):223–232, 2004.
- [27] C.M. Snow. Exercise and bone mass in young and premenopausal women. *Bone*, 18(1 Suppl):51S–55S, 1996.
- [28] S.M. Verschueren, M. Roelants, C. Delecluse, S. Swinnen, D. Vanderschueren, and S. Boonen. Effect of 6-month whole body vibration training on hip density, muscle strength, and postural control in postmenopausal women: a randomized controlled pilot study. *J Bone Miner Res*, 19(3):352–359, 2004.

Chapter 5

Synthesis

5.1 Main findings and implications

5.1.1 Background

The most common bone disease, osteoporosis, is a major health care problem, affecting approximately one third of women and one fifth of men aged 50 years and older [1]. In bones of osteoporosis patients there is a shift in the remodeling balance, with bone resorption exceeding bone formation, leading to a loss of bone mass and consequently a decline in bone strength. The reduced bone strength puts osteoporosis patients at an increased risk for fractures, with the most common fracture sites being the hip, spine, and forearm. About forty percent of white women and thirteen percent of white men are expected to sustain at least one fracture in a lifetime [2]. Fractures are associated with pain, morbidity (decrease in physical and social function) [3], and increased mortality in patients. Of the patients with a hip fracture, only 15% are able to return to unassisted ambulation 6 months after fracture, and 24% die within 1 year [4]. Furthermore, the health care costs associated with the hospitalization and treatment of osteoporosis are a major financial burden on the society. Annual costs for treatment of osteoporotic patients was about \$20 billion in the US and €25 billion in Europe in 2005 [5]. Based on the demographic shift these numbers are expected to rise tremendously in the coming years, with expected costs of €77 billion in 2050 in Europe [6].

The cause of the shift in the bone remodeling balance which leads to increased bone fragility in osteoporosis, is not well understood. It is thus important to gain a more fundamental understanding in the mechanisms underlying bone remodeling in health and disease, as it is expected that this will lead to a better diagnosis and safer and more efficient treatment for bone diseases. One important

regulator of bone remodeling is the mechanical force acting on the bone. Thus, to understand the mechanisms underlying bone remodeling, it is useful to investigate the effect that mechanical forces play on bone remodeling. *In vivo* mouse models, that resemble human physiology and allow controlled mechanical loading to the bones, are an invaluable tool to investigate this. Furthermore, imaging modalities that offer the visualization of bone microstructure as well as bone dynamics in a longitudinal manner are essential.

For these reasons, the final aim of this doctoral thesis was to develop a functional bone imaging approach to assess how bone remodeling is influenced by mechanical loading, aging and disease. To provide an informed background to this field of research, in *Chapter 2* firstly the most important signaling molecules for bone adaptation were outlined. Secondly, the existing *in vivo* loading models and their main findings were described. Thirdly, the influence of aging and bone diseases on the bone microstructure were portrayed. At the end of *Chapter 2*, a review on the benefits of functional imaging and multimodality systems in bone research was provided. This included a description of the available imaging systems for molecular and anatomical imaging, as well as multimodality imaging strategies. A review of the application of these imaging techniques was conducted for several fields of bone research, including bone metabolism, fracture healing, mechanical loading response, bone metastases, and cell imaging on biomaterials. Generally, in the field of bone research, there has been little focus on multimodality imaging techniques, but it is becoming more established, and when it is performed, provides a robust and potent method, which allows to monitor changes in the bone microstructure, as well as the biological pathways underlying these changes.

5.1.2 Novel *in vivo* imaging methods

The first major achievement of this thesis, as described elsewhere (<http://e-collection.library.ethz.ch/collection/>), was the establishment of a functional bone imaging approach. In the first part a method was developed to enable reproducible *in vivo* micro-computed tomography (micro-CT) scans of caudal vertebrae and tibiae of mice. For scanning of the caudal vertebrae, a holder was designed in which the mice were maintained at body temperature and from which the tail was extending and tightly fixed. For scanning of the tibiae, a similar holder was developed, from which the leg of the mice could be stretched and constrained. Further, by using rigid image registration, it was granted that the serial scans had the same orientation, and enabled longitudinal extraction of static and dynamic bone para-

meters. Because radiation associated with *in vivo* micro-CT is a concern, a study was described that assessed this effect. As bone remodeling is more sensitive to radiation than the bone microstructure itself, the influence of radiation on static and dynamic parameters was compared between groups scanned 5 times over four weeks, and a group scanned only at the start and end point over the same period. It was found that radiation of *in vivo* micro-CT scans did not influence bone dynamic or static parameters in the 4 week period. Thus, the scan-intensity used in this study does not have an effect on either bone remodeling rates or on the bone microstructure and justified the use of *in vivo* micro-CT. Thus, with this prerequisite fulfilled, the functional bone imaging approach, with access to changes in static and dynamic bone parameters, could now be used. Nevertheless, to gain more insight into osteoblast activity at a shorter time span than with the dynamic formation parameters, an imaging strategy using fluorescence molecular tomography (FMT) was developed. In the development of this technique for bone imaging, it was found that the mouse tail has to be embedded in a silicon phantom, to provide constant illumination. Furthermore, it was found that the timing and exact volume for probe injection were very important for gaining reproducible results.

5.1.3 New findings in load adaptation

The major findings of *Chapter 3* concerned load adaptation. In *Chapter 3.1* the functional bone imaging approach was applied to investigate the influence of mechanical loading on bone remodeling. To this end, dynamic mechanical loading was applied three times per week for four weeks at a load of 8 N (8N) or 0 N (0N, control), to the sixth caudal vertebra of 15 week old female C57Bl/6 mice. *In vivo* micro-CT scans were performed weekly, with the first scan before the loading started. From these scans static and dynamic parameters were calculated. Furthermore, micro-finite element models were created to determine changes in mechanical properties. Results of static bone parameters showed that loading significantly increased trabecular bone volume fraction by 20% ($p < 0.001$), where most trabeculae, regardless of their size, increased in thickness as an effect of bone adaptation. The cortical area fraction increased by 6% ($p < 0.001$), with new bone formed on both the endosteal and periosteal side. Dynamic bone parameters showed that on average the bone formation rate was 23% greater ($p < 0.001$) for 8N than 0N and that the bone resorption rate was on average 25% smaller ($p < 0.001$). This was an effect of the significantly increased surface of bone formation sites (on average 16%, $p < 0.001$), while the thickness of bone formation packages was less affected (on average 4.9% greater, $p < 0.05$). At the same time, the surface of bone

resorption sites was significantly reduced (on average 15%, $p < 0.001$), while the depth of resorption pits remained constant. Furthermore, the amount of remodeling sites per bone volume was similar for both groups. This indicated that there were not more remodeling sites where osteoblasts were recruited, but that there was a greater net osteoblastic activity per formation site, likely caused by an increase in number of osteoblasts. Similarly, there were not less sites where osteoclasts were recruited, but there was less net osteoclastic activity per resorption site, either through a decrease in number of osteoclasts, or a decrease in activity per osteoclast. From results of the mechanical properties, it was found that the strength increased significantly by 24% ($p < 0.001$) for 8N over the loading period, while the strain energy density in the trabecular bone decreased significantly by 24% ($p < 0.001$). Changes in mechanical properties were significantly correlated with changes in bone structural parameters, showing that loading resulted in targeted bone adaptation, with an increase in overall bone strength.

In *Chapter 3.2* the functional bone imaging approach was applied to test whether a reduction of loading bouts or a reduction in load could still produce an anabolic response. Firstly, changes in static, dynamic, and mechanical properties were compared between a group loaded once per week and a group loaded three times per week. For most properties the mice loaded three times per week had significantly greater values than the mice loaded once per week. This indicated that loading once per week was not sufficient to induce an anabolic response in the sixth caudal vertebra. Secondly, changes in static, dynamic, and mechanical properties were compared between groups loaded at 0 N (0N), 4 N (4N), and 8 N (8N). After four weeks of loading, the bone volume fraction and trabecular thickness were significantly greater for 8N compared to 0N, while 4N was not significantly different from 8N and 0N. The cortical area fraction and thickness were significantly different between 8N and 0N, but not between 8N and 4N or between 4N and 0N. There was a tendency for greater formation and lower resorption parameters for 8N than for 4N and 0N, but only a significant difference was found between 8N and 0N, and between 4N and 0N for MS. This indicated that the anabolic response achieved by loading at 4N is hardly different from the 0N group, while for the 8N group a significant anabolic effect is present, and suggested that for future loading studies three times per week at 8N load should be used. The fact that no anabolic response was found for 4N can also be explained by a recent finding, where it was shown that physiological loading in the mouse caudal vertebra is on the order of 4 N [7], and therefore no additional benefit can be expected from a 4N loading regime.

To further investigate load adaptation, and to find out how many weeks of loading are needed for the bone to fully adapt to 8 N load, the functional bone imaging approach was used over a longer period in *Chapter 3.3*. *In vivo* micro-CT scans were performed at the start, after four weeks of loading, and afterwards every two weeks, until no further increase in bone volume density was found. Results showed that the sixth caudal vertebra had adapted to 8 N after 8-10 weeks of loading, at which point the bone static parameters and bone strength stabilized, while the dynamic parameters returned to the control values.

5.1.4 Novel multimodality imaging approach for bone dynamics

Chapter 3.4 further investigated load adaptation by using a multimodality imaging approach. Next to *in vivo* micro-CT, the mechanical loading response was imaged with FMT at multiple time points. To gain a fluorescence signal as a measure for osteoblast activity, OsteoSense[®]680 had to be injected 24 h before measurement. Osteoblast activity was measured at the first day, two weeks after loading, and at the end time point. Furthermore, from differences in fluorescence intensity from 24 h after probe injection until right before new probe injection, the decrease in fluorescence intensity was calculated, and provided an estimate for the osteoclast activity. To test the reproducibility of FMT measurements, three measurements with repositioning between measurements, were performed at each time point. It was found that FMT measurements were highly reproducible and that the single animals could be distinguished, as was shown by the precision errors, expressed as coefficient of variation, which ranged between 0.21% and 0.45%, and intra-class correlations, which ranged between 0.699 and 0.869. Loading induced significant changes in static and dynamic parameters calculated from *in vivo* micro-CT data in the whole bone. The increase in average volume density of 6.5% for 8N was significantly greater than the 2.3% increase for 0N. Furthermore, bone formation rate was on average 36% and mineralizing surface 19% greater for 8N than 0N, when calculated from *in vivo* micro-CT measurements. On the contrary, no significant differences in osteoblast and osteoclast activity, as measured with FMT, were found between groups. Nevertheless, on average the osteoblast activity was 26% greater and osteoclast activity 14% lower for loaded than control group. One explanation for this discrepancy could be that osteosense was injected 24 h before measurement, and also approximately 24 h before loading was applied for the first injection, and 24 h before and after loading for the second and third injections, at which time

points the osteoblast activity might not have been upregulated anymore, or to a lesser extent. Also, osteoblast activity was measured over a 24 h time frame only, which was maybe not long enough to pick up the difference between 8N and 0N. Furthermore, the region of interest for the FMT measurement included also the vertebrae adjacent to the loaded vertebra, which might have obscured the results. Even though no significant differences between 8N and 0N were found for FMT measurements, significant correlations between bone resorption parameters calculated from CT and osteoclast activity from FMT were found. At the same time, bone formation parameters were less correlated with osteoblast activity, probably owing to the different time frame over which these parameters were calculated. This underlines that FMT measurements provide a complimentary technique to measure osteoblast activity. It was concluded that the combination of *in vivo* micro-CT and FMT was feasible, and could be performed reproducibly at multiple time points throughout a study to gain information about changes in bone microstructure, and the underlying osteoblast and osteoclast activity, but did not show a great advantage over dynamic parameters calculated from *in vivo* micro-CT measurements. Therefore, in the following chapters only the functional bone imaging approach using *in vivo* micro-CT was applied.

5.1.5 Novel *in vivo* model to study osteoporosis

The major achievement of *Chapter 4.1* was the validation of the caudal vertebra mouse model for the study of postmenopausal osteoporosis. The motivation to use this bone was that it is more easily accessible for high-resolution imaging, facilitates finite element analysis, includes both cortical and trabecular bone, contains a relatively large content of trabecular bone, is less dependent on rodent activity, and is accessible for mechanical loading. To test whether this bone was suitable as a valid model for osteoporosis, responses to ovariectomy (OVX) were monitored in static bone parameters, dynamic bone parameters, and mechanical properties and compared to sham operated mice (SHM). The first requirement for a valid model was that the bone mass should decrease, as occurs in postmenopausal women. Accordingly, a significant decrease was observed in bone volume fraction for OVX (-35%) compared to SHM (+16%) in the trabecular bone ($p < 0.001$) and a significant decrease in cortical area fraction for OVX (-9%) compared to SHM (+3%, $p < 0.001$). The second requirement was that both bone formation and resorption rate should be greater for OVX than SHM, with an earlier rise in bone resorption rate, as most osteoporotic humans show high turnover bone loss. In agreement, BFR was on average 1.6 times greater for OVX than SHM ($p < 0.05$), and BRR 3.7 times greater

for OVX than SHM ($p < 0.001$). The increase in BFR lagged behind the instant increase in BRR, implicating that the osteoclastic activity was directly augmented by OVX, while the osteoblastic activity was augmented later on. The third requirement was that the bone fragility should increase, as the risk for fractures increases with osteoporosis. In resemblance, there was a significant decrease in bone strength of the whole bone for OVX (-18%) compared to SHM (+13%, $p < 0.001$). From these results we concluded that the mouse tail vertebra mimics postmenopausal bone loss and is a suitable model for postmenopausal osteoporosis.

5.1.6 New insight into mechanosensitivity with age

The major finding of *Chapter 4.2* was that with age the bone microstructure in the caudal vertebrae and tibiae changed, but did not influence the mechanical properties negatively. This observation was gained by scanning the sixth caudal vertebra and left tibia of C57Bl/6 female mice at multiple time points between an age of 16 and 88 weeks using *in vivo* micro-CT. From these scans the bone microstructure and density were evaluated, and mechanical properties were analyzed longitudinally. It was found that even with age, bone adapts to mechanical forces, and is able to optimize its bone strength. In the sixth caudal vertebra, this observation was supported by an increase in bone strength, a slight increase in mineralization, and significant correlations between bone strength and apparent volume density between all time points, up to 88 weeks of age. In the tibia, this was further substantiated by sustained resistance against bending and torsion, as measured with *in vivo* micro-CT, and a constant mineralization with age.

The novel finding of *Chapter 4.3* was that the sixth caudal vertebra in mice remained mechanosensitive during the aging process. To investigate this, load-induced bone adaptation was analyzed longitudinally in mice aged 15 weeks, 52 weeks, and 82 weeks at the start of loading. The effect of 6 weeks of loading was evaluated by monitoring the bone microstructure, bone remodeling and bone strength. Furthermore, to more accurately assess mechanosensitivity, initial strain energy density (SED) at sites where bone formation or bone resorption followed was compared to initial SED level at sites where no bone remodeling occurred subsequently. Several observations confirmed that the vertebra remained mechanosensitive during aging. Firstly, loading had a beneficial effect on the bone microstructure in all three age groups, by either increasing bone volume density and/or cortical area fraction, or by counteracting the bone loss that occurred for the 12 month old control mice. Also, loading had a beneficial effect on bone remodeling

in all three age groups, by increasing bone formation rate and decreasing bone resorption rate. Furthermore, for all three age groups loading had a beneficial effect on mechanical properties, by increasing bone strength significantly greater for the loaded than control group, or by keeping the bone strength constant in the loaded group, where the bone strength declined for the control group. Additionally, in all three age groups, for the loaded groups, the initial strain energy density (SED) could predict the change in bone volume fraction, with the observation that the sites where formation followed had significantly greater initial SED values than sites where bone remained constant, and sites where bone resorption followed had significantly lower initial strain energy density than constant sites. This indicated that not only globally, but also locally the bone of aged mice was still mechanosensitive, and formed bone at sites where necessary for mechanical integrity (high SED), while bone was resorbed at sites where load was no longer transferred through the bone, with a global positive effect of loading.

5.2 Limitations / evaluation of methods

5.2.1 *In vivo* micro-computed tomography

In vivo micro-CT allows to monitor changes in the bone microstructure. The great advantage of the analysis approach used, is that image registration is performed, which enables to observe the bone at follow-up time points using matched volumes of interest. This is very helpful when visualizing the quantitative data. Furthermore, by overlaying the follow-up scans, this enables to visualize locations of bone formation and bone resorption, and gives access to the calculation of dynamic bone parameters. These parameters are very sensitive both when bone formation is induced (loading), and when bone resorption is induced (OVX). A consideration with this technique is that in mice the mineral apposition rate is about $1.8 \mu\text{m}/\text{d}$, and that there should thus be at least 6 days between scans to pick up the differences (at a voxel size of $10.5 \mu\text{m}$). On the other hand, when there is too much time between scans, the intermediate remodeling cannot be picked up with this technique. Because values are calculated per day, this leads to values that are lower than the actual value. For the best estimation of dynamic bone parameters a time frame of 7-14 days is thus probably ideal. Here, the most important factor is that when longitudinal measures are required, the time frame over which the serial parameters are calculated should be the same. A limitation of *in vivo* micro-CT is that the scanned volume of interest has to be tightly fixed to prevent motion artifacts. For scanning of extremities like the caudal vertebra or tibia, this does not represent a

problem, but for scanning the trunk which is inherent to breathing motion, this is more challenging. Furthermore, there is always a trade-off between the volume that can be scanned, and the length of the anesthesia for the animal. When long measurements are performed the holder of the animal should be warmed, to maintain the animal at body temperature, to prevent hypothermia. Additionally, there is always a trade-off between the resolution of the scan and the radiation dose that the animal receives. To have no detrimental effects of ionizing radiation, the dose should be kept to a minimum. At the same time, the resolution of the scan should be good enough to resolve single bone structures. The resolution of $10.5 \mu\text{m}$ was sufficient for monitoring bone microstructure and for visualizing single trabeculae over time, and was sensitive enough for detecting changes in bone remodeling. At the same time, the associated radiation dose did not influence the bone microstructure or dynamic bone parameters. Also, a total of no more than 5 scans is recommended to allow to follow bone microstructure, and calculate dynamic bone parameters, but to keep radiation effects at a minimum.

5.2.2 Fluorescence molecular tomography

FMT allows to monitor osteoblast and osteoclast activity at multiple time points. The advantage of this technique is that it is very sensitive, fast, and that fluorescence distribution can be quantified (as opposed to 2D optical imaging). By using fiducial markers, the measurements are highly reproducible. Nevertheless, for our purposes the technique was not optimal, as the spatial resolution was too low to allow selection of only the loaded vertebra, and too low to distinguish from which region the fluorescence signal originated (growth plates or metaphysis). Nevertheless, when direct osteoblast activity needs to be measured in a 24 h time interval, FMT measurements would be preferred over dynamic bone parameters calculated from *in vivo* micro-CT. A limitation with the use of OsteoSense[®]680 was, that it remained bound to the bone for a long time (still present after 4 weeks). When multiple measurements are planned, a background image to detect fluorescence intensity of the previous probe, should be performed, to allow correction of the actual measure of osteoblast activity. Another consideration is that it is unclear whether the bound OsteoSense[®]680 influences binding of a subsequent probe injection. Likely, other probes for bone imaging which are cleared from the body will be marketed in the future. Cathepsin-K bound to a fluorophore, is such a probe, which represents osteoclast activity, and so far has only been available in one research group [8].

5.2.3 Mechanical loading model

The loading model allowed to induce load adaptation in the sixth caudal vertebra (CV6), with highly reproducible responses between experiments. There are several advantages of the tail loading model. Firstly, CV6 is not weight-bearing, thus responses seen in this bone are more directly an effect of loading. Secondly, it allows to study load adaptation both in trabecular and cortical bone. Thirdly, there is a large trabecular content in CV6. This is often necessary for gene detection technologies, and will prove useful in future studies which investigate load regulated genes. Fourthly, owing to the small size of CV6, the complete bone can be scanned within a feasible time, and a reasonable size of dataset. Due to the shape of CV6, the loading configuration is more simple, because the presence of bending stresses and shear stresses is minimal. Thus, realistic finite element analysis can be facilitated more readily and enables to characterize the spatial relationship between load induced bone adaptation and the associated micromechanical environment more closely. Fifthly, CV6 contains yellow or fatty bone marrow, and is consequently less sensitive for radiation and suitable for studies investigating aging or ovariectomy. A limitation of the loading model is that surgery has to be performed, and that problems with infections around the pins in the tails can arise. The occurrence of infections was not predictable: for some studies no infections were present at all, while in the worst case, half of the mice had to be sacrificed due to infections, even though hygiene standards were increased. Furthermore, surgery could in principle lead to a systemic acceleratory effect. Nevertheless, no such effect was observed in a previous control study where pinned mice were compared to age matched controls [9]. Another limitation of the loading model is that the applied load is always the same for each mouse and at each time point. But, because the bone volume density differs between mice, this leads to different strains between mice, and influences the load adaptation response. This could, however, be solved in the future, by performing FE analysis on the first scan, and using this for determination of the load needed to have the same strain for all mice.

5.2.4 Finite element analysis

The use of finite element analysis allowed to estimate bone strength non-invasively and to determine the strain energy density distribution over time. This was crucial information for investigating the relation between load adaptation and the micromechanical environment. The limitations of the finite element analysis are in the assumptions that have to be made. It is assumed that all voxels have the same

Young's Modulus, although this probably depends on the tissue mineral density, which is not constant in the bone. Nevertheless, with loading the tissue mineral density does not change significantly, indicating that this error is similar for all time points. Furthermore, discs are added on both sides of the model to represent the intervertebral discs. The discs were assigned the same properties as the bone, which is not representative for cartilage tissue. Nevertheless, when the discs were modeled with different properties to the enhance model, the results were the same.

5.3 Future research

During this doctoral thesis several ideas for future directions came up that would be interesting to further explore. These ideas for future research can be divided into methods that would be useful to implement, and hypotheses which could be investigated with the current imaging approach and loading model and would lead to novel insights in bone remodeling. The ideas for methods include the following:

Activation frequency from *in vivo* micro-CT data

Activation frequency describes the number of times per year that a spot on the bone surface begins the formation period in a BMU, and is often brought into relation with osteoporosis, where activation frequency rises during peri-menopause [10]. Thus when further investigating osteoporosis, it would be interesting to explore the possibility to determine the activation frequency from *in vivo* micro-CT data. Currently, the activation frequency can be calculated from histology and is defined by the bone formation rate at the surface, divided by the wall thickness. With *in vivo* micro-CT the resolution is not sufficient to determine the wall thickness of single remodeling sites. But, a BMU is also described as resorption followed by formation. By using serial *in vivo* micro-CT data it would be quite easy to determine the sites where resorption was followed by formation, and to use this to calculate a measure of activation frequency, e.g. the number of sites where resorption was followed by formation divided by the time between scans. Limitations related to such a procedure, however, are that many artifacts (partial volume effect) would be included in the analysis, and that the time frame chosen between scans would influence the parameter.

Regional evaluation of bone microstructure

Changes in the complete trabecular and cortical volumes have been presented in this thesis. When subregions were analyzed, a very clear trend was observed that

cortical adaptation to mechanical loading is the greatest in the center of the vertebra, while load-induced bone adaptation in the trabecular bone is the greatest close to the endplates (data not shown). To better understand relations between microstructure, remodeling, and micromechanical environment, it would be worthwhile to investigate subregional changes in these parameters more closely, and to correlate them. The challenge here is the large amount of data that this generates and the complicated statistical design with hundreds of values per mouse. Nevertheless, this can be simplified when taking into account only percentage changes between first and last time point, and not the weekly changes.

Evaluation of single trabeculae

For investigating the bone microstructure, several standard parameters have been defined. One of those, Tb.N. describes the amount of trabeculae per mm and is calculated from the inverse of the mean distance between the mid-axes of the structure (which are derived from center points of spheres that fill the trabecular structure). But since *in vivo* micro-CT allows tracking of single trabeculae, it would be interesting to determine changes in the single trabeculae, and to determine the amount of trabeculae. Skeletal decomposition, a procedure which was developed by Stauber et. al. [11], enables to separate an interconnected volume into single elements. This procedure could be applied to the data to find out how many trabeculae of a certain diameter exist, and whether all trabeculae are modulated by treatment, or only several, what the orientation of the trabeculae compared to the loading direction is, and enable to get a more thorough understanding of trabecular bone adaptation. A limitation in this procedure is, however, that it works well on rod-like trabecular bone, but less on plate-like trabecular bone, which is the type of bone present in the sixth caudal vertebra.

Load adaptation in bone ultrastructure

For the present work, microstructural load adaptation was investigated, while the ultrastructure of bone was neglected. Likely, an investigation of load-induced changes in the osteocyte lacunar network would enhance the understanding of load-induced bone adaptation, especially when these data can be related to changes observed at the microstructural level, so called hierarchical imaging. To investigate whether changes in the ultrastructure occur as an effect of loading, loaded and control vertebrae could be scanned with synchrotron radiation at the Swiss Light Source at a resolution of 1.2 μm . With recently developed scripts, it would be possible to determine the osteocyte lacunae number, size, shape, and orientation, and when these

data would be registered with the overlaid serial *in vivo* micro-CT scans, would enable to determine distances of osteocytes to remodeling sites, which could be useful information for computer simulations. Furthermore, the combination of finite element analysis on high resolution data with the overlaid serial *in vivo* micro-CT scans, would enhance understanding of influence of micromechanical environment on load adaptation. Actually, these high resolution data are available from the second experiment described in Chapter 3.2, but have not been analyzed. A limitation associated with synchrotron radiation, is that only end time points can be analyzed. Furthermore, the difficulty in registering ultrastructural with microstructural data is the large difference in resolution, and that for the ultrastructural scans not the whole vertebra was scanned, making it difficult to find the corresponding locations.

Cortical porosity

It has been shown that cortical porosity increases with age, by trabecularization of the cortex [12]. It is unknown whether this could be counteracted by loading. Cortical porosity can be evaluated from high resolution scans. Thus by scanning the bones of loaded and control mice of the different age groups (which are available), this could be investigated. Nevertheless, a limitation is that the mouse is probably not the best model for imitating human aging in cortical bone.

Ultrastructural mechanical properties of bone

Bone strength is attributed to the bone structure and the mechanical properties of the bone tissue. In the characterization of bone strength, it would be interesting to not only investigate mechanical parameters at a global level, assessed from micro-finite element analysis, but to also look more locally at the mechanical properties of the bone tissue, by using nano-indentation. These data could give insight in how load-induced adaptation influences bone mechanical properties at the local level and how the local mechanical properties are influenced by age or ovariectomy. It would also be interesting to gain a better idea in the relation between mineral density of the bone and the local bone strength, as this might enable to perform more accurate finite element analysis of bone strength, where voxel properties can be related to mineral density. Furthermore, this would allow to more directly compare remodeling sites to the local mechanical environment. Limitations considered with nano-indentation are that the preparation of the sample is tedious and laborious, and that the outcomes depend on the exact locations of indentation.

Hypotheses which would be interesting to extend upon include:

Continued increase of load

In the current implementation of load adaptation, the loading peak is always kept constant at a force of 8 N. It was shown that the sixth caudal vertebra was completely adapted to this load after 8-10 weeks of loading. Here, it would be interesting to investigate whether, when the bone has adapted to a certain load, the load can be increased, and with that can improve bone strength to an even greater extent. These loads could be chosen to match a certain strain energy density, which can be calculated from micro-finite element analysis. It could be hypothesized that as bone remodeling seems to be coupled tightly to the micromechanical environment, that bone will continue to adapt, as long as the load does not induce supra-physiological strains or microfractures. A limitation in investigating this with the current set up could be that the pins might not resist much higher loads.

Memory of bone cells

If bone cells would have the capacity to remember their loading history, and react faster a second time the same load is applied, this would be promising for elderly that were physically active in their younger years, and underpin the importance of physical activity for maintenance of bone strength with age. It could be hypothesized that load-adaptation occurs faster in the presence of a loading history. This could be tested by applying load-induced adaptation sequentially, with a period of no loading in between and by comparing changes in bone microstructure, dynamic bone parameters, and mechanical properties between the first time loading and the second time loading, and with a group that had no history of loading. Related questions to this hypothesis would be: Does the bone return to the initial bone microstructure when no loading is applied anymore? Is the bone losing period as fast as the bone gaining period (likely the bone losing period is faster, as osteoclasts are in greater abundance)? Limitations in investigating this would be that many scans have to be performed, and that the effect of aging might become a confounding factor.

Finally, a hypothesis which cannot be tested with the current imaging approach or equipment, but would be very interesting, is that cyclic loading in elderly would still be effective in increasing bone mass and bone strength. Although the mouse cannot directly be compared to the human, the fact that aged mice still respond to mechanical loading, is promising for human interventions. Currently,

whole body vibration systems exist for humans to improve the bone mineral density, and aerobic exercise, even though not anabolic, at least help to preserve bone mass. Results are, however, inconclusive. Thus, more experiments where humans are subjected to physiological activity should be performed to find out whether cyclic loading can improve bone mass in elderly, or could maintain a larger bone mass from adulthood on. Furthermore, greater physiological activity strengthens the muscles, which is important to prevent falls. A limitation in implementing such strategies is the availability of volunteers and ethical considerations.

5.4 Conclusions

In conclusion, the application of a functional bone imaging approach, as developed in this doctoral thesis, was shown to be very successful. The visualization of bone at multiple time points, allowed to monitor changes in bone microstructure accurately. Extraction of formation and resorption sites in 3D, allowed fast and sensitive measures for bone remodeling. Mechanical properties could be evaluated quickly, and provided good estimations for bone strength. The combination of these methods made it possible to discern how bone microstructure, bone remodeling, and bone strength are related with one another, and gave new insights in how bone remodeling is influenced by mechanical loading, aging or disease. The most important novel findings were firstly that load-induced bone adaptation is mostly governed by an increase in net osteoblastic activity and a decrease in net osteoclastic activity, leading to an overall increase in bone strength. Secondly, the sixth caudal vertebra was shown to be a suitable model for mimicking postmenopausal osteoporosis. Thirdly, the sixth caudal vertebra remains mechanosensitive during the aging process, by forming bone at sites subjected to high loads, and resorbing bone at sites subjected to low loads.

References

- [1] L. J. 3rd Melton, E. J. Atkinson, M. K. O'Connor, W. M. O'Fallon, and B. L. Riggs. Bone density and fracture risk in men. *J Bone Miner Res*, 13(12):1915–1923, 1998.
- [2] L.J. 3rd. Melton, E.A. Chrischilles, C. Cooper, A.W. Lane, and B.L. Riggs. Perspective. How many women have osteoporosis? *J Bone Miner Res*, 7(9):1005–1010, 1992.

- [3] P. Lips and N.M. Schoor. Quality of life in patients with osteoporosis. *Osteoporos Int*, 16(5):447–455, 2005.
- [4] M.J. Gronholz. Prevention, diagnosis, and management of osteoporosis-related fracture: a multifactorial osteopathic approach. *J Am Osteopath Assoc*, 108(10):575–85, 2008.
- [5] J.Y. Reginster, N. Sarlet, and M.P. Lecart. Fractures in osteoporosis: the challenge for the new millennium. *Osteoporos Int*, 16 Suppl 1:S1–S3, 2005.
- [6] J.A. Kanis and O. Johnell. Requirements for DXA for the management of osteoporosis in Europe. *Osteoporos Int*, 16(3):229–238, 2005.
- [7] B. Christen, B. van Rietbergen, F.M. Lambers, R. Müller, and K. Ito. Bone morphology allows estimation of loading history in a murine model of bone adaptation. *Biomech Model Mechanobiol*, accepted, 2011.
- [8] K.M. Kozloff, L. Quinti, S. Patntirapong, P.V. Hauschka, C.H. Tung, R. Weissleder, and U. Mahmood. Non-invasive optical detection of cathepsin K-mediated fluorescence reveals osteoclast activity in vitro and in vivo. *Bone*, 44(2):190–198, 2009.
- [9] D.J. Webster. *A combined experimental and computational model for genetic control of micro structural bone adaptation*. DISS. ETH NO. 17851, 2008.
- [10] E. Seeman. Reduced bone formation and increased bone resorption: rational targets for the treatment of osteoporosis. *Osteoporos Int*, 14 Suppl 3:S2–S8, 2003.
- [11] M. Stauber and R. Müller. A sensitivity analysis of the volumetric spatial decomposition algorithm. *Comput Methods Biomech Biomed Engin*, 10(1):25–37, 2007.
- [12] R. M. Zebaze, A. Ghasem-Zadeh, A. Bohte, S. Iuliano-Burns, M. Mirams, R. I. Price, E. J. Mackie, and E. Seeman. Intracortical remodelling and porosity in the distal radius and post-mortem femurs of women: a cross-sectional study. *Lancet*, 375(9727):1729–1736, 2010.

Curriculum Vitae

Floor M. Lambers

Born 25th September, 1981, in Amsterdam, The Netherlands

Education

03/2007 – 07/2011 Ph.D. student (Dr. sc. ETH), ETH Zurich, Institute for Biomechanics, Switzerland, under the supervision of Prof. Dr. Ralph Müller and Dr. med. vet. Gisela Kuhn

09/2000 – 10/2006 Master Biomedical Engineering (MSc), Eindhoven University of Technology, The Netherlands

10/2005 – 10/2006 Master thesis, Eindhoven University of Technology, The Netherlands, under the supervision of Dr. ir. Bert van Rietbergen, Dr. ir. Julienne Brouwers, and Prof. Dr. ir. Rik Huiskes

05/2005 – 09/2005 Internship, AO Research Institute, Davos, Switzerland, under the supervision of Dr. Marije van der Werf, Patrick Lezuo, and Prof. Dr. Keita Ito

01/2005 – 05/2005 Internship, Isotis/Twente University of Technology, The Netherlands, under the supervision of Dr. Lorenzo Moroni and Prof. Dr. Clemens A. van Blitterswijk,

08/1999 – 08/2000 Senior year, William Christmas Highschool, Missouri, USA

09/1993 – 07/1999 Gymnasium, College het Loo, Voorburg, The Netherlands

Work experience

03/2007 – 10/2011 Scientific research assistant at ETH Zurich, Institute for Biomechanics, Switzerland

09/2002 – 012/2006 Events-assistent at Music Hall Frits Philips, Eindhoven, The Netherlands

Publications

- 2011 F. A. Schulte, F. M. Lambers, G. Kuhn and R. Müller. *In vivo micro-computed tomography allows direct three-dimensional quantification of both bone formation and bone resorption parameters using time-lapsed imaging*. Bone, 48:433-442, 2011.
- 2011 P. Christen, B. van Rietbergen, F. M. Lambers, R. Müller, and K. Ito. *Bone morphology allows estimation of loading history in a murine model of bone adaptation*. Biomechanics and Modeling in Mechanobiology, DOI: 10.1007/s10237-011-0327-x, 2011.
- 2011 F. A. Schulte, F. M. Lambers, D. J. Webster, G. Kuhn, and R. Müller. *In vivo validation of a computational bone adaptation model using open-loop control and time-lapsed micro-computed tomography*. Bone, DOI: 10.1016/j.bone.2011.08.018, 2011.
- 2011 F. M. Lambers, F. A. Schulte, G. Kuhn, D. J. Webster, and R. Müller. *Mouse tail vertebrae adapt to cyclic mechanical loading by increasing bone formation rate and decreasing bone resorption rate as shown by time-lapsed in vivo imaging of dynamic bone morphometry*. Bone, accepted, 2011.
- 2011 A. Roshan-Ghias, F. M. Lambers, M. Gholam-Rezaee, R. Müller, D. P. Pioletti. *In vivo loading increases mechanical properties of scaffold by affecting bone formation and bone resorption rates*. Bone, accepted, 2011.
- 2011 F. A. Schulte, F. M. Lambers, T. L. Mueller, M. Stauber, and R. Müller. *Quantitative outcomes after image registration of micro-computed tomography scans critically depend on interpolation technique*. Computer Methods in Biomechanics and Biomedical Engineering, conditionally accepted, 2011.
- 2011 F. M. Lambers, G. Kuhn, F. A. Schulte, K. Koch, and R. Müller. *Transient bone morphometry in a mouse tail model of postmenopausal osteoporosis*. Calcified Tissue International, conditionally accepted, 2011.

- 2011 F. M. Lambers, G. Kuhn, M. Rudin, and R. Müller. *Advances in functional imaging and multimodality systems in bone research*. in preparation, 2011.
- 2011 F. M. Lambers, F. Stuker, C. Weigt, G. Kuhn, K. Koch, F. A. Schulte, J. Ripoll, M. Rudin, and R. Müller. *Multimodality imaging of load-induced bone adaptation*, in preparation, 2011.
- 2011 F. M. Lambers, G. Kuhn, C. Weigt, K. Koch, F. A. Schulte, and R. Müller. *Bone strength but not microstructure is retained in aging mice*. in preparation, 2011.
- 2011 F. M. Lambers, K. Koch, G. Kuhn, C. Weigt, F. A. Schulte, and R. Müller. *Longitudinal effects on bone strength and dynamic morphometry during 14 weeks of cyclic loading in a mouse model of bone adaptation*. in preparation, 2011.
- 2011 F. M. Lambers, C. Weigt, K. Koch, F. A. Schulte, G. Kuhn, and R. Müller. *Caudal vertebrae of mice remain mechanosensitive with age after cyclic loading*. in preparation, 2011.
- 2011 F. A. Schulte, D. Ruffoni, F. M. Lambers, G. Kuhn, D. Christen, D. J. Webster, R. Müller. *Local mechanical environment regulates osteoblast and osteoclast activity*. in preparation, 2011.
- 2011 F. A. Schulte, A. Zwahlen, F. M. Lambers, G. Kuhn, D. J. Webster, R. Müller. *Predictive model for bone adaptation using local load-adaptive feedback control*. in preparation, 2011.
- 2009 J. E. M. Brouwers, F. M. Lambers, B. van Rietbergen, K. Ito, and R. Huiskes. *Comparison of bone loss induced by ovariectomy and neurectomy in rats analyzed by in vivo micro-CT*. Journal of Orthopaedic Research, 27(11):1521-1527, 2009.
- 2008 J. E. M. Brouwers, F. M. Lambers, J. A. Gasser, B. van Rietbergen, and R. Huiskes. *Bone degeneration and recovery after early and late bisphosphonate treatment of ovariectomized Wistar rats assessed by in vivo micro-CT*. Calcified Tissue International, 82(3):202-211, 2008.

- 2007 L. Moroni, F. M. Lambers, W. Wilson, C. C. van Donkelaar, J. R. de Wijn, R. Huiskes, and C. A. van Blitterswijk. *Finite element analysis of meniscal anatomical 3d scaffolds: implications for tissue engineering*. The Open Biomedical Engineering Journal, 1(1):23-34, 2007.

Awards and honors

- 2010 ECTS Travel Award.
- 2009 ECTS Travel Award.